Technische Universität München
Max-Planck-Institut für extraterrestrische Physik
Garching bei München

Swift-BAT studies of AGN and the Cosmic X-ray Background.

Marco Ajello

Vollständiger Abdruck der von der Fakultät für Physik der Technischen Universität München zur Erlangung des akademischen Grades eines

Doktors der Naturwissenschaften

genehmigten Dissertation.

Vorsitzender:		Univ. Prof. Dr. A. J. Buras
Prüfer:	1.	Hon.-Prof. Dr. G. Hasinger
	2.	Univ. Prof. Dr. F. von Feilitzsch

Die Dissertation wurde am 21.02.2007 bei der Technischen Universität München eingereicht und durch die Fakultät für Physik am 25.04.2007 angenommen.

Contents

Summary

I have studied different aspects of Active Galactic Nuclei (AGN) and of the Cosmic X-ray background (CXB) using data from the Burst Alert Telescope (BAT) on board the *Swift* mission. BAT, which is currently performing the most sensitive all-sky hard X-ray survey ever, will provide the first unbiased census of the AGN population. The first three Chapters give an overview of:1) the interconnection of AGN and CXB, 2) the working principles of coded mask telescopes and the different imaging algorithms employed and 3) the *Swift* mission.

In Chapter 4, I describe an imaging reconstruction algorithm developed on the basis of the Maximum Likelihood (ML) method which allows to reach the statistical limit of the survey. The test bed application is a 90x90 $\deg^2$ region of the sky which BAT had surveyed to 1 Ms (at the time of this study) and which was used as a target for a campaign of optical spectroscopic identification of BAT selected AGN. I present all the details about ML method implementation, survey data processing, source detection and source identification. Chapter 5 reports the details of the ESO campaign for optical spectroscopic identification of BAT selected AGN. Even though it is not part of this thesis work it is reported here for completeness of discussion.

In Chapter 6, a method to extract accurate X-ray spectra for all BAT sources is presented and the detailed spectral analysis of all sources described. I investigated the capabilities of BAT to detect the photoelectric cut-off using known Compton-thick AGN. The Chapter ends with the derivation of the extragalactic source count distribution, with its comparison with previous measurements and with a discussion about the statistical properties of the source sample.

In Chapter 7, I derive, using BAT survey data, a new measurement of the CXB spectrum in the 15-150 keV energy band. This measurement relies on the modulation of the CXB signal caused by the Earth when it transits in the BAT field of view. Using a detailed Earth's emission model (based on observations and Monte Carlo simulations), the CXB and the Earth's emission spectra are derived without any assumption on their spectral shape. The Chapter presents the detail of the Earth model, the analysis of the systematic errors and the comparison of the CXB and Earth's spectra with previous measurements.

Chapter 1

Introduction

1.1 Active Galactic nuclei

“ Active galactic nuclei (AGN) constitute a somewhat vaguely defined class of objects. It is well possible that most galaxies have nuclei and that these are active in the sense that there is an energy source in addition to the thermonuclear sources inside the constituent stars. Something is called an AGN if this activity is “substantial” (Woltjer, 1990).

The observational studies of AGN started almost a century ago with the work of Fath (1908) who, first, recognized in the spectrum of one galaxy, NGC 1068, six emission lines. In 1943, Carl K. Seyfert, noted in the spectra of apparently “normal” spiral galaxies strong emission lines signaling the presence of photo-ionized gas (Seyfert, 1943); he stated that these nuclei are invariably luminous and their emission lines are wider than the absorption lines in normal galaxies.

Other classes of objects, together with the “Seyfert” galaxies, are today part of the AGN family, among them are: Radio galaxies, Quasi stellar objects (QSOs, radio-loud/-quiet), Blazars and Low Ionization Nuclear Emission-Line Regions (LINERs). They are all characterized by the fact that their energy output is not related to ordinary stellar processes. The different observed properties of such objects are today explained in the framework of the AGN unification model (Antonucci, 1993). The model is based on galaxies hosting super-massive black holes ($10^{6-10} M_{\odot}$, SMBH) which actively accretes from a disk radiating from the optical to X-ray energies. In proximity of the SMBH there are two gaseous regions with different velocities: the Broad-Line Region (BLR) and the Narrow-Line Region (NLR). The BLR with an electron density of at least 10^8 cm^{-3} (deduced by the absence of broad forbidden emission lines) and a typical gas velocity of 3000-10000 km/s

extends from 0.05 pc, for Seyfert 1 galaxies, to $\sim$ 1pc for luminous quasars. The NLR has lower gas density and velocity (10^{3-6}cm^{-3}, 300-1000 km/s), but can be much larger than the BLR since no clear variation of the narrow lines is observed in objects undergoing large continuum variation. The NLR has been resolved, in the Optical, for close-by Seyfert galaxies (e.g. NGC 1068), showing dimensions of 100-300 pc (see Kraemer & Crenshaw, 2000).

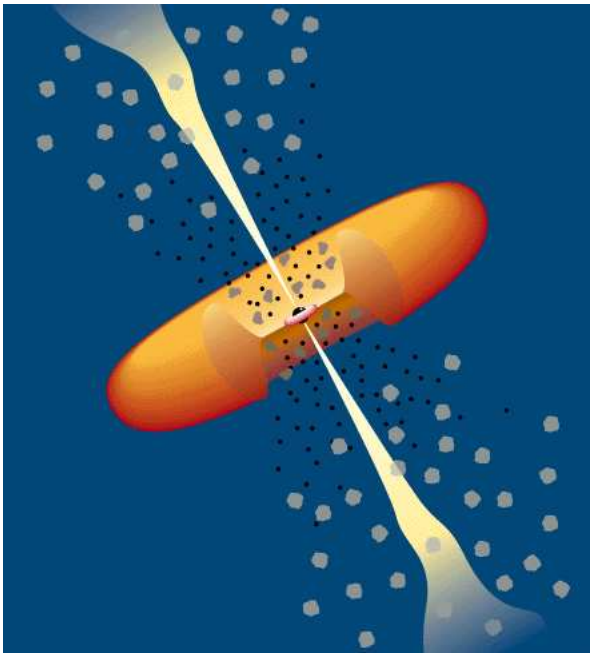

Figure 1.1: Schematic picture of an AGN, with collimated radio jets escaping along the axis of a thick torus of dust and gas. Depending on orientation, the torus hides or reveals the luminous continuum emission from the central super-massive black hole and its surrounding accretion disk. Relativistic beaming of the jet radiation generates an aspect-dependent appearance along the same axis (Urry & Padovani, 1995).

A fundamental ingredient of the AGN unification model is the presence of an obscuring torus of gas and dust that prevents infrared through ultraviolet from penetrating some lines of sight, in particular hiding the BLR. The presence of pc-sized obscuring torus has been recently confirmed by mid-infrared observations of the nuclear region of NGC 1068 (Jaffe et al., 2004). The last item of the unification paradigm is the presence of a relativistic jet formed within $\sim$100 Schwarzschild radii of the SMBH and extending outwards for tens of kpc. A simplified picture of the AGN unification scheme is reported in Fig. 1.1. The inherently axisymmetric model of AGN implies a radically different AGN appearance at different aspect angles. In practice, AGN of different orientations will be assigned to

different classes. Geometrical considerations (derived by the opening angles of ionizing cones described in section 1.1.1.2), indicate that the nucleus sees 1/4 of the sky and thus the fraction of obscured sources predicted by the unified scheme is 75% of the total AGN.

Below, we briefly discuss the observational evidences which support the unification model.

1.1.1 Observational evidence supporting the unified scheme

1.1.1.1 Super-massive black hole

Soon after the discovery of powerful radio galaxies and quasars, it was argued that their power was ultimately gravitational in origin as nuclear and atomic processes are just too inefficient. The main arguments in favour of the presence of a black hole are:

- rapid variability, with timescales as short as 1 min in low-luminosity Seyfert galaxies has been observed (Kunieda et al., 1990); the associated light travel time across the source can be as small as the Schwarzschild radius of a $\sim 10^7$ $M_\odot$ black hole. The characteristic variability timescale increases roughly with the luminosity of the AGN;

- the luminosity of an average quasar, assuming a 1% efficiency of thermonuclear processes, requires that 10^9 $M_\odot$ be packed into a volume size not larger than the solar system; in this case the gravitational binding would be comparable (or greater) than the nuclear energy source and the end state is a SMBH (Rees, 1984). Moreover, accretion onto a SMBH with 10^{7-9} $M_\odot$ meets the basic requirements of energy and variability;

- many of the brighter flat spectrum radio sources have been shown to exhibit superluminal expansion; superluminal expansion is expected when matter is moving at relativistic speeds;

- in some galaxies the velocity dispersion of stars within the nucleus has been measured. A dynamical determination of the mass gives values in the range $10^{6-8}M_\odot$ (e.g. the mass determination of the SMBH in our own galaxy produced by Eckart et al. 2004);

- HST observation of M87 directly proved the existence of a rapidly rotating disk of ionized gas (feeding a SMBH); the measured velocities are in agreement with the disks being Keplerian and they require the presence of a SMBH (Ford et al., 1994).

1.1.1.2 Broad and Narrow Line Regions

The characteristic spectral feature of Seyfert 1-1.5 and broad-line radio galaxies (BLRGs), as opposed to Seyfert 2 and narrow line radio galaxies (NLRG), is their broad permitted H I emission lines; however the broad-line spectra of AGN show a great deal of diversity in terms of relative line strengths and profiles. It is assumed that the lines are Doppler-broadened and their widths (full width half maximum, FWHM) usually range from 500 to 10^4 km/s with typical values of $\sim$5000 km/s. The strongest observed lines are the hydrogen Balmer-series lines (Hα λ6563, Hβ λ4861, Hγ λ4340), hydrogen Lyα λ1216, and prominent lines of abundant ions (Mg II λ2798 C III λ1909 and C IV λ1549). Emission-line fluxes vary with time in a way that is highly correlated with the continuum fluxes, which argues convincingly that photoionization by the central source drives the emission lines and that a large fraction of the recombination emission originates in clouds that are optically thick in the ionizing continuum. If the broad-line widths reflect purely thermal motions, the gas temperature would be $\sim 10^9$ K; clearly some other broadening mechanism is required, and this is usually attributed to differential Doppler shifts due to bulk motions of individual-emitting clouds. The absence (or extremely weakness) of forbidden lines (O III λ4363, λ4959, λ5007), explained as collisional de-excitation of the $^1S_0$ level in O^{++}, gives a lower limit for the electron density of $10^8 cm^{-3}$.
The equivalent width of the Lyα line allows to estimate how much of the continuum emission is absorbed by the BLR (Peterson, 1997) and thus the covering factor (f=$\Omega/4\pi$) of the BLR which results to be $\sim$10%.
Evidence of circumnuclear obscuration comes from spectropolarimetry of Type 2 objects (Antonucci & Miller, 1985). The polarization is likely produced by a population of electrons above the SMBH in the torus (see later). Tran (2001) has found that at least 35% of Type 2 objects have broad emission lines like Type 1 in polarized light.

Unlike the BLR, the electron density in the NLR is low enough that many forbidden transitions are not collisionally suppressed. A wide variety of ionization states are present in narrow-line spectra. Both low-ionization lines (e.g., O I λ6300) and high-ionization lines (e.g. O III λ4959, λ5007) are strong. The [O III]λ5007/Hβ flux ratio is usually larger than 3 and the FWHM for narrow emission lines falls in the range 200-900 km/s.
The presence of anisotropic continuum emission can be inferred from the extended narrow-line regions, sometimes tracing ionizing light cones, seen in direct imaging of many nearby Type 2 AGN. High resolution *HST* images of NGC 1068 (Evans et al., 1991) in the light of [O III] show evidence for an ionization cone with apex at an obscured nucleus. *In this and other cases the conical shape suggests that an obscured nuclear source*

with quasar-like luminosity is photoionizing gas in the extended narrow-line region (Urry & Padovani, 1995).

1.1.1.3 Relativistic beaming

When an emitting plasma has a bulk relativistic motion relative to a fixed observer, its emission is beamed in the forward direction (in the observer frame) as a direct consequence of the transformation of angle in special relativity. The detection of more than 40 blazars, at > 100 MeV energies, by the *EGRET* experiment on board the *Compton Gamma-Ray Observatory* (CGRO, von Montigny et al., 1995) is a confirmation of the existence of relativistically beamed radiation. In several blazars, the observed high-energy gamma-rays are highly variable, on time scales of a few days. Maraschi et al. (1992), using the variability to constrain the source dimension, have shown in a model independent way that the true blazar luminosity must be much smaller than the observed one and this can be explained as relativistic beaming as $L_{obs} = \delta^4 L$ where δ is the Doppler beaming factor. It is interesting to note that all *EGRET* blazars are radio-loud. Even though it is possible that radio-quiet AGN are below the detection sensitivity of *EGRET*, *OSSE* (on board CGRO) Seyfert 1 spectra show a steep cut-off in contrast to radio-loud objects. Thus it is likely that gamma-ray and radio properties are correlated and in turn are closely associated with relativistic beaming. In AGN usually only 1 side of the jet (approaching) is seen; in microquasars both jets are seen, with expansion speeds and brightness differences consistent with relativistic beaming.

1.1.2 AGN appearance in the Optical and at X-rays

In this section we mainly focus on the observational optical and X-ray properties of radio-quiet AGN. The radio-loud AGN are similar to radio-quiet AGN (as shown table 1.1), but are likely characterized by an extra component, i.e. a synchrotron-emitting jet which, when seen at small angles, allows the sources to be detected at high (gamma-ray) energies.

In the AGN unification model, schematically reported in table 1.1, Seyfert 1s and BLRGs are distinguished from their opposites, Seyfert 2s and NLRGs, by the orientation of the obscuring torus. If the torus is seen face-on, the view of the central regions is unobstructed and the observer sees the BLR detecting the broad emission lines; in this case the observer will identify the AGN as a Seyfert 1. In case the observer's line-of-sight is closer to edge-on, the central regions, and thus the BLR, are not seen directly and no broad emission lines are detected. The observer would classify this AGN as a Seyfert 2. The typical AGN optical spectra are shown in Fig. 1.3. For Seyfert 2 galaxies, a natural

question arises: if the torus is highly opaque, why is the AGN continuum visible? The key ingredient that make the torus model viable is an additional component, namely a "scattering medium" that lies above the hole in the torus, and scatters the nuclear light to an observer in the disk plane. A confirmation to this model comes from the detection of weak broad emission line in the optical spectrum, in linear polarized light, of the Seyfert 2 galaxy NGC 1068 and other sources (Antonucci & Miller, 1985). A polarized spectrum can result from scattering or reflection of the AGN continuum either by dust or by electrons. The polarization of the NGC 1068 continuum is wavelength independent, which indicates that the scattering particles are electrons rather than dust. Thus, it is very likely that Seyfert 2 galaxies (which show such polarized spectrum) have hidden BLRs. These observations confirm that *at least some* Seyfert 2 galaxies are intrinsically similar to Seyfert 1s.

Line flux ratios are often used to distinguish Seyfert galaxies from other type of emission-line galaxies. The most commonly used is the [O IIIλ5007]/Hβ flux ratio; unfortunately the criterion that [O III]/Hβ $>$3 for AGN is not robust since this flux ratio is also typical of low metallicity H II regions. Baldwin et al. (1981) have shown that various type of emission line spectra can be distinguished using two pairs of lines; the relative strengths of various lines are a function of the shape of the ionizing continuum. Fig. 1.2 demonstrates how LINERs can be distinguished, using the "BPT" diagram (Baldwin et al., 1981), from normal H II regions and AGN on the basis of the [O III]/Hβ and [N II]/Hα flux ratios.

Table 1.1: AGN unification scheme.

Radio Properties	**Face-On**	**Edge-On**
Radio Quiet	Seyfert 1	Seyfert 2
	QSO	
Radio Loud	BL Lac[1]	FR I[2]
	BLRG	NLRG
	Quasar/OVV[1]	FR II[2]

[1] BL Lac objects and optically violent variables (OVV) are usually referred to as blazars

[2] FR I and FR II (Fanaroff & Riley, 1974) are radio galaxies separate into two different luminosity classes (low and high luminosity respectively)

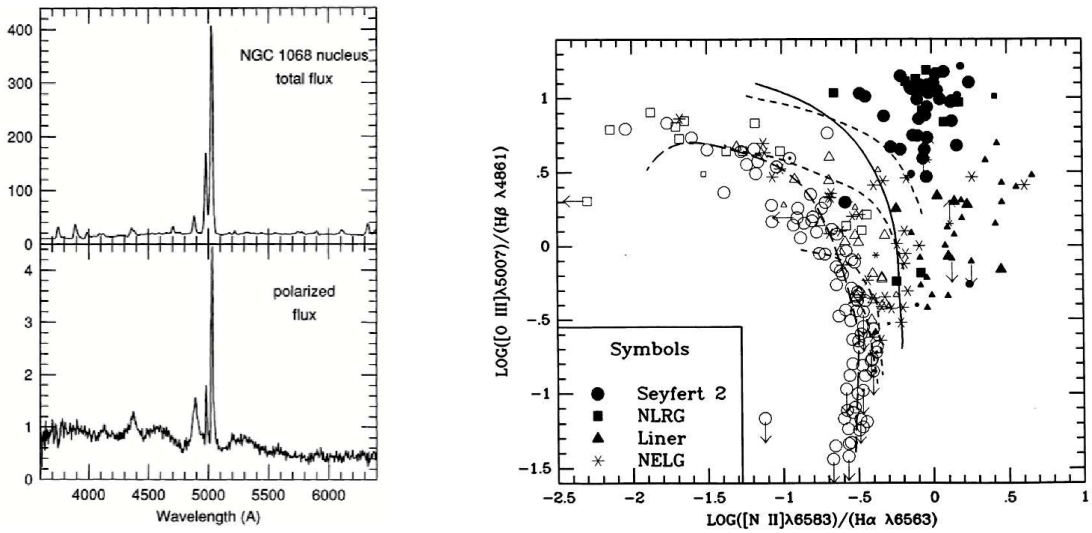

Figure 1.2: *Left Panel:* The top panel shows the nuclear flux of the Seyfert galaxy NGC 1068 while the bottom panel shows the linearly polarized flux (Miller et al., 1991). The broad Hβ line, in polarized light, points in favor of a hidden BLR and thus to the fact that Seyfert 2 galaxies are intrinsically similar to Seyfert 1. *Right Panel:* Diagnostic diagram for emission-line galaxies. The vertical axis is the [O III] λ5007/Hβ flux ratio and the horizontal axis is the [N II] λ6583/Hα flux ratio. Both ratios are based on lines close in wavelength and are therefore reddening independent. The open circles are for H II regions and similar sources which are clearly ionized by hot stars. The solid line separates AGN from H II region-like objects. Adapted from Veilleux & Osterbrock (1987).

1.1.2.1 The high energy emission

The origins of X- and gamma-ray emission in AGN is not completely understood. In many models, the X-ray emission is produced by inverse-Compton (IC) scattering of lower-energy photons by more energetic electrons. The basic idea is that the UV/optical continuum from the accretion disk is up-scattered (in energy) by IC scattering off hot (possibly relativistic) electrons in a corona surrounding the disk, a process commonly referred to as "Comptonization" of the input spectrum. However, the origin of the electron population is still a matter of debate. At X-ray energies, AGN spectra are characterized by a power-law with a photon index of $\sim$1.9 which is consistent with a saturated pair-production model (i.e. all gamma-rays convert into electron-positron pairs). In ad-

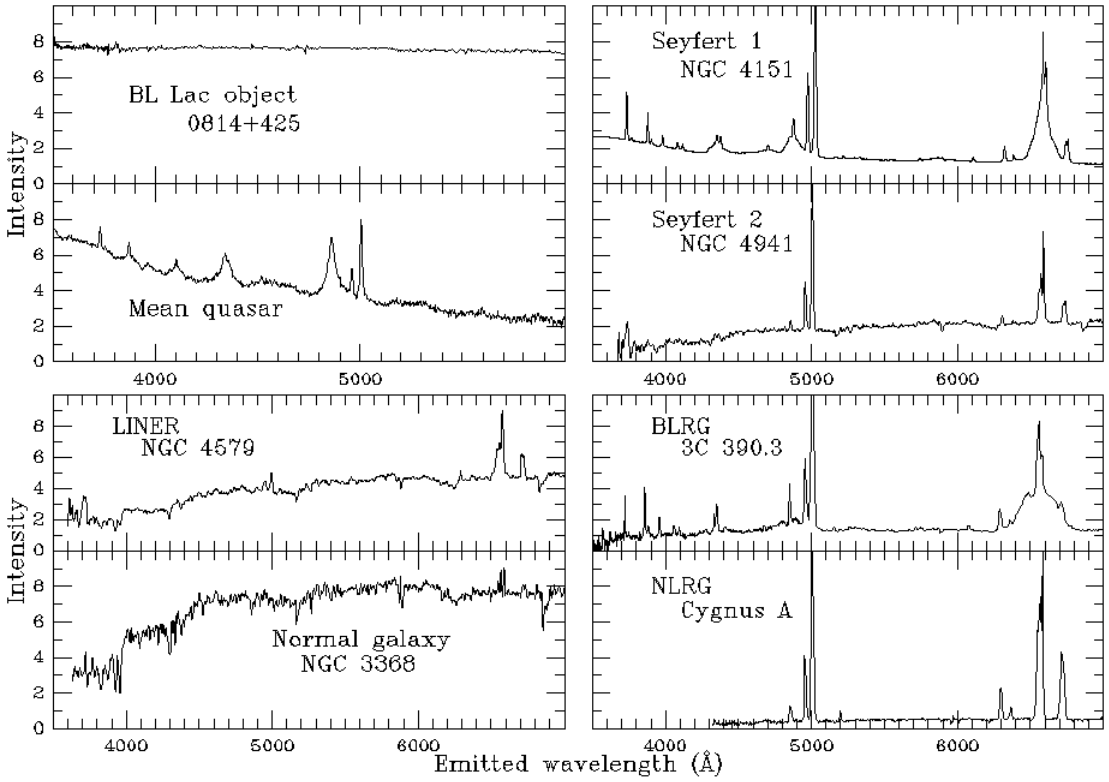

Figure 1.3: Optical spectra of different members of the AGN family; as a comparison a spectrum of a normal galaxy is shown on the bottom left part of the graph. Spectra have all been shifted to rest frame wavelength for ease of comparison. Adapted from Keel (1983) and Owen et al. (1990).

dition to the basic power-law, AGN usually show other components. At low energies, $<$2 keV, absorption from heavy elements is often detected (Reichert et al., 1985). These are primarly K- and L-shell ionization edges from Fe, Mg, Si, and S. By assuming solar abundances, the equivalent hydrogen column densities necessary to produce the observed absorption are of order $\sim 10^{22}$ cm^{-2}. The strength of the absorption can vary with time, leading to the deduction that these are 'warm absorbers', i.e. they have ionization fronts that are variable in position within the absorber.

In the soft X-ray range (< 2 keV) many AGN show a steep rise in the spectrum towards low energies (Turner & Pounds, 1989). This is referred to as "soft excess". Its origin is not yet clear; it has been argued that this feature is the Comptonized Wien tail of the UV/optical emission from the putative accretion disk (referred to as blue bump).

At higher energies (E$\geq$10 keV), AGN X-ray spectra rise above the typical power-law spectrum; this is usually attributed to inelastic scattering of high-energy photons off low-

energy electrons (Compton electrons) perhaps in the accretion disk itself. At least one emission line, Fe Kα, is clearly detected. The observed widths of the Kα line often corresponds to velocities of $\sim 10^4$km/s (Mushotzky et al., 1995); in one extreme case, MCG-6-30-15, the Kα line has a width of 10^5 km/s and is apparently gravitationally redshifted, which argues strongly in favour of an origin near a SMBH (Tanaka et al., 1995).

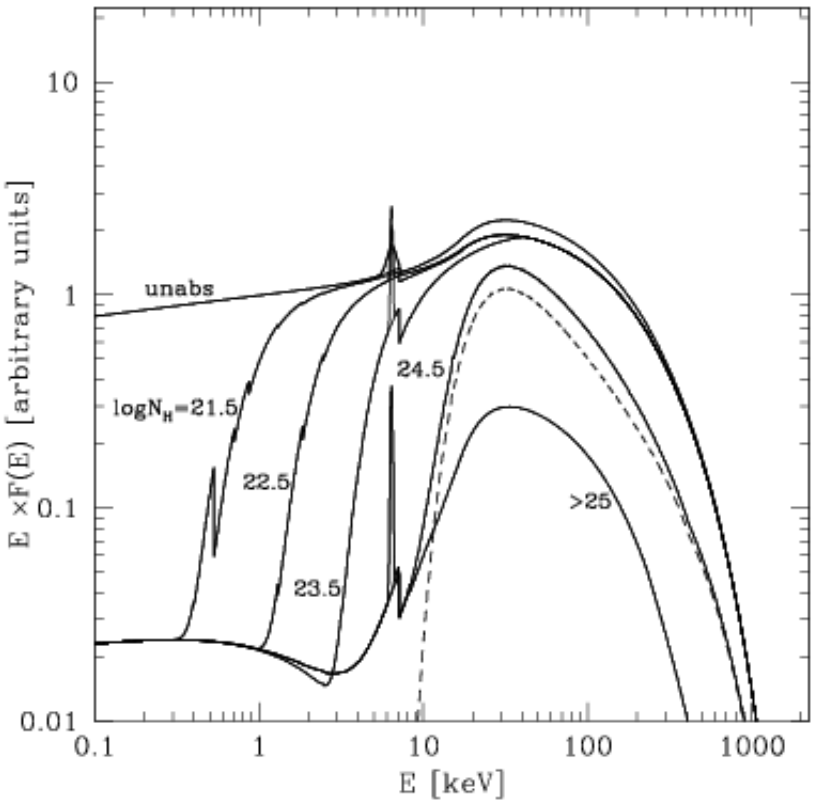

Figure 1.4: AGN spectra with different level of absorption. Solid lines from top to bottom: NH = 0 (i.e. unabsorbed AGN), logNH = 21.5, 22.5, 23.5, 24.5, $>$ 25. A primary power-law with photon index 1.9 and cut off energy Ec = 200 keV is assumed. The reflection "hump" around 10 keV and the Fe Kα emission line are visible. Adapted from Gilli et al. (2006).

The one here described, and shown as the upper curve in Fig. 1.4, is the typical spectrum of an unabsorbed AGN, i.e. the spectrum which an observer would see if his line-of-sight does not intersect the torus. If the observer's line-of-sight passes through the torus, photoelectric absorption starts to suppress the X-ray emission, the amount of absorption being determined by the angle relative to the obscuring torus. Unabsorbed AGN appear, usually,

in the Optical as Seyfert 1 galaxies whereas absorbed ones should appear in the optical as Seyfert 2; this is not a one-to-one relation as 10% of Seyfert 1 galaxies have absorbed X-ray spectra and a few Seyfert 2 objects seem to be unabsorbed. The effect of absorption on the AGN spectral template is shown in Fig. 1.4; for a Compton-thick AGN (see discussion in section 1.2.7) the absorbing column density is of order 10^{24-25}H-atoms/cm^2 and the $<$ 10keV emission is suppressed to a small fraction ($\sim$ 2%) of its original flux. These objects are clearly best detected and studied in the $>$ 15 keV band.

1.2 The X-ray background

1.2.1 Early history

The goal of one of the first X-ray experiments, flown on a missile outside the Earth atmosphere, was detecting fluorescent X-rays produced on the lunar surface since it was believed to be the strongest source (Giacconi et al., 1962). Instead, it achieved two major discoveries: the detection of the first X-ray point-like source (Sco X-1) and of a diffuse isotropic, and thus extragalactic, X-ray emission which was subsequently referred to as the X-ray background (XRB). Since the discovery of the XRB, its origin was discussed in terms of two alternative interpretations: the truly diffuse hypothesis (e.g. hot intergalactic gas) and the discrete source hypothesis. The first important steps towards the understanding of the XRB have been done with the first all-sky surveys (UHURU and ARIEL V, Giacconi et al. (1974); McHardy et al. (1980)) at the beginning of the seventies. The high degree of isotropy revealed by these surveys led immediately to realize that the origin of the XRB has to be extragalactic and that in the discrete source hypothesis the number of sources contributing to the XRB has to be very large (N$>$ 10^6sr^{-1}, Schwartz & Turner (1988)). At the beginning of the eighties two different sets of measurements led additional fire to the debate between supporters of the discrete source and diffuse hypotheses. On the one hand, the excellent HEAO-1 data showed that in the energy range 3-50 keV the shape of the XRB is very well fitted by an isothermal bremsstrahlung model corresponding to an optically thin, hot plasma with kT of the order of 40 keV (Marshall et al. 1980). Moreover, it was shown by Mushotzky (1984) that essentially all the Seyfert 1 galaxies with reliable 2-20 keV spectra ($\sim$ 30 objects, mostly from HEAO-1 data) were well fitted by a single power law with an average photon index of the order of 1.65, significantly different from the slope of the XRB in the same energy range. These two observational facts were taken as clear "evidences" in favour of the diffuse thermal hypothesis. On the other hand, the results of the EINSTEIN deep survey showed that about 20% of the soft XRB (1-3 keV) are resolved into discrete sources at fluxes of the order of a few 10^{-14}erg

$cm^{-2}s^{-1}$ (Giacconi et al. 1979, Griffiths et al. 1983). A large fraction of these faint X-ray sources have been identified with Active Galactic Nuclei (AGN). The final resolution of the controversy came from the incredibly neat result obtained with the FIRAS instrument on board COBE: the absence of any detectable deviation from a pure black body of the cosmic microwave background set an upper limit on the contribution of an uniform hot intergalactic gas to the XRB of $< 10^{-4}$ (Wright et al., 1994).

1.2.2 Deep X-ray surveys

1.2.2.1 ROSAT observation of the Lockman Hole

Having the COBE data definitely eliminated the possibility of an important contribution of diffuse gas emission to the XRB, the important question to be addressed subsequently was: what are the sources that are responsible for the observed XRB?
The good angular resolution and sensitivity of the Position Sensitive Proportional Counter (PSPC), in the 0.1–2.4 keV band, aboard ROSAT have allowed to extend to significantly lower fluxes the deep imaging studies first performed with EINSTEIN.
The deepest ROSAT image has been obtained by Hasinger et al. (1993) in the direction of the Lockman Hole, characterized by an extremely low neutral hydrogen column density. These data have been used by Hasinger et al. (1993), together with additional data from 26 other shallower ROSAT exposures, to obtain the log N - Log S relation shown in Figure 1.5. The total number of sources used in the construction and analysis of the log N - log S relation is 661 and they cover a range of more than two decades in flux. The main result is that at least 60% of the XRB emission is resolved into (detected) sources above 10^{-15}erg $cm^{-2}s^{-1}$ (and up to 85% above 10^{-16}erg $cm^{-2}s^{-1}$ considering the fluctuation analysis results). Optical identification of the sources in the Lockman Hole revealed that a fraction as high as $\sim$ 85% of the detected objects are AGN (Lehmann et al., 2000). This showed without any doubt that AGN are the dominant population among the X-ray sources at this flux and the main contributors to the XRB emissions.

1.2.3 AGN evolution from Deep X-ray surveys

Recently, deep X-ray surveys with the *Chandra* and *XMM-Newton* satellites (Brandt et al., 2001; Alexander et al., 2003; Hasinger et al., 2001), paralleled by multiwavelength campaigns (e.g. GOODS, Giovalisco et al., 2004) provided several crucial information on the evolution of the AGN populations. The important result from the two deepest X-ray fields, the Chandra Deep Field North (CDFN, observed for 2 Ms) and the Chandra Deep Field South (CDFS, observed for about 1 Ms) is constituted by the resolution of the XRB

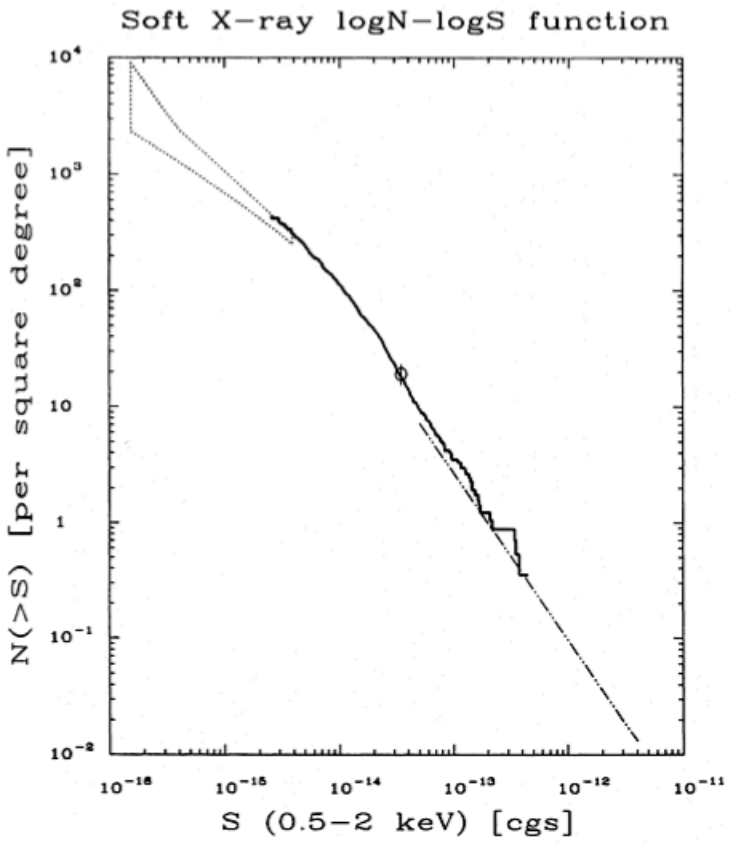

Figure 1.5: Integral source count distribution from the ROSAT observation of the Lockman Hole (Hasinger et al., 1993). The solid line is the ROSAT distribution while the dot-dashed line is the source count distribution from the Einstein Medium Sensitivity Survey (EMSS, Gioia et al., 1991). The dotted area at lower fluxes shows the 90% confidence region from fluctuation analysis performed in the Lockman Hole.

into single sources, mostly AGN, at a level between 80% and 90% (Hickox & Markevitch, 2005) in the 0.5-8 keV band. These surveys provide an almost complete census of the accretion history of matter onto super-massive black holes through cosmic epochs. However, the most interesting outcomes go well beyond the demographic characterization of the extragalactic X-ray sky. Indeed, the physical and evolutionary properties of the AGN population are now revealing how they formed and how they are linked to their host galaxies. A striking feature is the *downsizing*, or anti-hierarchical, behavior of the nuclear activity: the space density of the brightest Seyfert 1 and QSO peaks at $z \geq 2$ while the less luminous Seyfert 2 and 1 peak at $z \leq 1$ (Hasinger et al., 2005). This is clearly

shown in Fig. 1.6, where the number density of more luminous AGN (QSOs) peak earlier in the history of the universe, while the low luminosity arise later. An analogous behavior is presently observed in the cosmic star formation history: at low redshift star formation is mostly observed in small objects (e.g. Kauffmann et al., 2004), while at redshift 2 or higher, star formation activity is observed also in massive galaxies with $M_* \sim 10^{11} M_\odot$ (Daddi et al., 2004).

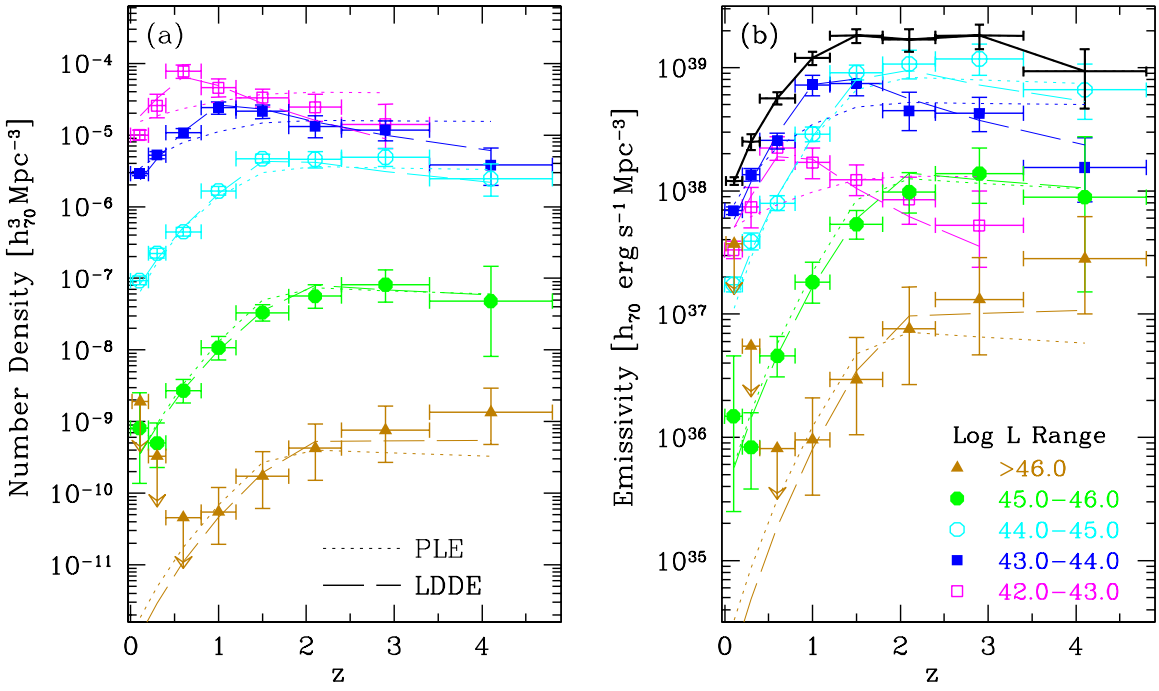

Figure 1.6: (a) The space density of AGN as a function of redshift in different luminosity classes and the sum over all luminosities with $\log L_x \geq 42$. Densities from the pure luminosity evolution and luminosity-dependent density evolution models, as defined in Hasinger et al. (2005), are overplotted with solid lines. (b) The same as (a), except that the soft X-ray emissivities are plotted instead of number densities. The uppermost curve (black) shows the sum of emissivities in all luminosity classes plotted. Adapted from Hasinger et al. (2005).

"*These new results paint a dramatically different evolutionary picture for low-luminosity AGN compared to the high-luminosity QSOs. Obviously, the rare, high-luminosity objects can form and feed very efficiently rather early in the universe. Their space density declines by more than two orders of magnitude at redshifts below z=2. The bulk of the AGN, however, has to wait much longer to grow with and shows a decline of space density by less than a factor of 10 at redshifts below one*" (Hasinger et al., 2005).

As a consequence, half of the total black hole mass density was accumulated at redshift z < 1. This is consistent with the most recent results from XRB studies. After the deep Chandra and XMM surveys have revealed the redshift distribution of the obscured sources that most contribute to the XRB (Alexander et al., 2001; Barger et al., 2002; Mainieri et al., 2002), the newest synthesis models seem to suggest that indeed a substantial fraction of the locally measured mass density of super massive black hole (SMBH) (maybe up to 50%) was accumulated in (obscured) type-2 low-mass AGN (with M $< 10^8 M_{\odot}$) at z < 1 (see e.g. Gandhi & Fabian 2003, and references therein).

1.2.4 Fitting the XRB and population synthesis models

A major liability of the discrete source model has been the "spectral paradox" as summarized by Boldt (1987):

"*While the majority of the extragalactic sources detected with the* HEAO 2 Einstein Observatory *are probably AGN, the broad band continuum of the brightest objects as measured with* HEAO 1 *exhibit spectra quite different from that of the XRB; these AGN exhibit power-law spectra with a photon index of 1.7, apparently independent of classification and luminosity. Such power-law fails to fit the XRB spectrum* " which in the 2-10 keV range can be approximated with a power-law with photon index of 1.4.
The main problem connected with the spectral paradox was the assumption that the AGN spectra are described by a single power law from 3 to 100 keV. Schwartz & Turner (1988) were among the first ones to show that AGN spectra which tend to flatten with energy, integrated through redshift with reasonable assumptions on the cosmological evolution, could provide an adequate fit to the shape of the observed XRB from 3 to 100 keV. Their assumption was confirmed few years later by the GINGA observations (2-30 keV); indeed, Pounds et al. (1990) and Nandra (1991) have shown convincingly that the typical spectrum of Seyfert 1 galaxies shows a flattening at $\sim$10 keV, with respect to the observed power law slope in the range 2-10 keV. Such flattening has been interpreted either as a partial coverage of an underlying X-ray power law continuum or as reprocessed emission (reflection) from thick relatively cold matter, possibly in an accretion disk. This discovery led a number of groups to construct models for fitting the XRB spectrum with various combinations of AGN spectra (see, for example, Morisawa et al. (1990) and Fabian et al. (1990)). Although qualitatively in agreement with the overall shape of the XRB in the energy range 3-100 keV, these first models have been shown not to be able to fit satisfactorily the position and the width of the peak of the XRB spectrum (Zdziarski et al., 1993). It must be said, however, that such early models assumed a strongly enhanced reflected

component, much larger than (today) observed in Sy1 galaxies.

A different approach based on the X-ray properties of the AGN unified scheme was suggested by Setti & Woltjer (1989). By playing with reasonable masses, sizes and inclination angles of the tori, whose existence was confirmed by HST observations (Jaffe et al., 1993), they demonstrated that is possible to reproduce the XRB spectrum requiring that the number of absorbed sources (Sy2) is approximately equal to the number of unobscured ones. However, it was shown that almost equally good fits to the XRB spectrum can be obtained under significantly different assumptions on the source spectra and evolution; thus as pointed out by Zamorani (1994), a good fit to the XRB spectrum does not mean that the synthesis of the XRB is understood.
Comastri et al. (1995) were among the first ones to produce a self-consistent model for the synthesis of the XRB which successfully fits the XRB spectrum in the 3-100 keV range; they start from the observed soft X-ray luminosity function (XLF, Boyle et al. (1993)) and under the assumption that the shape of the XLF and evolution of absorbed objects is the same as that of unabsorbed ones (i.e. the N_H distribution *does not* depend on luminosity) derive the best fit parameters, essentially the model N_H distribution, which reproduce the observed XRB spectrum. Their model, which determines that the fraction of absorbed objects is 75% of the total AGN, is also able to reproduce a set of other observational constraints like the ROSAT logN-logS and redshift distributions (Hasinger et al., 1993) and the redshift distribution of the HEAO-1 A-2 sample (Piccinotti et al., 1982).

It is only with the availability of sensitive and highly complete surveys, performed mainly with *ASCA, Chandra* and *XMM-Newton* that fine modeling of the AGN properties can start. Ueda et al. (2003) derive the hard XLF (HXLF, above 2 keV) combining a set of highly complete surveys which cover 5 decade in flux down to 10^{-15}erg cm^{-2} s^{-1}. Main results of their work is that the fraction of absorbed AGN decreases with X-ray intrinsic luminosity, as shown in the left panel of Fig. 1.12, and that the evolution of the HXLF of all AGN is best described by a luminosity-dependent density evolution (LDDE, i.e. luminous AGN evolve faster at high redshift) of the form:

$$\frac{d\Phi(L_X,z)}{dlog\,L_X} = \frac{d\Phi(L_X,0)}{dlog\,L_X} e(z,L_X) \tag{1.1}$$

where,

$$e(z,L_X) = \begin{cases} (1+z)^{p_1} & [z < z_c(L_X)], \\ e(z_c)\left[\frac{1+z}{1+z_c(L_X)}\right] & [z \geq z_c(L_X)], \end{cases} \tag{1.2}$$

and

$$z_c(L_X) = \begin{cases} z_c^* & (L_X \geq L_a), \\ z_c^* \left(\frac{L_X}{L_a}\right)^{\alpha} & (L_x < L_a), \end{cases} \tag{1.3}$$

with L_a and z_a^* fixed at 44.6 and 1.9 respectively.
In equations 1.1 and 1.2 $e(z, L_X)$ is the evolution factor whose cut-off redshift z_c, the redshift above which the evolution terminates, is a function of luminosity L_X as expressed in 1.3. Their finding that the the cut-off redshift z_c increases with luminosity, translates into a ratio of the peak spatial density to that of present day which is smaller for AGN with Log L_X <44.5 than for more luminous AGN as also shown in the Fig. 1.6 from Hasinger et al. (2005). Their fit to the XRB spectrum suggests the presence of roughly an equal number of Compton-thick AGN of Log N_H=24-25 as those with Log N_H=23-24 in agreement with the distribution of Risaliti et al. (1999) discussed in section 1.2.6.

La Franca et al. (2005), using an even larger sample, extend the HXLF up to z=4 confirming most of the results from Ueda et al. (2003): the LDDE behavior of the HXLF and the decrease in the ratio of obscured AGN with luminosity. Moreover, they are able to determine the increase of the number of obscured sources with redshift; this dependence which is shown in the right panel of Fig. 1.12 was also recently confirmed by Tozzi et al. (2006).
On the other hand Treister & Urry (2005), after correcting for selection effect, find that the simple AGN unification scenario, which assumes that obscured AGN outnumber the unobscured ones by a factor 3 and that this ratio does not vary with luminosity nor redshift, reproduces the XRB spectrum well. They also show that a luminosity-dependent N_H distribution allows an equally good fit to the XRB spectrum and allow an estimate of the number counts in the 2-10 keV band which is in very good agreement with present observations.

Gilli et al. (2006) recently presented a new modeling of the XRB based on a slightly different approach with respect to the past. Given all the discrepancies among different measurements of the XRB spectrum (see discussion in section 1.2.8), they optimize their model in order to be able to reproduce the robust and established observational data like the logN-logS and luminosity functions in both the 0.5-2 keV and 2-10 keV ranges and then they verify a posteriori the resulting XRB spectrum. As shown in Fig. 1.7, they adopt the soft-XLF (SXLF, 0.5-2 keV) from Hasinger et al. (2005) as the XLF of unab-

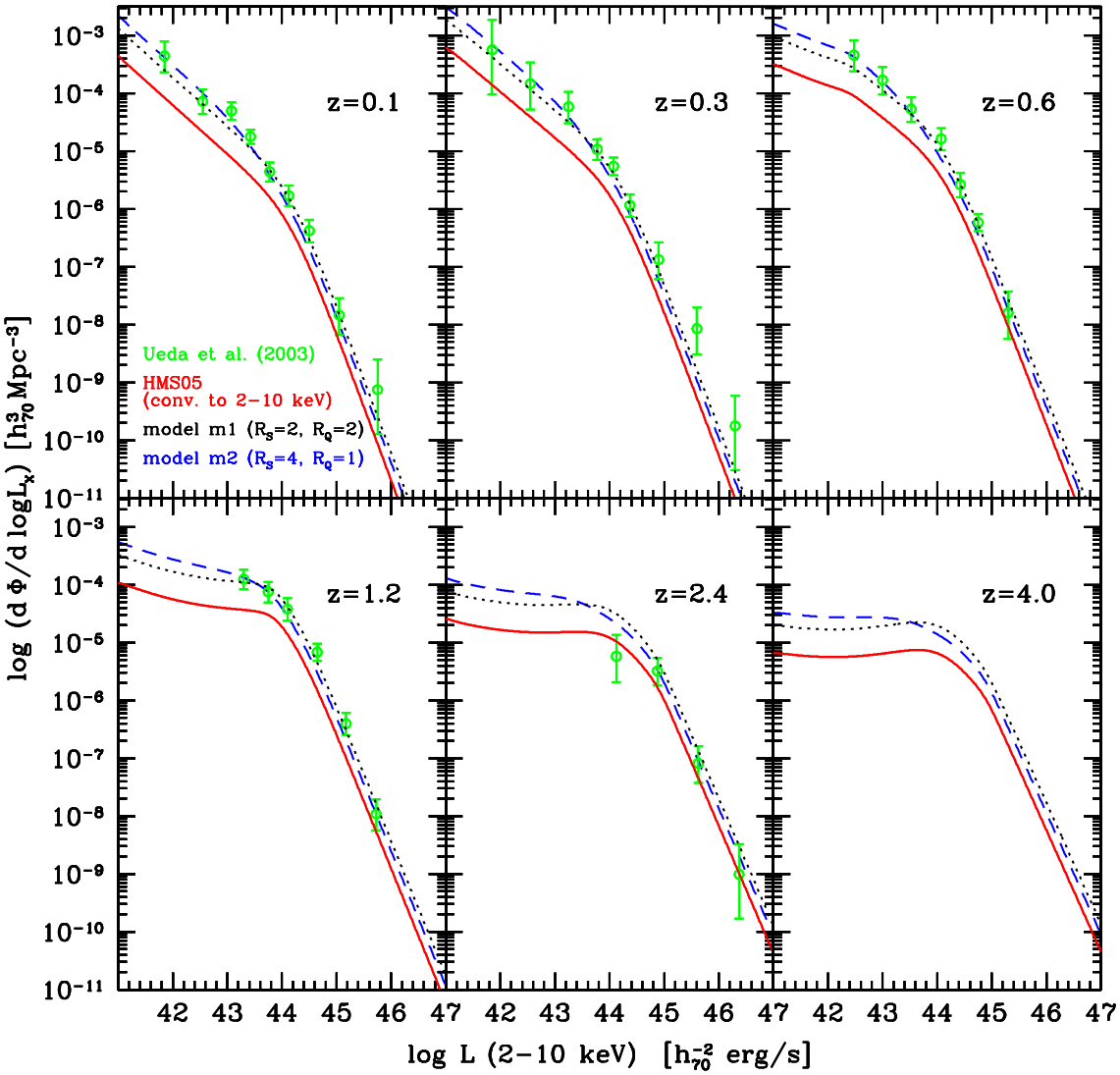

Figure 1.7: X-ray luminosity functions adapted by Gilli et al. (2006). Green datapoints are the Ueda et al. (2003) HXLF; the red solid line is the SXLF from Hasinger et al. (2005) converted to the 2-10 keV band. The dotted and dashed lines refer to two different models where the ratio of obscured and unobscured does not depend and depends on the luminosity respectively (as discussed in Gilli et al., 2006).

sorbed AGN and the HXLF, 2-10 keV, from Ueda et al. (2003) as the one for unobscured *and* Compton-thin (Log N_H <24) AGN; the difference between the HXLF and the SXLF, converted to the 2-10 keV band, provides the XLF of Compton-thin AGN. The fit to the

source counts in the 0.5-2 keV, 2-10 keV and 5-10 keV bands provides the absorption distribution which is shown, for comparison together with other N_H distributions, in Fig. 1.8. They find, in agreement with Ueda et al. (2003) and La Franca et al. (2005), that the obscured to unobscured AGN ratio decreases from 4 (8 including Compton-thick AGN) at low luminosities to 2 at high luminosities. The fit to the XRB spectrum, shown in Fig. 1.9, allows to constrain the number of Compton-thick AGN (otherwise undetermined); in agreement with Risaliti et al. (1999) they are found to be as numerous as the Compton-thin ones. The uncertainty on this number, however, follows closely the uncertainty on the overall normalization of the XRB spectrum at 30 keV, thus, since the HEAO-1 A-2 XRB spectrum (as used in Gilli et al. (2006)), is found to be $\sim$10% lower than more recent determinations (see section 1.2.8) the number of Compton-thick sources could be a factor 2 larger. The number of the expected Compton-thick sources at the flux levels of the CDFS (Tozzi et al., 2006) and Swift and INTEGRAL hard X-ray surveys (Markwardt et al., 2005; Beckmann et al., 2006; Bassani et al., 2006) are consistent with the observations.

1.2.5 Resolving the XRB

However, quoting the resolved fraction of the XRB in the < 10 keV band is somewhat misleading. Indeed, in a recent study Worsley et al. (2005) showed that the three deepest X-ray surveys, the XMM-Newton observation of the Lockman Hole, CDFS and CDFN (Hasinger et al., 2001; Giacconi et al., 2002; Alexander et al., 2003) point to a significant reduction in the resolved fraction of the XRB at the hardest energies. This is also shown in Fig. 1.10, which reports the resolved fraction of the XRB, for these 3 surveys, as a function of energy; in particular, above 5 keV, the resolved fraction can be as low as 50%. The spectral analysis of the missing fraction (difference between the total and resolved part) is consistent with the spectrum of highly obscured AGN and could be evidence of the large population of heavily absorbed objects which are thought to account for the 30 keV peak of XRB intensity(Worsley et al., 2005). The same authors conclude that the most plausible population would be of objects at redshift $\sim 0.5-1.5$, with unabsorbed luminosity of 10^{43}erg s^{-1}, but heavily absorbed by column densities of $\sim 5\times10^{23}$ H-atoms cm^2.

This finding opens again the issue of the resolution of the XRB, requiring the presence of a still undetected population of strongly absorbed AGN at moderate redshift, as can be inferred from the spectral shape of the missing XRB.

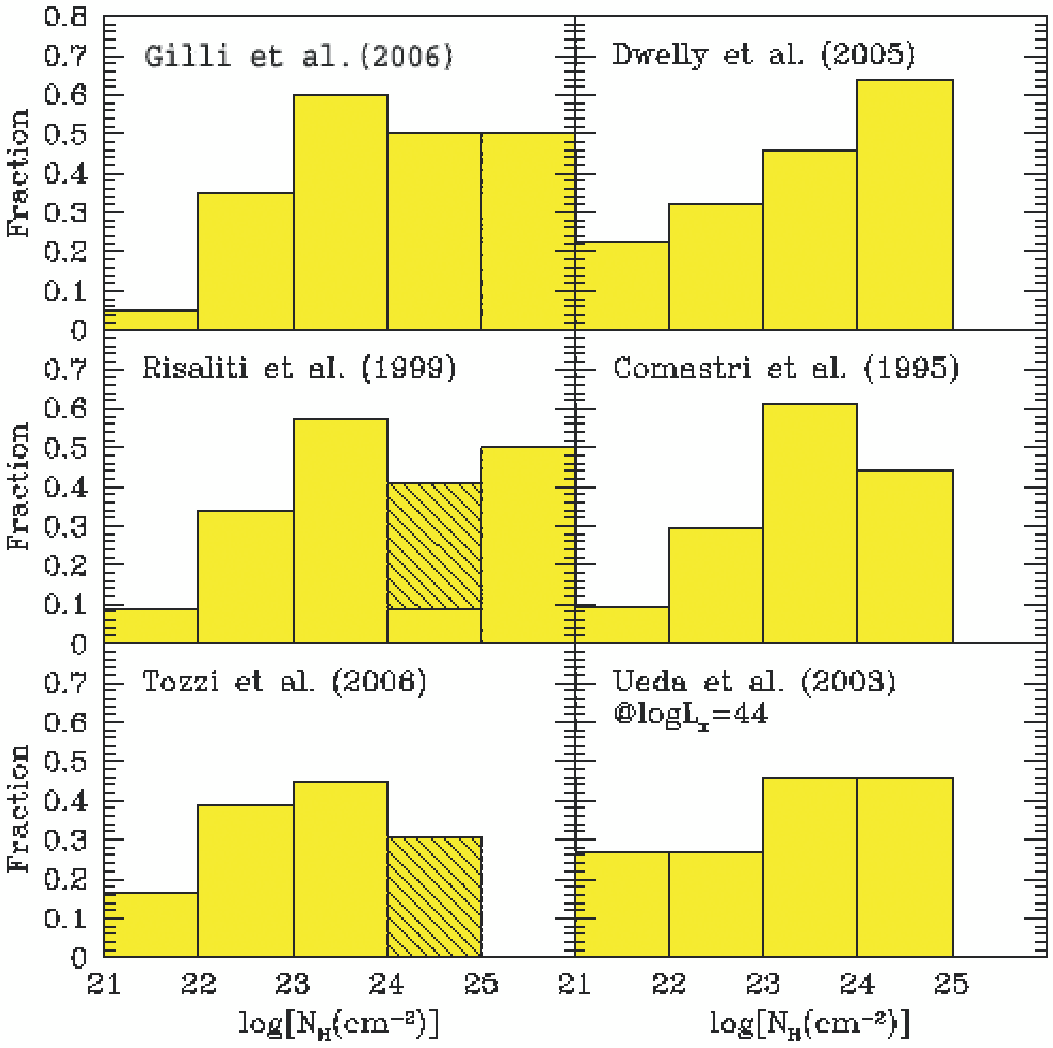

Figure 1.8: N_H distribution from Gilli et al. (2006) model as compared to other distributions from previous works. The number of objects in each N_H bin is normalized to the total number of Compton-thin ($21<\log<24$) AGN. Shaded areas refer to lower limits to N_H. Adapted from Gilli et al. (2006).

1.2.6 Absorption distribution

According to the so-called unified model (Antonucci, 1993), the same engine is at work in all AGN. The difference between type 1 and type 2 AGN are ascribed solely to orientation effects: our line of sight to the nucleus may (type 2) or may not (type 1) be obstructed by optically thick material, perhaps distributed in a toroidal geometry. Knowing the amount

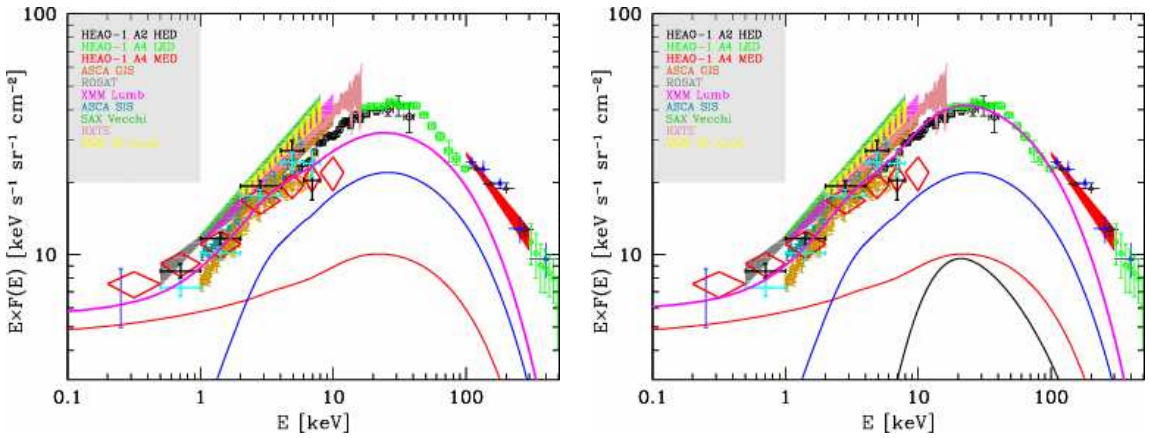

Figure 1.9: *Left Panel:* The XRB spectrum and the predicted contribution of Compton-thin AGN from Gilli et al. (2006) model. The different XRB measurement are explained on the left. The red solid line shows the contribution of unabsorbed objects while the blue solid line shows the contribution of AGN with Log N_H=22-24. *Right Panel:* Same as previous panel, but including also the contribution of Compton-thick AGN (black line). Both figures were adapted from Gilli et al. (2006).

of obscuring gas in Seyfert galaxies is important to understanding the physical properties and the nature of the putative torus. It is, in fact, the geometry of the dust torus which determines the amount of obscuring material along the observer's line of sight to the central X-ray-emitting regions. If we assume that all AGN have the same geometry, then it is only the properties of the torus that determine the observed absorption distribution in the AGN population as a whole. A typical zeroth-order approach is to speculate that this characteristic geometry is independent of the luminosity of the central engine, and has not evolved over cosmological time-scales. Thus, measuring the AGN absorption distribution, becomes a crucial test for the validity of the AGN unified scheme as in this case the fraction of absorbed objects to the total population is expected to be 3/4 and to be independent of redshift and luminosity. The first instruments able to derive a measurement of the absorption distribution, in the 2-10 keV band, were HEAO-1 A-2 and EXOSAT (Piccinotti et al., 1982; Turner & Pounds, 1989). In the EXOSAT sample, which include the HEAO-1 A-2 sample, absorption is found in $\sim$ 50% of the sources, thus denoting either a problem with the unification scheme or, as proven later, a bias against the detection of absorbed sources. The reported distribution, as all the other ones we will describe, is bimodal with a threshold between absorbed and unabsorbed sources usually fixed at $N_H = 10^{22}$H-atoms cm^{-2}; the unabsorbed sources are also usually reported in a sinlge bin as their absorption is often comparable or less than the absorption taking place in our

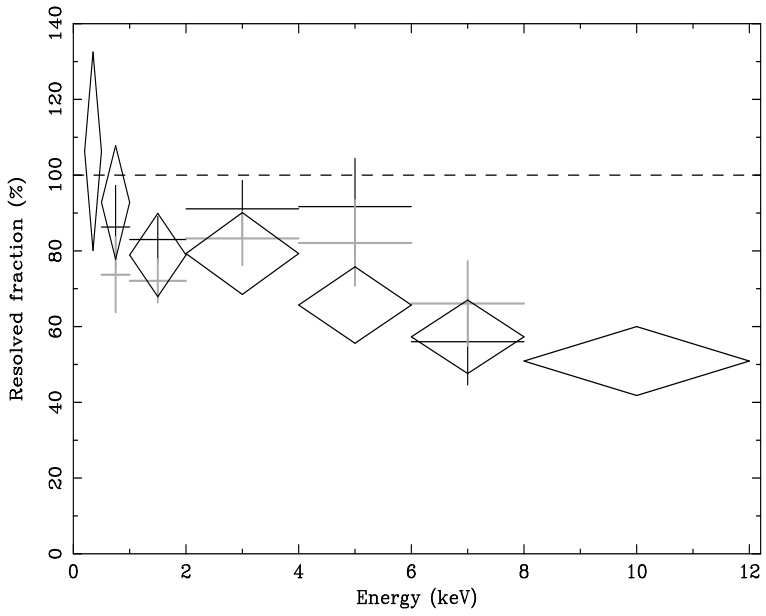

Figure 1.10: The fraction of the total extragalactic XRB intensity resolved by simply summing the fluxes of sources in the CDFs and XMM-LH. CDF-N and CDF-S data are shown as the black and grey crosses respectively; the XMM data are shown with diamonds. Adapted from Worsley et al. (2005).

own galaxy and X-ray instruments are not sensitive enough to measure with precision very low column densities.

Things improved dramatically with the advent of the *Chandra* and *XMM-Newton* telescopes. In particular, the deep field observations of the Lockman Hole (Mainieri et al., 2002) and the CDFS (Tozzi et al., 2006), with their high completeness (100% and 99% respectively), both find that $\sim$75% of the AGN population shows absorbing column densities $> 10^{22}$atoms cm^{-2} in excellent agreement with the unified scheme. Fig. 1.11 shows the absorption distribution for the extragalactic sources detected in the CDFS; the distribution steeply increases with N_H, peaking at Log $N_H \sim 23$, and bridges smoothly with the Compton-thick population. However, as pointed out by Worsley et al. (2005), even the deepest survey, in the 2-10 keV band, are likely missing a fraction of sources due to large obscuration. Indeed, the fraction of Compton-thick sources found in the XMM-Newton observation of the Lockman Hole and in the CDFS are very different as reported in table 1.2. The only way to remove such observation bias is to perform imaging studies at higher energies, $>$ 10keV, where the effect of source obscuration is less severe. The BAT and ISGRI telescopes on board the *Swift* (Gehrels et al., 2004) and INTEGRAL (Winkler et al., 2003) missions respectively are surveying the hard X-ray sky ($>$ 15keV) to compara-

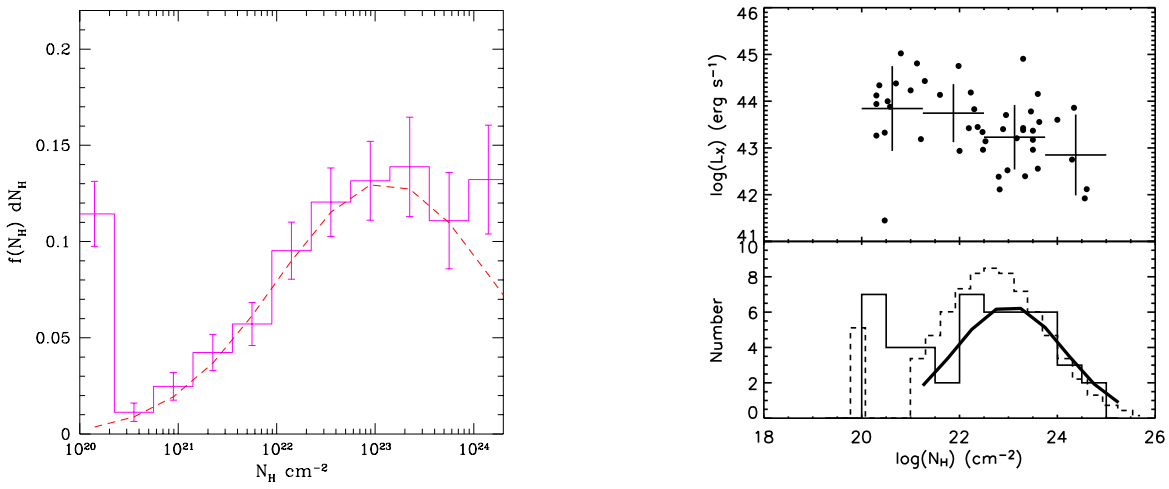

Figure 1.11: *Left Panel:* Intrinsic N_H distribution for the AGN detected in the CDFS corrected for incompleteness and sampling-volume effect(Tozzi et al., 2006); the dashed line is a lognormal distribution with $\sigma = 1.1$. The figure shows a continuity between the class of Compton-thin and Compton-thick sources. *Right Panel:* Luminosity vs. absorption and absorption distribution from the BAT high latitude survey (Markwardt et al., 2005).

ble limiting fluxes with different purposes. In such energy range, the decrease in flux due to $N_H \sim 10^{24}$H-atoms cm^{-2} is only $\sim 4\%$ and becomes $\sim 30-40\%$ for $N_H \sim 10^{25}$H-atoms cm^{-2}. Thus, such instruments are well suited to probe the Compton-thick AGN population. The preliminary results from the BAT high latitude survey (Markwardt et al., 2005) and from the INTEGRAL surveys (Beckmann et al., 2006; Bassani et al., 2006; Sazonov et al., 2006) show that the fraction of absorbed source is close to 65%, somewhat lower than the 75% required by the unified scheme and that the fraction of Compton-thick sources can be as high as 10% even though a large scatter in this value is present as testified by the results summarized in table 1.2.

1.2.6.1 Luminosity and redshift dependence of the fraction of X-ray absorbed AGN

As already discussed, the AGN unification model explains all the observed phenomenology of the detected AGN as due to an orientation problem where the characteristic geometry is independent of the luminosity of the central engine, and has not evolved over

Table 1.2: Absorption distributions from different instruments/samples.

Reference	Completeness	% Abs.	% C-thick	Band (keV)	Instrument
Mainieri et al., 2002	100%	∼75%	0	0.5-7	XMM
Tozzi et al., 2006	99%	∼75%	5%	0.5-7	Chandra
Markwardt et al., 2005	95%	∼64%	∼10%	15-200	Swift-BAT
Beckmann et al., 2006	100%	$\sim 64\%$	$\sim 10\%$[1]	20-40	INTEGRAL
Sazonov et al., 2006	90%	$\sim 50\%$	$\sim 1\%$[2]	17-60	INTEGRAL
Bassani et al., 2006	77%	$\sim 65\%$	$\sim 14\%$[1]	20-100	INTEGRAL
Ueda et al., 2003	96%	$< 55\%$	$\sim 25\%$		Sample[3]

[1] Some care must be used when quoting statistical results from the INTEGRAL survey as the impact of observations aiming at specific sources is not addressed (e.g. it is not a truly serendipitous survey)

[2] The sample in Sazonov's work consists of 66 of which 7 are unidentified; if these sources are all Compton-thick the fraction of such population would be $\sim 10\%$

[3] The authors merged several samples, detected with different instruments, into a larger one

cosmological time-scales. Following Hasinger et al. (2004), we call the original version of the unification scheme *strong*.

Several independent measurements (Ueda et al., 2003; Hasinger et al., 2004; La Franca et al., 2005; Barger et al., 2005; Markwardt et al., 2005) show an apparent decrease in the fraction of absorbed sources with intrinsic X-ray luminosity. This trend is clearly shown in the left panel of figure 1.12. The reason behind it is not fully understood and for some time it was claimed that such trend was due to a selection effect since supposed high redshift obscured AGN are difficult to detect. Barger et al. (2005) have recently reported that this dependence of ratio on luminosity still pertains at low redshift where selection effects are not important. Fabian (1999) proposes a model for the formation of galaxy bulges and central black holes in which young spheroidal galaxies have a significant distributed component of dusty clouds, which account for the absorption. In this model, the central black hole emits a slow wind which eventually becomes powerful enough to eject the cold gas from the galaxy, so terminating the growth of both black hole and the galaxy (unless a merging event does not bring fresh gas from the outside). Basically, quasars would undergo a major obscured growth phase during which the bulk of the XRB is created and then a briefer unobscured phase after the gas is ejected. The existence of the obscured growth phase find confirmation in the recent works of La Franca et al. (2005) and Tozzi et al. (2006) which show a dependence (increase) of the AGN absorbed fraction with red-

shift as shown in right panel of Fig. 1.12.

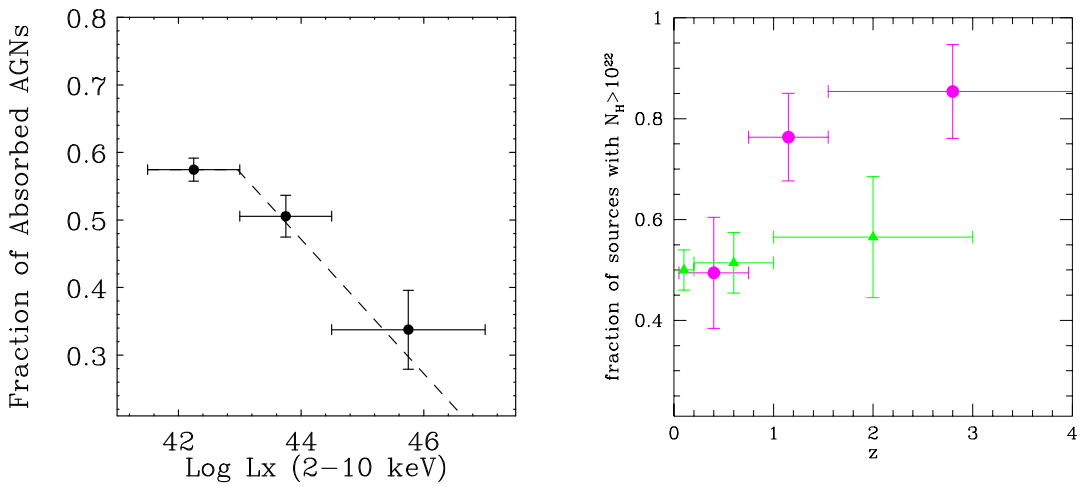

Figure 1.12: *Left Panel:* Fraction of absorbed AGN with Log $N_H > 22$ to all AGN with Log $N_H < 24$ as a function of luminosity from Ueda et al. (2003). *Right Panel:* Fraction of absorbed AGN ($N_H > 10^{22}$atoms cm^{-2}) to total as a function of redshift for sources detected in the CDFS (Tozzi et al., 2006). Green triangles are from Ueda et al. (2003).

All these elements show a breakdown of the *strong* unification model.

Nevertheless, we must mention two (very) recent studies (Dwelly & Page, 2006; Wang et al., 2006) of the absorption distribution of AGN in the CDFS, with *Chandra* and *XMM-Newton* respectively, which show that *" there is little evidence that the absorption distribution is dependent on either redshift or intrinsic X-ray luminosity"* (Wang et al., 2006); thus the previously reported trends were given by selection effects. Both studies agree that the fraction of obscured AGN is 75% of the total population, consistent with the *strong* unification models.

On the other hand, recently developed population synthesis models (i.e. Gilli et al., 2006) requires both dependences of the absorption distribution (redshift and luminosity) to successfully reproduce the observational evidences and the XRB emission. Moreover, the BAT high latitude survey ($>$ 15 keV, and thus unbiased towards absorption, Markwardt et al., 2005) shows a weak anti-correlation of column density and intrinsic luminosity (see left panel of Fig. 1.11). It is thus clear, that studies in the $>$ 10keV band will help under-

standing whether the *strong* AGN unification model is correct or AGN properties do not just depend on orientation, but also on luminosity and/or redshift.

1.2.7 Compton thick AGN

Most of the AGN in the local universe are obscured in the X-ray band by large amounts of gas and dust, which prevent the observation of their nuclear emission up to energies that depend on the amount of intrinsic absorption. If the X-ray obscuring matter has a column density which is equal to or larger than the inverse of the Thomson cross-section ($N_H \geq \sigma_T^{-1} \simeq 1.5 \times 10^{24}$ cm^{-2}), then the source is called, by definition, "Compton thick". The cross-sections for Compton scattering and photoelectric absorption have approximately the same value for energies of order 10 keV, which can be considered as the low energy threshold for probing the Compton thick absorption regime. Indeed, if the column density does not exceed a value of order 10^{25} cm^{-2}, then the nuclear radiation is visible above 10 keV, and the source is called mildly Compton thick. For higher column densities (heavily Compton thick), the entire high energy spectrum is down-scattered by Compton recoil and hence depressed over the entire X-ray energy range. The presence of Compton thick matter may be inferred through indirect arguments, such as the presence of a strong iron K line complex at 6.4-7 keV and the characteristic reflection spectrum (see lower spectrum in Fig. 1.4).

Studying, and first of all *detecting*, the Compton-thick AGN population has today become a major interest for several reasons:

- Most of the population synthesis models (Comastri et al., 1995; Treister & Urry, 2005; Ueda et al., 2003) predict that Compton-thick AGN (LogN_H >24) provide a significant contribution to the bulk of the CXB emission at ∼30 keV (Marshall et al., 1980);

- Analysis of the "unresolved" fraction of the XRB in the 0.4-12 keV band (Worsley et al., 2005) shows that its spectral shape is consistent with that which would be expected from a population of faint, heavily obscured AGN, with intrinsic absorption columns of $\sim 10^{23}$-10^{24} located at redshift $\sim 0.5 - 1.5$;

- Risaliti et al. (1999), using an hard X-ray selected sample of optical identified Sy2 limited in [O III] flux, have shown that, at least in the local Universe, there are as many Compton-thick sources (Log $N_H > 24$) as Compton-thin objects (22 <Log $N_H < 24$);

- the absorbed luminosity eventually will be reemitted in the far-infrared (far-IR), making Compton thick sources potential contributors to the long wavelength background (Comastri et al., 2004);

- accretion in the Compton thick AGN may contribute to the local black hole mass density.

Moreover, the study of such objects can provide useful insights about the validity of the AGN unification scenario. For example: fast changes in the X-ray column density advocate rather for matter closer to the Broad Line Region (BLR) (Elvis et al, 2004); correlation of the presence of "dust lanes" (as revealed by HST/WFC2) with large column density ($23 <$Log $N_H < 24$) is interpreted as due to the large covering fraction of the gas associated with the dust lane, with respect to the compact, pc-scale, Compton-thick torus (Guainazzi et al., 2005); X-ray spectra of highly obscured AGN often show a soft excess ($\sim$1 keV) which is generally unobscured suggesting an origin in gas structures, which extend beyond the material responsible for the obscuration of the nuclear continuum.

Even though there are good arguments in favor of the existence of such population, only an handful ($\sim$10) of Compton-thick objects was successfully detected in the past. The main problem arises from the fact that Compton-thick matter with column density $> 1.5 \times 10^{24}$atoms cm^{-2} suppresses the intrinsic nucleus flux to $\sim$ 2% of its original value in the 2-10 keV band thus making difficult the detection of such objects even for sensitive instruments like *Chandra* and *XMM-Newton*. Indeed in order to be detected by such state-of-the-art telescopes, Compton-thick sources must be very bright (and thus local, z$<$0.1, e.g.: NGC 1068, the Circinus galaxy, etc.) or must be at high redshift; in the latter case, the photo-electric cut-off moves into the 2-10 keV thanks to source redshift. This is confirmed by the recent study of Tozzi et al. (2006) which claims a detection of 14 Comtpon-thick objects (5% of the total extragalactic sample) in the CDFS. The fact that the mean redshift of the Compton-thick sample is 1.6 while the mean redshift of the whole sample is $\sim$ 1.1 can be explained in terms of absorption bias. In fact Compton-thick sources must be at high redshift in order to be detected by Chandra in the 2-10 keV band. However, the same authors admit that the typical signal-to-noise of the CDS sample makes it difficult to efficiently select Compton-thick sources on the basis of the shape of the X-ray spectrum and thus a fraction up to 20% ($\sim$3 sources) of the CDFS Compton-thick sample might be spurious.

Unfortunately, the most efficient energy range to search for mildly Compton thick sources is just above the highest energy accessible to the past and present generation of satel-

lites with imaging capabilities for faint limiting fluxes. As a consequence, the search for Compton thick sources has been limited, so far, to the relatively bright fluxes accessible to the high energy detectors onboard BeppoSAX and RXTE (Comastri et al., 2004).

Thus, our knowledge of the Compton-thick AGN population is mostly limited to those few ($\sim$10), bright, objects detected by the PDS instrument on board BeppoSAX (Matt et al., 2001; Comastri et al., 2004).
The *Swift* and *INTEGRAL* satellites with their coded mask hard X-ray detectors, BAT and ISGRI respectively, have a chance to shed light on the properties of this population.

1.2.8 The challenging measurement of the XRB spectrum

Exact determinations of the XRB spectrum are difficult mainly because instruments attempting such a measurement were expressly designed (and calibrated) for the study of point-like sources and not for the imaging and/or spectroscopy of diffuse sources. For such instruments, the XRB radiation is just part of the overall background against which point-like sources have to be detected. Thus, the measurement of the XRB spectrum relies on the capability of discriminating such component among all the other background components (often unknown) which in general have very close signatures. Moreover, as already mentioned, most telescopes were never calibrated with diffuse sources and thus the transformation from raw detector counts to source photons relies on response matrices which were optimized for (and from) the study of point like sources. Thus, it is not surprising that different measurements, sometimes with the same instrument, produce results which differ by 10-20% in normalization.
Unfortunately, as already shown in the past sections, population synthesis models rely on the XRB measurement to estimate the properties of the different classes of AGN by assessing their contribution to the XRB spectrum. In particular, the paucity and differences of the XRB measurements around the bulk of the XRB emission at 30 keV make complex, if not impossible, to understand the contribution of Compton-thick sources to the overall background spectrum.

The discussion about the historical and most recent XRB measurements is reported in the following sections.

1.2.8.1 HEAO-1 measurement

The *High Energy Astronomical Observatory (HEAO-1)* Matteson et al. (1978) was specifically designed for a broad band measurement, 3-300 keV, of the XRB spectrum. The

observatory was equipped with 4 different instruments; the broad band measurement of the XRB spectrum was obtained as a set of three partially overlapping measurement performed with different instruments. They are described in the following paragraphs.

The **Cosmic X-Ray Experiment, A-2,** Rothschild et al. (1979) consisted of six mechanically collimated multi-anode gas proportional counters sensitive in the 3-50 keV range; the experiment was designed in such way that even anodes had a solid angle which was the double than the solid angle of odd anodes. Since the instrument response to the XRB is supposed to increase linearly with the subtended solid angle while the instrumental background should not, the difference between the signal in the even and odd anodes gives a direct measurement of the XRB. Marshall et al. (1980), who produced the XRB measurement using the A-2 experiment, report that the *"equality of internal backgrounds was verified prior to launch"* and that there was no evidence indicating an imbalance in orbit. Moreover, the high energy detectors had a veto layer above the X-ray detecting volume which allowed to reduce the particle-generated background by a factor ~ 100. Only data without point sources in the field of view (FOV) and pointing more than 20° away from the galactic plane were used. Moreover, veto layer rates were used to exclude periods of high particle background like the South Atlantic Anomaly (SAA).

The **Hard X-Ray and Gamma-Ray instrument, A-4** consisted of three separate detectors: a low energy, a medium energy and a high energy detector respectively called LED, MED and HED. More in detail, the A-4 was made of 7 NaI/CsI "phoswich" detectors collimated with a thick CsI active anticoincidence shield and optimized to cover different subranges over the 13 keV-10 MeV total range. Gruber et al. (1999) used only LED data, 13-180 keV, to perform the measurement of the XRB spectrum. The LED was equipped with a 5 cm thick CsI(Na) movable crystal which could block the various aperture so that intrinsic detector background could be separated from celestial signal. The authors selected only "good" events, events which did not produce a signal in the CsI(Na) part of the phoswich and in the anticoincidence shield, and avoided periods close in time to SAA passage. After correcting for gain variations and assessing the emission from the blocking crystal, the difference between unblocked and blocked data yields essentially the XRB emission.
Kinzer et al. (1997) produced a measurement of the XRB spectrum over the 80-400 keV band using the MED detectors in a similar way as done by Gruber et al. (1999).

The overall measurement performed by HEAO-1 thus extends from 3 to 300 keV as shown in the left panel of Fig. 1.13. The figure shows nicely what is referred to as the "peak"

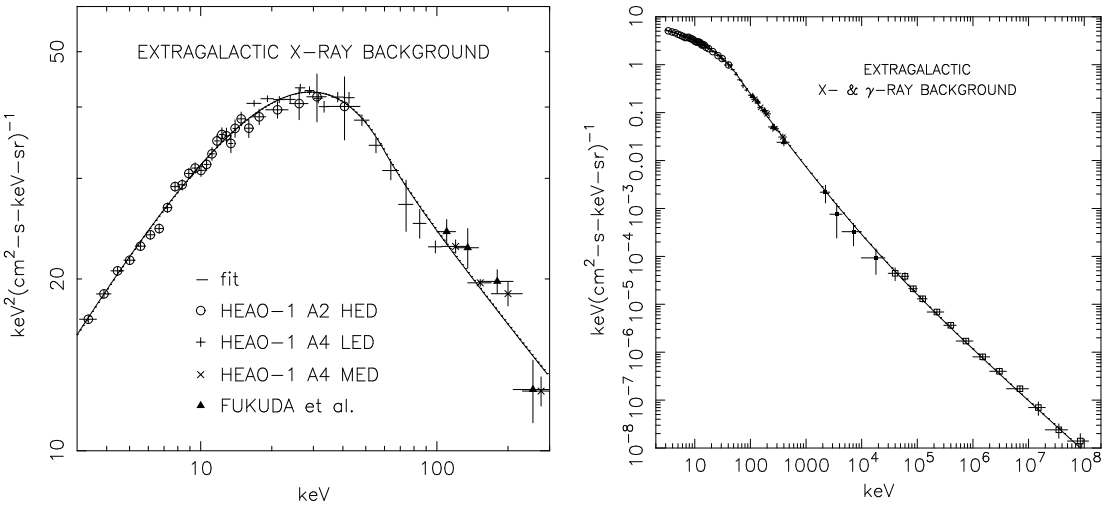

Figure 1.13: *Left Panel:* Spectral intensity of the XRB as measured by several instruments on board HEAO-1. *Right Panel:* Spectrum of the X- and γ-ray diffuse background from 3 keV to 100 GeV. Data below 400 keV are from HEAO-1 while above this energy are from Comptel and EGRET respectively. The data were fit with a simple model described in Gruber et al. (1999).

of the XRB emission at 30 keV. The intensity of the XRB at this energy is confirmed by the overlapping measurements of the A-2 and A-4/LED instruments on board *HEAO-1* (Marshall et al., 1980; Gruber et al., 1999). However, as noted by (Marshall et al., 1980), a 10% systematic error of the intensity of the XRB at 10 keV is intrinsic in the data. As shown in section 1.2.4, population synthesis models require a substantial population of Compton-thick AGN to explain the intensity of the XRB peak, thus the exact knowledge of the XRB spectrum has today become a way to constrain the number and properties of this class of objects which are otherwise unconstrained.
The right panel of Fig. 1.13 shows that the *HEAO-1* measured XRB spectrum smoothly joins the Comptel and EGRET measured diffuse γ-ray background (Kappadatah et al., 1997; Kniffen et al., 1996).

1.2.8.2 Scatter in XRB normalization

Several instruments have measured the XRB emission over different energy ranges and with different techniques. As already shown, an accurate broad band measurement was obtained with the large FOV collimated spectrometers aboard *HEAO-1*; numerous other measurements were performed with focused imaging telescope. As noted by Barthelmy et al. (2000) for small FOV instruments like *XMM-Newton* or *Chandra*, cosmic variance

can account only partially for the scatter of the XRB measurements; the large observed scatter, visible in Fig. 1.14, is probably due to systematic cross-calibration problems and incorrect background subtraction. A recent reanalysis of *HEAO-1* A-2 data (Revnivtsev et al., 2005) shows that the MED and HED detectors give a reciprocally consistent measurement of the XRB intensity in the 2-10 keV band and that assuming a common template for the Crab nebula spectrum (used as celestial calibration sources) the XRB intensity would be 17% larger than what reported by Marshall et al. (1980). The authors also scaled, when

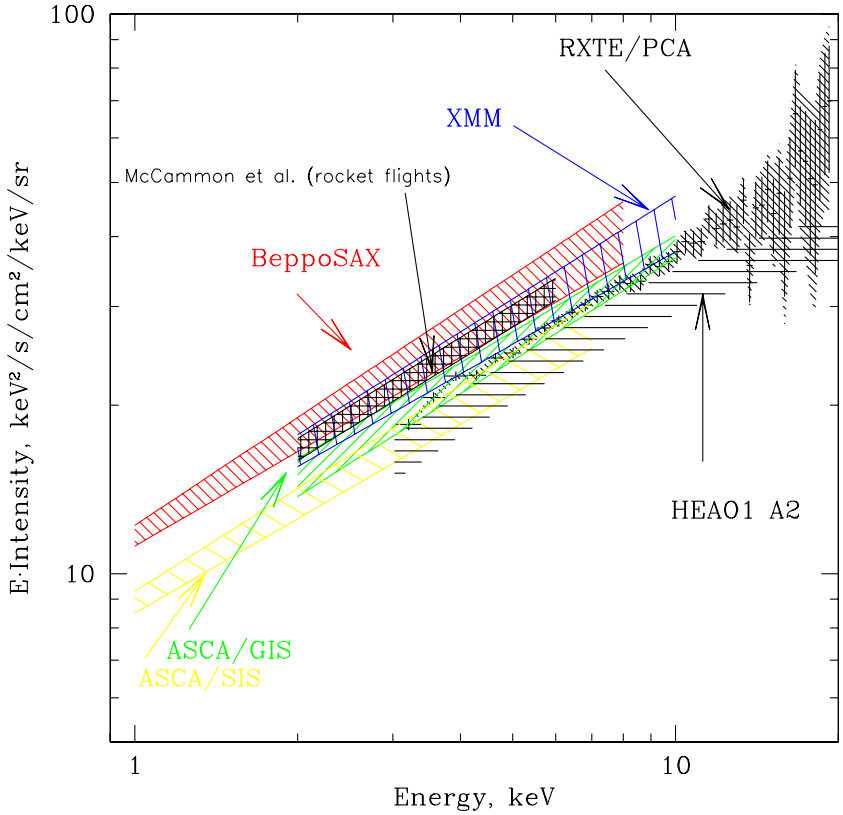

Figure 1.14: XRB spectrum as measured by the RXTE/PCA and other instruments (see Revnivtsev et al., 2003 and references therein).

information were available, the XRB measurements by the ratio between the original Crab flux (as measured by each single instrument) and the flux from the common template they used. The corrected XRB measurements are in good agreement with a maximum deviation of 2σ. All these facts point in favor of the "cross-calibration" issue which may affect

the measurements of the XRB.

1.2.8.3 The INTEGRAL measurement of the XRB emission

Early in 2006 the *INTEGRAL* (the **Inter**national **G**amma-Ray **A**strophysics **L**aboratory; Winkler et al., 2003) observatory performed a series of 30 ks observations with the Earth disk crossing the FOV of the instruments; the modulation of the aperture flux due to the Earth disk was used to derive the spectrum of the XRB. The main goal was to determine the XRB spectrum from 5 to 100 keV, thus across the XRB " peak" at 30 keV, where the only previously existing measurement was the one performed by *HEAO-1*.

The approach used in the *INTEGRAL* observation is similar to the one used by the *HEAO-1* experiment with the difference that Earth disk is used to partially block the FOV as the movable 5 cm thick CsI crystal was used in *HEAO-1*. The main, not-subtle, difference between the two approaches is that the CsI shutter in *HEAO-1* was an "active" detector thus, in combination with the main instrument, it allowed a measurement of the leaked radiation, whereas the Earth disk is used as a passive screen and its emission is not directly measured.

The *INTEGRAL* measurement is performed through the assessment of all background components. The authors selected periods when: 1) the Aurora emission was not observed, 2) the dark side of the Earth was in the FOV instead of its day-side 3) the Galactic Ridge (and compact source) emission gave a negligible contribution. During the Earth observations, the recorded flux can be described as a function of energy E and time t as:

$$F(E,t) = C(E) - S_{XRB}(E)[1 - A(E)]\Omega(t) + S_{ATM}(E)\Omega(t) \tag{1.4}$$

where $C(E)$ is the sum of all background terms, $S_{XRB}(E)$ is the XRB emission, $A(E)$ is the fraction of the XRB which is reflected by the Earth atmosphere (albedo), $S_{ATM}(E)$ is the Earth emission and $\Omega(t)$ is the solid angle subtended by the Earth. Since the atmospheric and XRB emission are modulated by the same quantity $\Omega(t)$, they cannot be easily discriminate, thus in each the flux becomes:

$$F(E,t) = B(E) - S_{Earth}(E)\Omega(t). \tag{1.5}$$

Churazov et al. (2006) used the observed light curves $F(E,t)$ in each energy bin and the known effective solid angle $\Omega(t)$ subtended by the Earth in the FOV of each instrument the to derive the $F_{Earth}(E)$ counts spectra (i.e. $S_{Earth}(E)$ convolved with the effective area

and the energy redistribution matrix). Then, they fit $F_{Earth}(E)$ counts spectra with a 2-component model where the first component is the XRB template spectrum from Gruber et al. (1999) (plus a fixed multiplicative term which takes into account the Earth albedo) and the Earth X-ray emission template spectrum from Sazonov et al. (2006b). The best fit, shown in Fig. 1.15, yields the normalization of the two spectral templates.

Thus, The *INTEGRAL* observation can be regarded as a measurement of the XRB normalization and **not** as a determination of the XRB spectrum as the spectral shape of the XRB is assumed to be the same as the one determined by Gruber et al. (1999).

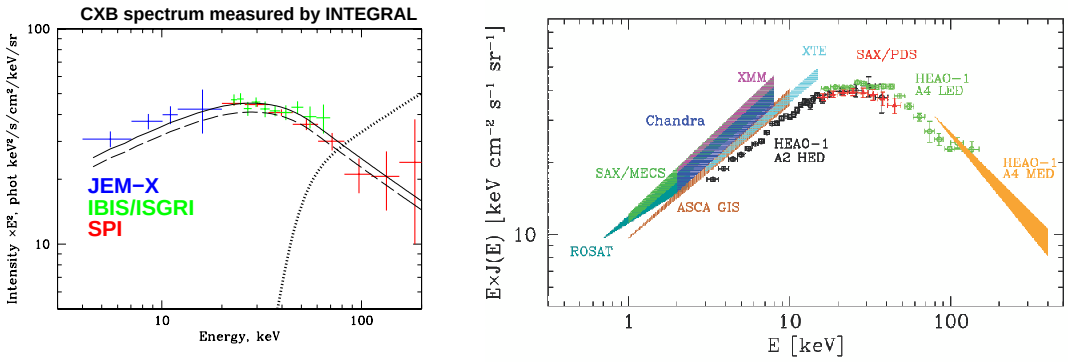

Figure 1.15: *Left Panel:* XRB spectrum measured by *INTEGRAL*. The dashed line shows the analytic approximation of the CXB spectrum by Gruber et al. (1999). The solid line shows the same spectrum with the best fit normalization obtained by Churazov et al. (2006). The thick dotted line shows the best-fit spectrum of the Earth atmospheric emission Sazonov et al. (2006b). *Right Panel:* XRB spectrum as observed with the PDS instrument on board BeppoSax compared to previous measurements (see Frontera et al., 2006 and references therein.)

1.2.8.4 The BeppoSax measurement of the XRB emission

A similar observation of the XRB, as the one performed by *INTEGRAL*, was done by the *Phoswich Detection System* (PDS) on board the *BeppoSax* satellite Frontera et al. (1997). The authors performed a ON-OFF measurement using the dark side of the Earth as a shutter to occult the XRB radiation. The difference spectrum (i.e. ON-OFF spectrum) is fitted, as in Churazov et al. (2006), with a 2-component model where one is the assumed

spectral shape of the XRB (the one determined by Gruber et al. (1999)) and the second is the assumed spectral shape of the Earth atmospheric emission. The best fit yields the normalization of the two spectral components. The *BeppoSax* results, shown in the right panel of Fig. 1.15, are in full agreement with the *HEAO-1* XRB spectrum Gruber et al. (1999) and discard an higher normalization of the XRB spectrum.

The *BeppoSax* measurement is thus in contrast with the *INTEGRAL* observation.

1.3 Current picture

In the previous sections it has been shown that it is reasonable to believe that most of the XRB radiation, above 2 keV, is the glow emission of many AGN. The most sensitive X-ray surveys (Brandt et al., 2001; Alexander et al., 2003; Hasinger et al., 2001) have resolved below 8 keV a relevant ($\sim$80%) fraction of the XRB into extragalactic sources. It is also established that luminous AGN form and feed efficiently rather early in the Universe while the bulk of the AGN population peaks at redshift < 1 (Ueda et al., 2003; Hasinger et al., 2004).

On the other hand, the picture is not yet complete. The analysis of the resolved fraction of the XRB as a fraction of energy (< 12keV) shows that the unresolved component is consistent as being the emission of a yet undetected population of highly absorbed AGN; such AGN should be characterized by having column densities $\sim 10^{24}$ cm^{-2} and a space density peaking at redshift below 1 (Worsley et al., 2005).
The AGN unification model predicts that 3/4 of all AGN are obscured. Even though a great wealth of X-ray data are nowadays accessible, only a few surveys (Dwelly & Page, 2006; Wang et al., 2006) report a result consistent with the unified model; the puzzling circumstance is that the first sensitive X-ray surveys at energies > 15keV (Markwardt et al., 2005; Beckmann et al., 2006) and thus "absorption-unbiased", claim that the fraction of absorbed sources is ~ 65% of the total AGN population.
Very recent spectral analyses of the highly complete survey in the CDFS shows that the fraction of absorbed sources does *not* vary with either luminosity or redshift (Dwelly & Page, 2006; Wang et al., 2006) in contrast with previous claims (Ueda et al., 2003; La Franca et al., 2005; Barger et al., 2005). However the newest population synthesis models need such dependences (Gilli et al., 2006; Treister & Urry, 2005) to successfully reproduce the observational constrains.
Population synthesis models predict that Compton-thick AGN give a substantial contribution to the bulk of the XRB emission around 30 keV (Ueda et al., 2003; Treister & Urry,

2005; Gilli et al., 2006); a [O III] selected sub-sample drawn from a hard X-ray selected sample of Seyfert 2 galaxies shows that, at least in the local universe, Compton-thick AGN are as numerous as Compton-thin ones (Risaliti et al., 1999). This is in contrast with the few ~ 10 Compton-thick AGN known (Comastri et al., 2004) and the ones (14) recently claimed (Tozzi et al., 2006). Again what is puzzling is that > 15keV surveys are "just" detecting previously known (the few ones) Compton-thick AGN (Markwardt et al., 2005; Beckmann et al., 2006; Bassani et al., 2006; Sazonov et al., 2006).
The normalization of the XRB spectrum as measured by HEAO-1 was recently questioned by many authors (e.g. see Revnivtsev et al., 2003, 2005 and references therein). In particular the intensity (and position) of the peak of the XRB spectrum is used by population synthesis models to constrain the density of Compton-thick AGN; the two recent (and only ones after HEAO-1) measurements of the XRB peak normalization are not consistent with each other (Churazov et al., 2006; Frontera et al., 2006).
Gilli et al. (2006) in their XRB modeling also add that in case of an higher XRB normalization it is difficult to match the XRB spectrum without violating other constrains, in particular the source counts.

It is thus clear that new sensitive observations of the hard X-ray sky (> 15keV) are needed in order to determine the fraction of obscured AGN and the space density of Compton-thick objects and to constrain their contribution to the XRB emission. In the next chapters, we will try to address such problems.

Chapter 2

Imaging at high energies

Photons in the energy range 10-200 keV are usually called hard X-rays from gamma-ray astronomers and gamma-rays from the X-ray community. At this energies where the Compton scattering does not quite take over the photoelectric absorption, the dichotomy arises by the fact that both classical X-ray focusing techniques and Compton telescopes are difficult to use. This energy range, at the overlap of the X- and gamma-ray energy bands, is, still, the undisputed reign of coded mask detectors.
Here, we briefly discuss the techniques currently used to image the X-ray (from 0.1 keV to 200 keV) sky, focusing in particular on coded mask detectors. We also discuss the factors which determines the sensitivity of an instrument and show that the instrumental background has the largest weight in it. The components of the orbital background which are discussed in details at the end of this chapter are relevant afterwards for the measurement of the Cosmic Diffuse X-ray background (see Section 7) and for the calibration of the MEGA Anticoincidence system reported in Appendix A.

2.1 X-ray focusing telescopes

In order to detect X-rays for energies < 100 keV, the detector absorbing material is usually chosen to ensure that photoelectric absorption is the dominant effect. This is done so that all the incident energy is initially deposited at a point in the detector; this makes possible the precise determination of incident energy and event location. The information carriers (electrons, holes, photons, or phonons) liberated by the photoelectric interaction are then collected to determine at least, if not all, one of following parameters: interaction location (imaging), energy (spectrometry), polarization of the incident X-rays and arrival time.

Techniques for imaging can be broken down into two broad categories. The first involves

the use of mechanical collimators that restrict the field of view to a narrow portion of the sky or modulate the source flux from the object of interest in a manner that is sky-position dependent. The second one involves focusing optics, akin to optical astronomy, where X-rays can be easily reflected. The former techniques which dates back to the earliest days of X-ray astronomy are not anymore in use, except for the case of coded mask detector discussed later.
Focusing optics represent a major step in sensitivity since by concentrating the source photons to a small area on the detector plane the background is reduced by many orders of magnitude, and a point is quickly reached where the observation becomes limited only by the statistics of the source photons themselves (photon-limited). In addition, the ability to focus X-rays permits the use of small high-performance detectors, such as CCDs or calorimeters, which are not usually available in large area configurations.

2.1.1 X-ray mirrors

X-rays mirror can be realized because X-rays can undergo nearly total external reflection from surfaces at very small "grazing" angles. Away from any absorption edges, it is approximately given by:

$$\theta_c = (4\pi r_0 \lambda^2 n)^{0.5} \tag{2.1}$$

where r_0 is the classical electron radius, n is the electron density and λ the X-ray wavelength (Aschenbach, 1985). The largest critical angles are therefore obtained at low X-ray energies (long λ) and with dense, and thus heavy, reflectors as shown in Figure 2.1 which gives grazing incidence angles as a function of energy for different elements. When these conditions are met then the phenomenon of total external reflection can be used to construct X-ray mirrors as focusing and imaging devices. However, as the grazing angles are typically only a degree or so, the effective reflecting area is very small. Nevertheless, by careful design, including nesting of the reflecting surfaces, large effective area can be obtained, bringing a vast increase in sensitivity and image quality over non-focusing instruments.

Very high angular resolutions, at the arc sec level, have been achieved with grazing incidence X-ray optics used in conjunction with a position-sensitive detector in the focal plane. In a typical X-ray telescope (see Aschenbach, 1985 for a review), reflections from two surfaces are used to form an X-ray image. In the case of Wolter Type-1 mirrors, the incoming photons are first reflected by a parabolic mirror, which concentrates off-axis

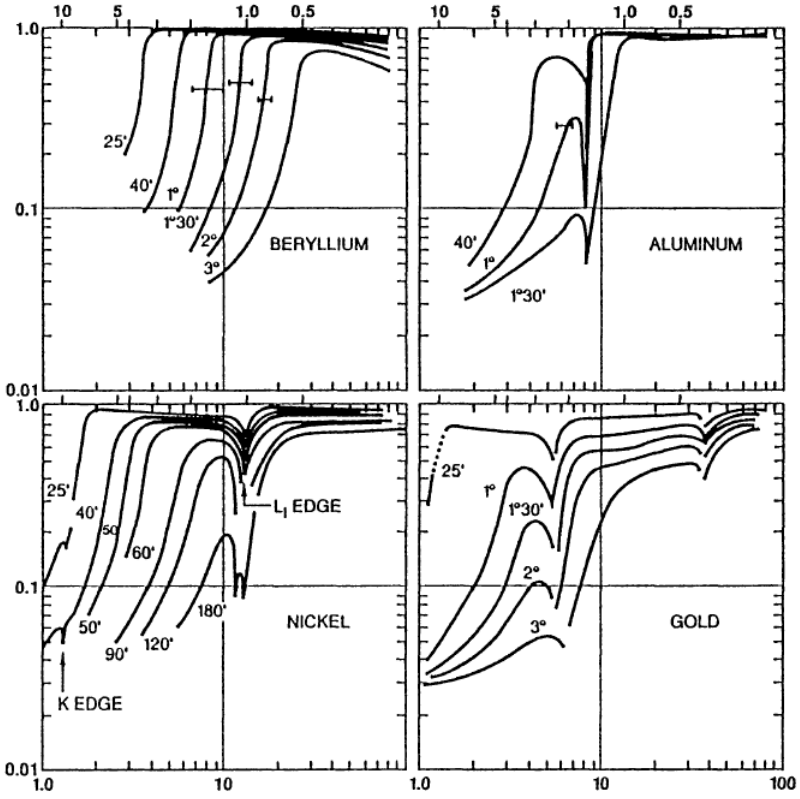

Figure 2.1: X-ray reflectivities versus energy for several materials and grazing angles (from Zombeck, 1990). Energy (x axis) is shown in keV at the top and wavelength (Angstrom) at the bottom.

rays into an annulus, and then by a hyperbolic mirror, which brings the annulus to a point in the focal plane. To increase the effective collecting area, several pairs of parabolic and hyperbolic mirrors can be nested as shown in figure 2.2.

The two presently flying X-ray observatories, Chandra and XMM-Newton, both adopt a Wolter Type-1 configuration, using respectively 4 and 58 nested mirrors. The main difference is that the optics of XMM-Newton were designed in order maximize the effective area over a wide range of energies, with particular emphasis in the region around 7 keV. Thus, the mirror system had to utilize a very shallow grazing angle of 0.5° in order to provide sufficient reflectivity at high energies.

Future planned mission like XEUS and Constellation-X will still use Wolter Type-1 mirrors.

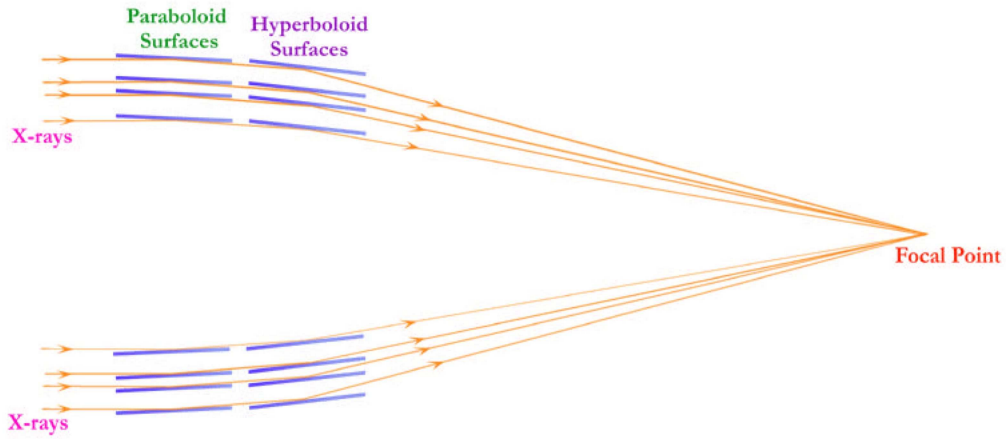

Figure 2.2: Schematic drawing of nested X-ray mirrors.

2.1.2 X-ray detectors

An X-ray photon interacting with the detector medium ultimately liberates charges, and these provide the means to measure the event. In some detectors, the charged particles are collected directly to generate an electrical signal at the output of the detector; whereas in calorimeter detectors, for example, the absorbed energy of the incident photon causes a small temperature increase of the absorber material, and this temperature change is converted, via a thermometer, into an electrical signal. Regardless of the detector type, each photon interaction generates a discrete electrical signal which is amplified and processed by the detector electronics to obtain information about the properties of the incoming radiation (intensity, energy, direction and arrival time).

Most of state-of-the-art X-ray detectors use Charge-couple devices (CCDs) based on semiconductor materials. The advantage of semiconductors over other solid materials for detecting radiation is the ease with which information carriers (in this case electrons and holes) can be formed by the absorption of radiation. The most important feature of CCDs is the method of storage and information retrieval of electrons and holes when the

device is exposed to radiation. The produced charge (photoelectrons) are stored in the depletion region of a metal insulator semiconductor (MIS) capacitor, and CCD arrays simply consist of many of these capacitors placed in close proximity. Voltages, which are static, during collection, are manipulated during readout in such as way as to cause the stored charges to flow from one capacitor to another, providing the reason for the name of these devices. The very low noise, high efficiency, and broad-band usability, from Optical to X-ray, made CCDs one of the most used detector in astronomy. Figure 2.3 shows that the quantum efficiency (ratio of incoming photons to stored photoelectrons) of modern CCDs is particularly high at X-ray energies. In particular, back-side illuminated CCDs approach a quantum efficiency of 100%. The X-ray telescopes aboard XMM-Newton and Chandra use CCDs as their detectors (Marshall et al. (2004), Sembay et al. (2004)).

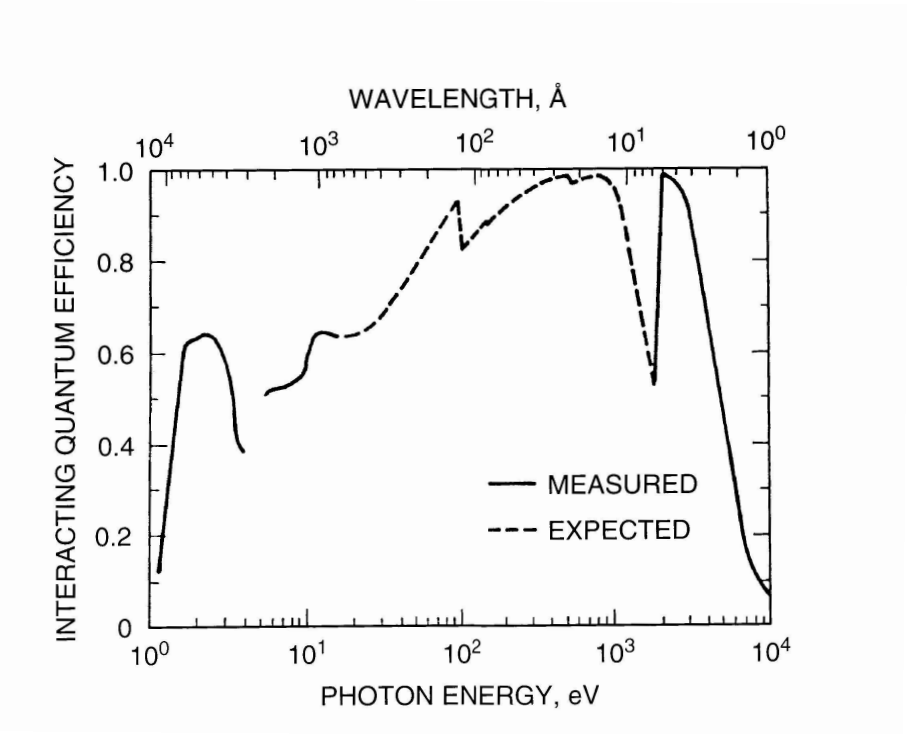

Figure 2.3: Quantum efficiency for a typical thinned, back-side illuminated CCD from the X-ray to the optical spectral regions. From Janesick et al. (1988).

2.2 Coded mask detectors

Focusing of high-energy radiation is so far technically feasible only for photon energies up to about 10 keV through grazing incidence reflection (Aschenbach, 1985). This method

can provide a very good angular resolution, i.e. down to 0.5 arc-sec which is the value reached by the High Resolution Camera (HRC) aboard Chandra (Weisskopf et al., 2002). The collecting area is optimized through the use of nested grazing incidence mirrors. The field of view (FOV) is limited by the grazing incidence to about 1 degree, but can be enlarged by using a special configuration of the mirrors ('Lobster-eye' telescopes, Aschenbach 1985). At higher energies than 10 keV, focusing is possible in limited ways (very narrow field of views and narrow passbands) through a Laue diffraction lens (Halloin, 2004) or (very long focal lengths, million of km) through diffraction-limited phase Fresnel lenses (Skinner et al., 2003).

In all the previous techniques it exists a near one-to-one correspondence between photon arrival directions and the positions at which the photons are detected in the focal plane, though the correspondence is never perfect.
However, imaging with photons of any energy above 50-100 keV and up to the GeV range involves indirect techniques. In the hard X-ray domain (above 10 keV), these indirect techniques have one common signature: the direction of the incoming rays is, before detection, encoded; the image of the sky has to be reconstructed by decoding the observation afterwards. It is apparent that this method of producing sky images is a two-step procedure, in contrast to the direct or one-step imaging procedure of focusing techniques. These alternative techniques are referred to as multiplexing techniques. Another important difference in any astrophysical applications between both types of imaging concepts is that in multiplexing techniques an imaged point source experiences the noise of all photons detected over the whole detector while in focusing techniques are only the photons in a small part of the detector. Thus, for equal collecting areas the sensitivity of a focusing instrument is always better than that one of a multiplex instrument.
Two types of multiplexing techniques are generally used: temporal and spatial multiplexing (Caroli et al., 1987).

A straightforward example for the temporal multiplexing is a scanning collimator when the direction of a collimator is moved across a part of the sky which contains an X-ray point source, the number of counts per second that is detected as a function of time has a triangular shape. The position of the maximum of the triangle provides the position of the source along the scanning direction and the height of the triangle provides the flux of the source. A second scan along another direction completes the two-dimensional position determination of the source. More scans may be necessary if the source is extended or when there are more sources in the FOV of the collimator. As an example, the UHURU and HEAO-1 satellites used this technique (Forman et al., 1978; Wood et al., 1984) . Temporal multiplexing techniques in principle do not need a position-sensitive

detector, contrary to spatial multiplexing techniques.

Detectors based on spatial multiplexing techniques are usually referred to as coded mask telescopes. In these instruments a coded aperture (i.e.: a plate with areas that are transparent or opaque to photons in a certain energy range) is used to modulate (coding phase) the incoming celestial radiation. A position sensitive detector, whose spatial resolution, matches roughly the mask pattern grid size is used to record the modulated signal. Ideally, the mask pattern is designed in such a way that each source at different positions in the FOV cast a unique shadow onto the detector plane. Thus, the incident directions can later be reconstructed from the count rates recorded in the detector. Figure 2.4 shows the working principle of a coded mask telescope.

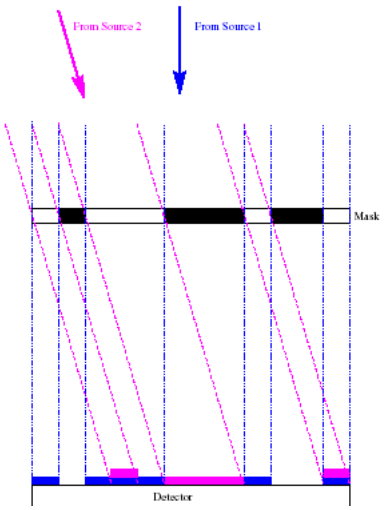

Figure 2.4: Working principle of a coded mask detector in the presence of two sources.

As shown in figure 2.5, typically two FOVs can be distinguished in a coded mask instrument:

- the fully coded field of view (FCFOV) where all the source radiation arriving at the detector plane is modulated by the mask (the radiation is 100% coded)
- the partially coded field of view (PCFOV) where only part of the source radiation is modulated by the mask and the rest is uncoded (0%$<$ coding fraction $<$100%); in this part of the FOV the instrument looses its ability of detecting sources as soon as the coding fraction approaches zero.

Both sensitivity and angular resolution depend on the instrument geometry, in fact the sensitivity is proportional to the opening fraction (fraction of opaque and transparent mask elements) while the angular resolution is given by the ratio of a transparent element and the distance of the mask above the detector plane ($\Theta = arctg(H/L)$ of figure 2.5). So, decreasing the mask element size without modifying the opening fraction would achieve an increase in angular resolution and no change in the telescope sensitivity. Practically the best angular resolution is constrained by the minimum dimension (and thus by its cost) of a single detector; in fact the pixel detector must have a size comparable (or smaller) than the typical mask element in order to *detect* the shadowgram mask edges.

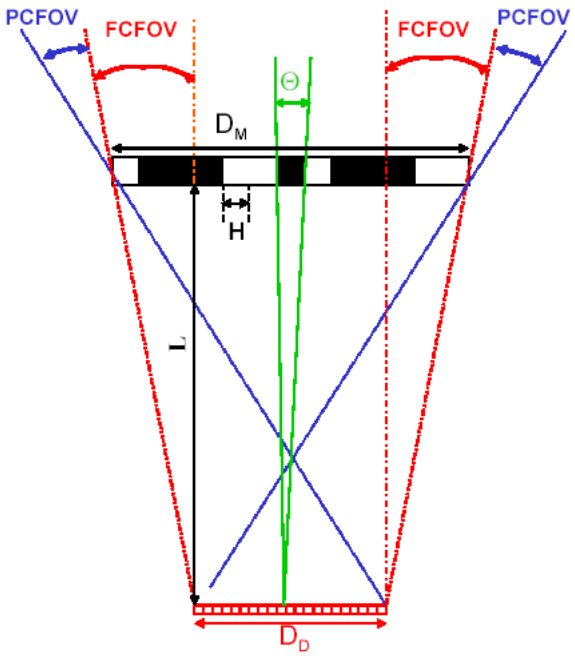

Figure 2.5: Schematic drawing of a coded mask telescope. D_D and D_M are respectively the dimensions of the detector plane and the mask, H is the typical dimension of a mask element and Θ is the angular resolution.

2.2.1 Coding phase

In coded mask telescopes, the sky image is thus encoded by the mask which in mathematical terms translate into:

$$C = M * S + B \tag{2.2}$$

where $*$ denotes the convolution operator [1], C is the information recorded in the detector plane, S is the sky distribution to be imaged, M the mask transmission function and B the (signal-independent) detector background. The mask transmission function is, ideally, made up of zeros (opaque elements) and ones (transparent elements).

In order to derive the original sky image S, one needs to deconvolve the recorded information using a suitable decoding function D.

$$\hat{S} = D * C = D * (M * S) + D * B \tag{2.3}$$

Equation 2.3 shows that the quality of the image reconstruction depends on the choice of the aperture (M), the decoding function used (D) and on the properties of the detector background noise.

In order to obtain a good image reconstruction, the mask pattern must be optimized. Beyond the requirement that for each incident direction the shadow pattern must be unique, it is important that the similarities between patterns be as poorest as possible; otherwise the discrimination between the two corresponding directions becomes difficult in the presence of statistical and / or background noise.
The best choice of aperture design and decoding function is the one which produces $D * M = \delta$ and with $D * B$ as small and uniform as possible.

2.2.2 Point spread function and autocorrelation function

The point spread function (PSF) of an imaging instrument is defined as its response to a point like source. Independent on the type of the instrument, the ideal PSF is a Kronecker δ function. Clearly, for coded mask telescopes the instrumental PSF depends on both the instrument design and the decoding algorithm used. On the contrary the Autocorrelation Function (ACF, defined as the correlation of the mask pattern with itself) depends only on the aperture geometry and it is preferred to the PSF when comparing different mask designs. As for the PSF, an ideal mask design has an ACF coincident with a δ function.

The ACF is calculated either assuming the mask to be uniform (all opaque or all open) outside of the coded field, or by assuming the mask pattern to be repetitive (cyclic ACF). Cyclic ACFs are particularly useful in determining the characteristics of mosaiked mask

[1] The convolution operator defined here is of the form:

$$(A * B)_{i,j} \sum_k \sum_l A_{k,l} B_{(i+k),(j+l)}$$

patterns. For a rectangular mask M with $m \times n$ elements, the basic and cyclic ACFs are defined as follows:

$$\text{ACF}: \quad A_{i,j} = \sum_{k=1}^{m-(i-1)} \sum_{l=1}^{n-(j-1)} M_{k,l} M_{(i+k),(j+l)} \tag{2.4}$$

$$\text{Cyclic ACF}: \quad A_{i,j} = \sum_{k=1}^{m} \sum_{l=1}^{n} M_{k,l} M_{(i+k) mod m,(j+l) mod n} \tag{2.5}$$

Most of mask patterns have not flat ACF side-lobes which translate into high frequency noise in the reconstructed image. These side-lobes can be flattened by applying a balanced correlation as introduced by Fenimore & Cannon (1978). In the balanced correlation the mask M is multiplied not with itself but with a slightly modified M'. The modification depends on the open fraction of the mask ρ:

$$\text{Balanced ACF}: \quad A_{i,j} = \sum_{k=1}^{m-(i-1)} \sum_{l=1}^{n-(j-1)} M_{k,l} M'_{(i+k),(j+l)} \tag{2.6}$$

$$\text{where} \quad M_{i,j} = \begin{cases} 1 & \text{for} \quad M_{i,j} = 1 \\ \frac{-\rho}{1-\rho} & \text{for} \quad M_{i,j} = 0 \end{cases}$$

The ACF function (or better its side-lobes) gives a measure of the inherent noise of the coded aperture; this kind of noise is usually referred to as *coding noise* and thus the coded mask design must be optimized in order to reduce it.
As already pointed out by Wunderer (2002), the *balanced* ACF is closer to the PSF than to the ACF, since the modified mask M' can already be considered (and actually is) a decoding algorithm.

2.2.3 Aperture design

The mask pattern has a great influence on the performance of a coded aperture telescope. The simplest kind of coded aperture is the pinhole camera and the principles of imaging via a simple hole has been known to Chineses from the fifth century BC. The philosopher Mo Ti (later Mo Tsu) was the first to our knowledge to record the formation of an inverted image with a pinhole or screen. Here we present, in chronological order, the mask patterns used in the past and nowadays. Comprehensive reviews about mask patterns and their properties are presented in Wunderer (2002) and in Caroli et al. (1987).

2.2.3.1 Pinhole camera

The pinhole camera, when used as a coded mask, provides a perfect δ function as ACF, but a very low signal-to-noise ratio (S/N) due to the small collected light; the latter problem

can be avoided enlarging the pinhole size at the expense of the angular resolution. The idea behind the random pinhole camera (later random coded mask) is to increase the open area of the plate, while preserving the angular resolution, by placing many duplicate pinholes at random in the plate. The random character is necessary to have an ACF as close as possible to a δ function.

2.2.3.2 Fresnel Zone Plate

Fresnel zone plates have first been suggested by Mertz & Young (1962), motivated in particular by the possibility to reconstruct the images without the need for computers. They suggested replacing the lens of a normal camera (optical light) by a large coarse zone plate, intended to cast clear shadows, not to focus the incoming radiation. Several sources in the field of view of the instrument result in an overlaid shadowgram. To reconstruct the image, the "photographic result" should be demagnified such that the individual zone plates in the recorded photography act as lenses and have short focal lengths for visible light. When the demagnified photographic plate is illuminated, each individual Fresnel plate shadow acts as a lens and thus forms an image of the star that generated it.
Even though this type of coded aperture has not found a place in high energy astronomy it was implemented successfully in X- and γ-ray tomographic imaging (Ceglio et al., 1977). The pattern arrangement is such that the resulting overall transmission is $\sim$50%. The ACF exhibits a central peak surrounded by a series of concentric lobes as shown in figure 2.6. These lobes can be reduced by using suitable filtering techniques.

2.2.3.3 Random mask

A natural extension of the pinhole mask is the random pinhole aperture. Independently proposed by Dicke (1968) and Ables (1968), this aperture consists of a large number of randomly spaced pinholes having an overall transmission $\sim$50%. Invented as a natural consequence of the pinhole camera which has ideal imaging capabilities (the ACF is a perfect δ function), but suffers greatly from a conflict between resolution and sensitivity, a random pattern allows to increase the sensitivity maintaining the original angular resolution. The autocorrelation of this aperture, as shown in figure 2.6, consists of a large central peak surrounded by pronounced side lobe structures. Imaging of many point like sources can cause these side-lobes to produce spurious peaks in the background.

2.2.3.4 Non- and Uniformly-redundant arrays

While seeking aperture designs whose ACF present flat side-lobes, Golay (1971) introduced a class of coded apertures with nearly perfect imaging capabilities, known as non-

redundant arrays (NRA's). In such a masks the vector separation between any two holes must occur once, and only once throughout the entire mask. The ACF is then a single peak with no side-lobes up to a certain lag δ (where the maximum distance between any two holes is 2δ). Thereafter the ACF fluctuates between 1 and 0. The disadvantage of NRA is that it can never have many transparent holes (typical opening fraction of 10%) and this affects severely the sensitivity. For these reasons these apertures have not found use in high energy astronomy.

By contrast a class of arrays which has been successful in X- and γ-ray astronomy is that based on cyclic difference sets (CDS) (Baumert, 1969). A cyclic difference set $\Delta(N, M, \lambda)$ is a sequence of M residues, modulus N, such that for any residue $\rho \neq 0(\mathrm{mod} N)$ the congruence:

$$\delta_i - \delta_j \equiv \rho(\mathrm{mod}\, N) \tag{2.7}$$

admits λ solution pairs (δ_i, δ_j) with δ_i and δ_j in Δ. To each difference set it is possible to associate a binary sequence α_i of length N, wherein α_i takes the value 1 if i belongs to Δ and 0 otherwise. A simple example of a finite difference set is $\Delta(7,4,2) = \{0,1,2,4\}$ and the corresponding mask would be 1110100. In this example $\Delta(7,4,2)$ means that the 4 members of the set give 2(=λ) different possibilities to form any of the number from 1 to 7-1 by compiling two numbers from the set.
The cyclic ACF of the binary α_i sequence has always a central peak of height N and perfectly flat side-lobes as shown in figure 2.6. The name *uniformly redundant* array comes from the fact that the vector distance between any holes occurs exactly λ times.
The opening fraction of such mask is always given by λ/N and so it can be very close to 50%. Rectangular masks can be generated from a one- dimensional CDS either by filling the rows or columns of a matrix one after another with the 1-D mask elements or by the method of the extended diagonal, provided that the length N of the CDS can be factorized into a product of two (mutually prime) integers which will give the length and width of the mask.

2.2.4 Decoding techniques

Coded mask telescopes encode the sky radiation and thus the recorded information needs to be decoded in order to derive the original sky image. Here we give an overview of the different decoding techniques that can be applied to the image deconvolution problem for coded mask instruments.

2.2.4.1 Inversion problem

If we write eq. 2.3 using matrices instead of employing the convolution operator, we get that the deconvolution problem can be solved if we find the matrix $D = M^{-1}$. This obviously requires that the mask patterns originates a non-singular matrix (i.e., the rows of the M are linearly independent). The noise in the reconstructed image is, as shown by Caroli et al. (1987), $\sigma^2 \propto Trace(MM^T)^{-1}$, thus the desired property of M is that its entries have large values. This will produce small values in M^{-1} which will minimize also the background term $M^{-1}B$ which otherwise tends to dominate. The inversion problem can still be solved if the matrix M is singular or not square (as most of the cases) by use of the so-called *generalized inverse* (Penrose, 1955). Unfortunately the conditions of having large entries in M and its non-singularity cannot be guaranteed and this translates in both statistical and background noise to be amplified in the reconstructed image when such method is used.

2.2.4.2 Cross - Correlation

The simplest deconvolution method is obtained using a matrix D (which is the aperture itself) which satisfies both conditions at the same time:

$$D * M = \delta \quad \text{and} \quad D * B \approx 0 \tag{2.8}$$

This can be achieved using the balanced ACF presented in eq. 2.7. In this case, ACF and PSF coincide and this technique is usually referred to as *matched filtering*. This technique is optimal with respect to the treatment of quantum noise, but will result in systematic errors (coding noise) if the PSF does not have flat side-lobes (Busboom et al., 1998)

2.2.4.3 Iterative methods

Iterative decoding algorithms are used to determine the source distribution without a decoding matrix or function D. These try to solve the sky vector S by an iterative search for the solution that is most consistent with the detector data. An initial guess (model) of the sky distribution $\hat{S_0}$ is folded through the instrumental response function (IRF) to model the expected count rates $\hat{C_0}$ which would result from the sky model $\hat{S_0}$. The iterative algorithm compares the expected count rates $\hat{C_0}$ with the measured one C and determines a new estimate $\hat{S_1}$. By successive iterations, these algorithms find a value of $\hat{S_i}$ which yields $\hat{C_i}$ in good agreement with $\hat{C_0}$. The success of any iterative procedure depends on the method adopted to update $\hat{S_i}$ to $\hat{S}_{i+1}$ using the difference between $\hat{C_i}$ and C and the method to measure the "goodness of fit" between $\hat{C_i}$ and C.

Maximum Likelihood (ML) looks for the sky model $\hat{S}$ that makes the obtained measurement C most likely. The ML estimate therefore is the $\hat{S}$ which maximizes the likelihood:

$$\mathcal{L}(\hat{S}_i) = \prod_{l=1}^{M} P(\textit{measurement } l \textit{ given sky } \hat{S}_i) \tag{2.9}$$

$$= \prod_{l=1}^{M} e^{-\frac{(C_l-(\hat{C}_i)_l)}{2\sigma_l^2}} \tag{2.10}$$

where eq. 2.10 assumes Gaussian statistics, and therefore the solution is determined by χ^2. Often, the logarithm of $\mathcal{L}$ (called log-likelihood LL) is maximized instead of L itself. The ML method can be applied to Poissonian as well as Gaussian statistics. We want also to point out that in the absence of noise the ML solution is formally the same as the one determined by cross-correlation.

The **Maximum Entropy** (MaxEnt) adds an a-prior knowledge about the problem to respect to the ML method. In particular the information which is usually added is of *smoothness* (i.e. the actual sky distribution is smooth). The problem of determining the optimum $\hat{S}$ thus can be reformulated as minimizing:

$$\Delta = \Delta_1(\hat{S}, \hat{S}_{data}) \; + \; h \cdot \Delta_2(\hat{S}, \hat{S}_{smooth}) \tag{2.11}$$

where Δ is a measure of "distance" of the different source maps. The choice of h determines the relative weighting of the two opposite criteria of perfect agreement with the measured data and smoothness (note that for ML the problem reduces to $\Delta = \Delta_1(\hat{S}, \hat{S}_{data})$). $\Delta 2(\hat{S}, \hat{S}_{smooth})$ can be interpreted as a penalty function which takes large values whenever the sky map is not smooth.

In the Maximum Entropy method entropy is a measure of the number of distinct ways a certain system (i.e. of particles or sky pixels in different states) can be constructed. Maximizing entropy is equivalent to determining the solution which can be realized in the greatest number of distinct ways, given our constraints (Bevensee, 1993).

In MaxEnt eq. 2.11 becomes:

$$Q(\hat{S}) = h\mathcal{S}(\hat{S}) - \mathcal{L}(\hat{S}) \tag{2.12}$$

where $\mathcal{L}(\hat{S})$ is given by eq. 2.10.

Old MaxEnt algorithms started at h=inf (prior source distribution) and computed the solution which maximized $Q(\hat{S})$ for lower and lower h until the remaining discrepancy from

the data $\mathcal{L}(\hat{S})$ was equal to N, the number of data points (for χ^2). Thus, one $\hat{S}$ on the maximum entropy trajectory is the optimum solution (Lucy, 1994). Newer MaxEnt algorithms find a probability cloud of possible $\hat{S}_i$, centered on an $\hat{S}$ which lies on the maximum entropy trajectory, representing the multitude of solutions that are feasible considering the constraints of equation 2.12.
MaxEnt methods are known for producing the flattest sky distribution compatible with the data which make them suitable tools for analyzing diffuse emissions (Strong, 2003). Conversely they are not optimum for point source search.

2.3 Sensitivity

An instrument's sensitivity is defined as the minimum detectable source flux F_{min} at a given significance (usually 5σ), during an observation time ΔT. Thus, the sensitivity is a fundamental parameter to describe the instruments' performances. The minimum detectable flux is defined as:

$$F^{lim}(\theta,\phi) = \frac{C_S^{MIN}}{Exp(\theta,\phi)\cdot A_{eff}(\theta,\phi)} \quad [ph/cm^2 s] \tag{2.13}$$

where C_S^{MIN} is the minimum number of source counts to obtain a significant detection, $Exp(\theta,\phi)$ is the *net* exposure and $A_{eff}(\theta,\phi)$ is the effective area (at the source position θ,ϕ) The source counts are usually computed as an integral (or more generally as a sum) under the instrumental PSF:

$$C_S = \int_A \int PSF(\theta,\phi,A)\cdot S(\theta,\phi)\cdot d\theta\, d\phi\, dA \tag{2.14}$$

where $S(\theta,\phi)$ is the intensity profile of the imaged object and A is the detector area where its counts are spread. Assuming the object is a point source, and its intensity profile can be expressed as $S(\theta,\phi) = K\cdot\delta(\theta,\phi)$ (with K and δ being a constant and the δ function respectively), the previous equation simplifies to:

$$C_S = K\cdot\int_A PSF(A)\, dA \tag{2.15}$$

If we refer to the simple case of one source and background, then the total number of counts and the error on the source counts can be expressed as:

$$C_T = C_S + C_B \tag{2.16}$$

$$\sigma_S^2 = \sigma_T^2 + \sigma_B^2 = C_T + C_B = C_S + 2C_B \tag{2.17}$$

where C_T is the total number of counts, C_B [2] is the background counts and $\sigma_{S,T,B}$ are the errors on the different components. If we define the significance of the detection as:

$$\frac{C_S}{\sigma_{C_S}} = n = \frac{C_S}{\sqrt{C_S + 2C_B}} \tag{2.19}$$

then it can be shown that the minimum number of source counts required to achieve a $n\sigma$ detection is:

$$C_S^{MIN} = \frac{n(n + \sqrt{n^2 + 8C_B})}{2} \tag{2.20}$$

It is thus clear that the sensitivity of an instrument depends on the background level and scales $\propto \sqrt{C_B}$. Focusing instruments, as opposed to non-focusing, concentrates the source photons onto a small part of the detector area so the background term of eq. 2.19 is small. Conversely, coded mask detectors spread the whole source counts on the detector plane and so the whole detector background must be considered when computing the source significance.

Eq. 2.14 is equally applicable to focusing and non-focusing (as coded mask) telescopes. The near one-to-one correspondence between photon arrival directions (θ, ϕ) and position coordinates in focusing telescopes means that, for a given (θ, ϕ), the function $PSF(\theta, \phi, A)$ has a compact peak in instrumental coordinates (x, y).
Since the net exposure time is actually:

$$Exp(\theta, \phi) = \Delta T - \tau * C \tag{2.21}$$

where ΔT is the duration of the observation (also called *on-time*) and $\tau * C$ is the dead-time correction (see section 2.3.2 for a discussion), the instrument's sensitivity can be finally expressed as :

$$F^{lim}(\theta, \phi) \propto \frac{\sqrt{C_B}}{(\Delta T - \tau * C) \cdot A_{eff}(\theta, \phi)}. \tag{2.22}$$

Hence, it is clear that while designing an instrument, some care must be used in order to minimize the foreseen detector background and maximize both the effective area and the net exposure time. Moreover, all quantities described above depend on energy, thus the sensitivity itself is a complex function of the energy of the incoming radiation. In the following sections, we briefly discuss the factors which play a role in determining an instrument's sensitivity. In particular we will focus on the background describing in details the background components of a space mission.

[2] the background counts are summed over the same detector area where the source counts are computed so in general:

$$C_B = \int_A B(A) \cdot dA \tag{2.18}$$

2.3.1 Effective area

The simplest definition of effective area comes directly from equation 2.13; it is in fact defined such that the total number of photons received by the detector in time δt from a point source of unit intensity S in direction (θ,ϕ) is $S \cdot A_{eff}(\theta,\phi)\delta t$. The effective area is thus the instrument's response to the incoming radiation and it is a direct measurement of the goodness of the instrument as dictates the total signal detected from the source. As equation 2.13 shows, the sensitivity improves with the increase of the effective area. In general, each type of instrument has its definition of effective area; a common (at least to focusing X-ray and coded mask telescope) definition can be:

$$A_{eff}(\theta,\phi) = A_{geom}(\theta,\phi) \cdot \varepsilon_q \cdot h \cdot \varepsilon_{image} \cdot \varepsilon_{trans} \tag{2.23}$$

where $A_{geom}(\theta,\phi)$ is the geometrical area of the detector (e.g. the CCD for focusing telescopes), ε_q is the quantum efficiency of the detecting device (e.g. see figure 2.3), h is usually referred to as the concentration factor, ε_{image} is the efficiency of the imaging reconstruction algorithm employed (if any) and ε_{trans} is the transmission through support structures. The (quantum) efficiency is defined as the probability of detecting an event (i.e. recording of an electrical signal) if it has taken place and thus it is always lower than (albeit, for modern CCDs, very close to) 1.

Focusing telescopes adopt reflecting mirrors to concentrate radiation and this means that the concentration factor h can take large values ($\gg 1$) as reported in table 2.1. Hence, the dimensions of the CCDs are dictated only by the size of the FOV to be imaged and they do not play a role in the determination of the effective area. Indeed, for focusing optics, the product $A_{geom} \cdot h$ is equal to the area of the mirror assembly. Moreover, focusing optics form, directly, an image in the focal plane, where the CCD is placed, and thus no image reconstruction algorithm has to be employed; thus for such system $\varepsilon_{image} = 1$.

In contrast, coded instruments are designed without reflecting (or refracting) optics. Photons entering the aperture may strike the detector and (potentially) be recorded or they may be stopped by intervening material. Hence, for coded mask detectors the concentration factor h is always 1 (i.e. not concentration is taking place). The efficiency of the image reconstruction takes also into account that part of the detector is blocked by the opaque elements of the mask; typical values for this efficiency are $\sim 50\%$. Moreover, the mask support elements contribute to partially stop the incoming radiation making $\varepsilon_{trans} < 1$. Thus, the mask makes possible the formation of an image at the cost of $> 50\%$ of the incoming source flux.

As already noted, all the quantities presented here have a not-subtle dependence on energy.

Table 2.1: Concentration factors for focusing X-ray telescopes.

Mission	Einstein (HRI)	ROSAT (HRI)	ASCA	Chandra
Concentration factor	3×10^4	2×10^6	2×10^3	9×10^7
Reference	(1)	(2)	(3)	(4)

reference: (1) Giacconi et al. (1979), (2) Trümper (1984), (3) Inoue (1993), (4) Weisskopf (1987).

2.3.2 Dead time

The dead time is the time during which the detector is "collecting" the information relative to an event and is insensitive to new detections. When radiation passes through a semiconductor it generates pairs of electrons and holes; if the semiconductor is fully biased the electrons drift, following the electric field, towards the anode while the holes drift in the opposite direction. The dead time can thus be defined as the time the detector needs to collect and extract (read-out) the information carriers (e.g. the electrons collected at the anode).
State-of-the-art semiconductor detectors have very small dead time and the real final dead time correction is dictated by other factors. As an example the pixel detector of the two coded mask telescopes BAT and ISGRI (Barthelmy et al., 2000; Lebrun et al., 2003) on board the Swift and INTEGRAL missions respectively have a similar event processing time (sum of charge drift time and read-out time) of $\sim 100\mu$s. From real flight data, we estimated that the dead time correction (see equation 2.21) for BAT is always very small; indeed considering a mean module (assembly of 16x8 detectors, see section 3.2 for details) rate of 100 Hz and a dead time $\tau = 100\mu$s, we get that the dead time correction is roughly 1% of the total observing time. On the other hand, in the case of ISGRI, the final dead time arise from the coincidences applied with the Anti-coincidence system (ACS), the PICSIT camera (Labanti et al., 2003) and the calibrating source; thus the overall dead time for ISGRI is 24% (Lebrun et al., 2003).

2.3.3 Background in space

The background of any space-borne hard gamma-ray instrument is highly complex and contains many individual components (Gehrels et al., 1992). It will always be high in relation to the true source counts and so its suppression is a necessity. Indeed, as we saw

in equation 2.22, the background level directly affects the instrument's sensitivity.
The position of the spacecraft with respect to the Earth affects the level of contributions of all the component. The Earth, though not the originator of X- and gamma-ray flux, supplies a flux via Cosmic Ray (CR) interactions with its atmosphere providing a Low-Earth Orbit (LEO) mission with a highly time dependent source of background. Indeed, the Earth can "shadow" the detector from CRs while the Earth's magnetic field can both shield the instrument from CR interactions and pool charged particle into radiation belts like the Van Allen belts and the South Atlantic Anomaly (SAA).

The background components can be split into two types, the photon induced background and the non-photon (Cosmic Ray) induced background. Though CRs may be responsible for most background radiation it is easier to break it down into the forms of flux as they reach the instrument. The various sources of background in space (for a X-/gamma-ray mission) will be described here in some detail in the following sections.

2.3.3.1 The Prompt Cosmic Ray Background

This source of background is due to spallation effects of incident CRs on the material of the spacecraft. A single energetic proton can pass straight through or interact creating hundreds of secondary interactions resulting in numerous X-/gamma-rays.
Whether the prompt cosmic-ray component of the background dominates or is even significant will depend on the orbit of the instrument. The Earth's magnetic field plays an important role in determining the flux of CRs reaching the spacecraft. Indeed, for a given position in the Earth's atmosphere, the magnetic field prevents particles below a certain energy reaching a certain depth in the atmosphere. This minimum cut-off energy can be derived from the Rigidity (R_c) which measures how easily a charged particle is deflected by the magnetic field expressed in gigavolts (GV) per nucleon (momentum per unit charge). From the values of rigidity, known at each point of the orbit, the cut-off energy can be derived as:

$$E_c = (0.938^2 + R_c^2)^{0.5} - 0.938 \quad (\text{GeV}). \tag{2.24}$$

The rigidity of the spacecraft's position plays a large part in determining the CR spectrum incident on the spacecraft as all particles below the cutoff energy will not reach that position in the orbit. Since the rigidity varies during the spacecraft's orbit, the background will modulate accordingly.

The prompt CR background can be partially shielded by using an active veto system; any coincident counts by charged particles in the veto and the detector will be ignored.

However should a count in the detector be delayed from the veto count because the incident CR left material in an excited state (with half-life larger than microseconds) then the resultant radiation from this decay cannot be veto-ed out and so constitutes a form of background.

2.3.3.2 The Delayed and Secondary Cosmic Ray Background

The delayed component of the CR background can be fully understood only when the spacecraft is in orbit. The spacecraft receives a CR flux which "activates" (interacts and excites) its materials. Therefore the delayed component is both slowly varying, highly specific to the instrument and builds up asymptotically over much longer time scale than any prompt CR background.

The secondary CR background is the component resulting from CR interactions with material outside the detector, producing photons and leptons. Also this component is highly specific to the spacecraft.

2.3.3.3 Solar flares

Solar energetic particles can be classed as "impulsive" or "gradual" (Klein & Trottet, 2001). The impulsive particles are a result of flares and vary with the solar cycle. Typically the impulsive flux has high electron and proton fluxes, high Helium fluxes, an enhanced heavy element ratio and a low ion intensity. The gradual particles are a result of Coronal Mass Ejections (CMEs). These mass ejections produce a shock-wave in the solar corona and in the interplanetary space accelerating charged particles. These ejections are dominated by protons and evolve over timescales of days. As a source of background each flare is different in spectra and evolution.

2.3.3.4 Magnetospheric trapped particles

Magnetospheric particles consist of protons and electrons that are constrained by the local magnetic field in the same way a "magnetic bottle" is used to confine energetic plasma (van Allen, 1958). The two Earth's radiation belts are populated by fluxes of energetic particles. The inner belt is compact and extends to about 6400 km above the Earth's surface and is filled by dense fluxes of energetic protons. The outer belt is less stable and contains a variety of ions (mostly protons) and electrons of much lower energy. It extends from about 20,000 to 27,000 km above the Earth's surface. The population of this outer belt fluctuates wildly, interacting with magnetic storms while being populated by the variable tail of the magnetosphere. Unlike the other constituent types of CR these

are confined to specific areas around the Earth and so need only to be considered if the instrument is passing through the belts directly. Due to the nature of the magnetic field surrounding the Earth, the southern hemisphere has an indentation in the magnetosphere called the South Atlantic Anomaly (SAA) and can be a major source of background for instruments in low Earth orbit. Moreover, after each SAA passage, instruments experience a delayed self-radiating background due to radioactive decay (mainly gamma and β decays) as a consequence of the sharp increase of proton flux.

During SAA passages the spacecraft experience a sharp rise in electron flux as well. These electrons do not cause a delayed component, but will produce a secondary component as well as a prompt component due to processes such as Bremsstrahlung.

2.3.3.5 The X-ray background

The X-ray background, which has already been extensively discussed in details in section 1.2, is one of the major background components for hard X-ray experiments. The XRB is the integrated emission of many AGN. As instrument sensitivity improves then the resolution of these sources becomes achievable; for hard X-ray instruments with a ∼arcmin resolution and mCrab sensitivity, the XRB remains a strong background component.

The XRB is isotropic unless the Earth is shadowing the spacecraft. Its spectrum has been measured by several instruments in the past (see section 1.2), but one of the best broad band measurement has been performed by HEAO-1; the following analytic approximation was suggested by Gruber et al. (1999):

$$S_{XRB}(E) = \begin{cases} 7.877E^{-0.29}e^{-E/41.13} & 3 < E < 60 \text{ keV} \\ 0.0259(E/60)^{-5.5} + & \\ 0.504(E/60)^{-1.58} + & E > 60 \text{ keV} \\ 0.0288(E/60)^{-1.05} & \end{cases} \tag{2.25}$$

where $S_{XRB}(E)$ is in units of keV/keV cm^{-2} s^{-1} sr^{-1}.
Given this spectral shape (see also Fig. 1.13), the XRB emission is usually the dominant background component up to 30-40 keV, then its spectrum becomes steeper (changing from a power law with photon index of 1.4 to a power law with index 2.4) and its contribution becomes less important.

2.3.3.6 Atmospheric Albedo Gamma radiation

The Earth's atmosphere is a strong source of radiation. CR particles, primarily protons, interact with the atmosphere producing X-/gamma-rays. Below 50 MeV the main source can be attributed to bremsstrahlung radiation from secondary electrons from CR interactions while above this energy the main source is the decay of mesons.

The flux that an instrument observes from the Earth's atmosphere varies with the spacecraft's position and the direction that the instrument is pointing. this is due to the amount of atmosphere that the instrument views and not due to nay directional component of the albedo emission. As the emission is secondary to the Cosmic Ray interaction, the flux is isotropic from each unit volume of atmosphere, but depth dependent.
Since the Earth's magnetosphere modulates the CR flux as a function of position, the same kind of modulation is observed in the Albedo component.
Recently, Sazonov et al. (2006b) have performed extensive simulations to determine the Earth's atmosphere emergent photon spectrum (in the X-/gamma-ray energy range) due to CR bombardment of the atmosphere. They found that the emergent photon spectrum due to mono-energetic protons (but it is also a good approximation for positrons and electrons) can be described as:

$$\frac{dN_\gamma}{dE} = \frac{C}{(E/44\text{keV})^{-5} + (E/44\text{keV})^{1.4}} \quad \text{keV}^{-1} \tag{2.26}$$

where C depends on the primary particle energy. The spectra for different proton energies are plotted in left panel of Fig. 2.7. Since the emergent spectral shapes are barely sensitive to the primary particle's energy, the integration of equation 2.26 over the CR spectrum affects only the normalization. The emergent atmospheric photon spectrum for different values of cut-off rigidities (R_c) is shown in the right panel of Fig. 2.7.

2.3.4 Example of active background suppression: MEGA ACS

Since in the gamma-ray energy range the fluxes from astronomical sources are generally much smaller than the instrumental background, it is necessary to make every effort to suppress the orbital background in order to achieve the best sensitivity. In Appendix A, we present in details the calibration of the Anticoincidence System (ACS) of the *Medium Energy Gamma-ray Astronomy* (MEGA) prototype. The calibration shows the good overall performances of the MEGA ACS. In particular, with a low energy threshold of $\sim$70 keV and a very good uniformity of the response over the entire surface we expect a suppression of up to 99.3% of the orbital background.

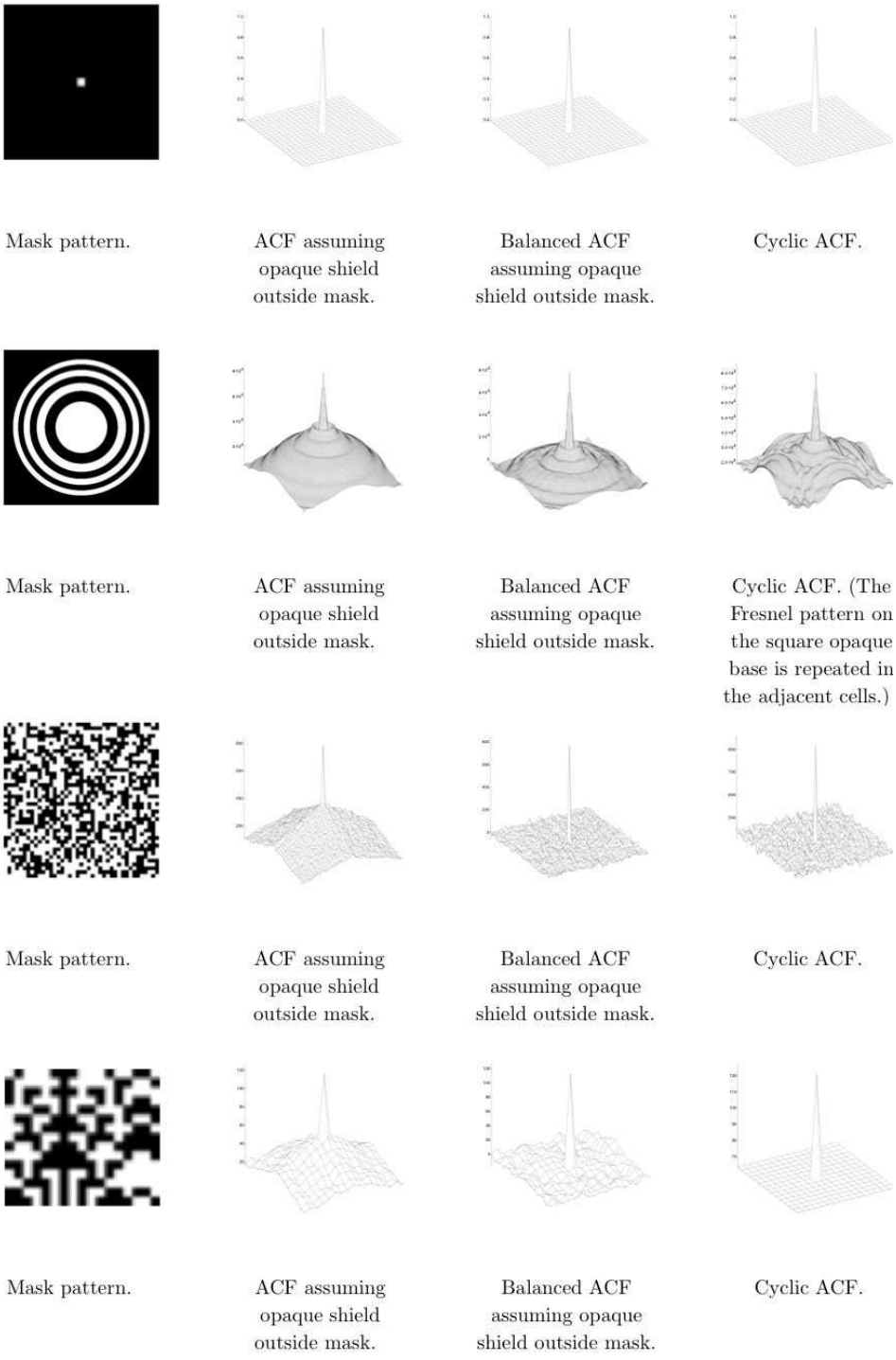

Figure 2.6: Different mask patterns with their ACFs. From up to bottom, the patterns are: random pinhole, Fresnel Zone Plate, random mask (50% opening) and two-dimensional URA mask. Freely adapted from Wunderer (2002).

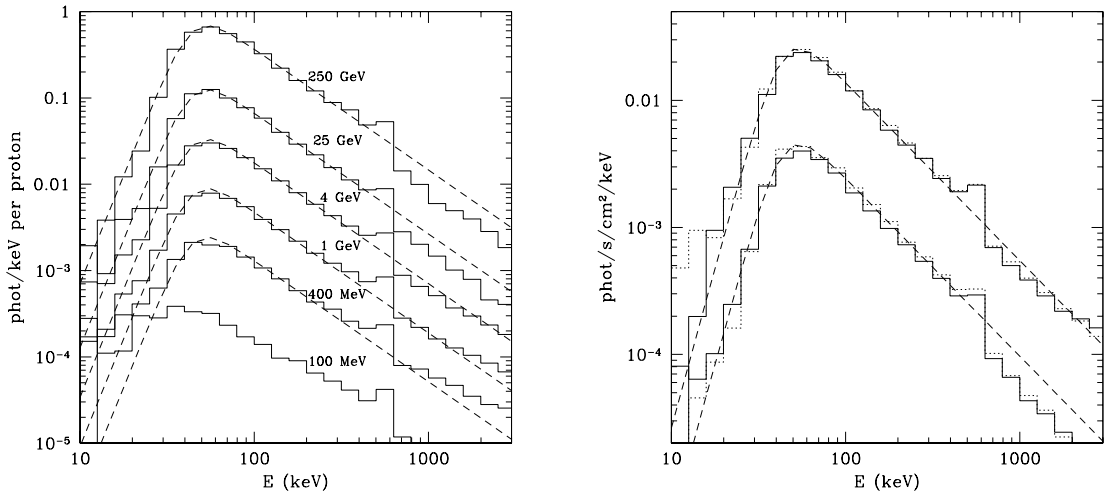

Figure 2.7: *Left Panel:* Emergent atmospheric spectra in the X-ray to soft gamma-ray range for different energies of incoming cosmic protons (labels near the curves). The dashed lines show the analytic approximation for the 25-300 keV range given by equation 2.26. This approximation breaks down at low proton energies E$\leq$ 400 MeV (Sazonov et al., 2006b). *Right Panel:* Simulated spectra of Earth's atmospheric emission due to CR bombardment for R_c = 0.5 GV and R_c = 15 GV (upper and lower curves respectively). The dashed lines show the corresponding predictions based on equation 2.26 integrated over all zenith angles. For a more detailed discussion see Sazonov et al. (2006b).

Chapter 3

The Swift Gamma-ray burst mission

Here we give a brief overview of the Swift mission. In particular, we focus on the Burst Alert and the X-ray telescopes as most of the results presented in the next chapters are based on these instruments.

3.1 The Swift mission

The Swift satellite, launched by NASA in November 2004, is a multi-wavelength observatory dedicated to the study of Gamma-ray bursts (GRBs, Gehrels et al., 2004). It is equipped with 3 instruments to detect and study GRBs and their afterglow. GRBs are flashes of gamma-rays with durations from fractions of a second to hours occurring at random position in the sky. Swift employes a, large FOV, coded mask telescope to detect and localize GRBs with a precision of 1-4 arcmin. After the burst detection, the spacecraft autonomously repoints itself (in approximately 25–75 seconds) to bring the burst location within the FOV of the narrow-field X-ray and UV/optical telescopes (XRT and UVOT respectively) to observe the afterglow emission. Thanks to its three instruments, Swift can provide redshifts and multi-wavelength lightcurves for the duration of the afterglow. The main scientific goals of the Swift mission are:

- determine the origin of gamma-ray bursts;
- classify GRBs and search for new types;
- determine how the blastwave evolves and interacts with the surroundings;
- use GRBs to study the early universe;
- perform the first sensitive survey of the hard X-ray sky.

Swift measurements are of great interest for the scientific community and all data are available to the public via the internet as soon as they are processed.
Two years after the launch, Swift achieved the detection of $>$ 200 GRBs and studied in detail the afterglow emission for many of those. In the next sections, we summarize the properties of the three instruments.

3.2 The Burst Alert Telescope

The BAT is a sensitive, large FOV, coded mask aperture dedicated to provide critical GRB triggers and accurate (1 to 4 arcmin) positions. BAT employes a random mask (see section 2.2.3.3 for a discussion) with a 1.4 sr FOV (half coded). The energy range is 15-200 keV for imaging, with an uncoded response extending up to 500 keV. Within several seconds of detecting a GRB, BAT determines an initial position, decides whether the burst merits a spacecraft slew and, if so, sends the position coordinates to the spacecraft.

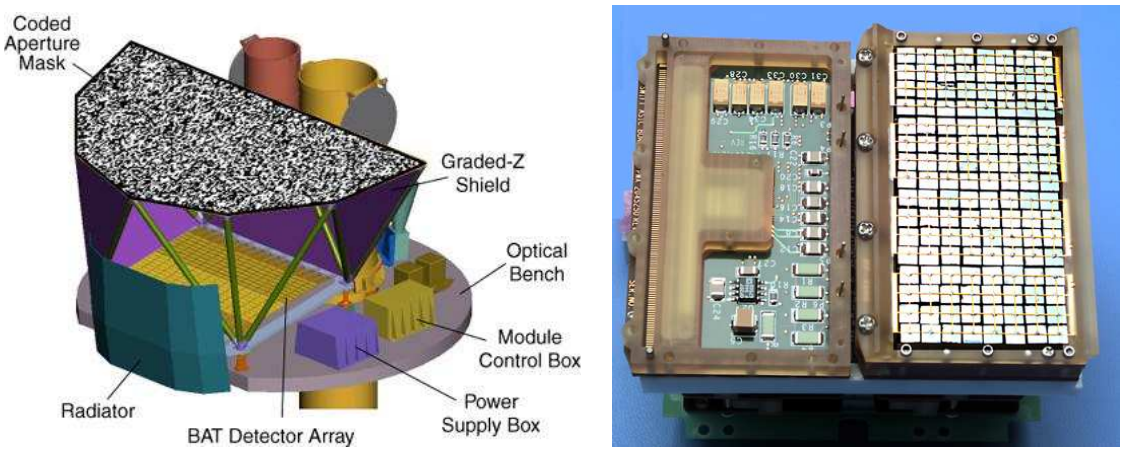

Figure 3.1: *Left Panel:* Schematic drawing of the BAT. BAT has a 3 m^2 D-shaped coded aperture with 5x5 mm^2 pixels. The 32768 CdZnTe elements form a 1.2 x 0.6 m^2 sensitive area. The Graded-Z Fringe Shield, which is not fully drawn, reduces the background due to cosmic diffuse and Cosmic-ray generated emission. *Right Panel:* The BAT detector module (DM). Two sub-arrays of 8x16 pieces (one not shown) of CdZnTe tile the top surface of the DM. The ASIC and all the read-out electronic is stacked under the CdZnTe layer (credit NASA/GSFC).

In order to study bursts with a variety of intensities, durations, and temporal structures, the BAT must have a large dynamic range and trigger capabilities. Moreover, as GRBs appear at random positions in the sky, the BAT was designed to have a large FOV in order

to monitor a large fraction of the sky. The Swift pointing directions are optimized so that each day BAT monitors 80% of the sky; the strategy of observation also favours night sky regions so that ground observatories can follow-up on GRB afterglows. As a result of the large FOV and the observing strategy, the BAT is currently surveying the hard X-ray sky (15-200 keV) to unprecedented sensitivities reaching $\sim$1 mCrab in 1Ms of exposure (Markwardt et al., 2005).

Table 3.1: BAT Instrument properties.

Property	**Description**
Aperture	Random coded mask
Detecting Area	5200 cm^2
Detector	CdZnTe
Detector Operation	Photon counting
Field of View	1.4 sr (half coded)
Detection Elements	256 module of 16x8 elements
Detector Size	4 mm x 4 mm x 2 mmm
Telescope PSF	22 arcmin
Energy Range	15-200 keV

3.2.1 Instrument description

The BAT telescope consists of a plane with 32768 CdZnTe (CZT) pixel detectors and a random mask, hosting $\sim$ 54000 (5x5x1 mm^3) lead tiles, 1 m above the detecting area. A schematic view of the BAT is shown in the left panel of Fig. 3.1.

Groups of 128 detector elements are assembled into 8 x 16 arrays, each connected to 128-channel readout Application Specific Integrated Circuits (ASICs). Detector modules, each containing two such arrays, are further grouped by eights into blocks (see right panel of Fig. 3.1). This hierarchical structure, along with the forgiving nature of the coded aperture technique, means that the BAT can tolerate the loss of individual pixels, individual detector modules, and even whole blocks without losing the ability to detect bursts and determine locations.
The D-shaped coded aperture is made of $\sim$ 54000 lead tiles randomly mounted on a 5 cm thick composite honeycomb panel which is maintained by aluminum structures (visible in Fig. 3.1) 1 m above the detector plane. Because the large FOV requires the aperture to be much larger than the detector plane and the detector plane is not uniform due to gaps

between the detector modules, the BAT coded-aperture uses a completely random, 50% open-50% closed pattern, rather than the commonly used Uniformly Redundant Array pattern. The mask has an area of 2.7 m^2, yielding a half-coded FOV of 100 degrees $\times$ 60 degrees, or 1.4 steradians.

A graded-Z fringe shield, located both under the detector plane and surrounding the mask and detector plane, reduces background from the isotropic cosmic diffuse flux and the anisotropic Earth albedo flux by $\sim$95%. The reduction of K X-ray from the shield itself is also desirable. A graded-Z shield, therefore, works by providing materials with decreasing atomic numbers toward the detector in order to absorb the K X-ray photo-electrically and emit a secondary X-ray of lower energy. The shield used on the BAT instrument is composed of layers of Pb, Ta, Sn, and Cu, which are thicker nearest the detector plane and thinner near the mask.

A figure-of-merit (FOM) algorithm resides within the BAT flight software and decides if a burst detected by the BAT is worth requesting a slew maneuver by the spacecraft. If the new burst has more "merit" than the pre-programmed observations, a slew request is sent to the spacecraft. Uploaded, rapid-reaction positions are processed exactly the same as events discovered by the BAT. The FOM is implemented entirely in software and can be changed either by adjusting the parameters of the current criteria or by adding new criteria.

3.2.2 Burst detection

The burst trigger algorithm looks for excesses in the detector count rate above expected background and constant sources. It is based on algorithms developed for the HETE-2 GRB observatory, upgraded based on HETE-2 experience. The algorithm continuously applies a large number of criteria that specify the pre-burst background intervals, the order of the extrapolation of the background rate, the duration of the burst emission test interval, the region of the detector plane illuminated, and the energy range. The BAT processor continuously tracks hundreds of these criteria sets simultaneously. The table of criteria can be adjusted. The burst trigger threshold is commandable, ranging from 4 to 11 sigma above background noise with a typical value of 6.0–6.5 sigma. A key feature of the BAT instrument for burst detection is its imaging capability. Following the burst trigger, the on-board software checks for and requires that the trigger corresponds to a point source, thereby eliminating many sources of background such as magnetospheric particle events and flickering in bright galactic sources. Time-stamping of events within the BAT has a relative accuracy of 100 microsec and an absolute accuracy from the spacecraft clock of $\sim$200 microsec. When a burst is detected, the sky location and intensity are immedi-

ately sent to the ground and distributed to the community through the Gamma-Ray Burst Coordinates Network (GCN) (Barthelmy et al., 2000).

3.2.3 The hard X-ray survey

While searching for bursts, the BAT performs an all-sky hard X-ray survey and monitor for hard X-ray transients. The BAT accumulates on board detector plane maps every 5 minutes, which are then included in the normal spacecraft telemetry stream. These exposures are then used to build the survey. Some of the results from the BAT high latitude survey (Markwardt et al., 2005) were already discussed in Chapter 1, but they will be summarized in the next paragraph.

The analysis of the first 3 months of data shows that BAT is a sensitive instrument for surveying the hard X-ray sky. Indeed, BAT reaches a 5σ sensitivity of 2 mCrab in $\sim$700 ks being already $>$5 times more sensitive than the last hard X-ray survey performed by HEAO-1 (Levine et al., 1984). The extragalactic sample includes 54 sources and a completeness level of $\sim$90%. The derived absorption distribution is bimodal with 64% of all AGN showing column densities $N_H > 10^{22}$ cm^2. The absorption also shows a weak anti-correlation with intrinsic luminosity with a turn-over at Log(L_X) = 43.5 erg/s; sources above this luminosity are mostly unabsorbed. Markwardt et al. (2005) conclude saying: *" based on these data, we expect the BAT catalog to have $>$ 200 AGN and reach fluxes of less than 10^{-11} erg cm^{-2} s^{-1} over the entire sky*".

3.3 The X-ray Telescope

Swift's X-Ray Telescope (XRT, Burrows et al., 2000) is designed to measure the fluxes, spectra, and lightcurves of GRBs and afterglows over a wide dynamic range covering more than 7 orders of magnitude in flux. The XRT can pinpoint GRBs to 5-arcsec accuracy within 10 seconds of target acquisition for a typical GRB and can study the X-ray counterparts of GRBs beginning 20-70 seconds from burst discovery and continuing for days to weeks. The XRT is a focusing X-ray telescope with a 110 cm^2 effective area, 23 arcmin FOV, 18 arcsec resolution (half-power diameter, HPD), and 0.2-10 keV energy range. The XRT uses a grazing incidence Wolter 1 telescope to focus X-rays onto a CCD. The X-ray mirrors are the units built, qualified and calibrated (twice at MPE's PANTER facility) as flight spares for the JET-X instrument on the Spectrum-X mission while the CCD is a copy of the EPIC-MOS instruments on the XMM-Newton mission.

The XRT supports three readout modes to enable it to cover the dynamic range and

Table 3.2: XRT Instrument properties.

Property	Description
Telescope	JET-X Wolter 1
Focal Length	3.5 m
Effective Area	110 cm^2 @ 1.5 keV
Telescope PSF	18 arcsec HPD @ 1.5 keV
Detector	EEV CCD-22, 600x600 pixels
Detector Operation	Imaging, Timing and Photon-counting
Pixel Scale	2.36 arcsec/pixel
Energy Range	0.2 - 10 keV
Sensitivity	2×10^{-14}erg/cm^2/s in 10 ks

rapid variability expected from GRB afterglows, and autonomously determines which readout mode to use. Imaging Mode produces an integrated image measuring the total energy deposited per pixel and does not permit spectroscopy, so will only be used to position bright sources. Timing Mode sacrifices position information to achieve high time resolution (2.2 ms) and bright source spectroscopy through rapid CCD readouts. Photoncounting Mode uses sub-array windows to permit full spectral and spatial information to be obtained for source fluxes ranging from the XRT sensitivity limit of 2×10^{-14} to 9×10^{-10} erg cm^{-2} s^{-1}. Table 3.2 summarizes the instrument's properties.

The XRT is also used to follow-up on BAT survey sources to determine their soft X-ray counterpart; given the 5 arcsec accuracy, XRT observations are successful in identifying the optical counterpart of the BAT sources (e.g. Tueller et al., 2005a, 2005b and Kennea et al., 2005).

3.4 The UV/Optical Telescope

The UltraViolet and Optical Telescope (UVOT, Roming et al., 2000) is a diffraction-limited 30 cm (12" aperture) Ritchey-Chretien reflector, sensitive to magnitude 24 in a 17 minute exposure. The optics used for Swift UVOT are the flight spares from the XMM-Newton Optical Monitor (OM). The detectors are copies of two micro-channel plate intensified CCD (MIC) detectors from the XMM-Newton OM design. They are photon counting devices capable of detecting very low signal levels, allowing the UVOT to detect faint objects over 170-650 nm. The design is able to operate in a photon counting mode, unaffected by CCD read noise and cosmic ray events on the CCD. The UVOT

can autonomously determine the spacecraft drift using guide stars in the FOV. The UVOT design includes the XMM-Newton OM 11 position filter wheel in front of the detectors. The two grisms can be used to obtain low resolution spectra of the brightest bursts with mB$<$ 17. The UVOT, with a 17x17 arcmin^2 FOV and a PSF full width at half maximum, of 2.0 arcsec, can locate the GRB position with sub-arcesec precision.

Ground observations of GRBs have shown that optical afterglows typically decline in brightness as $t^{-1.1}$ to $t^{-2.1}$. Therefore, rapid response is required to observe these counterparts and determine their redshift while they are still bright. The UVOT, with UV capability which is not possible from the ground, enables ground based observations by providing rapid optical images of the GRB field so that any optical or IR counterpart can be quickly identified and studied. Stars in the FOV of the UVOT provide an astrometric grid for the GRB field.

UVOT has so far provided accurate (sub-arcsec) positions for 43 (out of 203) GRBs .

Chapter 4

BAT extragalactic X-ray Survey - I: Methodology and X-ray Identification

M. Ajello, J. Greiner, G. Kanbach, A. Rau and A. W. Strong

abstract

We applied the Maximum Likelihood method, as an image reconstruction algorithm, to Swift/BAT survey data. This method was specifically designed to preserve the full statistical information in the data and to avoid the usual mosaicking of many exposures with different pointing directions, thus reducing systematic errors when co-adding images. We reconstructed, in the 14-170 keV energy band, the image of a sky region which BAT surveyed with an exposure time of $\sim$ 1Ms (at the time of this study). The investigation is partly motivated by a campaign for optical spectroscopy identification of BAT-selected extragalactic objects (Rau et al., 2007). The best sensitivity in our image is ~ 0.8mCrab or 1.9×10^{-11} erg cm^{-2}. 61 hard X-ray sources are detected above the 4.5σ level; of these, only 12 were previously known as hard X-ray sources ($>$15 keV). Swift/XRT observations allowed us to firmly identify the counterparts for 15 objects, while 2 objects have Einstein IPC counterparts (Harris et al., 1990); in addition to those, we found a likely counterpart for 13 objects by correlating our sample with the the ROSAT All-Sky Survey Bright Source Catalog (Voges et al., 1999). 19 objects are still unidentified. Analysis of the noise properties of our image shows that $\sim$ 75% of the area is surveyed to a flux limit of < 0.9 mCrab and that systematic noise is negligible. This study shows that the coupling of the Maximum Likelihood method to the most sensitive, all-sky surveying, hard X-ray instrument, BAT, is able to probe for the first time the hard X-ray sky to the sub-mCrab flux level.

The successful application of this method to BAT demonstrates that it could also be applied with advantage to similar instruments like INTEGRAL-IBIS.

4.1 Introduction

More than 40 years after its discovery, the nature of the Cosmic X-ray Background (CXB) is still debated. X-ray observations, interpreted in the context of CXB population synthesis models based on unified AGN schemes, (Comastri et al., 1995; Gilli et al., 2001), explain the CXB spectrum using a mixture of obscured and unobscured AGN. According to these models, most AGN spectra are heavily absorbed, and about 85% of the radiation produced by super massive black hole accretion is obscured by dust and gas (Fabian & Iwasawa, 1999).

Deep soft X-ray surveys (0.5–2.0 keV) were able to resolve the majority ($\approx$ 80%) of the Cosmic X-ray Background (CXB) flux into discrete sources (Hasinger et al., 1998). However the resolved fraction decreases with energy, being $\sim$50-60% in the 6–8 keV band (Giacconi et al., 2002; Rosati et al., 2002) and even less above $>$8 keV; the missing CXB component has a spectral shape that is consistent with a population of yet undetected, highly obscured AGN (see Worsley et al., 2005).

It is important to realize that highly obscured objects are detectable in X-rays only above 10 keV. Moreover, most of the energy of the CXB is emitted around 30 keV (Marshall et al., 1980) and the exact nature of the source population responsible for the background at these energies is unknown primarily because of the low sensitivity of previous X-ray telescopes operating above 15 keV.

All these reasons together motivate more sensitive observations of the hard X-ray sky.

The Burst Alert Telescope (BAT) (Barthelmy et al., 2005), on board the Swift mission (Gehrels et al., 2004), launched by NASA on 2004 November 20, represents a major improvement in sensitivity for X-ray imaging of the hard X-ray sky. BAT is a coded mask telescope with a wide field of view (FOV, $120^o \times 90^o$ partially coded) aperture sensitive in the hard X-ray domain (15-200 keV). BAT's main purpose is to locate Gamma-Ray Bursts (GRBs). While chasing new GRBs, BAT surveys the hard X-ray sky with an unprecedented sensitivity. Thanks to its wide FOV and its pointing strategy, BAT monitors continuously a large fraction of the sky (up to 80%) every day. Already after one year the all-sky exposure ranges from 0.3 to 1.5 Ms reaching a sensitivity of $\sim$ 1 mCrab. This is more than ten times better than the previous hard X-ray all-sky survey performed by HEAO-1 (Levine et al., 1984).

Coded mask telescopes are, until the advent of next generation hard X-ray focusing optics, the only instruments able to image the sky in the hard X-ray domain. Objects in the FOV cast part of the mask pattern onto the detector plane. Since the sources' signal is coded by

the mask onto the plane this phase is also referred to as coding phase. Thus, a decoding procedure is required in order to reconstruct the original sky image. A variety of methods can be used to reconstruct the sky image in the case of a coded mask aperture (see Skinner et al., 1987, for a general discussion on reconstruction methods). Among them, standard cross correlation, via FFT transforms, of the shadowgram with a deconvolution array (the mask pattern) is the most often used. Generally, sky images are obtained for each observation (when the attitude is stable and constant) then another procedure (i.eg.: resampling and reprojecting) is needed in order to assemble the final images with different pointing directions into the final all-sky image.

We here describe the application of an alternative method which was designed to avoid some of the disadvantages of the standard mask unfolding technique. The primary goal is to increase the detection sensitivity, since most of the extragalactic sources are very faint in the hard X-ray band. Thus their detection is challenging and requires sensitive techniques.

This study has been developed in the framework of a campaign for optical spectroscopy analysis of a sample of "hard X-ray selected" extragalactic sources aimed at identifying new Sy2 galaxies. This paper discusses the method used to reconstruct the survey image and presents the source catalog. A second paper (Rau et al., 2007) describes in details the optical campaign and the source identification process while the spectral analysis and the statistical properties of our sample of sources are discussed in Ajello et al. (2007).

The structure of the paper is as follows. In Section 4.2 we present details of the Maximum Likelihood method that was developed to analyze the BAT data. In Section 7.3, we describe the analysis steps performed and we present and discuss the results of our image reconstruction algorithm. The last section summarizes the results.

4.2 Spatial Model Fitting

We apply "spatial model fitting", as described in Strong et al. (2005), to directly reconstruct the survey image from the raw detector data. "Spatial model fitting" means that a number of sky distributions, which constitutes the model, are forward -folded through the full instrumental response in order to generate a model shadowgram. Shadowgrams are then fitted in the full data space in order to get the most probable sky distribution given the model. The actual search for unknown sources is then realized by moving a source probe in a grid over the sky. It is worth noting that no other steps, as image mosaicking, are

required at the end of this process. This method was, in fact, invented with the goal of reducing systematic errors and noise e.g. the noise related with individual short images and the systematics when co-adding noisy images in the mosaicking procedure. This leads to an improvement in sensitivity over other methods, in particular reducing systematic errors from background variations and resampling. The full information in the data is preserved and correctly treated in a statistical sense.

The likelihood is the probability of the observed BAT data given the model. For our case it is defined as the product of the probability for each detector of each observation:

$$L = \prod_{ijk} p_{ijk}. \tag{4.1}$$

where

$$p_{ijk} = \frac{\theta_{ijk}^{n_{ijk}} e^{-\theta_{ijk}}}{n_{ijk}!}. \tag{4.2}$$

is the Poisson probability of observing n_{ijk} counts in pixel ij, during the k-th observation, when the number of counts predicted by the model is θ_{ijk}.

The model is a linear combination of components; in the simplest case of 1 non variable source and 1 background component for each observation, we get:

$$\theta_{ijk} = c_0 \times (A \otimes S^{\alpha_0,\delta_0})_{ijk} + c_k \times B_{ijk} \tag{4.3}$$

where $(A \otimes S^{\alpha_0,\delta_0})$ is the convolution of the detector response (A) and a source of unit flux (S) at the sky position α_0, δ_0 and thus $(A \otimes S^{\alpha_0,\delta_0})_{ijk}$ yields the prediction of counts from a unit flux source at the sky position α_0, δ_0 in detector ij, during observation k; B_{ijk} is the background prediction for pixel ij in observation k and c_0 and c_k's are the parameter we want to estimate.

In this first application, the background model comprises, for each observation, of an empirical model (i.e. a 2 dimensional quadratic function similar to the one used by the tool *batclean* as described in section 4.3.1) and of the model shadowgrams for all bright sources (see also section 4.3.1). The actual fit to the background is performed only once and during the source search the normalization of the whole background is allowed to vary. We verified that such variation was less than 10^{-3}. In the future, our method will allow to test more complex and physical background models (e.g. diffuse emissions).

4.2.1 Parameter model estimation

The parameter values are found by maximizing the likelihood function, or, which is the equivalent, maximizing its logarithm:

$$\frac{\partial \ln L}{\partial \Lambda_i} = \frac{\partial}{\partial \Lambda_i}\left[\sum_{ijk} n_{ijk}\ln(\theta_{ijk}) - \sum_{ijk}\theta_{ijk}\right]. \tag{4.4}$$

where Λ is the vector of the parameters. This translate into the following set of equations:

$$\frac{\partial lnL}{\partial c_0} = \sum_{ijk}(A\otimes S)_{ijk}\left(\frac{n_{ijk}}{\theta_{ijk}} - 1\right), \tag{4.5}$$

$$\frac{\partial \ln L}{\partial c_k} = \sum_{ijk} B_{ijk}\left(\frac{n_{ijk}}{\theta_{ijk}} - 1\right), \ \forall k \tag{4.6}$$

which allows to estimate all parameters simultaneously.
This set of equation can be solved only numerically and we are using a modified Newton algorithm in order to find the solution.

4.2.2 Source significance

In the case of a single source component, the source significance can be estimated using the likelihood ratio test. For this application, the null hypothesis is that no point source exists at the position under consideration and the background model can explain all the data. The alternative hypothesis is the converse. Two maximizations have to be done in order to calculate the likelihood L_0 of the background (null hypothesis) and the likelihood of both source and background for the alternative hypothesis L_1. The test statistics:

$$T_s \equiv -2(\ln L_0 - \ln L_1) \tag{4.7}$$

is expected, from Wilks's theorem (Wilks, 1983), to be asymptotically distributed as χ^2_1 in the null hypothesis because of the additional parameter of the alternative hypothesis. Thus, the significance of a detection can be addressed as:

$$S = \int_{T_s}^{\infty} \frac{1}{2}\chi^2_1(x)dx, \tag{4.8}$$

which, after changing variables, become:

$$S = \int_{\sqrt{T_s}}^{\infty} \frac{e^{-y^2/2}}{(2\pi)^{1/2}}dy. \tag{4.9}$$

Equation 4.9 is exactly the integral of the standard normal distribution from $T_s^{1/2}$ to ∞ and so the significance of the detection is:

$$T_s^{1/2}\sigma = \sqrt{-2(\ln L_0 - \ln L_1)}\sigma = n\sigma. \quad (4.10)$$

Hence, by definition, the significance fluctuations must be distributed as a normal Gaussian if everything is done correctly.

4.2.3 Method implementation

In case of large detector counts, the likelihood maximization is equivalent to the χ^2 minimization, with the advantage that the χ^2 problem can be solved faster analytically. We have verified that in the case of large detector counts and large numbers of observations the two solutions are very similar and from now on we use the χ^2 solution.

The algorithm used is a parallelized implementation of *spidiffit* (Strong et al., 2004) used for INTEGRAL-SPI data analysis. Parallelization was needed because of the size of the problem we are dealing with. The typical execution time needed to compute the analytical χ^2 solution scales with n^2 where n is the number of data points to fit (i.e.: number of BAT detectors, 32768, multiplied by the number of observations). A single minimization with 2600 observations takes nearly 90 s; the total execution time to generate a map of 450×450 pixel would be $\sim$200 days. This time has been reduced to $<$15 days using an average of 15 CPUs. We want to remark also that it is the first time that such an approach is applied to a problem of this large size.

As shown in equation 7.4, our model is a linear combination of different components which can be specified at the input of the program. This allows readily to handle more than one source, to include source variability in the analysis and to test different background models at the cost of a longer computational time. For the analysis which will be presented in the next sections, we have used the ability to fit simultaneously all sources found. In fact, after source candidates have already been found, the simultaneous fit yields the best parameters (significances and fluxes) for all of them and allows us to discard spurious detections. When the analysis is based on a large number of observations correlation ("cross-talk") between sources is negligible.

4.2.4 Instrumental response

As shown in equation 7.4, the first part of the model represents the source component (or components if more than one) and this is given in the most simple form by a point like

source at position α_0, δ_0 in the sky, forward-folded with the instrumental response. We have used a large set of Crab observations (> 1000) to developed a parametrized diagonal full instrumental response which enables us to predict the expected counts (essentially the term $A \otimes S^{\alpha_0,\delta_0}$ of equation 7.4) from a unit flux source as a function of energy and position in the field of view (FOV). To improve the speed of the code the full instrumental response was pre-computed over a 6 arcmin pitch grid in the whole BAT FOV.

To conclude, in Fig. 4.1 we show the imaging reconstruction capabilities of our approach; two closeby faint sources, LMC X-1 and PSR B0540-69.3, are clearly detected in $\sim$2600 observations. The good angular resolution of BAT is also preserved by our imaging reconstruction algorithm, in fact the two sources are separated by just $25'$ (for comparison the BAT Point Spread Function (PSF) is $22'$).

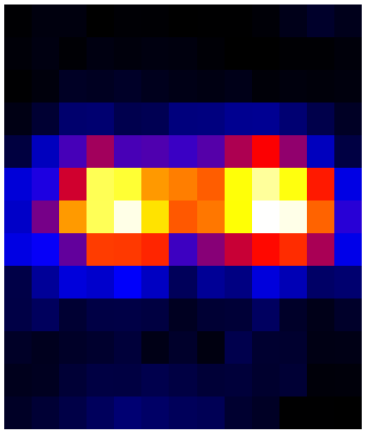

Figure 4.1: Image of LMC X-1 (right) and PSR B0540-69.3 (left) clearly separated. The pixel size is $5'$and the map is about 1×1 deg^2.

4.3 Analysis

In this section we describe the application of the Maximum Likelihood method to reconstruct the image of $\sim 1/8$ of the sky using 8 months of BAT data.

4.3.1 Data selection and screening

We used 8 months of data, from April 2005 (when BAT data became public) to November 2005. In order to secure optical follow-up with a dedicated observing campaign at La

Silla, Chile in January 2006, we selected only observations with angular separation less than 45 degrees fom the zenith (RA=105 degrees, DEC=−25 degrees).

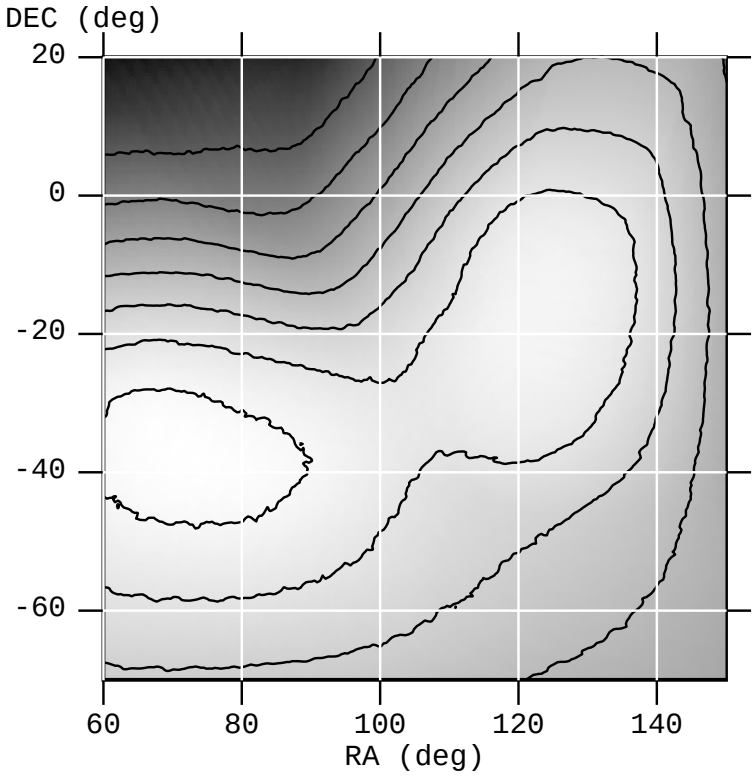

Figure 4.2: Exposure map, corrected for telescope vignetting, of the survey field presented in text after data screening. Contours spaced of 100 ks are also shown. The inner contour is for exposure greater than 900 ks.

Swift-BAT survey data are in the form of 80 channels detector plane histograms (DPH) with typical exposure time of 300 s.
In order to have a suitable clean dataset as input of the imaging reconstruction algorithm described in section 4.2, preprocessing must be carried out on the raw survey data. This preprocessing phase accomplishes two different goals: 1) data quality is monitored along the processing and 2) the very bright sources detected during each single observations are localized and inserted in the background model of the imaging reconstruction algorithm.

All the pre-processing was carried out using the latest available version of the Swift software contained in the HEASOFT 6.0.3. Below we report the name of the tools used during our pre-processing.

For each DPH, our preprocessing pipeline, does the following operations:

1. data are rebinned in energy channels according to the gain-offset map generated on board (*baterebin*)

2. the DPH is integrated along the energy axis, between 14 and 170 keV, and a detector plane image (DPI) is generated (*batbinevt*)

3. a detector quality mask is created, where hot and cold pixels are masked out (*bathotpix*)

4. an empirical background model is fitted to the DPI (*batclean*[1])

5. the DPI and the background model are input to a FFT deconvolution algorithm which generates the sky image (*batfftimage*)

6. source detection takes place on the sky image and a catalog with all sources detected above S/N$> 6\sigma$ is created (*batcelldetect*)

7. a model for each detected source (using its measured coordinates) is created and it is added to the background model of step 4

8. steps 4 to 7 are repeated until no new sources are detected in a single 300 s observation.

In order to have the cleanest dataset possible we have applied cuts on the quality of the data. During the steps above data are screened on the basis of the following conditions:

- lock of the star tracker and pointing stability
- spacecraft being outside of the South Atlantic Anomaly (SAA)
- BAT array rate $<$18000 counts/s
- exposure being larger than 200 s
- reduced χ^2 of the background fit $<$1.5
- $> 9\sigma$ detected sources must be within a distance of 0.1 deg from a known source otherwise they are thought to be spurious or transient. The observation is flagged for a later analysis, but not inserted into the final dataset.

In table 4.1, we have listed the fraction of exposure which is rejected if a single data quality cut is applied to the data used for this analysis. For the current dataset, $\sim$ 34% of the overall exposure time was rejected because the data did not meet one or more of the above mentioned criteria.

[1]the empirical background model built-in in batclean fits a quadratic function plus a series of models which take care of detectors edge effects for a total of 14 parameters. The user is also free to include sources or different background models.

Table 4.1. Fraction of rejected data

TYPE	FRACTION
Star tracker lock	9.7%
Pointing stability	17.4%
Outside SAA	10%
Exposure $>$ 200 s	7%
Others	$<$1 %
All conditions	34 %

If any of the previous conditions was not satisfied the observation was not included in the final dataset. All observations passing the filtering criteria are input of the imaging reconstruction algorithm described in section 4.2.

After processing and screening the data according to the above criteria the final dataset includes 2671 observations (see Fig. 4.2 for the exposure map).

All sources detected during the preprocessing phase are listed in table 4.2 along with their identification, their maximum and total significance (computed as the sum of the squared of significances), and the number of detections. The distribution of the offsets of sources in table 4.2 from their catalog counterpart is reported in Fig. 4.3. The same graph shows the extremely good location accuracy of BAT which locates 95% of all sources within $2.2'$ radius.

In order to understand the dependence of the offset on the source significance, we have analyzed all Crab Nebula detections and determined that the offset varies with significance accordingly to

$$\mathrm{OFFSET} = 0.43' + 5.74'/\mathrm{S/N} \quad [\mathrm{arcmin}]. \tag{4.11}$$

.

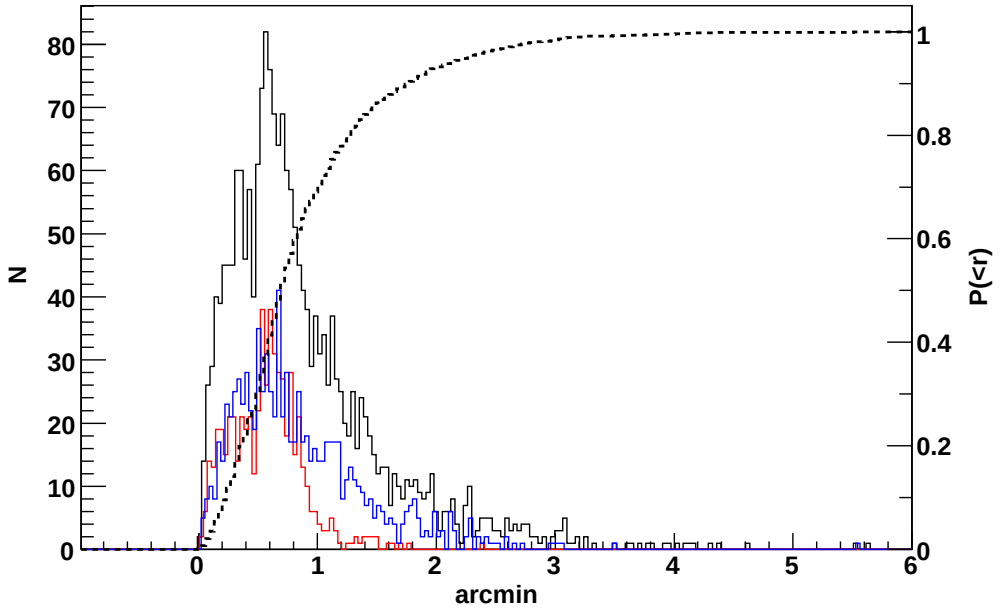

Figure 4.3: Black solid line is the distribution of the offsets of sources reported in table 4.2 from their catalog position. Red and Blue solid lines are the detections of Crab and Vel X-1 respectively, while the black dashed line is the cumulative distribution of all detections. 90% and 95% confidence limits are at radii of $1\farcm8$ and $2\farcm2$ respectively.

4.3.2 Imaging reconstruction

The 2671 DPIs along with their background model (created at step 4 in section 4.3.1) are input of the imaging reconstruction algorithm. For this analysis we have used 1 parameter for the source component and we have allowed the normalization of the background component to vary in each observation leading to a total of 2672 parameters. The map is built in small segments of 5×5 deg^2. A pixel size of $12'$ was chosen as the best compromise between computational time and the resampling factor of the PSF (~ 2 in this case). The significance image is shown in Fig. 4.4.

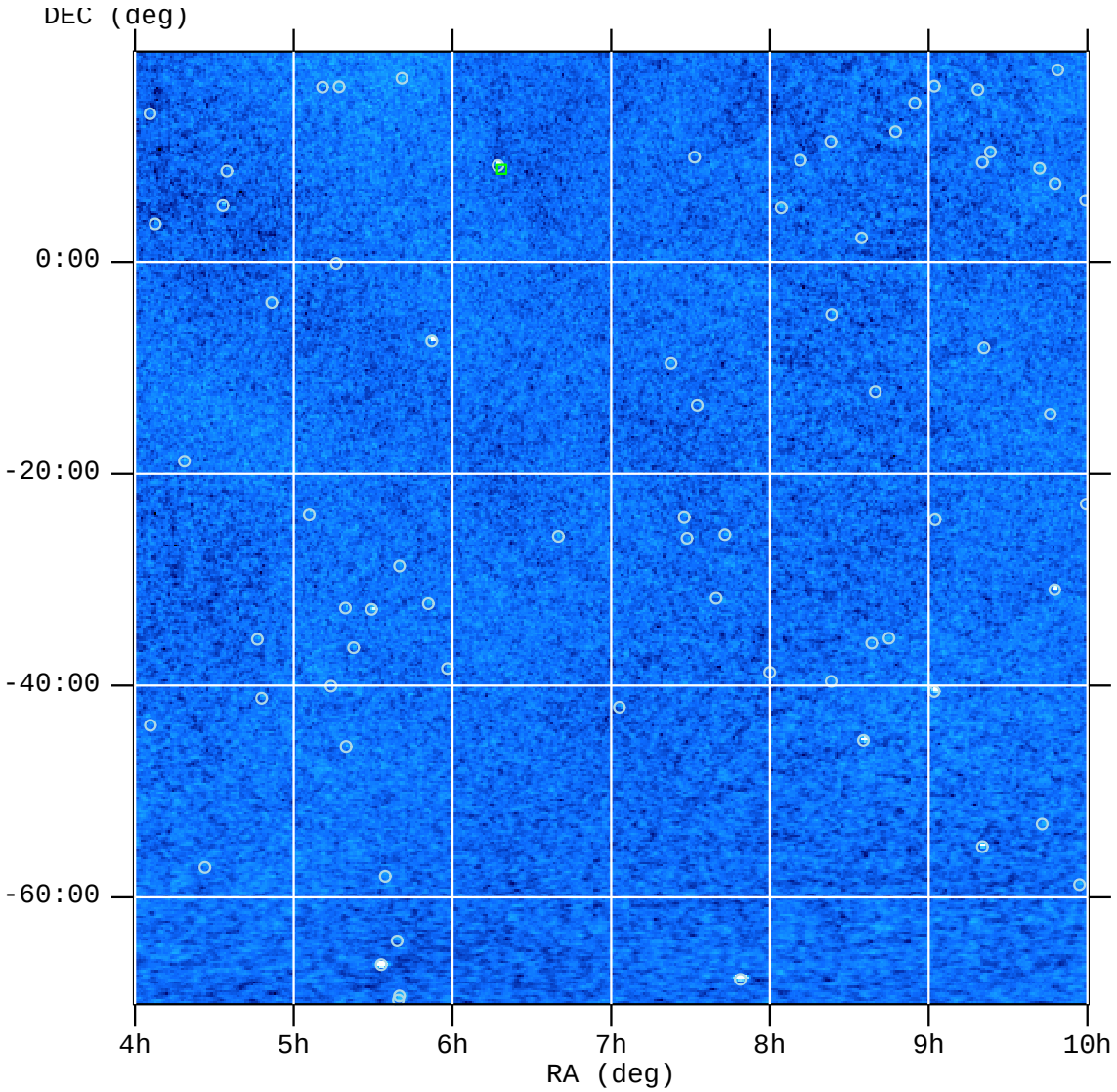

Figure 4.4: Significance map of the 90x90 deg^2 surveyed area. Circles mark all sources above 4.5 σ presented in Tab. 4.4.

Table 4.2. Sources detected during data screening

RA (J2000)	DEC (J2000)	S/N(max)	TOTAL S/N	# detections	Type	ID
19.1746	-73.4559	16.9	47.7	22	HXB	SMC X-1
58.8665	+31.0270	8.3	8.3	1	HXB	V* X Per
83.2654	-66.3567	11.5	35.0	17	HXB	LMC X-4
83.6265	+22.0079	126.9	1505	581	PSR	Crab
84.7121	+26.2949	90.5	195	61	HXB	1A 0535+26
94.2964	+9.1199	8.7	12.6	3	LXB	V* V1055 Ori
117.2030	-67.7483	8.0	30.0	15	LXB	EXO 0748-676
135.5234	-40.5565	139.3	917	888	HXB	Vel X-1
152.4996	-58.2222	13.7	38.8	18	HXB	GRO J1008-57
170.2396	-60.5556	50.2	161.7	79	HXB	Cen X-3
176.9183	-61.9794	8.9	8.9	1	HXB	V* V830 Cen
186.6980	-62.7649	98.0	401	284	HXB	GX 301-2
201.4286	-43.0056	8.8	12.6	2	Sy2	Cen A
235.5705	-52.3704	12.2	14.4	2	HXB	V* QV Nor
243.0916	-52.4028	16.1	40.7	19	LXB	H 1608-522
244.9860	-15.6526	25.5	76.0	24	LXB	Sco X-1
247.9922	-48.8173	8.8	11.5	2	HXB	IGR J16318-4848
250.2720	-53.7497	8.9	19.6	6	LXB	H 1636-536
251.4481	-45.6088	13.1	21.8	6	LXB	GX 340+0
255.1860	-41.6435	27.0	38.9	8	HXB	EXO 1657-419
255.9813	-37.8334	50.2	98.3	22	HXB	V* V884 Sco
256.4394	-36.4345	12.1	13.2	2	LXB	Sco X-2

[a]Note that the significance of the detection depends on the source intensity, exposure and on the position in the FOV. The "TOTAL S/N" was computed as the sum of the squared significances in each observation.

4.3.3 Setting the significance threshold

There are several approaches in order to derive the best significance threshold. Considering that the Maximum Likelihood method leads to perfectly symmetric Gaussian, normal, noise in the reconstructed image, the most straightforward one is setting the threshold as the absolute value of the lowest negative fluctuation. In this case, since the negative fluctuations are given by noise, one should expect no false detection above this threshold.

As it can be seen in the significance distribution reported in Fig. 4.6, no negative fluctuations larger than -4.3 are found. If we take into consideration the number of trials and the normal Gaussian distribution we get that above $S/N_{TH} > 4.5$ we expect a number of false detections of 0.7. We also made a Monte-Carlo simulation generating a large number ($>$1000) of sky images with Gaussian noise. We then counted all the excesses above the $4.5\,\sigma$ level and found out that the number of expected false detection is 1.01, in agreement with the previous finding. A contamination of our sample of sources by only 1 spurious detection was judged to be the best compromise between detection sensitivity and sample corruption. Hence we decided to fix the threshold to $4.5\,\sigma$.

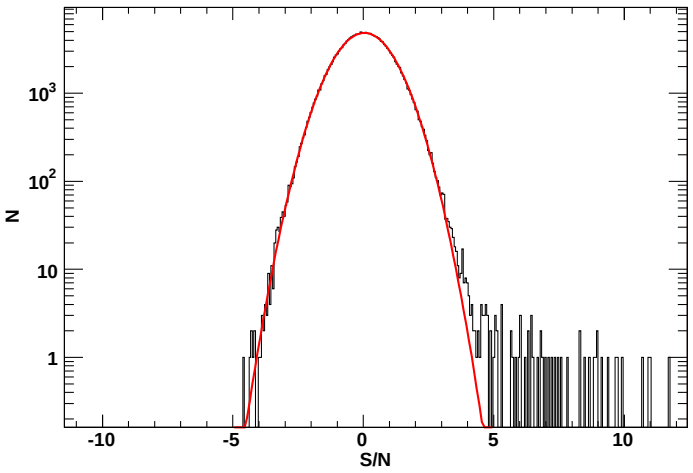

Figure 4.5: S/N distribution.The continuous line is an overlaid Gaussian with $\sigma = 1$.

4.3.4 Noise properties and Sky coverage

The sky coverage is, for a given survey, the distribution of the survey's area as a function of limiting flux. The knowledge about the sky coverage is particularly important when computing the number-flux relation (also known as LogN-LogS distribution). We leave the derivation of the number-flux relation to a separate paper (Ajello et al., 2007), but we

are interested in deriving the sky coverage here as it brings crucial information about the sensitivity and noise properties of the survey.

The sky coverage as a function of the minimum detectable flux F_{min} is defined as the sum of the area covered to fluxes $f_i < F_{min}$:

$$\Omega(< F_{min}) = \sum_{i}^{N} A_i \quad f_i < F_{min} \tag{4.12}$$

where N is the number of image pixels and A_i is the area associated with each of them.

We have followed two procedures to compute the sky coverage of our survey area:

- the ML method produces a flux map and an error map as output of the fitting procedure. In order to get the sky coverage we multiplied the error map by the S/N$_{TH}$ =4.5σ and then counted the area as in Equation 4.12;

- using *batcelldetect* we computed the local (flux) image variance using an encircled area whose radius was 30 pixels. This map is a true representation of the noise in our image. Again, we multiplied this noise map by our detection threshold of 4.5σ and then counted the area as in Equation 4.12.

The sky coverage computed in both ways does not present any significant differences testifying that the error computed by the ML method is very close (if not the same) as the real noise term of the sky image.
In the left panel of Fig. 4.6 we report the sky coverage of the entire area and for the extragalactic portion of the sky (selected imposing $| b | > 15^{\circ}$). As it can be seen from the sky coverage, >75% of the surveyed area is sensitive to fluxes $<$ 0.9 mCrab and all of it to fluxes <1.8 mCrab. The limiting sensitivity in our image is a bit less than 0.8 mCrab (or 1.9×10^{-11}erg cm^{-2}s^{-1}).

The analysis of the image noise properties as a function of exposure time (reported in the right panel of 4.6) shows that the survey sensitivity scales $\propto T^{-0.5}$ denoting absence of large systematic errors. We then compared our survey sensitivity to recent results from the BAT and INTEGRAL-ISGRI hard X-ray surveys (Markwardt et al., 2005; Bassani et al., 2006). In order to perform the comparison, we transformed the sensitivities provided by the authors in different bands to sensitivities in a common band (20-100 keV); the comparison, which is shown in table 4.3, is done taking into account either the S/N$_{TH}$ used by the authors in their work and using a common 5σ-equivalent sensitivity. The main result is that for 1 Ms of exposure, our survey is the most sensitive of the three.

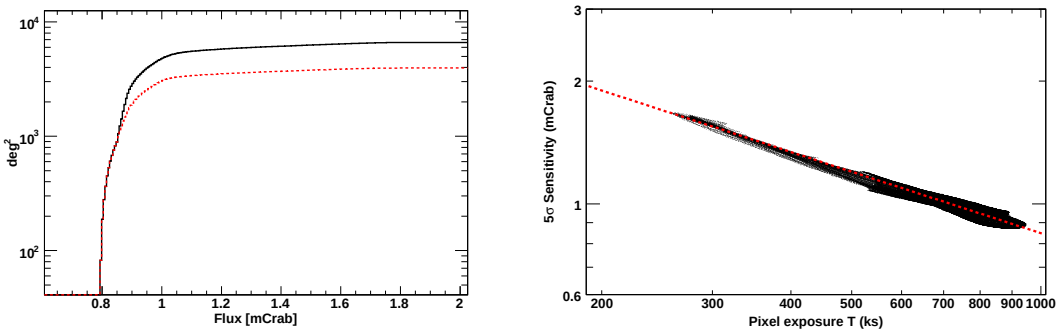

Figure 4.6: Left Panel: Sky coverage as a function of minimum detectable flux for S/N=4.5 in the 14-170 keV band. As it can be seen 75% of the surveyed area is covered to 1 mCrab. The dashed red line is the sky coverage for $|b| > 15^{\circ}$. **Right Panel:** Pixel 5σ sensitivity threshold as a function of exposure time. The red dashed line is the fit to data points corresponding to the function $2.6\text{mCrab}(T/100ks)^{-0.5}$.

4.3.5 Source detections and fluxes

Source detection on the reconstructed image is a straightforward process since a significance map as well as a flux map is output to a file. All not-neighbouring pixels which meet the criterion $S/N > S/N_{TH}$ are identified and a fit with the instrumental point spread function (the *batcelldetect* tool is used here) is done in order to determine the most accurate source position. Contrary to other wavelengths where the integral of the PSF yields the source intensity, for coded mask detectors it is the PSF peak value which gives the intensity of the source.

4.3.6 Detected sources

We have detected 61 hard X-ray sources in our survey. Four of these sources are residuals caused by imperfect modeling (and inclusion in the background model) of bright sources which are detected in individual DPHs. These 4 sources (LMC X–4, EXO 0748−676, Vel X−1 and V* V1055 Ori) are still detected in the reconstructed image with a S/N of 20–40.

For the remaining 57 serendipitous objects detected above the 4.5σ detection, we have reported source locations and observed fluxes along with their tentative ID in tables 4.4.

We have correlated our sources with the ROSAT All-Sky Survey Bright Source Cata-

Table 4.3. Sensitivities of different hard X-ray surveys.

Instrument	Ref.	S/N_{TH}	Sensitivity[a] (@1Ms [mCrab])	Equivalent 5σ Sens[b] (@1Ms [mCrab])
INTEGRAL	Bassani et al., 2006	5.	0.8	0.8
BAT	Markwardt et al., 2005	5.5	1.3	1.2
BAT	this work	4.5	0.74	0.82

[a]The sensitivity is computed by considering the noise-exposure relation provided by the authors (e.g. Fig. right panel of 4.6) multiplied by the S/N_{TH} they used to detect sources.

[b]Sensitivities are computed assuming S/N_{TH}=5 for all instruments/surveys.

logue (Voges et al., 1999) in the same way as in Stephen et al. (2006). In Fig. 4.7, we report the number of BAT sources which have at least one ROSAT source within a given radius. Also, to understand the contribution of chance coincidences to these associations, we performed a Monte Carlo simulation using 5×10^5 positions randomly distributed in our field. Due to non-uniformity in the distribution of ROSAT sources, the probability of a chance association increases slightly towards negative Galactic latitudes. Taking into account the highest density of ROSAT sources (for $-40^\circ <$b$< -20^\circ$), we get from Fig. 4.7 that using a radius of $300''$ for the identification of our sources will yield a probability of chance coincidence of 0.015 (1 wrong identification overall). The same figure yields also information about the BAT point spread function location accuracy (PSLA), as the BAT uncertainty in the position dominates the ROSAT error. Thus, assuming that the ROSAT position is the "true" source position and considering only the ROSAT associations, we fitted an inverted gaussian to the curve of Fig. 4.7 (see Fig. 4.8) and derived that 95% and 99% of all spatial coincidences are within $3.3'$ and $5'$ respectively. Thus, using a $5'$ radius for source identification yields the best compromise between probability of finding the BAT counterpart and chance coincidence. It is not surprising that $<$50% of our sample is correlated with the ROSAT catalog since photoelectric absorption might play an important role. Thanks to this approach we managed to identify 30 of our sources. These sources are generally the brightest of our sample and they were already detected by previous observatories (Macomb & Gehrels, 1999).

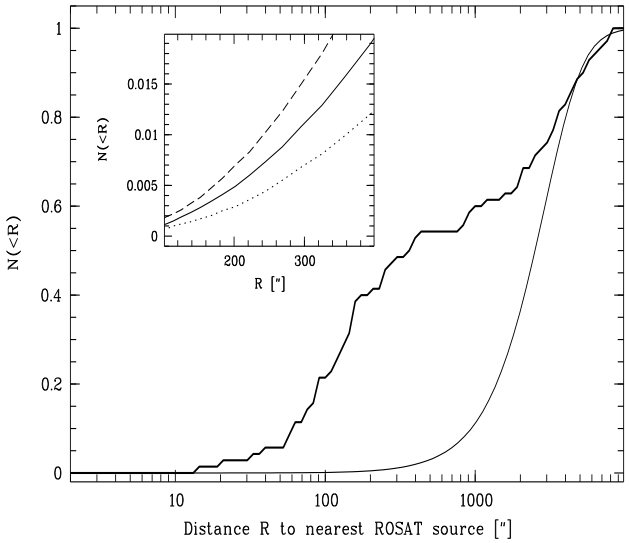

Figure 4.7: Probability of finding at least one ROSAT source within a given radius for our source sample of table 4.4. The thick solid line is the probability for the real sample while the thin line is the expected contribution of chance coincidences. The inset shows a closeup view of the chance coincidence curve for the region of interest ($200'' < R < 300''$); dashed line is the distribution for $-40° < b < -20°$, while the dotted line is for $0° < b < 20°$

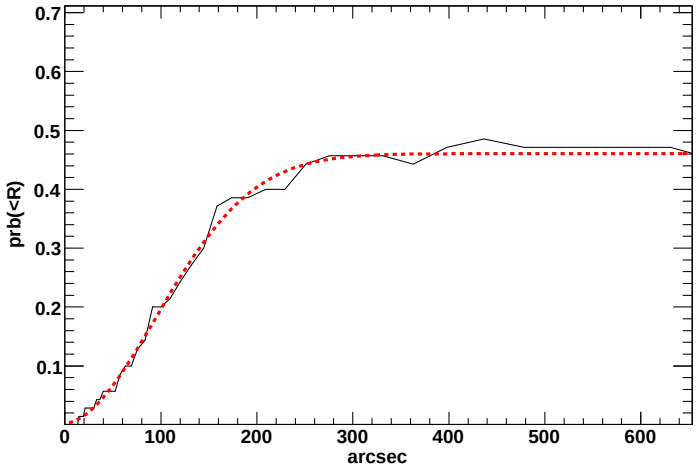

Figure 4.8: Gaussian fit to the curve of Fig. 4.7. The PSLA at 95% and 99% confidence is respectively $3.3'$ and $5'$.

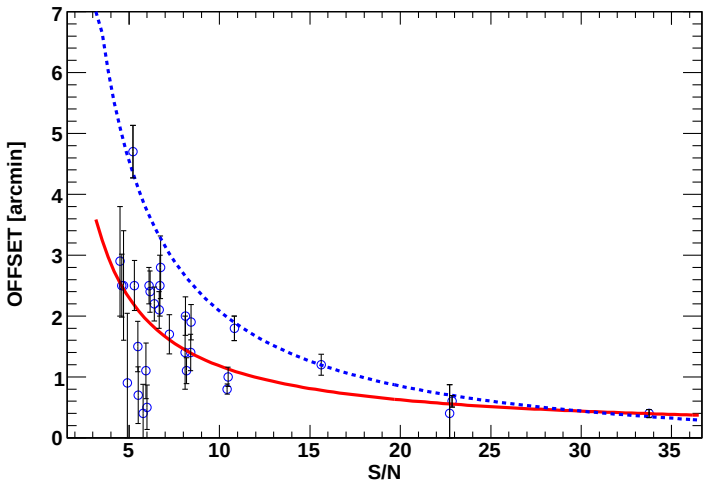

Figure 4.9: Offset of the detected sources as a function of their significance. The red solid line is the fit to the data with the function Offset = 0.065′ +11.15′/(S/N). The blue dashed line is the fit to $> 3\sigma$ deviations from the previous fit and gives the maximum expected offset for a given significance.

Using the same 300″ error radius, we searched for spatial coincidences between our sources and both the HEAO-1 catalog of high energy sources (Levine et al., 1984) and the 2nd INTEGRAL-IBIS catalog (Bird et al., 2006). We found that 2 sources were already detected in hard X-rays by HEAO-1 and 7, including also the previous 2, by INTEGRAL. All these 7 sources were already detected at low energy by ROSAT. Two additional sources, 3C 227 and V* BG CMi have an Einstein IPC counterpart (Harris et al., 1990). 3C 227 was also detected during a long (11 ks) ROSAT-PSPC observations (Crawford & Fabian, 1995).

Some of the new sources can be identified using the narrow field X-ray telescope (XRT) on board Swift. With its 5″ position accuracy XRT is able to pinpoint the source counterpart in less than 2 ks. We requested and obtained 3 followup observations of our targets (J0732.5-1330, J0823.3-0456 and J0918.6+1617) and this allowed us to firmly identify the counterpart of those sources (Ajello et al., 2006). Other sources (e.g. J0916.4-6221, J0519.5-3240, J0505.8-2351 and J0920.8-0805) were observed by XRT as part of the ongoing effort of the BAT all-sky survey (Tueller et al., 2005,?; Kennea et al., 2005). We also searched the Swift archive for XRT observations covering the fields of our sources. A total of 17 sources can be firmly identified thanks to XRT. The results of all the identification efforts using X-ray catalogs and XRT, are reported in table 4.4. Details of all

sources identified using XRT are given case-by-case in the next section.
Using the sources with a known X-ray counterpart, we report, in Fig. 4.9, the sources' offsets from their catalog position as a function of significance. A fit to the data shows that the offset varies with S/N as Offset = $0.065' + 11.15'/(S/N)$. Moreover, from the same plot we expect that for a 4.5σ detection the maximum offset be $5'$; this is in perfect agreement with what is shown in Fig. 4.8.
The offset derived for a 10σ source from the previous relation and from equation 4.11 (i.e. the same 10σ source is detected in the single 300 s sky image) is $1.1'$ and $1'$ respectively. Thus, we can affirm that our survey analysis preserves the good location accuracy of BAT.

Table 4.4. Detected hard X-ray sources

SWIFT NAME	R.A. (J2000)	DEC (J2000)	Flux (10^{-11} cgs)	S/N	Exposure (100 ks)	ID	Offset (arcmin)	Type	Catalogs[b]	XRT position (ref.)
J0405.8-4345	61.4522	-43.7520	2.24	4.5	903	···	···	···	···	···
J0407.6+0336	61.9178	3.6517	4.21	5.2	330	3C 105.0	4.7	Sy2	X	04 07 16.2, +03 42 23
J0418.6-1847	64.6653	-18.7978	2.23	4.8	743	···	···	···	···	···
J0426.4-5710	66.6021	-57.1775	2.02	4.5	803	1AXG J042556-5711[a]	3.5	Sy1	R	···
J0433.1+0520	68.2982	5.3374	7.0	10.4	316	3C 120[a]	1	Sy1	R	···
J0446.2-3537	71.5631	-35.6275	2.36	4.5	939	···	···	···	···	···
J0447.8-4112	71.9631	-41.2020	3.84	5.4	935	···	···	···	···	···
J0451.6-0349	72.9205	-3.8240	3.73	4.9	416	MCG -01-13-025[a]	0.9	Sy1.2	R	···
J0505.8-2351	76.4674	-23.8666	2.62	7.2	816	SWIFT J0505.7-2348	1.7	Sy2	X	05 05 45.4 -23 51 17.0 (1)
J0510.8+1631	77.7224	16.5265	7.37	4.7	231	CSV 6150[a]	2.5	Sy1.5	R	···
J0514.0-4003	78.5146	-40.0558	5.02	10.4	934	4U 0513-40 [a]	0.8	LXB	R	···
J0516.0-0007	79.0096	-0.1332	7.6	6.1	373	QSO B0513-002[a]	2.5	QSO-Sy1	R	···
J0517.1+1633	79.2839	16.5605	3.80	5.8	233	···	···	···	···	···
J0519.5-3240	79.8844	-32.6720	4.78	8.2	909	ESO 362- G 018[a]	1.1	Sy1.5	R, X	05 19 35.5, -32 39 22 (1)
J0519.7-4545	79.9460	-45.7557	4.48	5.3	904	Pictor A[a]	1.5	Sy1	R	···
J0522.6-3625	80.6581	-36.4233	3.65	4.7	927	ESO 362-G021[a]	4.6	BLLAC	R, X	05 22 57.9, -36 27 29
J0528.0+1435	82.0246	14.5874	6.04	5.1	251	···	···	···	···	···
J0529.4-3247	82.3541	-32.7965	5.15	10.9	904	V* TV Col[a]	1.3	CV-DQ*	R	···
J0534.5-5801	83.6470	-58.0200	1.8	5.6	800	V* TW Pic[a]	2.1	CV	R, I	···
J0539.0-6406	84.7717	-64.1148	2.10	6.6	726	LMC X-3[a]	2.1	HXB	R	···
J0539.5-6943	84.8917	-69.7210	4.48	8.4	681	LMC X-1[a]	1.4	HXB	R, I	···
J0539.9-6919	84.9878	-69.3230	6.30	8.1	681	PSR B0540-69.3[a]	1.4	Pulsar	R, I	···
J0539.9-2842	84.9953	-28.7029	5.68	4.6	858	PKS 0537-286[a]	2.5	QSO	R, X	05 39 54.1, -28 39 54
J0550.8-3215	87.7165	-32.2610	3.40	6.1	883	PKS 0548-322[a]	2.4	QSO	R, X	05 50 40.4, -32 16 15
J0552.1-0727	88.0411	-7.4554	32.04	33.7	477	NGC 2110	0.4	Sy2	X	05 52 11.5 -07 27 24
J0558.0-3822	89.5237	-38.3799	3.62	6.7	913	LEDA 75476[a]	2.8	Sy1	R	···
J0640.0-2553	100.0031	-25.8931	2.54	5.3	793	ESO 490- G 26[a]	2.5	Sy1.2	R, X	06 40 11.8, 25 53 41
J0722.6-0931	110.6593	-9.5224	1.84	4.8	778	···	···	···	···	···
J0727.5-2406	111.8951	-24.1039	1.9	5.3	850	···	···	···	···	···

4.3.7 XRT observations

J0407.6+0336. XRT observed this source field for 7 ks on Jul 11, 2006. The only detected object, RA(2000)= 04 07 16.2 Dec(2000)=+03 42 24.3, is coincident with the Sy2 galaxy 3C 105.0 and distant 4.7′ from the BAT position. It is the first time that 3C 105.0 is detected in X-rays.

J0505.8-2351. XRT observed this source field for 3.2 ks on Aug. 20, 2005. Only one source is detected within the BAT error box at RA(200)=05 05 45.4 Dec(2000)=-23 51 16.8 coincident with the Sy2 galaxy 2MASX J05054575-2351139. This object was already identified as the BAT counterpart in Tueller et al. (2005b).

J0519.5-3240. A 7ks XRT observation was performed on Nov. 26, 2005. In the XRT field only two objects are detected. The brighter one at RA(2000)=05 19 35.5 Dec(2000)=-32 39 22.4 is only 1.1′ from the BAT position. The fainter one is detected at RA(2000)=05 19 25.8 Dec(2000)=-32 42 32.3 and it is only a 2σ detection. The bright source is associated with the nearby Sy1.5 galaxy ESO 362- G 018 (also detected by ROSAT as 1RXS J051936.1-323910). ESO 362- G 018 was already identified as the BAT counterpart by Tueller et al. (2005b).

J0522.6-3625. XRT observed this field for 899 s in May 26 2005. Only one source is detected at RA(2000)=05 22 57.8 Dec(2000)=-36 27 29.7 at 4.6′ from the BAT position. The XRT source is coincident with ESO 362-G021 a BL Lac object already detected by ROSAT and XMM at lower energies and by BeppoSAX in hard X-rays (Donato et al., 2005).

J0539.9-2842. A XRT observation of 14 ks took place on Dec. 8, 2005. A faint source is detected at RA(2000)=05 39 09.3 Dec(2000)=-28 41 01.5 coincident with the z=3.1 QSO PKS 0537-2843 and distant 2.5′ from the BAT position. The QSO was discovered in X-rays by the Einstein observatory (Zamorani et al., 1981) and then studied by ROSAT, ASCA and lately by XMM. The BAT detection in hard X-rays is the first to date.

J0550.8-3215. A 9ks XRT observation took place on May 21, 2005. A very bright source is detected at RA(2000)=05 50 40.4 Dec(2000)=-32 16 15.5 distant 2.4′ from the BAT position. The XRT source is associated with a well known blazar PKS 0548-322 already detected in hard X-ray (see Donato et al., 2005). The blazar is then the BAT counterpart.

Table 4.4 (cont'd)

SWIFT NAME	R.A. (J2000)	DEC (J2000)	Flux (10^{-11} cgs)	S/N	Exposure (100 ks)	ID	Offset (arcmin)	Type	Catalogs[b]	XRT position (ref.)
J0728.6-2604	112.1626	-26.0696	1.87	4.7	851	V* V441 Pup[a]	3.5	HXB	R	···
J0731.5+0955	112.8752	9.9214	3.30	5.9	578	V* BG CMi	1.3	CV	E	···
J0732.5-1330	113.1328	-13.5037	1.85	5.9	820	SWIFT J0732.5-1331	1.1	CV	X	07 32 37.8, -13 31 07 (3)
J0739.6-3144	114.9127	-31.7496	2.77	6.2	846	···	···	···	···	···
J0759.9-3844	119.9822	-38.7422	4.90	6.0	804	IGR J07597-3842	0.5	Sy1.2	R, I, X	07 59 41.2, -38 43 57
J0804.2+0507	121.0552	5.1203	4.1	8.4	736	UGC 4203[a]	1.9	Sy2	R, X	08 04 05.4 +05 06 49
J0811.5+0937	122.8750	9.6214	2.26	4.6	700	···	···	···	R[d]	···
J0823.3-0456	125.8271	-4.9401	3.23	8.1	846	SWIFT J0823.4-0457	2.0	Sy2	X	08 23 01.0, -04 56 02 (3)
J0834.6+0217	128.6574	2.2926	3.32	5.4	780	···	···	···	···	···
J0835.3-4510	128.8308	-45.1771	17.1	22.7	705	Vela PSR[a]	0.4	PSR	R, I, H	···
J0837.1-3912	129.2970	-39.2024	4.81	4.6	753	···	···	···	···	···
J0838.4-3559	129.6151	-35.9976	4.01	5.5	791	FRL 1146	0.7	Sy1	R, I	···
J0839.8-1214	129.9556	-12.2467	2.43	5.8	866	3C 206[a]	0.4	QSO	R	···
J0844.9-3531	131.2411	-35.5313	2.97	5.0	780	···	···	···	···	···
J0847.4+1219	131.8676	12.3243	1.9	6.5	672	···	···	···	···	···
J0854.7+1502	133.6828	15.0371	5.58	5.1	646	···	···	···	···	···
J0902.4-2418	135.6084	-24.3074	2.36	4.6	800	···	···	···	···	···
J0917.2-6221	139.112	-62.359	2.07	4.5	830	LEDA 90443	2.9	Sy1	X	09 16 08.9, -62 19 29.6
J0918.6+1617	139.6505	16.2987	3.3	6.7	610	MRK 0704	2.5	Sy1.5	R, X	09 18 25.9, +16 18 20(3)
J0920.3-5512	140.0753	-55.2135	9.57	15.6	612	4U 0919-54[a]	1.2	LXB	R, I, H	···
J0920.8-0805	140.2134	-8.0872	3.03	6.4	742	MCG -01-24-012	2.2	Sy2	X	09 20 46.0, -08 03 21 (2)
J0923.3+1024	140.8256	10.4112	2.72	4.9	660	···	···	···	···	···
J0945.9-1421	146.4060	-14.3007	5.09	5.5	621	NGC 2992[a]	1.5	Sy1.9	R, X	09 45 42.1, -14 19 34
J0947.6-3056	146.9151	-30.9388	18.01	22.8	611	ESO 434- G 040[a]	0.6	Sy2	R, I, X	09 47 39.8, -30 56 55
J0947.7+0725	146.9447	7.4191	5.58	4.7	581	3C 227	0.4	Sy1	E,R[c]	···
J0957.0-5847	149.2537	-58.7979	2.56	4.9	545	···	···	···	···	···
J0959.3+0550	149.8280	5.8338	2.7	4.5	526	···	···	···	···	···
J0959.5-2251	149.8805	-22.8561	7.80	10.8	566	NGC 3081[a]	1.8	Sy2	R	···

[a]Source identified thanks to its proximity to a ROSAT Bright Source with the method described in the text.

[b]Catalogs and Instruments used to identify the source: R=ROSAT catalog, I= INTEGRAL catalog, H= HEAO-1 catalog, E= Einstein IPC catalog, X= XRT observations.

[d]3C 227 was detected in a long (11 ks) ROSAT-PSPC observations (Crawford & Fabian, 1995).

[e]Source J0811.5+0937 has a ROSAT counterpart, 1WGA J0811.5+0933, reported in the WGA catalog (White et al, 1994). This source coincides with RX J081132.4+093403.

References. — (1) Tueller et al. (2005); (2) Kennea et al. (2005); (3) Ajello et al. (2006);

J0552.1-0727. During 9 ks of exposure on Apr. 8, 2006, XRT detects a bright source located at RA(2000)=05 52 11.5 Dec(2000)=-07 27 24.2. The object is coincident with the well known Sy2 galaxy NGC 2110 and its position is only 0.4′ away from the BAT detection. The detection of NGC 2110 in the 3-20 keV band by RXTE (Revnivtsev et al., 2004) and the presence of no other source in the XRT field secure the identification of NGC 2110 as the BAT counterpart.

J0640.0-2553. During 2.8 ks of observation on Mar. 23, 2006, XRT detects only one bright source at RA(2000)=06 40 11.8 Dec(2000)=-25 53 41.5 coincident with the Sy1 galaxy ESO 490- G26 (already detected in soft X-rays by ROSAT as RX J064011-25536). The source position is 2.5′ distant from the BAT detection.

J0732.5-1330, aka SWIFT J0732.5-1331. XRT observed this field for 4 ks on Apr. 28, 2006. Only one source is detected in the XRT field at RA(2000)=07 32 37.7 Dec(2000)=-13 31 08.6. This source is coincident with an USNO B1 star J073237.64-133109.0. The source was already identified as the BAT counterpart by Ajello et al. (2006). Follow-up measurements in the optical determined that this source is a new intermediate polar (Wheatley et al. 2006 and references therein).

J0759.9-3844. XRT observed the field of this source for 7ks. Three sources are clearly detected. The brightest of them is located at RA(2000)=07 59 41.2 Dec(2000)=-38 43 57.9 being only 0.5′ away from the BAT position while the remaining two are distant more than 10′. The brightest object is coincident with the INTEGRAL source IGR J07597-3842 and with the ROSAT source RX J075942.0 -384359. The fact that the only source within 4′ from the BAT position is also detected by INTEGRAL in hard X-rays (den Hartog et al., 2004) makes this source the BAT counterpart. The probable association with an IR point source IRAS 07579-3835, and a 1.4-GHz radio counterpart (NVSS archive) makes the case for a AGN nature of the object. This source was identified as being a Sy1.2 galaxy during a recent optical spectroscopy followup (Masetti el al., 2006b).

J0823.3-0456. Only a single faint source is detected by XRT during 1.2 ks of exposure on Jan. 6, 2006. The source is located at RA(2000)=08 23 01 Dec(2000)=-04 56 02.5 and 2′ away from the BAT detection. The object is coincident with the galaxy FAIRALL 0272 and was already identified as the BAT counterpart by Ajello et al. (2006). An optical follow-up showed that the source is a Sy2 galaxy (Masetti et al., 2006a).

J0918.6+1617. SWIFT J0918.5+1617, aka SWIFT J0918.5+1618, is another source

found thanks to our algorithm (Ajello et al., 2006). During a XRT followup of 0.6 ks, the only detected source is located at RA(2000)=09 18 25.8 Dec(2000)=+16 18 20.8 and coincident with the galaxy Mrk 704. Mrk 704 was previously detected in soft X-rays by ROSAT (Schwope et al., 2000). In a recent optical followup, the galaxy was found to be a Sy1 (Masetti et al., 2006a).

J0920.8-0805. A XRT observation of 8.5 ks took place on Dec. 10, 2005. Only one source is detected in the entire field. Its position, RA(2000)=09 20 46.0 Dec(2000)=-08 03 21.8, is coincident with the Sy2 galaxy MCG-01-24-012 and distant 2.2′ from the BAT position. This object was already identified as the BAT counterpart by Kennea et al. (2005).

J0945.9-1421. An XRT observation of 11 ks took place on Jul. 8, 2006. The only source detected inside the BAT error box is located at RA(2000)=09 45 42.0 Dec(2000)=-14 19 33.7. The source is coincident with the Sy1.9 galaxy NGC 2992 and is distant 1.5′ from the BAT detection. The source was already detected in soft X-rays by ROSAT as 1RXS J094541.9-141927.

J0947.6-3056. XRT observed the source field for 10ks on Dec. 9, 2005. Only one bright source is detected at RA(2000)=09 47 39.8 Dec(2000)=-30 56 55.4 coincident with the Sy2 galaxy ESO 434- G 040 and distant only 0.4′ from the BAT position. The galaxy was also detected in hard X-ray by INTEGRAL (Bird et al., 2006).

4.4 Conclusions

We have presented an application of the Maximum Likelihood method as a deconvolution technique used to reconstruct the sky image when dealing with a coded-mask instrument like BAT. The main difference with other image reconstruction algorithms, such as the standard cross-correlation technique, is that a sky distribution model is forward-folded through the full instrumental response and fit to the detector plane counts in order to derive the most probable sky image. This is realized in a single step and thus, no image mosaicking is required. This study was motivated principally by the capabilities of ML to: 1) preserve the full statistical information in the data and 2) to reduce the systematic errors connected to mosaicking techniques which other methods cannot avoid. This leads to an improvement in sensitivity over other methods.

Moreover, this study is motivated by the needs to use sensitive imaging techniques for

the study of the hard X-ray sky. Although deep soft X-ray surveys (0.5-2.0 keV) were able to resolve the majority of the CXB emission into discrete sources (Hasinger et al., 1998), only a minor fraction of the CXB above 8 keV is resolved (Worsley et al., 2005). Furthermore, the bulk of the CXB radiation is emitted around 30 keV (Marshall et al., 1980) and the exact nature of the source population responsible for the background at these energies is unknown because of the low sensitivity of previous X-ray telescope. Since the BAT coded mask detector, on board the Swift mission, represents a major improvement in sensitivity for X-ray imaging of the hard X-ray sky, we used BAT survey data as a test-bed for our ML imaging algorithm.
This study was also performed in the framework of an optical spectroscopy campaign aimed at identifying BAT-discovered extragalactic hard X-ray objects (Rau et al., 2007).

The results presented in the previous sections can be summarized as follows:
After screening our dataset for bad data, the final survey image obtained using the ML method presents a perfect gaussian normal noise. Given the dimension of our map and the noise features, we expect 1 spurious source above our detection threshold of 4.5σ.
Above this threshold, we detected 61 hard X-ray sources. Only 12 were previously known as hard X-ray emitters (previously detected by INTEGRAL or HEAO-1). 49 are new sources detected by BAT due to our superior image reconstruction method.
The correlation of BAT sources with the ROSAT catalog shows the extremely good location accuracy of the BAT instrument which is also preserved by our algorithm. Also it is worth noticing that only $< 50\%$ of our sources are correlated with the ROSAT catalog; this is most probably due to the presence of photoelectric absorption in some of the new BAT sources. The analysis of the limiting flux as a function of exposure, presented in the right panel of Fig. 4.6, shows that our analysis has negligible systematic errors and that BAT can achieve, in the future, a sensitivity of 0.5 mCrab with 2Ms of exposure (if systematics remain at this level). The sky coverage shows that 75% of the survey is covered to flux < 0.9 mCrab and all of it to fluxes < 1.8 mCrab.
All of this makes this analysis one of the most sensitive surveys ever performed in the hard X-ray domain.

The optical spectroscopy identification of the new sources and a discussion about the statistical properties of our sample are left to separate papers (Rau et al., 2007; Ajello et al., 2007).

acknowledgments

MA acknowledges N. Gehrels and the BAT team for hospitality and discussions, A. Yoldas for all his tips&tricks about parallel programming and python. This research has made use of the NASA/IPAC Extragalactic Database (NED) which is operated by the Jet Propulsion Laboratory, of data obtained from the High Energy Astrophysics Science Archive Research Center (HEASARC) provided by NASA's Goddard Space Flight Center, of the SIMBAD Astronomical Database which is operated by the Centre de Données astronomiques de Strasbourg, of the Sloan Digital Sky Survey (SDSS) managed by the Astrophysical Research Consortium (ARC) for the Participating Institutions and of the Rosat All Sky Survey mantained by the Max Planck Institut für extraterrestrische Physik.

Bibliography

Ajello M., et al. , 2006, ATel, 697

Ajello M., et al. , 2007, in preparation

Arnaud, K. A. 1996, in ASP Conf. Ser. 101, Astronomical Data Analysis Software and Systems V, ed. G. H. Jacoby & J. Barnes (San Francisco: ASP), 17

Bassani, L., Malizia, A., & Stephen, J. B., astro-ph/0610455

Barthelmy, S. D., et al. 2005, SSRv 120, 143

Bird A. J., et al. 2006, ApJ 636, 765

Bolton J. G., et al. 1975, Aus. J. Phys. Ap. Suppl. 34, 1

Comastri, A., et al. 1995, A&A, 296, 1

Crawford, C. S., & Fabian, A. C., 1995, MNRAS, 273, 827

den Hartog, P.R.,et al. 2004, ATel, 261, 1

Donato, D., et al., 2005, A&A 433, 1163

Fabian, A. C., Iwasawa, K., 1999, MNRAS 303, 34

Gehrels, N., et al. 2004, ApJ 611, 1005

Giacconi, R., et al. 2002, ApJS 139, 369

Gilli, R., et al. 2001, A&A, 366, 467

Grandi, P., et al. 2006, ApJ, 642, 113

Götz, D., et al. 2006, A&A, 448, 873

Harris, D. E., et al. 1990, in *Imaging X-Ray Astronomy. A Decade of Einstein Observatory Achievements*, Editor, Martin Elvis; Publisher, Cambridge University Press, Cambridge, England, New York, 309

Hasinger, G., et al. 1998, A&A, 329, 482

Jonker, P.G. et al. 2001, ApJ, 553, 335

Kennea, J. A., et al. 2005, ATel, 677, 1

Levine, A. M., et al. 1984, ApJS, 54, 581

Macomb, D.J., Gehrels N., 1999. ApJS, 120, 335

Malizia, A., et al. 2002, A&A, 394, 801

Masetti N., et al. 2006, ATel, 735

Masetti, N., L. Morelli, E. Palazzi, et al. 2006, astro-ph/0608394

Markwardt, C. B., Tueller, J., Skinner, G. K., et al 2005, ApJ Lett., 633, L77

Marshall, F. E., et al. 1980, ApJ, 235, 4

Norton, A. J., et al. 2000, MNRAS, 312, 362

Rau, A., et al., 2007, in preparation

Rosati, P., et al. 2002, ApJ, 566, 667

Schwope A., et al. 2000, Astron. Nachr. 321, 1

Skinner, G. K., et al. 1987, Ap&SS, 136, 337

Sowards-Emmerd D., et al., 2004, ApJ, 609, 564

Steiner, J. E., et al. 1984, ApJ, 280, 688

Stephen, J. B., et al. 2006, A&A 445, 869

Strong, A. W., et al. 2004, A&A 411, 447

Strong, A. W., et al. 2005, A&A 444, 495

Revnivtsev, M., et al. 2004, A&A 418, 927

Revnivtsev, M., et al. 2006, A&A 448, L49

Tueller, J., et al. 2005, ATel, 668

Tueller, J., et al. 2005, ATel, 669

Voges, W., et al., 1999, A&A, 349, 389

Wheatley P.J., et al. 2006, ATel, 765

White, N. E., Giommi, P.,& Angelini, L., 1994, BAAS, 26, 1372

Wilks, S.S. 1938, Ann. Math. Stat., 9, 60

Worsley, M.A., et al. 2005, MNRAS 357, 1281

Zamorani, G., et al. 1981, ApJ, 245, 357

Chapter 5

BAT extragalactic hard X-ray Survey - II: Optical Follow-up of Unidentified Sources

A. Rau, J. Greiner, M. Salvato and M. Ajello

Abstract

We present the search for optical counterparts of 19 unidentified sources detected in the BAT extra-galactic hard X-ray survey (BEXS; Ajello et al., 2007a). For three BEXS sources, possible associations with Seyfert 2 galaxies at $z = 0.02598 \pm 0.00006, 0.0696 \pm 0.0002$ and 0.1220 ± 0.0002 were found. Two of these are new detections, while the third was classified using available SDSS spectroscopy. In addition, we detected one candidate X-ray Bright Optically Normal Galaxy at $z = 0.282 \pm 0.001$. Three out of the four sources show indications for (at least) a modest amount of extinction or domination by host galaxy emission. No plausible candidate counterparts could be identified for the remaining 15 BEXS sources to a limiting magnitude of $R = 18$. We present the field charts, spectra and their analysis.

5.1 Introduction

Extra-galactic hard X-ray surveys are a prime key for resolving the origin of the Cosmic X-ray Background (CXB) above $6-8$ keV. Population modeling (e.g., Gilli et al., 2006; Treister & Urry, 2006) predict that the main contribution arises from heavily obscured ($\log N_H > 24\,cm^{-2}$), so-called Compton-thick, Active Galactic Nuclei (AGN). Observational evidence of these sources is scarce, though.

A small number of wide angle hard X-ray surveys have been performed in the past (Levine et al., 1984; Revnivtsev et al., 2004; Markwardt et al., 2005; Bassani et al., 2006; Krivonos et al., 2007). However, the relative fraction of Compton-thick sources among the local AGN population eluded a convincing constraint so far. While Bassani et al. (2006) found that 14 ± 7 % of 62 AGN detected with *INTEGRAL* were Compton-thick, a three times smaller frequency was found among 44 AGN detected with the Burst Alert Telescope (BAT, Barthelmy et al., 2005) onboard the *Swift* satellite (Markwardt et al., 2005).

In a recent paper (Ajello et al., 2007a, AGK07 hereafter), we presented the methodology and source catalog for the BAT extra-galactic hard X-ray survey (BEXS). This survey is based on image reconstruction of $14-170$ keV BAT all-sky data using the Maximum Likelihood method. Here, 61 hard X-ray sources were detected within an area of 90° by 90°, centered on $\mathrm{RA(J2000)} = 105^\circ$ and $\mathrm{Dec(J2000)} = -25^\circ$. Two thirds of these objects were associated with X-ray sources detected by *ROSAT*, *INTEGRAL*, *HEAO-1* and *Swift*/XRT. However, 19 new detections remained without identification and classification. Here, we present the results of a dedicated optical search for candidate counterparts of these unidentified sources, performed at the 3.6-m ESO New Technology Telescope (NTT) in La Silla, Chile.

5.2 Target Selection

The positional uncertainty for a given BEXS source is proportional to its Signal-to-Noise ratio (S/N) in the $14-170$ keV band as:

$$r_{\mathrm{BAT}} = 30.36\ \mathrm{S/N}^{-1.2} \tag{5.1}$$

(dotted line in Figure 9 of AGK07). Within a typical error circle (few arcmin radius) several tens to hundreds optical sources can be found to a limiting magnitude of $R \sim 21$ (see for example Figure 5.2). It is immediately clear that a complete optical spectroscopic identification of all these sources is unfeasible.

Generally, the number of possible counterparts can be decreased significantly by follow-up observations at soft X-rays ($0.2-10$ keV), where the sky is scant of sources and high-resolution imagers are available (e.g., the X-ray Telescope onboard *Swift*). This has been successfully demonstrated for a number of previously detected BAT sources (Tueller et al., 2005; Kennea et al., 2005; Ajello et al., 2006) and 17 BEXS sources (AGK07). However, Compton-thick objects may evade detection at soft X-rays because of their large photoelectric absorption. Here, searches for their host galaxies at optical

wavelengths offer more reward.

For our identification program, we settled on selecting the optically brightest extended sources within a given BEXS error circle as targets for spectroscopy. This approach requires accurate understanding of the chance coincidence probability of having unassociated galaxies in a BEXS error circle. The probability, assuming that the surface distribution of galaxies is uniform and thus follows a Poisson distribution (i.e., we ignore clustering of galaxies) is given by

$$p_m = 1 - \exp(-r_{\rm BAT}^2 \pi \rho_m) \tag{5.2}$$

where ρ_m is the mean surface density of galaxies brighter than m, found using *Hubble* Deep Field number counts presented in Madau & Pozzetti (2000). The resulting probabilities for R-band AB-magnitudes of 16, 17 and 18 are presented in Figure 5.1. We find that chance coincidence is significant and for $r_{\rm BAT} = 5'$ (S/N=4.6) and $R = 16, 17$ and 18 reaches 20 %, 70 % and 95 %, respectively.

Keeping this in mind, we selected candidates for 8 out of the 19 unidentified BEXS sources. For the remaining cases (see Table 5.1) no targets suitable for our campaign were found and more accurate localizations will be required.

5.3 Observations, Data Reduction and Spectral Analysis

Observations were performed with the ESO Multi-Mode Instrument (EMMI) at the NTT in January 2006. The low dispersion (RILD) and medium dispersion (REMD) modes were used with grism #5 (instrumental line width FWHM= 4.5 Å) and grating #8 (FWHM= 4 Å), respectively. In order to minimize contamination by the host galaxy over a possible AGN component, we used a $1''$ slit, centered on the nuclei of the target galaxies. Data were reduced with customized IRAF[1] routines and flux calibrated using observations of the standard stars LTT2415 and LTT3218 (Hamuy et al., 1992). All spectra of extragalactic targets are corrected for Galactic foreground extinction according to the Schlegel et al. (1998) maps.

In total, 10 spectra at the positions of 8 unidentified BEXS sources were obtained (see Table 5.2 for a summary). For each target the redshift was determined through the identification of prominent features, typically Hα, Hβ, [OII] and [OIII] in emission or Ca H+K, MgI and NaI in absorption. Line centroids and fluxes were measured by fitting

[1]IRAF is distributed by the National Optical Astronomy Observatories, which are operated by the Association of Universities for Research in Astronomy, Inc., under cooperative agreement with the National Science Foundation.

a Gaussian profile (or multiple Gaussians in case of blended lines). A lower limit of the source intrinsic extinction can be derived using the decrement between two Balmer lines, e.g. Hα and Hβ. Here, we assumed the interstellar redding curve given in Osterbrock (1989) with $R = 3.1$ ($R = \mathrm{A_V/E(B-V)}$) and predicted ratios of $\mathrm{H\alpha_0/H\beta_0} = 3.1$ and 2.85 for Seyfert 2 and H II region galaxies, respectively.

The large majority of our targets are extra-galactic. For these, spectral classifications were performed by comparing with the spectro-photometric atlas of galaxies by Kennicutt (1992). Different types of emission line galaxies (HII, LINER, Seyfert) were discriminated using flux ratios of observed lines. Here we used the indicators of [OIII]/Hβ vs [NII]/Hα, [SII]/Hα and [OI]/Hα as discussed in (Kewley et al., 2006).

5.4 Results

Below we compile the results of the spectral analysis for all targeted BEXS source. A summary and emission line fluxes are given in Tables 5.3 and 5.4. For each source, a finding chart, which indicates our spectroscopy targets and all cataloged sources, is available in Figure 5.2. The spectra are presented (Figure 5.3) and the association to the hard X-ray sources discussed. Finding charts for the 11 BEXS sources without extended bright optical candidates can be found in Figure 5.4 (available online).

J0447.8−4112

Source A shows unresolved emission from Hβ, [OIII], Hα, [NII] and [SII] at $z = 0.0183 \pm 0.0001$ (Figure 5.3a). The line ratios and widths are typical for an H II region. No intrinsic extinction in addition to the Galactic foreground value of E(B−V)= 0.02 is required to fit the Balmer line ratio. Narrow Hβ and [OIII] emission together with Ca H+K in absorption are also detected for source B ($z = 0.0886 \pm 0.0001$, Figure 5.3b). The ratio of [OIII]/Hβ excludes a Seyfert classification. However, as further identifying features are shifted outside the spectral coverage, a more accurate classification could not be achieved. Whether one of the two targets is associated with the hard X-ray emission remains undecided.

J0739.6−3144

This low-Galactic latitude field ($l = 246.^\circ3$ & $b = -4.^\circ7$) contains only one bright extended candidate, source A (Figure 5.2b). Its spectrum shows numerous narrow emission lines (Balmer series, [OIII], He, [NII], [SiII] at $z = 0.02598 \pm 0.00006$, Figure 5.3c) and the line ratios and velocity widths ($\mathrm{FWHM_{H\alpha}} \sim 800\,\mathrm{km\ s^{-1}}$) suggest this to be a previously unknown Seyfert 2. The Balmer line decrement is consistent with no extinction

in addition to the Galactic foreground value of E(B−V)=0.61[2]. However, extinction in a patchy absorber can not be excluded. The source was also detected with IRAS[3] and NVSS[4] and is a good candidate counterpart for the BEXS source. We note that, while there is no known variable Galactic object in the field, an unrelated TXS[5] radio detection exists (square in Figure 5.2c).

J0811.5+0937

Source A is a cataloged NVSS radio source, which is located inside the 1′ error circle of the *ROSAT* X-ray detection 2RXP J081131.9+093434 (Figure 5.2c). The spectrum (Figure 5.3d) shows a single unresolved emission line ([OII]) and Ca H+K, g-band and MgI in absorption ($z = 0.282 \pm 0.001$). Hβ and [OIII] are not detected. The relative strength of [OII] and [OIII] indicate a low ionization level, while the Hβ emission may be hidden by stellar absorption. As Hα lies outside the covered wavelength, no accurate galaxy classification could be achieved. The association with a radio and X-ray source indicates that Source A is a likely counterpart for the BEXS detection. However, the apparent lack of activity in the optical spectrum suggest it to be an X-ray Bright Optically Normal Galaxy (XBONG; Comastri et al., 2002). XBONG, as the name indicates, are galaxies with a large nuclear X-ray-to-optical luminosity ratio and no tracers of nuclear activity in the optical spectrum. This can be caused by a strong stellar continuum diluting the optical nuclear emission or a strong obscuration. As the *ROSAT* hardness ratios (0.1–2.4 keV rate 0.035 ± 0.04 counts s^{-1}) do not indicate strong absorption, we consider a host dilution more probable.

J0834.6+0217

We observed the two brightest extended sources in the field (Figure 5.2d). Source A ($R = 18.8$) shows unresolved emission of [OII], Hβ and [OIII] together with Ca H+K in absorption at $z = 0.2003 \pm 0.0005$ (Figure 5.3e). The [OIII]/Hβ ratio excludes a Seyfert classification. However, the lack of further diagnostic lines make a more accurate identification impossible. The second source (B, $R = 18.1$) has Ca H+K, g-band and MgI in absorption at $z = 0.2611 \pm 0.0006$, resembling a typical early type galaxy (Figure 5.3f). Neither source A nor B show spectral indications for activity. Given also their optical faintness, we suggest that they are most likely chance coincidence events unrelated to the BEXS source (see also Figure 5.1). We note, that an NVSS radio source (square in Figure 5.2d) without detected optical counterpart is located inside the BEXS error circle.

[2]Note, however, that the Schlegel et al. (1998) extinction values are not precise at low Galactic latitudes.
[3]Infrared Astronomical Satellite
[4]NRAO VLA Sky Survey; (Condon et al., 1998)
[5]Texas Survey of Radio Sources; (Douglas et al., 1996)

J0854.7+1502

The field contains a single resolved source (A, Figure 5.2e) which is also detected by 2MASS[6]. Its spectrum shows representative narrow emission lines (Hβ, [OIII], [SiII], Hα, [NII], [SII] at $z = 0.0696 \pm 0.0002$, Figure 5.3g) and line ratios typical for a Seyfert 2. The intrinsic extinction derived from the Hα/Hβ flux ratio is E(B−V)$= 1.3 \pm 0.1$ ($N_H = 7.5 \pm 0.4 \times 10^{21}$ cm^{-2}), indicating a significant amount of obscuration. An association with the BEXS detection is likely.

J0902.4−2418

Source A is a cataloged 2MASS source and shows Ca H+K, g-band, MgI and NaI in absorption at $z = 0.0608 \pm 0.0002$ (Figure 5.3h). Furthermore, an NVSS radio source is located in the field (Figure 5.2f). No promising counterpart for the BEXS source was identified.

J0957.0−5847

This BEXS source is located at low Galactic latitude ($l = 282.^\circ0$ & $b = -3.^\circ2$) in a region with significant foreground extinction, E(B−V)=1.3. Source A (Figure 5.2g) is the suspected Galactic variable star NSV 4682 (Kukarkin et al., 1981). The spectrum resembles that of an F2IV-V star, showing Balmer, Ca H+K and NaI lines in absorption (Figure 5.3i). This classification is also in agreement with a previously obtained spectroscopic typing (Buscombe, 2001). The apparent brightness suggests a distance of approx. 200 pc. As NSV 4682 has no prior detection in X-rays (ROSAT upper limit of 1.5×10^{30} erg s^{-1} at 200 pc), it must either have exhibited a recent phase of activity or is unrelated to the BEXS source. Indeed, the large foreground extinction in the field may veil a background AGN.

J0959.3+0550

The only source (A, Figure 5.2h) brighter than $R = 18$ was found to be a Galactic star of late G or early K type (Figure 5.3j). In addition, two cataloged sources exist in the field; one NVSS radio source without optical counterpart inside the BEXS uncertainty region and one galaxy with spectroscopy provided by the Sloan Digital Sky Survey (SDSS)[7] located slightly outside the nominal error circle (offset=5.′3). The spectrum of SDSS J095857.43+054942.1 shows [OII], [OIII], Hα, [NII] and [SII] in emission together with Ca H+K in absorption at $z = 0.1220 pm 0.0002$. The line ratios and red continuum shape suggests this to be a Seyfert 2 with either significant extinction or host domination. We note that the Balmer line ratio (Hα flux and Hβ limit) does not require additional

[6] 2−Micron All Sky Survey; (Skrutskie et al., 2006)

[7] http://cas.sdss.org/dr4

intrinsic extinction. However, attenuation in a patchy absorber remains a possibility. We consider this galaxy a good candidate counterpart for the BEXS source, although its position is marginally outside our nominal uncertainty region.

5.5 Discussion and Conclusion

In the BAT extra-galactic hard X-ray survey, 19 out of 61 sources had no known optical counterpart or classification. Here we reported on NTT spectroscopic observations of candidate counterparts for eight of these sources. In two cases (J0739.6−3144, J0854.7+1502), previously unknown Seyfert 2 galaxies were discovered inside the BEXS error circle. One of those, J0854.7+1502, shows indications for a moderate intrinsic extinction of $N_H \sim 7.5 \times 10^{21}$ cm^{-2}. A third source (J0811.5+0937) shows evidence for being an X-ray Bright Optically Normal Galaxy, a claim which is supported by a radio detection and the tentative association with a *ROSAT* position. Finally, a Seyfert 2 was found slightly outside the nominal BEXS position of J0959.3+0550 in the SDSS Data Release 4. A joint analysis of the X-ray and optical properties of the four newly identified sources, together with the 42 identifications presented in AGK07, will be presented in a forthcoming paper (Ajello et al., 2007b).

No plausible counterparts were revealed for four fields with spectroscopic observations and for the eleven unidentified BEXS sources without bright ($R < 18$), extended objects in the field. This lack of candidate counterparts for approx. 1/4 of all BEXS detections can arise from a number of reasons. Four sources are located at low Galactic-latitude with foreground extinction exceeding $A_V = 4$. Here, the counterpart may be a new variable Star or binary system which recently increased in activity and was not detected previously with, e.g. *ROSAT*. Alternatively, the Galactic absorption may conceal the optical light of the X-ray emitter. Next, the hard X-ray emission can arise from low-to-high-redshift AGNs and QSOs with inconspicuous optical counterparts. Indeed, previous extensive optical identification programs showed that a significant X-ray source fraction is associated with faint galaxies or lies at high-redshift (e.g., Comastri et al., 2002). We also note that seven unidentified BEXS sources have non-classed radio detections, potentially Blazars, in their error circle. Blazars typically have faint optical counterparts and are nearly impossible to identify in arcminute-sized error boxes.

Intrinsic obscuration is another factor which can lead to an incorrect classification based on the optical spectra alone. Depending on the level of obscuration, the spectrum may resemble a type I (low nuclear extinction) or type II AGN (moderate nuclear extinction) or even be completely dominated by the stellar emission from the host galaxy (high extinction or low optical nuclear brightness). It is therefore challenging to optically iden-

tify heavily obscured AGN in large error circles. Indeed, accurate soft X-ray and/or radio position, as in the case of the candidate XBONG J0811.5+0937, are vital for a successful identification.

acknowledgments

This work is based on observations collected at the European Southern Observatory, Chile, under proposal 076.A-0861. We made use of the NASA/IPAC Extragalactic Database (NED) which is operated by the Jet Propulsion Laboratory, of data obtained from the High Energy Astrophysics Science Archive Research Center (HEASARC) provided by NASA's Goddard Space Flight Center, of the SIMBAD Astronomical Database which is operated by the Centre de Donn'ees astronomiques de Strasbourg and of the Sloan Digital Sky Survey (SDSS) managed by the Astrophysical Research Consortium (ARC) for the Participating Institutions.

Bibliography

Adelman-McCarthy, J., Agueros, M. A., Allam, S. A., Anderson, K. S. J., Anderson, S. F., Annis, J., Bahcall, N. A., & Bailer-Jones, C. A. L. 2007, ApJS, submitted

Ajello, M., Greiner, J., Kanbach, G., Rau, A., & Strong, A. W. 2007a, ApJ, submitted

—. 2007b, ApJ, submitted

Ajello, M., Greiner, J., Rau, A., Barthelmy, S., Kennea, J. A., Falcone, A., Godet, O., Grupe, D., Tueller, J., Markwardt, C., Mushotsky, R., Belloni, T., Mukai, K., Holland, S. T., & Gehrels, N. 2006, The Astronomer's Telegram, 697, 1

Barthelmy, S. D., Barbier, L. M., Cummings, J. R., Fenimore, E. E., Gehrels, N., Hullinger, D., Krimm, H. A., Markwardt, C. B., Palmer, D. M., Parsons, A., Sato, G., Suzuki, M., Takahashi, T., Tashiro, M., & Tueller, J. 2005, Space Science Reviews, 120, 143

Bassani, L., Molina, M., Malizia, A., Stephen, J. B., Bird, A. J., Bazzano, A., Bélanger, G., Dean, A. J., De Rosa, A., Laurent, P., Lebrun, F., Ubertini, P., & Walter, R. 2006, ApJ, 636, L65

Buscombe, W. 2001, VizieR Online Data Catalog, 3222, 0

Comastri, A., Mignoli, M., Ciliegi, P., Severgnini, P., Maiolino, R., Brusa, M., Fiore, F., Baldi, A., Molendi, S., Morganti, R., Vignali, C., La Franca, F., Matt, G., & Perola, G. C. 2002, ApJ, 571, 771

Condon, J. J., Cotton, W. D., Greisen, E. W., Yin, Q. F., Perley, R. A., Taylor, G. B., & Broderick, J. J. 1998, AJ, 115, 1693

Douglas, J. N., Bash, F. N., Bozyan, F. A., Torrence, G. W., & Wolfe, C. 1996, AJ, 111, 1945

Gilli, R., Comastri, A., & Hasinger, G. 2006, ArXiv Astrophysics e-prints

Hamuy, M., Walker, A. R., Suntzeff, N. B., Gigoux, P., Heathcote, S. R., & Phillips, M. M. 1992, PASP, 104, 533

Kennea, J. A., Markwardt, C. B., Tueller, J., Barthelmy, S., Burrows, D., Campana, S., Falcone, A., Gehrels, N., Grupe, D., Godet O., Krimm, H., Mangano, V., Mineo, T., Pagani, C., Page, K., Mushotzky, R. F., & Skinner, G. K. 2005, The Astronomer's Telegram, 677, 1

Kennicutt, Jr., R. C. 1992, ApJS, 79, 255

Kewley, L. J., Groves, B., Kauffmann, G., & Heckman, T. 2006, MNRAS, 372, 961

Krivonos, R., Revnivtsev, M., Lutovinov, A., Sazonov, S., Churazov, E., & Sunyaev, R. 2007, A&A, submitted

Kukarkin, B. V., Kholopov, P. N., Artiukhina, N. M., Fedorovich, V. P., Frolov, M. S., Goranskij, V. P., Gorynya, N. A., Karitskaya, E. A., Kireeva, N. N., Kukarkina, N. P., Kurochkin, N. E., Medvedeva, G. I., Perova, N. B., Ponomareva, G. A., Samus, N. N., & Shugarov, S. Y. 1981, in Moscow, Acad. of Sciences USSR Shternberg,1951 (1981), 0–+

Levine, A. M., Lang, F. L., Lewin, W. H. G., Primini, F. A., Dobson, C. A., Doty, J. P., Hoffman, J. A., Howe, S. K., Scheepmaker, A., Wheaton, W. A., Matteson, J. L., Baity, W. A., Gruber, D. E., Knight, F. K., Nolan, P. L., Pelling, R. M., Rothschild, R. E., & Peterson, L. E. 1984, ApJS, 54, 581

Madau, P. & Pozzetti, L. 2000, MNRAS, 312, L9

Markwardt, C. B., Tueller, J., Skinner, G. K., Gehrels, N., Barthelmy, S. D., & Mushotzky, R. F. 2005, ApJ, 633, L77

Osterbrock, D. E. 1989, Astrophysics of gaseous nebulae and active galactic nuclei (Research supported by the University of California, John Simon Guggenheim Memorial Foundation, University of Minnesota, et al. Mill Valley, CA, University Science Books, 1989, 422 p.)

Revnivtsev, M., Sazonov, S., Jahoda, K., & Gilfanov, M. 2004, A&A, 418, 927

Schlegel, D. J., Finkbeiner, D. P., & Davis, M. 1998, ApJ, 500, 525

Skrutskie, M. F., Cutri, R. M., Stiening, R., Weinberg, M. D., Schneider, S., Carpenter, J. M., Beichman, C., Capps, R., Chester, T., Elias, J., Huchra, J., Liebert, J., Lonsdale,

C., Monet, D. G., Price, S., Seitzer, P., Jarrett, T., Kirkpatrick, J. D., Gizis, J. E., Howard, E., Evans, T., Fowler, J., Fullmer, L., Hurt, R., Light, R., Kopan, E. L., Marsh, K. A., McCallon, H. L., Tam, R., Van Dyk, S., & Wheelock, S. 2006, AJ, 131, 1163

Treister, E. & Urry, C. M. 2006, ApJ, 652, L79

Tueller, J., Barthelmy, S., Burrows, D., Falcone, A., Gehrels, N., Grupe, D., Kennea, J., Markwardt, C. B., Mushotzky, R. F., & Skinner, G. K. 2005, The Astronomer's Telegram, 668, 1

Table 5.1: Unidentified BEXS sources without candidate counterparts and optical spectroscopic observations.

ID[a]	RA(J2000)	Dec(J2000)	BAT S/N[b]	r_{BAT} [c]	Com.[d]
J0405.8−4345	04:05:48.5	−43:45:07	4.5	5.′1	(1)
J0418.6−1847	04:18:39.7	−18:47:52	4.8	4.′8	(1)
J0446.2-3537	04:46:15.1	−35:37:39	4.5	5.′1	(1)
J0517.1+1633	05:17:08.1	16:33:38	5.8	3.′9	(2)
J0528.0+1435	05:28:05.9	14:35:15	5.1	4.′5	(1)
J0722.6−0931	07:22:38.2	−09:31:21	4.8	4.′8	(1)
J0727.5−2406	07:27:34.8	−24:06:14	5.3	4.′3	(1)
J0837.1−3912	08:37:11.3	−39:12:09	4.6	5.′0	(1)
J0844.9−3521	08:44:57.9	−35:31:53	5.0	4.′5	(2)
J0847.4+1219	08:47:28.2	12:19:27	6.5	3.′4	(1)
J0923.3+1024	09:23:18.1	10:24:40	4.9	4.′6	(1)

[a] BEXS Identifier in the form Swift Jxxx...

[b] 14−170 keV *Swift*/BAT Signal-to-Noise ratio from P1.

[c] positional uncertainty derived using Equation 5.1.

[d] (1): no candidate counterpart found at the BAT position; (2): added to source list after the spectroscopy campaign.

Table 5.2: Observation Log.

ID	S/N[a]	r_{BAT} [′]	#[b]	RA(J2000)	Dec(J2000)	Offset[c] [′]	Setup[d]	Exposure [s]
J0447.8−4112	5.4	4.2	A	04:47:33.6	−41:14:33	4.5	RILD/Gr5	2×500
			B	04:47:37.2	−41:14:50	4.0	RILD/Gr5	2×500
J0739.6−3144	6.2	3.6	A	07:39:44.7	−31:43:04	2.3	RILD/Gr5	3×300
J0811.5+0937	4.6	5.0	A	08:11:30.9	09:33:51	3.4	RILD/Gr5	3×600
J0834.6+0217	5.4	4.2	A	08:34:44.7	02:19:16	1.7	RILD/Gr5	3×500
			B	08:34:39.8	02:16:46	0.5	RILD/Gr5	3×500
J0854.7+1502	5.1	4.4	A	08:54:29.6	15:01:35	3.6	REMD/Gr8	3×600
J0902.4−2418	4.6	5.0	A	09:02:30.7	−24:14:01	4.6	RILD/Gr5	2×300
J0957.0−5847	4.9	4.6	A	09:56:46.0	−58:48:33	2.8	RILD/Gr5	1×100
J0959.3+0550	4.5	5.1	A	09:59:22.5	05:50:17	0.9	RILD/Gr5	1×500

[a] 14−170 keV *Swift*/BAT Signal-to-Noise ratio from P1.

[b] Identifier for candidate counterparts

[c] offset between source and center of BEXS position

[d] RILD/Gr5: Red Imaging and Low Dispersion Spectroscopy with grism#5 (0.83 Å pxl^{-1}); REMD/Gr8: Red Medium Dispersion Spectroscopy with grating#8 (0.79 Å pxl^{-1})

Table 5.3: Identifications of candidate counterparts

ID	#	z	Alternative Name	Classification
J0447.8−4112	A	0.0183±0.0001	ESO 304−G020	H II
	B	0.0886±0.0001		non-Sy NELG[a]
J0739.6−3144	A	0.02598±0.00006	IRAS 07378−3136	Sy 2
J0811.5+0937	A	0.282±0.001	2RXP J081131.9+093434	IO/Sb pec, XBONG
J0834.6+0217	A	0.2003±0.0005		non-Sy NELG[a]
	B	0.2611±0.0006		early type
J0854.7+1502	A	0.0696±0.0002	2MASX J08542969+1501362	Sy 2
J0902.4−2418	A	0.0608±0.0002	2MASX J09023068−2414020	early type
J0957.0−5847	A	–	NSV 4682	F2IV-V
J0959.3+0550	A	–		G/K star
	2	0.1220±0.0002	SDSS J095857.43+054942.1	Sy 2

[a] Narrow Emission Line Galaxy, line ratios inconsistent with Seyfert galaxy

Table 5.4: Emission line fluxes

ID	#	Emission line fluxes in 10^{-16} erg s^{-1} cm^{-2}						
		[OII]λ3727	Hβ	[OIII]λ5007	[OI]λ6300	Hα	[NII]λ@6583	[SII]λ(6717/31)
J0447.8−4112	A	–	2.0±0.2	2.4±0.2	–	4.6±0.2	1.4±0.2	2.9±0.3
	B	–	2.9±0.2	3.2±0.1	–	–	–	–
J0739.6−3144	A	–	17±2	220±20	14±1	110±10	54±2	60±1
J0811.5+0937	A	4.2±0.4	<1	<0.8	–	–	–	–
J0834.6+0217	A	3.2±0.1	1.3±0.1	1.2±0.1	–	–	–	–
J0854.7+1502	A	–	3.4±0.1	33±1	–	40±1	28±1	22±1
J0959.3+0550	2	2.7±0.2	<1	10±1	–	3.4±0.5	4.4±0.3	3.4±0.4

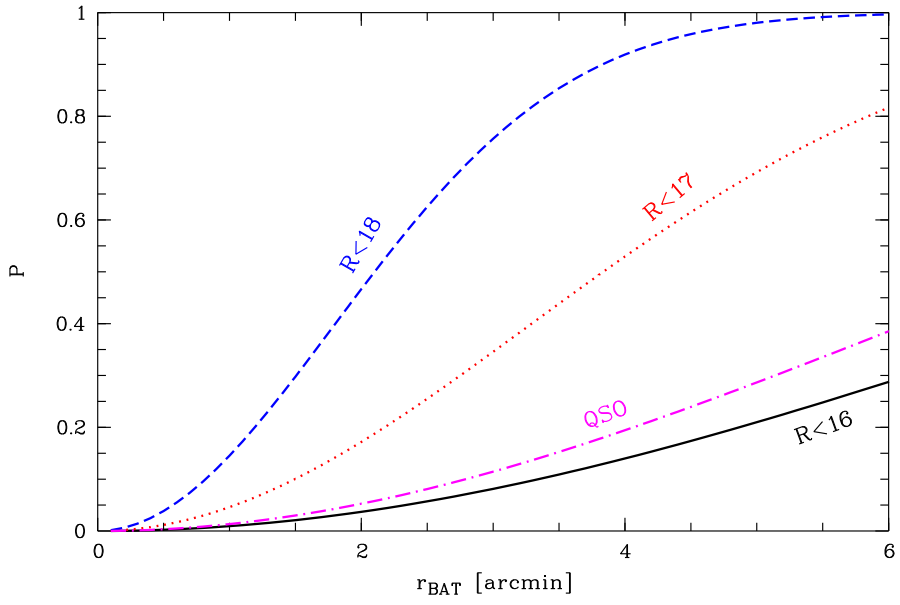

Figure 5.1: Chance coincidence probability for a galaxy with $R < 16$ (solid line), $R < 17$ (dotted), $R < 18$ (dashed) or a quasar (dot-dashed) at any brightness within a given BAT error circle of size $r_{\rm BAT}$ (Equation 5.2). Galaxy densities are derived from number counts presented in Madau & Pozzetti (2000). The quasar density was retrieved from SDSS DR5 (Adelman-McCarthy et al., 2007).

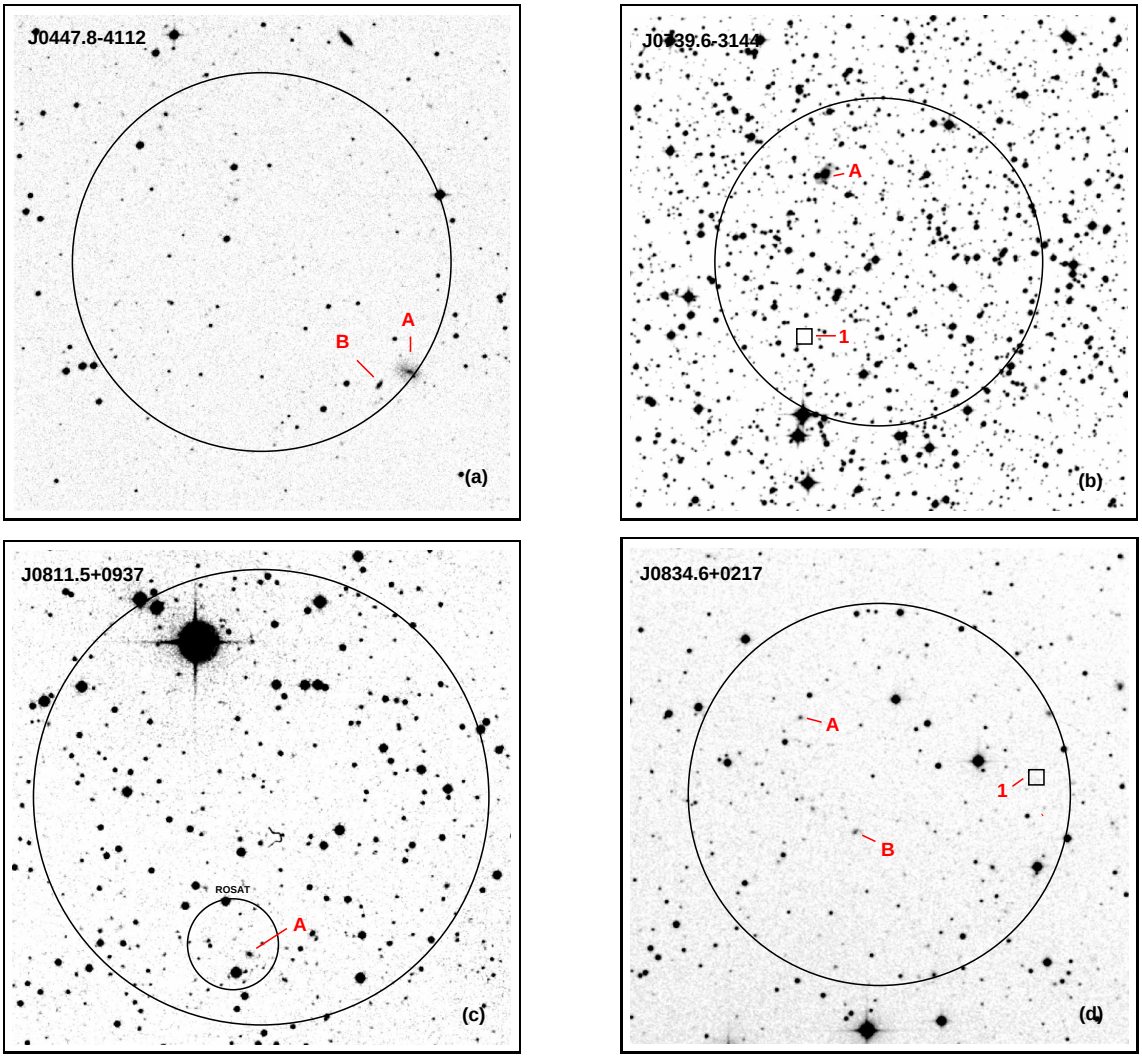

Figure 5.2: Digitized Sky Survey based images of the 8 unidentified BEXS with optical spectroscopy. Each image is $12' \times 12'$ and North is up and East to the left. The big circles mark the BEXS positional uncertainty. Small circles and squares show *ROSAT* X-ray and radio positions, respectively. Spectroscopy targets are marked with letters and unobserved cataloged sources are labeled by numbers. (a) - A: ESO 304−G020; (b) - A: IRAS 07378−3136, 1: TXS 0737−316; (c) - A: 2RXP J081131.9+093434, NVSS J081130+093350; (d) - 1: NVSS J083423+021755;

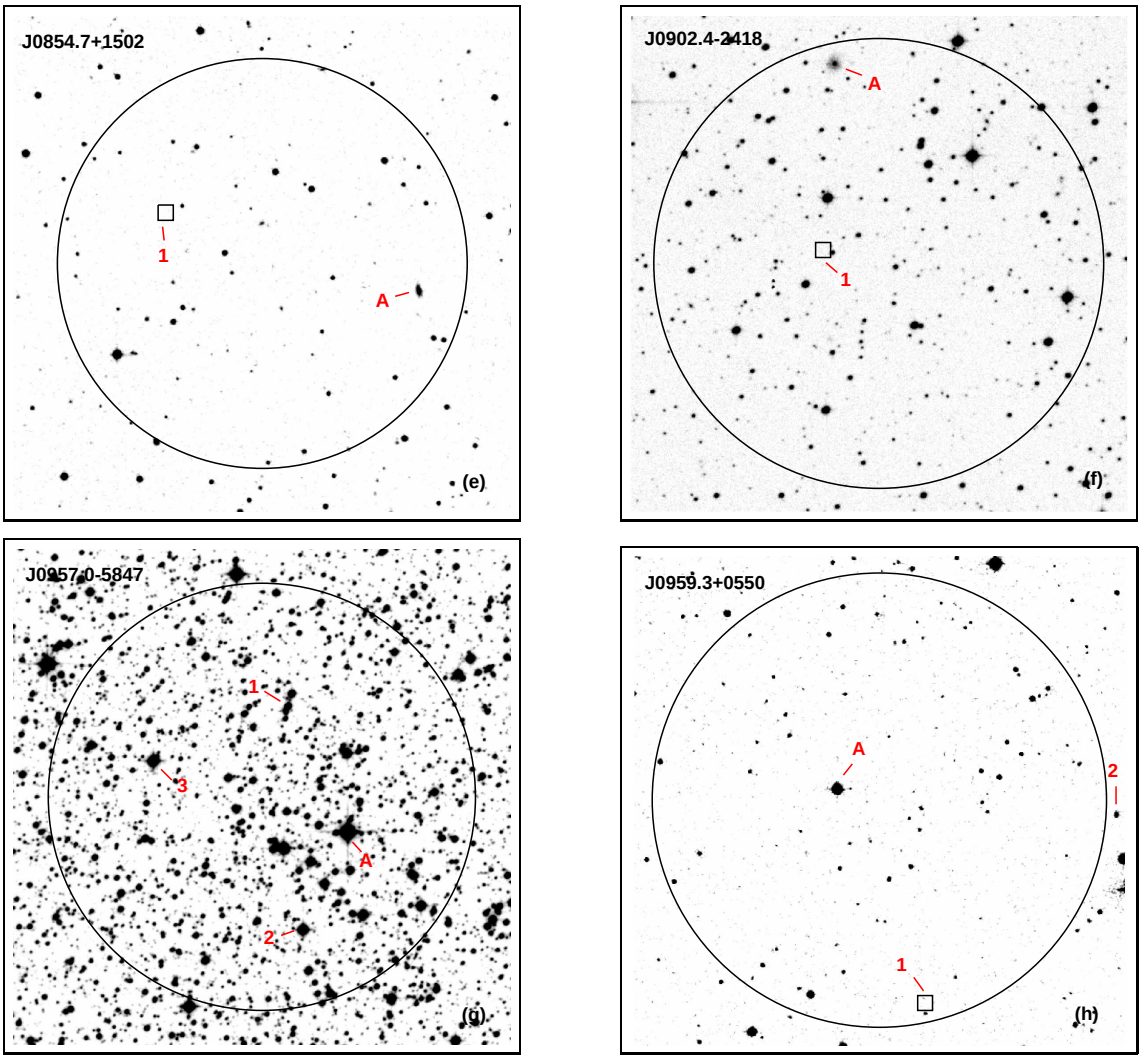

Figure 5.2: Continued. (e) - A: 2MASX J08542969+1501362, 1: NVSS J085452+150321; (f) - A: 2MASX J09023068−2414020, 1: NVSS J090231−241810. (g) - A: NSV 4682, 1: 2MASX J09565867−5846128, 2: HD 302446, 3: TYC 8610−2316−1; (h) - 1: NVSS J095914+054528, 2: SDSS J095857.43+054942.1

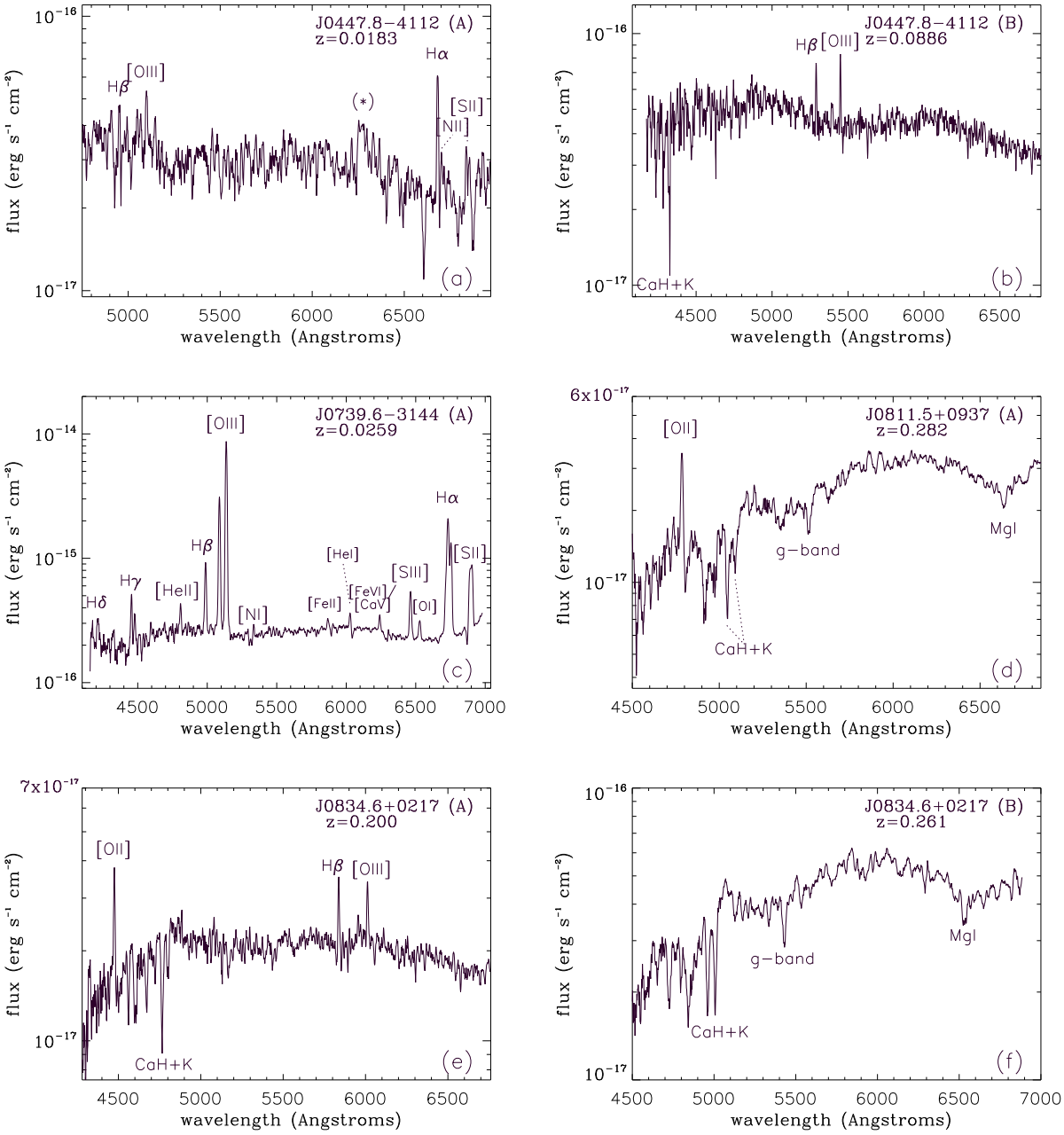

Figure 5.3: Galactic foreground extinction corrected EMMI spectra of candidate counterparts for unidentified BEXS sources. Swift ID and redshift are given in the top right of each panel. Prominent emission and absorption lines are marked and labeled. (*): detector artifact.

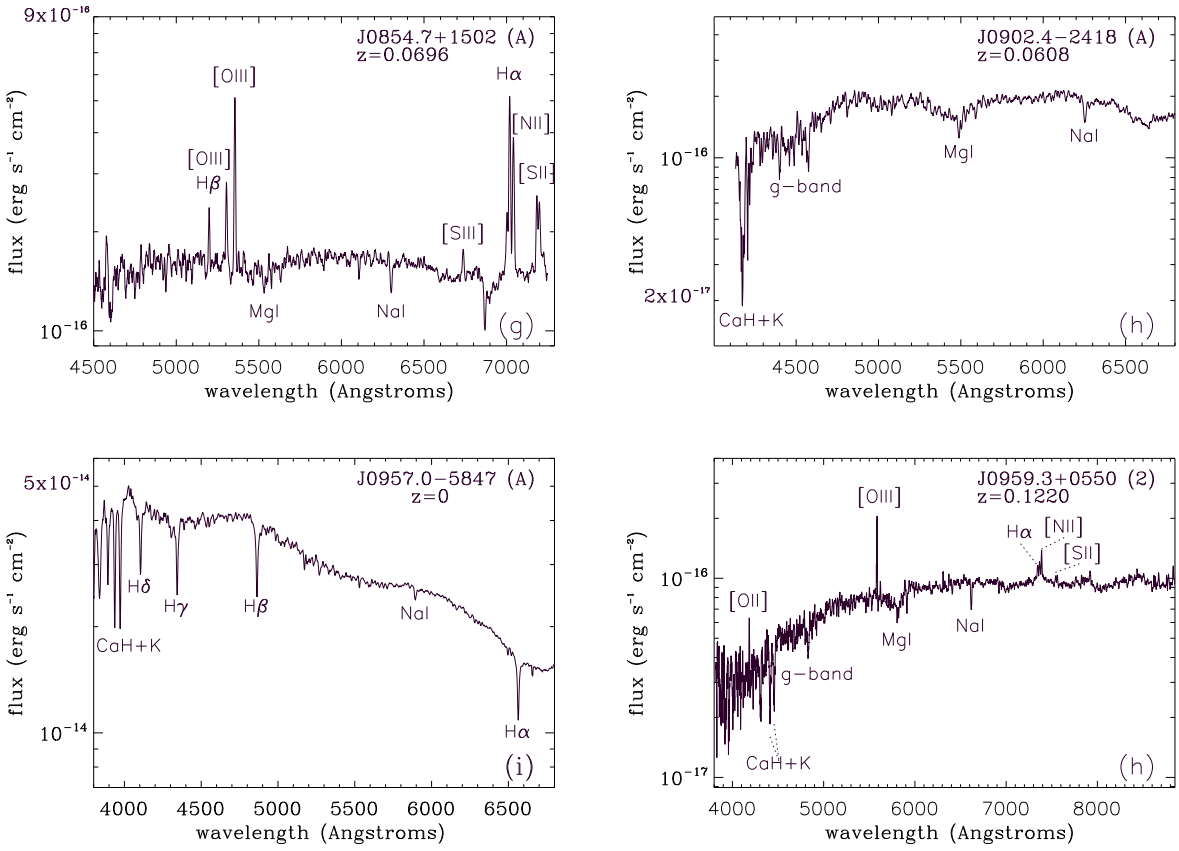

Figure 5.3: Continued.

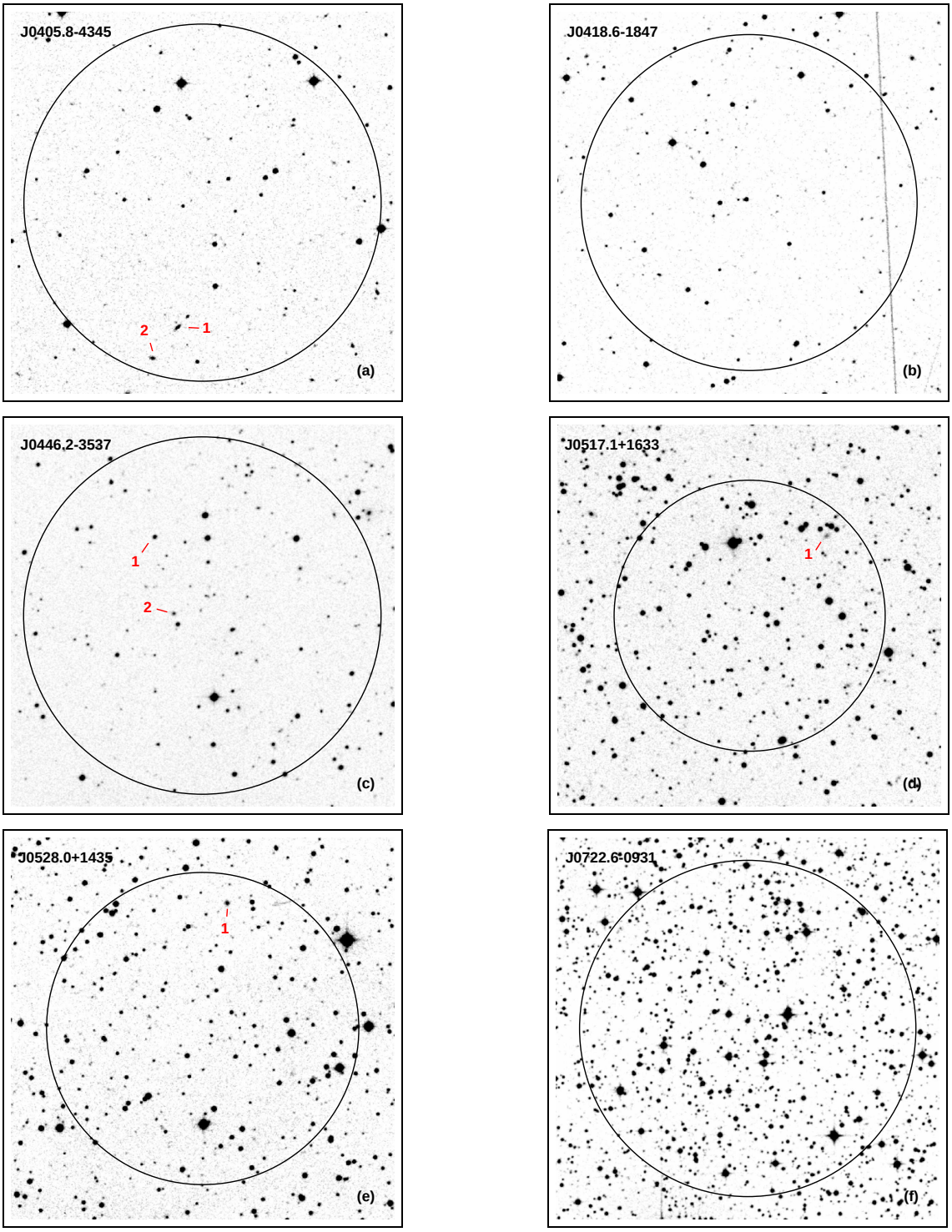

Figure 5.4: (for online version) Same as Figure 5.2 for unidentified BEXS sources without optical spectroscopy. Cataloged sources are reported. (a) - 1: APMUKS(BJ) B040414.65−435644.0, 2: APMUKS(BJ) B040418.52−435737.2; (c) - 1: HE 0444−3540, 2: APMUKS(BJ) B044430.88−354258.1; (d) - 1: 2MASX J05165899+1635525; (e) - 1: 2MASX J05280316+1438483.

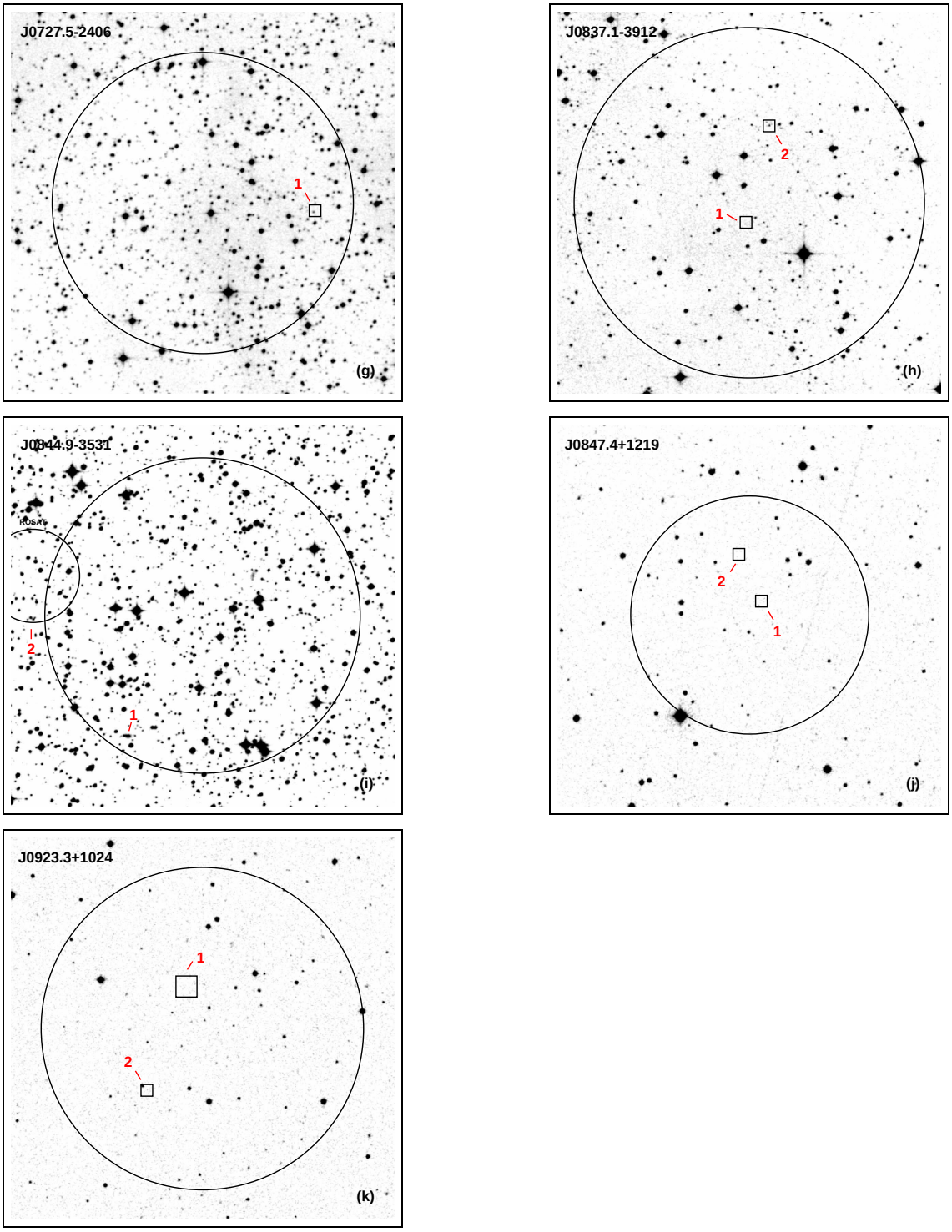

Figure 5.4: Continued. (g) - 1: RXS J072720.8−240629; (h) - 1: NVSS J083711−391242, 2: 2MASX J08370849−3909571; (i) - 1: 2MASX J08450818−3535202, 2: 1RXS J084521.7−353048; (j) - 1: NVSS J084726+121951, 2: NVSS J084729+122111; (k) - 1: NVSS J092320+102552, 2: SDSS J092324.57+102254.7 ($z = 0.519$).

Chapter 6

BAT extragalactic X-ray Survey - III: X-ray Spectra and Statistical Properties

M. Ajello, J. Greiner, G. Kanbach, A. Rau, A. W. Strong

Abstract

In this last of a series of three papers based on a test field of the *Swift*/BAT hard X-ray survey, we present a method to extract accurate X-ray spectra for the whole sample of detected sources. The analysis of their colors shows that some of the non-Galactic BAT sources may be highly absorbed. In order to test the capability of BAT of detecting and sampling the photoelectric cut-off, we investigate the summed spectra of the candidate Compton-thick objects compared to BAT spectra of well known Compton-thick objects. We find that BAT is a uniquely sensitive instrument for the detection of *new* Compton-thick sources. We derive the differential flux-number relation for the extragalactic sources in the 14-170 keV band. The data are best described by a power-law with a slope $\alpha = 2.58 \pm 0.26$ and a normalization of 0.0287 AGN deg^{-2} (or 1185 AGN all-sky) above a flux level of 10^{-11}erg cm^{-2} s^{-1}. The integration of the cumulative flux per unit area leads to the conclusion that BAT resolves 1-2% of the X-ray background emission in the 14-170 keV band. 21 extragalactic sources above $5\,\sigma$ detection limit constitute a 90% complete sample. In this sample, we find that: 63% of the objects are absorbed by column densities $N_H > 10^{22}$H-atoms cm^{-2}, 20% of the AGN are radio-loud, $\sim$ 33% of the Seyfert galaxies are type-1, and highly-luminous highly-absorbed QSO could constitute a fraction of 5-15% of the total AGN population.

6.1 Introduction

There is a general consensus that the cosmic X-ray background (CXB), discovered more than 40 years ago (Giacconi et al., 1962), is produced by integrated emission of extragalactic point sources. The deepest X-ray surveys to date, the 800 ks XMM-Newton observation of the Lockman Hole (Hasinger, 2004), the 1 Ms Chandra Deep Field South (Giacconi et al., 2002) and the 2 Ms Chandra Deep Field North (Alexander et al., 2003), showed that the detected X-ray sources account virtually for 100% of the CXB emission below 2 keV and that this fraction dramatically decreases ($< 50\%$) above 6 keV (Worsley et al., 2005). Optical spectroscopy of these sources showed that the vast majority of them are identified as being Active Galactic Nuclei (AGN) with different degrees of obscuration (Szokoly et al., 2004).
Population synthesis models, in the context of the AGN unified theory (Antonucci, 1993), explain the CXB spectrum as the emission of AGN with various level of obscuration and at different redshifts thus confirming partially the observational findings (Comastri et al., 1995; Gilli et al., 2001). According to these models, most AGN spectra are heavily absorbed, and about 85% of the radiation produced by super massive black hole accretion is obscured by dust and gas (Fabian & Iwasawa, 1999).

Notwithstanding all the advances in the field a major question remains. Worsley et al. (2005) determined that the fraction of the resolved-into-sources CXB emission decreases with energy being only $\sim$50% at 10 keV. They also showed that the unresolved component is consistent as being the emission of a yet undetected population of highly absorbed AGN; such AGN should be characterized by having column densities $\sim 10^{24}$ cm^{-2} and a space density peaking at redshift below 1. Furthermore, the existence of such population of Compton-thick AGN is required by population synthesis models (Comastri et al., 1995; Treister & Urry, 2005) to reproduce the peak of the CXB emission at 30 keV (Marshall et al., 1980). In synthesis, much evidence points towards the existence of Compton-thick AGN while only a handful of them is known and studied.

Very recent X-ray spectroscopy of the sources detected in the CDS (Tozzi et al., 2006), shows that 14 sources (5% of the total sample) are likely to be Compton-thick AGN. This number is in agreement with the expectations from the most recent population synthesis model (Gilli et al., 2006). Nevertheless, only $\sim$10% of the original source flux is seen in the Chandra band if a Compton-thick source is at z=1; moreover, the reflected component (by a cold medium) starts to contribute, at the level of 6% of the original flux, to the observed spectrum. However, the same authors (Tozzi et al., 2006) admit that, given

the typical signal-to-noise of the CDS sample, it is extremely difficult to efficiently select Compton-thick sources on the basis of the shape of the X-ray spectrum and that a contamination of 20% in the Compton-thick sample is thus likely.

Thus, the best and most accurate detections of Compton-thick sources rely on the exact determination of the photoelectric cut-off, which for such objects is in the hard X-ray band ($>$ 15keV). These elusive objects have, so far, been missed because of the difficulties of performing sensitive imaging of the hard X-ray sky.

The Burst Alert Telescope (BAT) (Barthelmy et al., 2005), on board the Swift mission (Gehrels et al., 2004), launched by NASA on November 20, 2004, represents a major improvements in sensitivity for X-ray imaging of the hard X-ray sky. The reader is referred to Ajello et al. (2007) for details about the BAT survey.

We have applied an innovative image reconstruction algorithm to 8 months of survey BAT data (Ajello et al., 2007); our survey covers $\sim$4000 deg^2 reaching a limiting sensitivity of < 0.9 mCrab. This makes it one of the most sensitive survey ever performed in the hard X-ray domain. We detected 61 hard X-ray sources of which 50 were previously unknown as hard X-ray emitters. In the framework of a campaign for spectroscopical identification of new hard X-ray selected AGN, we identified 3 new extragalactic sources (Rau et al., 2007).

The paper is organized as follows. In section we present the method to extract the spectra of our sources and we summarize the results of the spectral analysis in table 6.1; the details of the spectral analysis are reported in the Appendix 6.5. We also use the source spectra to build a color-color plot which is used to understand the mean properties of the source populations comprised in the sample. Moreover, we discuss the evidences for a population of newly detected Compton-thick sources. In section 6.3, we apply the V/V$_{MAX}$ test to better determine the significance at which the sample of extragalactic sources becomes complete. Such sample is then used to derive the number-flux relation and the results are compared with previous measurements in hard and soft X-rays. The section ends with a discussion about the statistical properties of the 5σ-selected extragalactic sample (90% complete). Finally, we discuss the BAT results in section 6.4. Throughout this work we use H_0 = 70 km s^{-1} Mpc^{-1} (h$_{70}$ =1), $k = 0$, Ω_{matter}=0.3 and Λ_0=0.7 and the luminosities are given in erg s^{-1} h^{-1}.

6.2 Spectral analysis

We have derived, for all our source candidates, a 6 channels energy spectrum in the 14-195 keV range. The energy channels used are (in keV): 14–22, 22–30, 30–47, 47–71, 71-121, 121–195. Each spectrum is obtained as a weighted average of the source spectra of all observations where the source is in the field of view. In particular, the averaged source count rates in the i-th energy channel, $\bar{R_i}$, and their error $\bar{\sigma_i}$, are given by the following equations:

$$\bar{R_i} = \frac{\sum_{j=0}^{N} r_j * w_j}{\sum_{j=0}^{N} w_j} \ , \quad \bar{\sigma_i} = \sqrt{\frac{\sum_{j=0}^{N} w_j V_j}{N \sum_{j=0}^{N} w_j}} \tag{6.1}$$

where r_j is the source count rate in the j-th observation, w_j is the weight used and the sums extend over all observations which contain the source. Using the inverse of the count rate variance V_j as a weight, the previous equations simplify to:

$$\bar{R_i} = \frac{\sum_{j=0}^{N} r_j \cdot 1/V_j}{\sum_{j=0}^{N} 1/V_j} \ , \quad \bar{\sigma_i} = \sqrt{\frac{1}{\sum_{j=0}^{N} 1/V_j}} \tag{6.2}$$

6.2.1 Rate variation as a function of off-axis angle

The detected count rates strongly vary with the position of the source in the FOV; a source at the far edge of the partially coded FOV (PCFOV) can experience a decrease in rate of a factor 2 (depending also on energy) when compared to its on-axis rate.

The standard Swift-BAT imaging software corrects for geometrical off-axis effects like cosine and partial coding (vignetting) effects; it is only when the response matrix is generated (tool *batdrmgen*) that other effects like detector thickness and effective area variation are taken into account.
Since in equation 6.2 we are averaging over spectra at different positions in the FOV, we need to take into account the variations in the rates produced by the detector response. In order to do so, we have analyzed a series of more than 1000 Crab observations. For each of our 6 energy channels we made a polynomial fit to the Crab rate as a function of the off-axis angle, and derived a set of corrective coefficients. These coefficients are then used to correct the rates of each source spectrum in order to transform them to the equivalent on-axis rates.
The variation of the Crab rates as a function of position in the FOV is reported in Fig. 6.1.

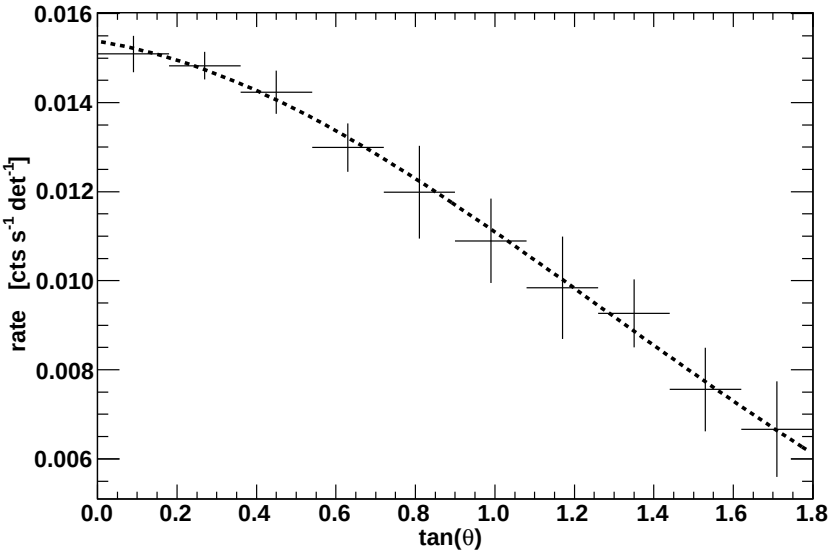

Figure 6.1: Crab rates in the 14-22 keV band as a function of the tangent of the off-axis angle. When the Crab is 50° off-axis the detected count rate are ∼30% lower than the on-axis count rate. The solid line is a polynomial fit to the rates.

6.2.2 Residual background contamination

In order to extract a source spectrum from survey data (in form of Detector Plane Histograms, DPH) the user must first produce a mask of weights (tool *batmaskwtimg*) for the source position and then use this mask to extract the detected counts from the array (tool *batbinevt*). The weights are chosen such that the resulting spectrum is already background-subtracted. This is an implementation of the standard mask weighting technique called *balanced correlation* (Fenimore & Cannon, 1978). The automatic background subtraction works as long as the noise in the array is flat and not correlated with the mask pattern. These conditions are not always satisfied and a small background contamination can arise.

The total background contamination for the case of the Crab is $< 2\%$ when compared to the Crab on-axis rate in the 14-195 keV band. Thus, this contamination does not pose problems for strong sources. However, it becomes relevant for for the spectral analysis of faint objects with intensities of ∼mCrab.
In order to correct for this residual background contamination, we fit the *batclean* background model to each energy channel in order to create a background prediction for each of them. Convolving these background predictions with the mask of weights generated for

the source under analysis yields the residual background term which the mask weighting technique did not manage to suppress.

6.2.3 Spectral fitting results

The final source rates in the i-th energy channel are computed as:

$$\bar{R_i} = \frac{\sum_{j=0}^{N}(r_j - b_j)\cdot K(E,\theta)\cdot 1/V_j'}{\sum_{j=0}^{N} 1/V_j'} \tag{6.3}$$

where b_j is the residual background term, $K(E,\theta)$ is the parametrized instrumental response as function of the energy channel and the off-axis angle and V_j' is the rate variance which takes into account both the uncertainty in the background correction and the parametrization of the response. The weighted averaged spectrum is then input, together with an on-axis response matrix, to XSPEC 11.3.2 (Arnaud, 1996) for spectral fitting.

We looked in the archives for *Swift*/XRT and ASCA observations of our sources. We found that 20 of our sources had at least one observation in the soft X-ray band carried out by one of the previous two instruments. For all these sources, we jointly fit XRT/ASCA and BAT data. The results of this combined analysis are reported in details for each source in Appendix 6.5.

Table 6.1 shows the results of the spectral fitting while the single spectra are reported in figures 6.9, 6.10, 6.11, 6.12, 6.13 , 6.14 , 6.15 , 6.16, 6.17 and 6.18 .

Table 6.1. Spectral parameters

NAME	RA (J2000)	DEC (J2000)	Type	z	Γ/E[kT][a]	Lx (10^{43} erg s^{-1})	N_H (10^{22}atoms cm^{-2})	MODEL	INSTR.
PSR B0540-69.3	84.9878	-69.3230	Pulsar	···	1.5 ± 0.21	···	···	pow	B
LMC X-1	84.8917	-69.7210	HXB	···	$2.5^{+0.26}_{-0.22}$	···	···	pow	B
LMC X-3	84.7717	-64.1148	HXB	···	$2.6^{+1.6}_{-0.9}$	···	···	pow	B
SWIFT J0917.2-6221	139.112	-62.359	Sy1	0.057	$1.77^{+0.1}_{-0.07}$	33.7	$1.2^{+0.20}_{-0.16}$	bb+wabs*pow	B
SWIFT J0957.0-5847	149.2537	-58.7979	NSV 4682[c]	···	2.6 ± 0.8	···	···	pow	B
V* TW Pic	83.6470	-58.0200	CV	···	$13.5^{+10.6}_{-5.6}$	···	···	brem	B
1AXG J042556-5711	**66.6021**	**-57.1775**	**Sy1**	**0.104**	$\mathbf{1.6^{+0.02}_{-0.02}}$	**79.0**	**0**	**pow**	**B, A**
4U 0919-54	140.0753	-55.2135	LXB	···	$36.2^{+160}_{-18.}$	···	···	bremss	B
Pictor A	**79.9460**	**-45.7557**	**Sy1**	**0.035**	$\mathbf{1.8^{+0.04}_{-0.02}}$	**7.4**	$\mathbf{0.12^{+0.007}_{-0.02}}$	**wabs*pow**	**B, A**
Vela PSR	128.8308	-45.1771	PSR	···	$1.4^{+0.3}_{-0.2}$	···	···	pow	B
SWIFT J0405.8-4345	**61.4522**	**-43.7520**	···	···	$\mathbf{3.8^{+2.7}_{-1.5}}$	···	$\mathbf{2.5^{+4.2}_{-1.7}\times10^{4}}$	**wabs*pow**	**B**
SWIFT J0447.8-4112	**71.9631**	**-41.2020**	···	···	$\mathbf{2.5\pm0.7}$	···	···	**pow**	**B**
4U 0513-40	78.5146	-40.0558	LXB	···	2.1 ± 0.3	···	···	pow	B
SWIFT J0837.1-3912	129.2970	-39.2024	···	···	$2.0^{+0.3}_{-0.4}$	···	···	pow	B
IGR J07597-3842	119.9822	-38.7422	Sy1.2	0.04	$1.9^{+0.2}_{-0.3}$	21.5	0.64	wabs*pow	B, X
LEDA 75476	**89.5237**	**-38.3799**	**Sy1**	**0.0338**	$\mathbf{2.0^{+0.5}_{-0.4}/0.25^{+0.08}_{-0.05}}$	**7.7**	$\mathbf{2.2^{+0.27}_{-0.14}}$	**wabs*(pow+ga)+bb**	**B, A**
ESO 362-G021	**80.6581**	**-36.4233**	**BLLac**	**0.05534**	$\mathbf{1.7\pm0.038}$	**23**	$\mathbf{0.1\pm0.017}$	**wabs*pow**	**B, A**
FRL 1146	129.6151	-35.9976	Sy1	0.031578	$2.15^{+0.48}_{-0.42}$	9.2	···	pow	B
SWIFT J0446.2-3537	**71.5631**	**-35.6275**	···	···	$\mathbf{2.16\pm0.5}$	···	···	**pow**	**B**
SWFIT J0844.9-3531	131.2411	-35.5313	···	···	1.6 ± 0.7	···	···	pow	B
V* TV Col	82.3541	-32.7965	CV-DQ*	···	$28.2^{+6.4}_{-5.0}$	···	···	bremss	B
ESO 362- G 018	**79.8844**	**-32.6720**	**Sy1.5**	**0.0126**	$\mathbf{1.5^{+0.07}_{-0.04}/3.7^{+0.7}_{-0.5}}$	**1.9**	**<0.01**	**wabs*(pow+bb)**	**B,X**
PKS 0548-322	**87.7165**	**-32.2610**	**BLLac**	**0.0690**	$\mathbf{1.78^{+0.03}_{-0.03}}$	**53.0**	$\mathbf{0.04\pm0.02}$	**wabs*pow**	**B, X**
SWIFT J0739.6-3144	114.9127	-31.7496	Sy2	0.0259	$1.86^{+0.57}_{-0.50}$	2.9	>2[b]	pow	B
ESO 434- G 040	**146.9151**	**-30.9388**	**Sy2**	**0.00848**	$\mathbf{1.75^{+0.017}_{-0.018}/\ 0.13^{+0.011}_{-0.016}}$	**2.9**	$\mathbf{1.5^{+0.026}_{-0.027}}$	**wabs*(pow+ga)+bb**	**B, A, X**
PKS 0537-286	**84.9953**	**-28.7029**	**BLAZAR**	**3.1**	$\mathbf{1.35^{+0.14}_{-0.14}}$	**1.8e5**	**< 0.01**	**wabs*pow**	**B, A**
V* 441 Pup	112.1626	-26.0696	CV	···	6.8	···	···	brem	B
ESO 490- G 26	100.0031	-25.8931	Sy1.2	0.02485	$1.74^{+0.1}_{-0.1}$	6.8	$0.32^{+0.05}_{-0.05}$	wabs*pow	B, X
SWIFT J0902.4-2418	135.6084	-24.3074	···	···	$3.3^{+1.1}_{-0.8}$	···	150 (fixed)	pow	B

6.2.4 Color-color plot

In order to understand the mean properties of our sample of sources, we have defined two hardness ratios HR1 and HR2 as follows:

$$HR_1 = \frac{I_{30-195} - I_{14-30}}{I_{14-195}}, \tag{6.4}$$

$$HR_2 = \frac{I_{22-30} - I_{14-22}}{I_{14-30}}, \tag{6.5}$$

where I_{30-195} is the sum of the count rates between 30 and 195 keV. The hardness ratios are normalized to the range -1 and +1. HR_1 gives hints about the steepness of the spectrum where hard and soft spectra are characterized by values > 0 and < 0 respectively. On the other hand, HR_2, being the difference between the first 3 energy channels, signals the presence of large absorption for positive values. The hardness ratios plot is shown in Fig. 6.2. In the same figure we indicate also the loci occupied by sources with a power law index in the range 1.0-3.5, or a bremsstrahlung spectrum characterized by a temperature in the range 5-35 keV or with an absorbed power law model with photon index 2 and absorbing column density in the range Log(N_H)=23-25. A few things can already be derived by the study of the hardness ratios. Galactic sources, which are usually characterized by steep X-ray spectra and are not detected by BAT at high energies, have HR_2 values < 0 and $HR_1 < 0.2$; so they have unabsorbed and soft spectra as expected. From the same plot it also follows that Sy2 galaxies have generally harder X-ray spectra than Sy1s (larger values of HR_1).

An interesting result is that there are 7 objects at $HR_2 > 0.3$ whose spectrum potentially requires large absorption. All of them are new source detected by BAT with the method presented in Ajello et al. (2006). Three of the objects, J0739.6-3144, J0823.4-0457 and Mrk 704, have a spectroscopic identification as Sy galaxies (2 type-2 and a type-1.5 respectively). Sources J0844.9-3531, J0902.4-2418, and J0405.8-4345 lie at galactic latitudes $|b| > 14^\circ$ and so their nature is unlikely to be galactic. The source J0528.0+1435 lie instead in the galactic plane. The combined XRT-BAT spectrum reveals that SWIFT J0823.4-0457 and Mrk 704 are absorbed respectively by a hydrogen column densities of 2.1 and 1.4×10^{23}atoms cm^{-2}.

6.2.5 Absorption in hard X-rays

Since a few sources might be heavily absorbed, we decide to investigate the capability of BAT of detecting the absorption cut-off in known Compton-thick sources. Thus, we have produced the averaged spectrum of two well known and studied Compton-thick sources:

Table 6.1 (cont'd)

NAME	RA (J2000)	DEC (J2000)	Type	z	Γ/E[kT][a]	Lx (10^{43} erg s^{-1})	N_H (10^{22}atoms cm^{-2})	MODEL	INSTR.
SWIFT J0727.5-2406	111.8951	-24.1039	···	···	$1.6^{+0.51}_{-0.41}$	···	···	pow	B
SWIFT J0505.7-2348	**76.4674**	**-23.8666**	**Sy2**	**0.0350**	$\mathbf{1.9^{+0.1}_{-0.1}}$	**11.0**	$\mathbf{5.3^{+1.1}_{-0.8}}$	**wabs*pow**	**B, X**
NGC 3081	**149.8805**	**-22.8561**	**Sy2**	**0.0798**	$\mathbf{1.7^{+0.16}_{-0.08}}$/ $\mathbf{0.57^{+0.09}_{-0.08}}$	**1.2**	$\mathbf{60^{+5.9}_{-5.6}}$	**wabs*(pow+ga) +bb**	**B, A, S**
SWIFT J0418.6-1847	**64.6653**	**-18.7978**	···	···	$\mathbf{2.5^{+1.4}_{-0.8}}$	···	···	**pow**	**B**
NGC 2992	**146.4060**	**-14.3007**	**Sy1.9**	**0.00771**	$\mathbf{1.20^{+0.05}_{-0.05}}$	**0.78**	$\mathbf{0.15^{-0.03}_{-0.03}}$	**wabs*(pow+ga)**	**B, A, X**
SWIFT J0732.5-1331	113.1328	-13.5037	CV	···	$2.3^{+0.37}_{-0.31}$	···	···	pow	B
3C 206	**129.9556**	**-12.2467**	**QSO**	**0.1976**	$\mathbf{3.4^{+1.8}_{-0.9}}$	**2.6e2**	$\mathbf{> 5}$[b]	**wabs*pow**	**B**
SWIFT J0722.6-0931	110.6593	-9.5224	···	···	$2.1^{+2.5}_{-1.2}$	···	···	pow	B
MCG -01-24-012	**140.2134**	**-8.0872**	**Sy2**	**0.01964**	$\mathbf{1.9^{+0.14}_{-0.13}}$	**3.8**	$\mathbf{6.8^{+1.1}_{-1.1}}$	**wabs*pow**	**B, X**
NGC 2110	**88.0411**	**-7.4554**	**Sy2**	**0.007789**	$\mathbf{1.7^{+0.2}_{-0.2}}$	**4.4**	$\mathbf{3.8^{+0.18}_{-0.15}}$	**wabs*(pow+ga)**	**B, A, X**
SWIFT J0823.4-0457	**125.8271**	**-4.9401**	**Sy2**	**0.023**	$\mathbf{1.76^{+0.21}_{-0.18}}$	**4.0**	$\mathbf{21.2^{+6.7}_{-5.4}}$	**wabs*pow**	**B, X**
MCG -01-13-025	**72.9205**	**-3.8240**	**Sy1.2**	**0.015894**	$\mathbf{1.8^{+0.74}_{-0.64}}$	**1.8**	$\mathbf{< 0.02(1)}$	**pow**	**B**
QSO B0513-002	**79.0096**	**-0.1332**	**QSO**	**0.0327**	$\mathbf{1.97^{+4.8e-3}_{-0.019}}$	**11.0**	$\mathbf{< 0.01}$	**pow**	**B**
SWIFT J0834.6+0217	**128.6574**	**2.2926**	···	···	$\mathbf{1.54^{+0.52}_{-0.54}}$	···	···	**pow**	**B**
3C 105.0	**61.9178**	**3.6517**	**Sy2**	**0.089**	$\mathbf{1.6^{+0.12}_{-0.33}}$	**1.2e2**	$\mathbf{31.0^{+8.3}_{-8.3}}$	**wabs*pow**	**B, X**
UGC 4203	**121.0552**	**5.1203**	**Sy2**	**0.01349**	$\mathbf{2.0^{+0.45}_{-0.45}}$/ $\mathbf{0.31^{+0.08}_{-0.05}}$	**1.7**	$\mathbf{15.1^{+6.2}_{-4.9}}$	**wabs(pow+ga)+bb**	**B, A, X**
3C 120	**68.2982**	**5.3374**	**Sy1**	**0.0330**	$\mathbf{1.80^{+0.04}_{-0.04}}$/$\mathbf{0.27^{+0.026}_{-0.025}}$	**21.2**	**0**	**wabs*pow+bb**	**B, A**
SWIFT J0959.3+0550	149.8280	5.8338	···	···	$1.9^{+1.3}_{-1.0}$	···	···	pow	B
3C 227	**146.9447**	**7.4191**	**Sy1**	**0.0858**	$\mathbf{1.37^{+0.42}_{-0.55}}$	**34.4**	$\mathbf{> 1}$[b]	**pow**	**B**
SWIFT J0811.5+0937	**122.8750**	**9.6214**	**XBONG**	**0.282**	$\mathbf{2.2^{+2.1}_{-0.9}}$	**272.6**	10[d]	**pow**	**B**
V* BG CMi	112.8752	9.9214	CV	···	$1.34^{+3.4}_{-1.4}$	···	···	pow	B
SWIFT J0923.3+1024	**140.8256**	**10.4112**	···	···	$\mathbf{10.6^{+17.2}_{-4.3}}$	···	···	**brems**	**B**
SWIFT J0847.4+1219	**131.8676**	**12.3243**	···	···	$\mathbf{24.0^{+26.3}_{-11.3}}$	···	···	**brem**	**B**
SWIFT J0528.0+1435	82.0246	14.5874	···	···	$3.7^{+3.0}_{-1.5}$	···	$2^{+2.0}_{-1.2} \times 10^4$	wabs*pow	
SWIFT J0854.7+1502	**133.6828**	**15.0371**	**Sy2**	**0.0696**	$\mathbf{1.37^{+0.7}_{-0.9}}$	**26.5**	$\mathbf{> 0.5}$[b]	**pow**	**B**
Mrk 0704	**139.6505**	**16.2987**	**Sy1.5**	**0.0292**	$\mathbf{1.36^{+0.07}_{-0.01}}$	**7.8**	$\mathbf{14.6^{+6.6}_{-3.4}}$	**pcfabs*(pow+ga)**	**B, A, X**
CSV 6150	77.7224	16.5265	Sy1.5	0.0178	$2.18^{+0.24}_{-0.21}$	4.6	···	pow	B
SWIFT J0517.1+1633	79.2839	16.5605	···	···	$3.17^{+0.77}_{-0.53}$	···	···	pow	B

[a]Photon index and/or plasma temperature for the model, specified in column "Model", to fit the data.

[b] Lower limit on absorption estimated through the non detection by ROSAT.

[c]Proposed identification in Rau et al. (2007).

[d]Order of magnitude of the absorption estimated imposing that the extrapolated source flux match the ROSAT-PSPC count rates.

References. — References: (1) Gallo et al. (2005).

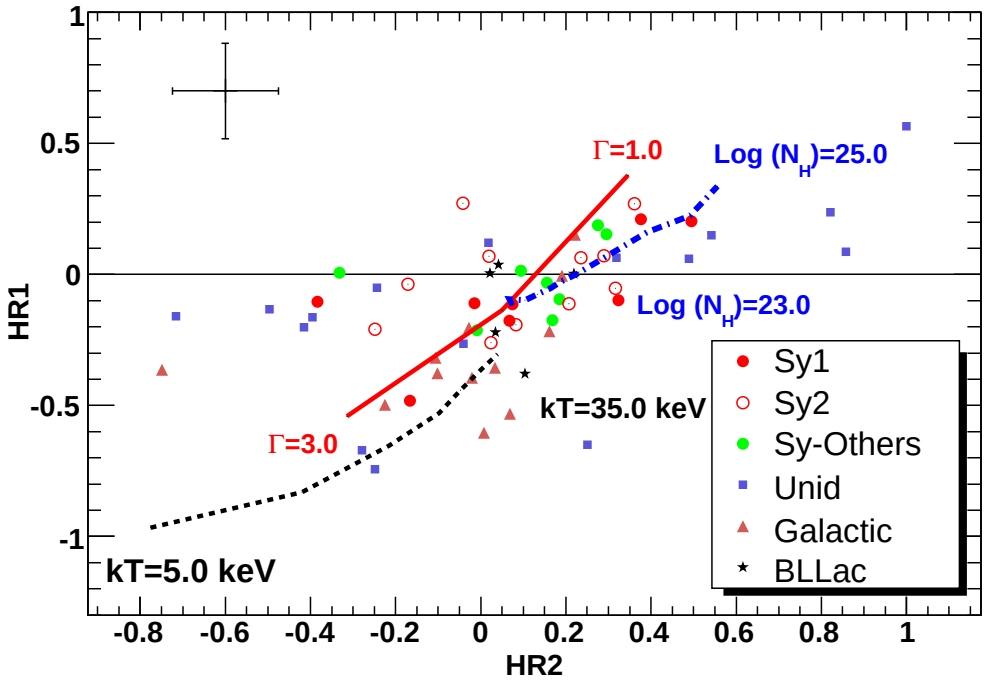

Figure 6.2: Plot of HR1 and HR2 hardness ratios. The solid line is the locus for sources with power law models with photon indexes in the 1.0-3.0 range and no absorption. The dot-dashed line is the locus of sources with photon index of 2.0 and variable absorption in the range Log(N_H)= 23-25. The dashed line is the locus for sources with a bremsstrahlung spectrum with temperatures in the range 5-35 keV. In the upper left corner the typical $\pm 1\sigma$ error for a 5σ source is shown.

the Circinus galaxy and NGC 4945 (Fig. 6.3). Both spectra are not consistent with a pure power law model ($\chi^2 > 5$) and require large absorption in order to produce a good fit. The model used for the Circinus galaxy is an absorbed power law model with a cut-off at 56 keV and photon index of 1.8. The absorbing column density is $3.8^{+1.6}_{-1.3} \times 10^{24}$atoms cm^{-2} (90% confidence level).

In the case of NGC 4945 a simple absorbed power law model fits the data well yielding a photon index of 1.9 and an absorbing column density of $9.8^{+8.5}_{-5.2} \times 10^{24}$atoms cm^{-2}.

All the fit values are in line with those presented in a recent INTEGRAL analysis (Soldi et al., 2005), with the important difference that, in the INTEGRAL analysis, the absorbing column densities are fixed at the values reported in literature and not estimated from the INTEGRAL data themselves. This is mainly because the low energy response of INTEGRAL-ISGRI stops at 20 keV not allowing for an estimate of absorption in the

range of $10^{24} - 10^{25}$ atoms cm^{-2}.
On the other hand, the BAT low energy response extends down to 14 keV allowing the detection of the photo-electric cut-off in the hard X-ray band; thus BAT is a very sensitive and unique instrument for detecting Compton-thick sources in the hard X-ray domain.

The spectral analysis and the hardness ratio distribution show evidences for the existence of a population of heavily absorbed, potentially Compton-thick, sources. Since all those sources have a low S/N (i.e. they are close to our detection limit), their spectra do not allow for an estimate of both the column density and the photon index at the same time.

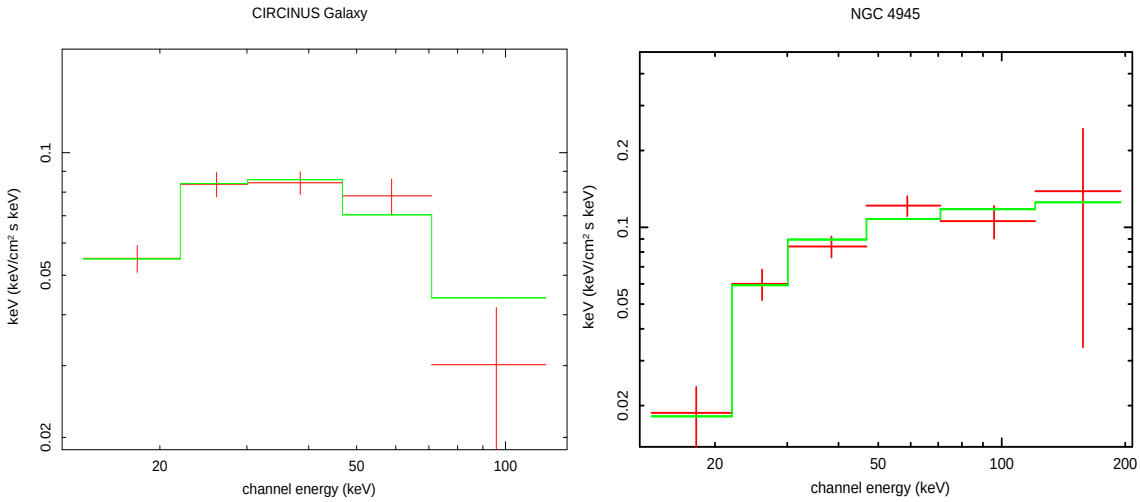

Figure 6.3: BAT photon spectra of two well known Compton thick sources: the Circinus galaxy and NGC 4945, respectively on the left and on the right. Both spectra show, clearly, spectral curvature at low energy due to absorption by Compton-thick matter.

In order to study in more detail the properties of our sample of candidate Compton-thick sources, we have divided the extragalactic sources presented in Tab. 6.1 (bold face) into three groups: Sy1, Sy2 and absorbed sources. From the Sy1 group we have removed Mrk 704 as the detailed spectral analysis, presented in section 6.5, shows that this is not a typical Sy1 object and is likely a Compton-thick object. The three Sy2 objects which show large absorption in the BAT spectrum are present in the sample of the candidate Compton-thick sources and not among the Sy2.
The spectra of the three classes of objects are shown in figure 6.4; the spectra were normalized to a power law model with photon index of 2.2 (the mean index of Sy1 objects, see below), in figure 6.4 to better highlight the relative differences. Sy2 objects have harder spectra than Sy1s and candidate Compton-thick sources present spectral curvature

in the lowest energy channels due, most probably, to absorption by Compton-thick matter. We plotted in Fig. 6.5 the confidence contours of N_H and photon index for the fit to the stacked spectrum of candidate Compton-thick sources; even though, a clear correlation between photon index and N_H is present, the stacked spectrum is consistent with a Compton-thick source at 3σ CL.

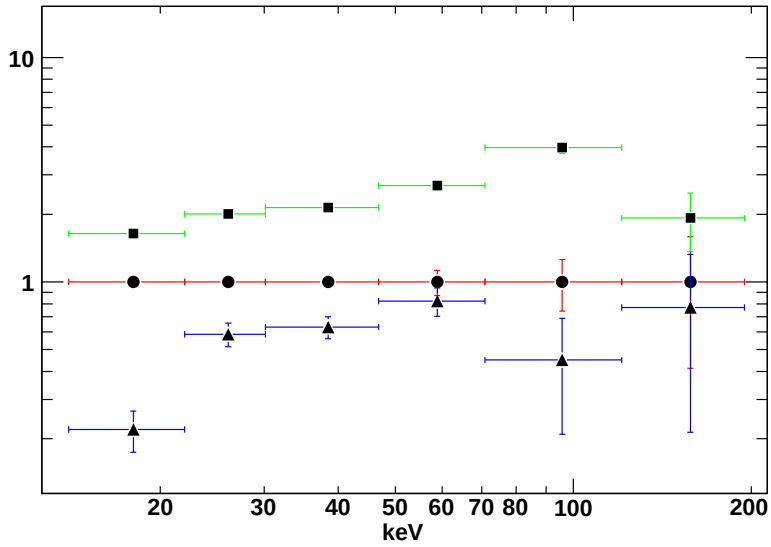

Figure 6.4: Stacked spectra of Sy1 (dots), Sy2 (squares) and candidate Compton thick (triangles) objects normalized by a power law model with photon index of 2.2. The y axis reports arbitrary intensity units. As clearly shown, Sy2 objects have an harder spectra than Sy1 galaxies. Compton-thick candidates show a strong decrease in flux in the first channel hypothetically due to photo-electric absorption from Compton-thick matter.

The spectral properties of the three classes are summarized in Tab. 6.2. The photon index of Seyfert objects is in the range of 2 even though the index of Sy2 is a bit harder (1.9) than the one for Sy1 (2.2) in agreement with the hardness ratio plot of section 6.2.4. BAT-detected Sy2s show absorption in the range of $\sim 10^{23}$ atoms cm^{-2} which even if it is not well constrained is statistically required by the fit. The candidate Compton-thick sources have a steeper photon index than 2 and require an absorption of $\sim 10^{25}$ atoms cm^{-2}; the F-test of the absorbed power law model, with respect to the simple power law model, yields a probability of 0.03 of the absorption model to be spurious. We also note that the stacked spectrum of the candidate Compton-thick sources looks very similar to the one of the Compton-thick source NGC 4945 shown in figure 6.3.

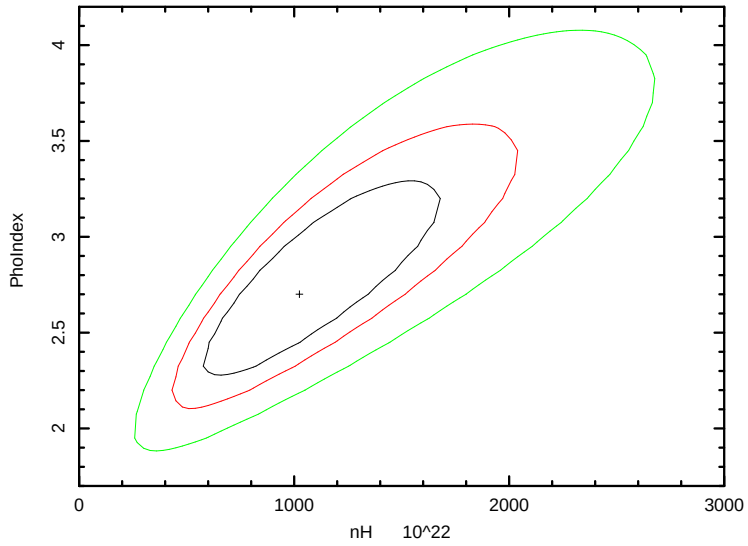

Figure 6.5: 68%, 95% and 99% confidence contours for photon index and hydrogen column density for the fit to the stacked spectrum of Compton-thick candidates.

Table 6.2. Spectral parameters for Sy1, Sy2 and candidate Compton-thick sources. Errors are 90% confidence level.

CLASS	Photon index	N_H (10^{24}atoms cm^{-2})
Seyfert 1	2.2 ± 0.1	$\cdots$
Seyfert 2	1.9 ± 0.1	0.6 ± 0.5
Absorbed	$2.7^{+0.6}_{-0.5}$	$10^{+7.1}_{-4.3}$

6.3 The hard X-ray extragalactic sample

The extragalactic sample was derived from the catalog reported in table 2 of Ajello et al. (2007) considering only objects at $|b| > 15^{\circ}$ and not spatially associated with the Large Magellanic Cloud. These sources are the ones highlighted in bold text in table 6.1. Here we describe the main properties of the sample.

6.3.1 Completeness of the sample

In order to compute the AGN number-flux relation it is necessary to have a complete and unbiased sample of sources. Because of the inhomogeneous nature of the survey expo-

sure map, we applied in Ajello et al. (2007) a significance limit rather than a flux limit to define our sample. Now we want to test our extragalactic sample for completeness (i.e. we want to find a significance limit which ensures that all objects above a given flux limit have been included). Here we are using the V/V_{MAX} method (Schmidt, 1968) to test for incompleteness. In this test V stands for the volume where the object has been detected and V_{MAX} is the accessible volume in which the object, due to the flux limit of the survey, could have been found. In case of no evolution $<V/V_{MAX}>$ = 0.5 is expected. This method can only be applied to samples complete to a well-defined significance limit. It can therefore also be used to test the completeness level of a sample. Thus, we performed a series of V/V_{MAX}-tests with the BAT extragalactic sample as a function of significance. For a significance limit below the true completeness level limit of the sample, the V/V_{MAX} returns a value less than $\langle V/V_{MAX}\rangle_{true}$ which would be the true test result for a complete sample. Above the completeness limit the $\langle V/V_{MAX}\rangle$ values should be distributed around $\langle V/V_{MAX}\rangle_{true}$ within the statistical uncertainties.

The V/V_{MAX} is computed for each source as $(F/(\sigma_{test}\delta F))^{-3/2}$, where F is the sources flux, δF is the 1σ statistical uncertainty, σ_{test} is the significance level we are testing for completeness (and thus the term $\sigma_{test}\delta F$ is the limiting flux of the sky region where we detected the source), and the exponent $-3/2$ comes from the assumption of no evolution and uniform distribution in the local universe. The $\langle V/V_{MAX}\rangle$ is computed as an average of all sources detected with S/N$\geq \sigma_{test}$. For a given mean value $m = \langle V/V_{MAX}\rangle$ and n sources, the error on $\langle V/V_{MAX}\rangle$ can be computed as (Avni & Bahcall, 1980):

$$\sigma_m(n) = \sqrt{\frac{1/3 - m - m^2}{n}} \tag{6.6}$$

The results of the test are shown in Fig. 6.6. We find a constant value for significances $> 4.5\sigma$. The deviation from the expected 0.5 value is insignificant being less than 1.5σ. We also remark that for completeness we are referring to the best significance threshold above which all sources above the correspondent flux limit are included in the sample. Furthermore, given the small redshift of the sample (see section 6.3.3) the hypothesis of no evolution is justified. Above the $4.5\,\sigma$ the sample contains 32 objects. 19 objects are classified as Seyfert galaxies and 4 as blazars. The remaining 9 are unclassified (i.e. they miss soft X-ray and/or optical identification). The identification completeness of such sample is quite low (73%). Given, the cut on galactic latitude ($|b| > 15^\circ$), the contamination due to Galactic sources (among the unidentified) objects is expected to be negligible. Indeed, in this energy band, > 15 keV, the chance probability that an high latitude source

is not an AGN (i.e. it can be a galaxy cluster) is low.

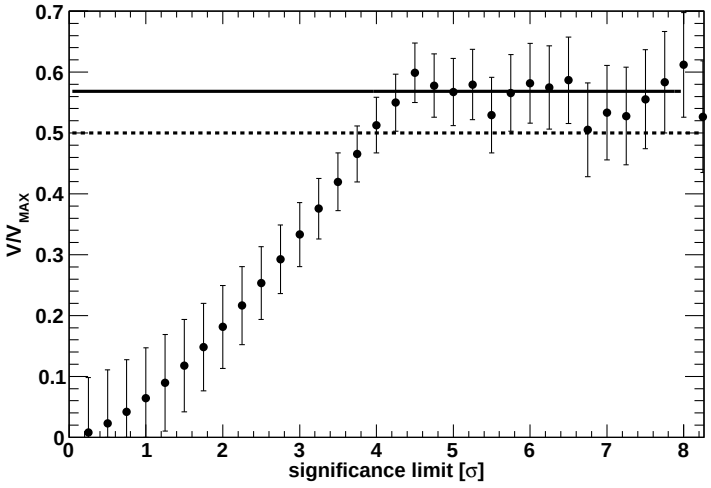

Figure 6.6: V/V_{MAX} as a function of detection threshold for our sample of extragalactic sources. The dashed line is the expected value (0.5) for a complete sample in an homogeneous distribution. The solid line shows the mean test value for S/N$>4.5\sigma$.

6.3.2 Extragalactic source counts

We have used the sky coverage, for $|b| > 15^{\circ}$, presented in figure 9 of Ajello et al. (2007) to assess the source counts distribution of the serendipitous extragalactic objects detected in the survey.

The cumulative source number density can be computed as:

$$N(>S) = \sum_{i=1}^{N_S} \frac{1}{\Omega_i} \quad [\mathrm{d}eg^{-2}] \tag{6.7}$$

where N_S is the total number of detected sources in the field with fluxes greater than S and Ω_i is the sky coverage associated to the flux of the i^{th} source.
The cumulative distribution is reported in Fig. 6.7. In order to parametrize the relation, we performed a maximum likelihood fit to the unbinned differential counts. We assumed a simple power-law model of the form:

$$n(S) = \frac{dN}{dS} = AS_{11}^{-\alpha}, \tag{6.8}$$

where A is the normalization, α is the slope and S_{11} is the flux in unit of 10^{-11} erg cm^{-2} s^{-1}. The maximum-likelihood fit is required since binning our sample of sources would

result in an unacceptable loss of accuracy in the fit results. Moreover, the normalization A is not a parameter of the fit, but it is obtained assuming that the number of expected sources from the best fit model is equal to the total observed number. The Poissonian error on the total number of sources provides a reliable estimate of the error on A.

In the 14–170 keV band the best fit parameters are: $\alpha = 2.58 \pm 0.26$ and A=0.028 deg^{-2}. The source count distribution is thus consistent with a pure Euclidean function ($\alpha = 5/2$), but the best fit gives a slope which is slightly steeper. From our data we derive a surface density of extragalactic objects of $(2.87 \pm 0.48) \times 10^{-2}$ deg^{-2} (or 1185±200 AGN all-sky) above the limiting flux of 10^{-11} erg cm^{-2} s^{-1}.
This corresponds to an integrated flux of $\sim 5 \times 10^{-12}$ erg cm^{-2} s^{-1} deg^{-2} or ∼1.5% of the intensity of the hard X-ray background in the 14-170 keV energy band above 2×10^{-11} erg cm^{-2} s^{-1}.
We can compare the surface density of extragalactic objects found by BAT, above 10^{-11}erg cm^{-2} s^{-1}, with previous measurements by converting the BAT fluxes to other energy bands assuming a power law spectrum with photon index of 2. The results of such comparisons are shown in Tab. 6.3. The BAT surface density is in agreement with all the reported measurements, except for the case of the 0.5–2 and 2–10 keV surveys. Indeed, such surveys, at limiting fluxes of 10^{-11} erg cm^{-2} s^{-1}, are biased with respect to the detection of absorbed sources. It is also worth noting that the recent XMM measurement of the 5–10 keV source counts distribution (Cappelluti et al., 2007) is in perfect agreement with our estimate.

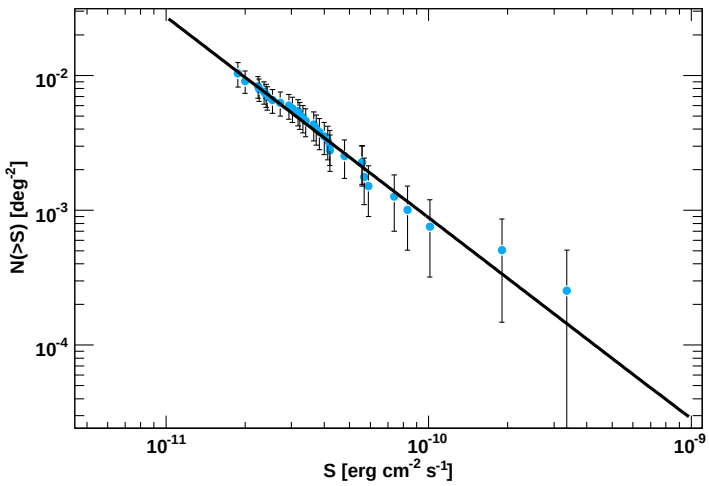

Figure 6.7: Extragalactic cumulative source count distribution in the 14-170 keV band. The solid line is the fit described in the text.

Table 6.3. Comparison with previous results

Instrument	Ref.	Energy keV	AGN density[a] 10^{-2} deg^{-2}	BAT density (this work)[b] 10^{-2} deg^{-2}
INTEGRAL-ISGRI	1	20 - 40	0.48±0.08	0.41±0.068
INTEGRAL-ISGRI	2	100 - 150	0.18±0.006	0.17±0.029
HEAO-1 A2	3	2 - 10	1.2±0.2	1.6 ±0.15
RXTE PCA	4	8 - 20	0.56±0.06	0.65±0.11
XMM	5	0.5 - 2	0.1±0.01	1.3 ±0.2
XMM	5	2 - 10	0.95±0.06	1.6 ±0.15
XMM	5	5 - 10	0.63±0.4	0.4±0.07

[a]AGN densities from different surveys above 10^{-11} erg cm^{-2} s^{-1}.

[b]The BAT AGN density was converted to the native energy band of the measurement we are comparing it with.

References. — (1)Beckmann et al., 2006; (2) Bazzano et al., 2006; (3) Piccinotti et al., 1982; (4) Revnivtsev et al., 2004; (5) Cappelluti et al., 2007

6.3.3 Statistical properties

As already discussed, the completeness of the sample of sources detected above 4.5σ is quite low (73%) and in order to derive solid statistical properties for the BAT extragalactic objects we consider here only those sources detected at $> 5\sigma$ level. This additional cut leaves us with a sample of 21 sources with 2 optically unclassified objects and a completeness of >90%. This sample includes 6 Sy1, 10 Sy1.9-2, 1 Sy1.5, 1 QSO and 1 Blazar. For additional clarity this sub-selected sample is shown in Tab. 6.4. Excluding the radio-loud objects, the median redshift of the sample is 0.021 (mean is 0.031) giving a median luminosity of $10^{43.6}$erg s^{-1} (mean is $10^{43.8}$) in the 14-170 keV band. Assuming 10^{22} atoms cm^{-2} as the threshold between absorbed and unabsorbed objects, we find that intrinsic absorption is present in ∼63% of the sample. This result is consistent with the high latitude BAT survey (Markwardt et al., 2005) and the INTEGRAL extragalactic survey(Bassani et al., 2006).

In Fig. 6.8 we show the intrinsic column density of the sources as a function of unabsorbed luminosity in the BAT band. Excluding the lower limits on the absorption, we see a weak anticorrelation of luminosity and absorption. We also note the presence of a rare very luminous ($L_x \sim 10^{45}$ erg cm^{-2}) highly absorbed ($N_H \sim 10^{23}$atoms cm^{-2}) type-2 QSO. If the lower limits on the absorption will be confirmed, the total fraction of such objects will be in the range 5-15%.

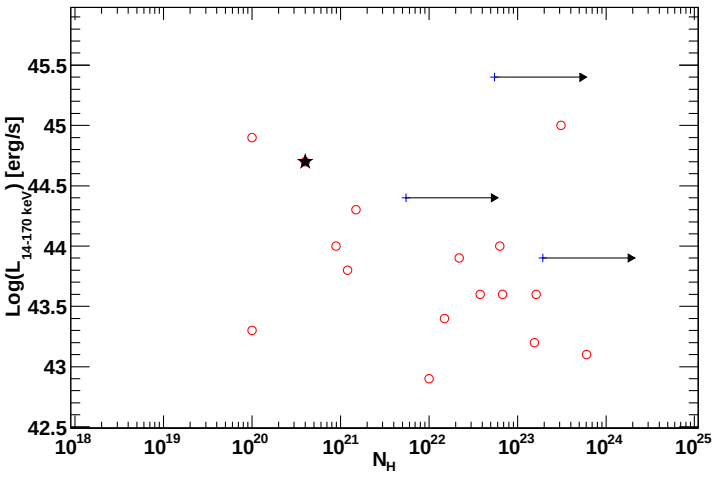

Figure 6.8: Luminosity, in the 14-170 keV band, vs. intrinsic column density for the 5σ-selection of the extragalactic sample. The blazar is highlighted with a black star.

Table 6.4. Extragalactic $> 5\sigma$ sample.

NAME	Type	z	Radio-loud	Fx (10^{-11} erg cm^{-2} s^{-1})	Lx (10^{43} erg s^{-1})	N_H (10^{22}atoms cm^{-2})	ref
Pictor A	Sy1	0.035	Y	3.18	7.4	0.12	1
LEDA 75476	Sy1	0.0338	N	4.45	10	1.8	1
ESO 362- G 018	Sy1.5	0.0126	N	4.78	1.9	$<$0.01	1
PKS 0548-322	BLLac	0.0690	Y	3.40	53.0	0.04	1
ESO 434- G 040	Sy2	0.00848	N	19.1	2.9	1.5	1
SWIFT J0505.7-2348	Sy2	0.0350	N	2.93	11.0	6.3	1
NGC 3081	Sy2	0.0798	N	10.0	1.2	60	1
NGC 2992	Sy1.9	0.00771	N	5.90	0.78	1	4
3C 206	QSO	0.1976	Y	2.43	2.6e3	$>$5	1
MCG -01-24-012	Sy2	0.01964	N	3.03	3.8	6.8	1
NGC 2110	Sy2	0.007789	N	33.6	4.4	3.8	1
SWIFT J0823.4-0457	Sy2	0.023	N	3.23	4.0	16.2	1
QSO B0513-002	Sy1	0.0327	N	7.40	11.0	0.02	3
SWIFT J0834.6+0217	...	...	...	3.32	...		
3C 105.0	Sy2	0.089	Y	5.4	1.0e3	31.0	1
UGC 4203	Sy2	0.01349	Y	4.20	1.7	20.5	1
3C 120	Sy1	0.0330	Y	8.30	21.2	0	1
SWIFT J0847.4+1219	...	...	...	1.9	...		
SWIFT J0854.7+1502	Sy2	0.0696	N	5.58	22.5	$>$0.5	1
Mrk 0704	Sy1	0.0292	N	4.13	7.8	$>$ 14.6	1
1AXG J042556-5711	Sy1	0.104	N	2.99	79.0	0	1

References. — References: (1) this work; (2) Lutz et al. (2004); (3) Gilli et al. (2001)

6.4 Discussion

We have used the BAT X-ray survey to study key properties of the local ($z \leq 0.1$) AGN population. Our survey is based on the 14-170 keV fluxes and it is equally sensitive to AGN with column densities up to $N_H \sim 10^{25}$ atoms cm^{-2}. Indeed, for a typical source with photon index of 2, the decrease in flux for column densities of $N_H \sim 10^{24}$ atoms cm^{-2} is only $\sim 5\%$ and $\sim 25\%$ for column densities of $\sim N_H \sim 10^{25}$ atoms cm^{-2}. Thus, we can affirm that this survey is relatively unbiased with respect to photoelectric absorption.

Most of the population synthesis models (Ueda et al., 2003; Treister & Urry, 2005; Gilli et al., 2006) predict that Compton-thick AGN ($\mathrm{Log}N_H > 24$) provide a significant contribution to the bulk of the CXB emission at 30 keV(Marshall et al., 1980). Although studies of the local Universe (e.g. Risaliti et al., 1999) have shown that Compton-thick objects should be as numerous as moderately obscured AGNs ($\mathrm{Log}N_H < 24$) and thus roughly 1/3 of the total AGN population, only a handful of these sources are known (Comastri, 2004) . The density of Compton-thick objects is today practically unknown and the only constraints are provided by population synthesis models trying to match the intensity of the CXB peak at 30 keV (e.g. Gilli et al., 2006). However, given the numerous assumptions (X-ray luminosity function and evolution of absorbed objects) such constraints appear loose. Thus, the detection of *new* Compton-thick objects is a major test for the validity of models synthesizing the CXB radiation in terms of integrated AGN emission. Gilli et al. (2006) estimate that the expected fraction of Compton-thick objects at limiting fluxes probed by BAT and INTEGRAL ($\sim 10^{-11}$erg cm^{-2} s^{-1}) is $\sim 20\%$. However the measured fraction of detected Compton-thick objects by these instruments is, so far, close to, or less than, 10% (Markwardt et al., 2005; Beckmann et al., 2006).

Contrary to other hard X-ray surveys (Markwardt et al., 2005; Beckmann et al., 2006; Sazonov et al., 2006) which have not detected new Compton-thick AGN, this work shows that BAT, thanks to its low-energy response, is a uniquely sensitive instrument for detecting new Compton-thick sources. We have verified the capability of BAT of sampling the photoelectric cut-off by deriving the spectra of two known, and bright, Compton-thick sources (Circinus galaxy and NGC 4945). The BAT spectra for these sources show a clear spectral curvature at low energy which allows a reliable estimate of the absorbing column densities (consistent with what was reported already in the literature). On this basis, we select, among our sample 61 sources, 7 candidate Compton-thick sources. The stacked spectral analysis confirms that the averaged spectrum shows evidence for absorption by Compton-thick matter $N_H \sim 10^{25}$ atoms cm^{-2}. Due to the low completeness of our extragalactic sample (73%), it is not possible to estimate the fraction of Compton-thick sources

relatively to the total population of AGN. If the 3 Compton-thick candidates (out of the 7) which lie at $|b| > 15^{\circ}$ will be confirmed in future soft X-ray observations we would conclude that the fraction of Compton-thick objects is >10%. However, for a definitive solid estimate we must wait for the optical identification of all the sources to be complete and for sensitive observations in the $<$ 10keV regime to confirm the objects' nature.

The best power-law fit to the extragalactic source counts distribution yields a slope of 2.58$\pm$0.26 which is a bit steeper than, but consistent with, an Euclidean distribution. From the best fit, we derive a surface density of AGN of $2.87\pm0.48 \times 10^{-2}$deg^{-2} above the flux limit of 10^{-11}erg cm^{-2} s^{-1}; this estimate is in very good agreement, when converted to the 20-40 keV band, with the recently derived source counts distribution based on INTEGRAL data (Beckmann et al., 2006). Nevertheless, Beckmann et al. (2006) find a slope of 1.66$\pm$0.11 which is also consistent with our measurement, but is sensibly steeper than the 1.5 Euclidean value. Even though this could be due to a non-perfectly computed sky coverage, the authors suggest that the distribution of AGNs in the local Universe may not be isotropic because of local clustering of sources (e.g. the local group of galaxies).

The BAT source count distribution resolves only 1-2% of the CXB into extragalactic sources; nevertheless as it is unbiased with respect to absorption it can give important information relative to the fraction of obscured sources which are missed by deep $<$ 10keV surveys because of absorption. The extrapolation of the BAT source count distribution to the 2-10 keV band assuming an unabsorbed spectrum with photon index 2 yields a surface density of AGN of $1.6\pm0.15 \times 10^{-2}$deg^{-2} above 10^{-11}erg cm^{-2} s^{-1}; while the surface density as extrapolated to brighter fluxes by XMM (Cappelluti et al., 2007) and as predicted by the model of Gilli et al. (2006) is 0.9×10^{-2}deg^{-2}. The factor ~ 2 more sources BAT sees can be explained in term of absorption. Indeed, if we take into account the absorption distribution derived for BAT AGNs by Markwardt et al. (2005) (thus assuming that 65% of all AGN are absorbed with a mean column density of 10^{23} atoms cm^{-2}) we get a surface density $0.86\pm0.04 \times 10^{-2}$deg^{-2} which is consistent with the XMM extrapolation and the model prediction.

Our 5σ selected sample, whose completeness is $\sim$90%, shows a ratio of absorbed to total AGN of 68^{+2}_{-8}% which is in agreement with measurements in similar bands (Markwardt et al., 2005; Beckmann et al., 2006). Our sample does not show anti-correlation between intrinsic luminosity and absorption as claimed by Markwardt et al. (2005) and Bassani et al. (2006), but this could be due to the small extent of the sample used here. A relevant fraction ($\sim$20%) of the detected AGN is radio-loud. Our sample also comprises 1 (and possibly up to 3 considering the ROSAT lower limits on the absorption) highly luminous highly absorbed QSO.

acknowledgments

MA acknowledges N. Gehrels and the BAT team for hospitality, M. Capalbi for assistance during Beppo-SAX and Swift-XRT data analysis and N. Cappelluti for useful discussions on the source count distribution derivation. This research has made use of the NASA/IPAC extragalactic Database (NED) which is operated by the Jet Propulsion Laboratory, of data obtained from the High Energy Astrophysics Science Archive Research Center (HEASARC) provided by NASA's Goddard Space Flight Center, of the SIMBAD Astronomical Database which is operated by the Centre de Données astronomiques de Strasbourg, of the Sloan Digital Sky Survey (SDSS) managed by the Astrophysical Research Consortium (ARC) for the Participating Institutions and of the ROSAT All Sky Survey maintained by the Max Planck Institut für Extraterrestrische Physik.

Bibliography

Ajello, M., et al. , 2006, ATel, 697

Ajello M., et al. , 2007, in preparation

Alexander, D. M., Bauer, F. E., Brandt, W. N., et al. 2003, AJ, 126

Antonucci, R. R. J., 1993, ARA&A, 31, 473

Arnaud, K. A. 1996, in ASP Conf. Ser. 101, Astronomical Data Analysis Software and Systems V, ed. G. H. Jacoby & J. Barnes (San Francisco: ASP), 17

Avni, Y., &, Bahcall, J. N., ApJ, 235, 694

Barthelmy, S. D., et al. 2005, SSRv 120, 143

Bassani, L., Molina, M., Malizia, A., et al., 2006, ApJ, 636, 65

Bazzano, A., et al., 2006, ApJ 649, 9

Beckmann, V., et al. 2006, ApJ, 652, 126

Bird A. J., et al. 2006, ApJ 636, 765

Bolton J. G., et al. 1975, Aus. J. Phys. Ap. Suppl. 34, 1

Cappelluti, N., et al. 2007, ApJS NNN

Comastri, A., et al. 1995, A&A, 296, 1

Comastri A., 2004, in Barger A. J., ed., Astr. Space Sci. Libr. Vol. 308, 245

Crawford, C. S., & Fabian, A. C., 1995, MNRAS, 273, 827

den Hartog, P.R.,et al. 2004, ATel, 261, 1

Donato, D., et al., 2006, A&A 433, 1163

Fabian, A. C., Iwasawa, K., 1999, MNRAS 303, 34

Fenimore, E. & Cannon, T., 1978, Appl. Opt. 17, 337

Gallo, L. C., Lehmann, I., Pietsch, W., Boller, Th., Brinkmann, W., Friedrich, P. & Grupe, D., 2005, MNRAS, 365, 688

Gehrels, N., et al. 2004, ApJ 611, 1005

Giacconi, R., Gursky, H., Paolini, F. R., Rossi, B. B. 1962, Phys. Rev. Lett., 9, 439

Giacconi, R., et al. 2002, ApJS 139, 369

Gilli, R., Maiolino, R., Marconi A., et al., 2000, A&A, 355, 485

Gilli, R., et al. 2001, A&A, 366, 407

Gilli, R., Comastri, A. & Hasinger, G., 2006, submitted to A&A, astro-ph/0610939

Giommi, P., et al. 1991, ApJ 378, 77

Grandi, P., et al. 2006, ApJ, 642, 113

Götz, D., et al. 2006, A&A, 448, 873

Guainazzi, M., Matt, G. & Perola, G. C., 2005, A&A, 444, 119

Hasinger, G., et al. 1998, A&A, 392, 482

Hasinger. G. 2004, Nuc. Phys. B Proc. Supp., 132, 86

Jonker, P.G. et al. 2001, ApJ, 553, 335

Kennea, J. A., et al. 2005, ATel, 677, 1

Levine, A. M., et al. 1984, ApJS, 54, 581

Lutz., D., Maiolino, R., Spoon, H. W. W., et al. , 2004, A&A, 418, 465

Macomb, D.J., Gehrels N., 1999. ApJS, 120, 335

Malizia, A., et al. 2002, A&A, 394, 801

Masetti N., et al. 2006, ATel, 735, 1

Masetti, N., L. Morelli, E. Palazzi, et al. 2006, astro-ph/0608394

Markwardt, C. B., Tueller, J., Skinner, G. K., et al 2005, ApJ Lett., 633, L77

Marshall, F. E., et al. 1980, ApJ, 235, 4

Norton, A. J., et al. 2000, MNRAS, 312, 362

Piccinotti, G., et al., 1982, ApJ 253, 485

Rau, A., et al., Paper-2

Revnivtsev, M., et al., 2004, A&, 418, 927

Risaliti G., Maiolino R., & Salvati M., 1999, ApJ, 522, 157

Rosati, P., et al. 2002, ApJ, 566, 667

Sazonov, S., et al. 2006, in press, astro-ph/0608418

Szokoly, G., Bergeron, J., Hasinger, G., et al. 2004, ApJS, 155, 271

Schwope A., et al. 2000, Astron. Nachr. 321, 1

Schmidt, M., ApJ, 151, 393

Skinner, G. K., et al. 1987, Ap&SS, 136, 337

Slowikowska, A. et al., 26th Meeting of the IAU **2E** (2006), 8

Soldi, S., Beckmann, V., Bassani, L., et al., 2005, A&A, 444, 431

Sowards-Emmerd D., et al., 2004, ApJ, 609, 564

Steiner, J. E., et al. 1984, ApJ, 280, 688

Stephen, J. B., et al. 2006, A&A 445, 869

Strong, A. W., et al. 2004, A&A 411, 447

Strong, A. W., et al. 2005, A&A 444, 495

Revnivtsev et al. 2006, A&A 448, L49

Tozzi, P., Gilli, R., Norman, C., et al., 2006, A&A, 451, 457

Treister, E. & Urry, M., 2005, ApJ, 630, 115

Tueller, J., et al. 2005, ATel, 668, 1

Tueller, J., et al. 2005, ATel, 669, 1

Ueda Y, Akiyama M, Ohta K, Miyaji T., 2003, ApJ, 598, 886

Voges, W., et al., 1999, A&A, 349, 389

Wheatley P.J., et al. 2006, ATel, 765, 1

Wilks, S.S. 1938, Ann. Math. Stat., 9, 60

Worsley, M.A., et al. 2005, MNRAS 357, 1281

Zamorani, G., et al. 1981, ApJ, 245, 357

6.5 Notes on individual sources

We report a brief description of the source spectra for all new, or interesting, sources found in this analysis. All quoted errors are 90%.

PSR B0540-69.3 is a young rotation-powered pulsar recently detected up to 60 keV also by INTEGRAL (Götz et al., 2006; Slowikowska et al., 2006). The Pulsar is detected in BAT up to 200 keV and it is spectrum can be modeled as power law with photon index of 1.5 ± 0.21.

LMC X-1 is a well known black hole candidate. It is detected up to 200 keV with a steep photon index of 2.5 ± 0.2. The flux is a factor 2 lower than the one measured by INTEGRAL (Götz et al., 2006), suggesting variability.

LMC X-3 is high mass X-ray binary (HXB). The BAT spectrum is consistent with a power law whose photon index is 2.6 ± 1.

SWIFT J0917.2-6221 is a new hard X-ray source. We analyzed a 7 ks XRT observation of this source. The XRT and BAT data are well fit by an absorbed power law model whose photon index is $1.77^{+0.1}_{-0.07}$ and absorbing column density of $1.2^{+0.2}_{-0.16}$atoms cm^{-2}. A clear excess is present at energies <1 keV and this can be well described as a black body component peaking at 0.13 keV.

J0957.0-5847 is a new hard X-ray source detected in Ajello et al. (2007) The BAT spectrum can be modeled as a power law with photon index of 2.14 ± 0.8 in the energy range 14-200 keV.

V* TW PIC is a cataclysmic variable of the DQ Her type (Norton et al., 2000). The BAT spectrum is best fitted by a bremsstrahlung model with a plasma temperature of $13.5^{+10.6}_{-5.6}$ keV. The flux of 5.5×10^{-12}erg cm^{-2} s^{-1} in the 20-40 keV band is a factor 2 lower than the one reported in a recent INTEGRAL measurement (Götz et al., 2006) suggesting variability.

1 AXG J042556-5711 (also known as 1H 0419-577LB 1727, 1ES 0425-573 and IRAS F04250-5718) is a radio-quiet Seyfert galaxy which has been observed over recent years by ASCA, ROSAT, BeppoSAX and recently also by XTE (Revnivtsev et al., 2006). The ASCA and BAT data are well fit by a simple power law model with photon index of

1.6±0.02; the source is not detected above 70 keV.

4U 0919-54, detected at very high significance, is a LXB also known to produce X-ray bursts (Jonker et al., 2001). Its spectrum is characterized by a steep photon index of 2.35 ± 0.25, alternatively a bremsstrahlung model with a plasma temperature of 36.2±18keV yields a better χ^2.

Pictor A is a radio-loud Sy1 galaxy initially detected in X-ray by the EINSTEIN observatory. The spectrum is characterized by a hard power law photon index of 1.6 ± 0.26 extending up to 200 keV. A recent analysis of Beppo-SAX data (Grandi et al., 2006) in the 2-10 keV band finds the same photon index of 1.6. The extrapolation of the BAT flux to the 2-10 keV band is in very good agreement with the Beppo-SAX analysis, thus pointing in favor of an unbroken power law spectrum extending from 2 to 200 keV.
ASCA data are available for this source and a joint BAT-ASCA fit determines that this source shows an absorption level of 1.2×10^{21}atoms cm^{-2} slightly in excess of the galactic one (4×10^{20} atoms cm^{-2}).

Vela PSR has a spectrum consistent with a power law whose photon index is 1.4±0.2.

J0405.8-4345 is a new hard X-ray source detected in Ajello et al. (2007). A fit to BAT data with a simple power law model does not yield satisfactory results (reduced $\chi^2 >$2.2). A bremsstrahlung model with a temperature of fits the data better ($\chi^2 >$1.6).
The best model fitting the data is either an absorbed power law with a high energy cutoff and photon index fixed at the typical AGN value of 2 or alternatively a very steep (photon index of $3.8^{+2.7}_{-1.5}$) absorbed power law. In both cases the source is obscured by an extremely large column density of $2.5^{+4.2}_{-1.7} \times 10^{26}$atoms cm^{-2}. The F-test for the absorbed power law model, to respect the simple power law model, yields a probability of 3% of the absorbed model to be spurious.

J0447.8-4112 is a new hard X-ray source detected in Ajello et al. (2007). Its spectrum can be modeled as a simple power law with photon index of 2.5±0.7.

4U 0513-40 is a low mass X-ray binary detected in X-rays by EXOSAT (Giommi et al., 1991). The BAT spectrum can be fit by a single power law model whose photon index is 2.1±0.3.

J0837.1-3912 is a new hard X-ray source detected in (Ajello et al., 2007). Its spectrum

can be modeled as a single power law with a photon index of 2.0±0.4.

IGR J07597-3842 is a source first detected by INTEGRAL in the VELA region (den Hartog et al., 2004). It was identified as being a Sy1.2 (Masetti el al., 2006b). This source was also observed by XRT and when jointly fitting XRT and BAT data we get that the best fit is an absorbed power law with photon index of 1.9 ± 0.05 and column density of 6.4×10^{21}atoms cm^{-2}.

LEDA 75476, also known as 3A 0557-383, EXO 055620-3820.2 and CTS B31.01, is a Sy1 galaxy. The BAT spectrum is consistent with a power law model with photon index of 2.0 ± 0.4. The ASCA and BAT are well fit by an absorbed power law model with photon index of 1.7±0.05 and absorbing column density of $2.2^{+0.27}_{-0.14} \times 10^{22}$atoms cm^{-2}. A clear excess below 2 keV is detected in the ASCA data and this can be modeled as a black body component with a temperature of $0.25^{+0.08}_{-0.05}$ keV. A Fe K_α line is also required by the fit (F-test yielding a probability of the line being spurious of 10^{-8}) and its equivalent width is 0.132 keV. The reduced χ^2 of the overall fit is 1.1.

ESO 362-G021 is a BL Lac object. ASCA and XRT data are available for this source. The best fit to ASCA, BAT and XRT data is an absorbed power law with photon index of 1.7±0.03 and column density of $1.0 \pm 0.1 \times 10^{21}$atoms cm^{-2} which is larger than the galactic absorption in that region of the sky (3×10^{20}atoms cm^{-2}).

FRL 1146 is a Sy1 galaxy detected in hard X-ray by INTEGRAL (Bird et al., 2006). The BAT spectrum is characterized by a power law with photon index of 2.15 ± 0.42 extending up to 200 keV. The flux is in agreement with the INTEGRAL measurement. FRL 1146 was also detected in the ROSAT all-sky survey at 12 count/s, considering the extrapolation of the BAT power law to the ROSAT band yields ∼8 counts/s so it is very likely that the source in unabsorbed.

J0446.2-3537 is a new hard X-ray source detected in Ajello et al. (2007). The BAT spectrum is consistent with a power law model with photon index 2.15 ± 1.1.

J0844.9-3531 is a new hard X-ray source detected in Ajello et al. (2007). The BAT spectrum is consistent with a power law model with photon index 1.66 ± 0.7.

TV Col is a DQ Her type cataclysmic variable already detected at soft and hard X-rays. A power law fit to the BAT spectrum does not yield acceptable results instead a

bremsstrahlung model with a plasma temperature of 28.2 ± 0.5 keV fits the data well.

ESO 362- G 018 is a Sy1 galaxy detected at hard X-ray by BAT (Tueller et al., 2005). The BAT spectrum is consistent with a power law model with photon index of 1.8 ± 0.2, however when jointly fitting BAT and XRT data the best fit is the sum of a power law model (photon index 1.5 ± 0.03) and a black body component with a temperature of 3 ± 0.6 keV. The source is unabsorbed.

PKS 0548-322 is a well known blazar already detected in hard X-rays (see for example Donato et al., 2006). For this source, Swift-XRT data are also available in the range 0.2-10 keV. A joint spectrum of XRT and BAT data with an absorbed power law model yields a photon index of 1.78 ± 0.03 and an absorption of $4. \times 10^{20}$ atoms cm^{-2} slightly in excess of the galactic one.

J0739.6-3144 is a newly discovered hard X-ray source (Ajello et al., 2007), recently identified as a Sy2 galaxy (Rau et al., 2007). A simple power law fit to the BAT spectrum yields a photon index of 1.78 ± 0.5. However the reduced χ^2 is 1.46. If we try an absorbed power law model, both column density and the photon index are not well determined. If we fix the photon index in the range of 2, we get a column density of 1×10^{25} atoms cm^{-2}. We also estimated the lower limit on the absorbing column density considering the non-detection by ROSAT; this limit is $\sim 2 \times 10^{22}$ atoms cm^{-2}.

ESO 434-G 040 is a known Sy2 galaxy recently detected in hard X-rays also by INTEGRAL (Bird et al., 2006). A joint fit to ASCA, XRT and BAT data with an absorbed power law model yields a photon index of $1.75^{+0.016}_{-0.018}$ and a column density of $1.5 \pm 0.026 \times 10^{22}$ atoms cm^{-2}. A clear excess below 2 keV can be modeled as a black body component with a temperature of $0.13^{+0.011}_{-0.016}$. An Iron K_α line, with an EQW=85.5^{+27}_{-33}, is also detected. The probability of the line being spurious is $\sim 10^{-14}$.

PKS 0537-286 at z=3.1 is one of the most luminous high-redshift quasar. Recognized first as a radio source (Bolton et al., 1975) it was discovered in X-rays by the Einstein observatory (Zamorani et al., 1981) and then studied by ROSAT, ASCA and lately by XMM. The BAT detection in hard X-rays is the first to date, however there is a claim that PKS 0537-286 be the MeV counterpart of the EGRET source 3EG J0531-2940 (Sowards-Emmerd et al., 2004). A joint spectral fit to XRT and BAT data reveals an exceptionally hard spectral slope of 1.35 ± 0.1 and a Fe K_α line redshifted at ~ 1.4 keV.

V* V441 Pup is a high mass X-ray binary where the companion was optically identified as a Be star. The BAT spectrum is very steep and it can either be fitted by a power law with a photon index of 4.5±1.5 or by a bremsstrahlung model with a plasma temperature of 6.8 ± 5 keV.

ESO 490-G 26 is a Sy1.2 galaxy. We have analyzed XRT data for this source. When we perform a joint XRT-BAT fit we get that the source spectrum can be described as a power law with photon index of 1.74±0.1 and an intrinsic, in addition to the galactic, absorption of 2. $\pm 0.5 \times 10^{21}$ atoms cm^{-2}.

J0902.4-2418 has a spectrum not consistent with a simple power law model ($\chi^2 > 2.4$). Trying a fit with an absorbed power law model we get that the source is obscured by Compton-thick matter (being the probability of this obscuration to be spurious 10%) and has a steep photon index of 3.3. Freezing the absorbing column density at 1.5 $\times 10^{24}$ atoms cm^{-2} yields an error on the photon index of ±0.8.

J0727.5-2406 has a spectrum consistent with a power law model with photon index of 1.6 ± 0.4.

SWIFT J0505.7-2348, also know as XSS J05054-2348 (Revnivtsev et al., 2006) was identified as a Sy2 galaxy by Rau et al. (2007). When combining both XRT and BAT data for this source we get an intrinsic, rest frame, absorption of $6.3 \pm 1.3 \times 10^{22}$ atoms cm^{-2} and a photon index of $1.92^{+0.16}_{-0.13}$.

NGC 3081 is mis-catalogged in SIMBAD as Sy1 galaxy. In fact the available 6dF spectrum shows clearly that this object is a Sy2 object. We have analyzed BeppoSax-MECS and ASCA data for this source. The best fit is a sum of a black body component, peaking at 0.6 keV, an absorbed power law with column density of $6 \pm 0.5 \times 10^{23}$ atoms cm^{-2} and photon index $1.74^{+0.16}_{-0.08}$ and an Iron line of equivalent width (EW) of 241^{+184}_{-131} eV.

J0418.6-1847 is a new source of Ajello et al. (2007). The BAT spectrum is consistent with a power law model whose photon index is $2.55^{+1.45}_{-0.87}$.

NGC 2992 is a Sy 1.9. The best fit for combined XRT and BAT data is an absorbed power law with photon index of 1.20±0.05 and intrinsic hydrogen column density of $1.5^{\pm 0.37} \times 10^{21}$ atoms cm^{-2}. We also detected the presence of an unresolved Fe K_α line whose equivalent width is $0.52^{+1.0}_{-0.1}$ keV in agreement with an old Beppo-Sax measure-

ment (Gilli et al., 2001) where the reported column density is 1×10^{22}atoms cm^{-2}.

SWIFT J0732.5-1331 was detected for the first time by BAT in hard X-rays (Ajello et al., 2006a). It was then identified as a new intermediate polar (Wheatley et al. 2006 and references therein). The BAT spectrum is consistent with a power law with photon index 2.3 ± 0.3.

3C 206 is a narrow line, radio loud, QSO detected for the first time in hard X-rays ($>$20 keV). The BAT spectrum when fitted with a pure power law model gives a reduced $\chi^2 > 1.5$. We tried a fit using an absorbed power law model and we got a photon index of $3.4^{+1.8}_{-0.9}$ and an absorbing column density of $8.2^{+7.6}_{-6.7}\times10^{24}$ atoms cm^{-2}. The F-test yields a probability of the absorption being fake of 0.08. 3C 206 was detected by the ROSAT PSPC with 0.37 ct s^{-1} during the all-sky survey (Voges et al., 1999); if we use the BAT power law spectrum and we extrapolate it to the 0.1-2.4 keV band, we get that an intrinsic absorbing column density of at least 5×10^{22} atoms cm^{-2} is required to match the observed ROSAT count rate. Lawson & Turner (1997) report a detection of 3C 206 by GINGA in the 2-10 keV; even though they quote the source to be unobscured, the minimum absorbing column density needed to match, by extrapolation of the BAT fit, the observed GINGA count rate is $\sim10^{23}$ atoms cm^{-2}. Thus, 3C 206 is a candidate highly obscured QSO.

J0722.6-0931 is a new hard X-ray source detected by BAT (Ajello et al., 2007). Its spectrum is consistent with a power law with a photon index of $2.1^{+2.51}_{-1.2}$.

MCG -01-24-012 is a Sy2 galaxy already detected in hard X-rays by BEPPO-SAX (Malizia et al., 2002). When fitting both XRT and BAT data we get that the spectrum is consistent with an absorbed power law whose photon index is 1.90 ± 0.14 and intrinsic absorption is 6.6 ± 0.5 atoms cm^{-2}.

NGC 2110 is a well known Sy2 galaxy. The BAT, ASCA and XRT data can be fit by an absorbed power law model with photon index of 1.7 ± 0.2 and hydrogen column density of $3.8^{+0.18}_{-0.16}\times10^{22}$ atoms cm^{-2}. We also detected an unresolved Fe K_α of equivalent width of $155.^{+82}_{-80}$ eV.

SWIFT J0823.4-0457 is a source detected for the first time in hard X-rays by BAT and associated, during an XRT follow-up, with the galaxy FAIRALL 0272 (Ajello et al., 2007). An optical follow-up showed that the source is a Sy2 (Masetti et al., 2006a). XRT and

BAT data are best fit by a highly absorbed power law. The photon index is $1.76^{+0.21}_{-0.18}$ and the absorbing column density is $21.2^{+6.7}_{-5.4}$atoms cm^{-2}.

MCG -01-13-025 is a Sy1.2 (in NED, but Sy1 in SIMBAD) galaxy detected in soft X-rays by ROSAT (Voges et al., 1999). The BAT spectrum is consistent with a power law with photon index of $1.8^{+0.74}_{-0.64}$ and it extends up to 200 keV.

QSO B0513-002 is a Sy1 galaxy. The BAT spectrum can be fitted by a power law with photon index of 1.86 ± 0.4.

J0834.6+0217 is a new source detected by BAT (Ajello et al., 2007). The BAT spectrum is consistent with a power law whose photon index is 1.57 ± 0.5.

3C 105.0 is a Sy2 galaxy. The BAT and XRT data can be fitted by an absorbed power law model with photon index of $1.6^{+0.1}_{-0.3}$ and hydrogen column density of $3.1\pm8\times10^{23}$ atoms cm^{-2}.

UGC 4203 is a Sy2 galaxy. We have analyzed ASCA and XRT data for this source. The best fit to ASCA, XRT and BAT data is an absorbed power law model, with photon index of $2.0^{+0.45}_{-0.42}$ and N_H=$15.1^{+6.18}_{-4.19}\times10^{22}$ atoms cm^{-2} and a black body component with a temperature of $0.3^{+0.08}_{-0.05}$ keV. Moreover we detected the presence of an Iron line whose equivalent width is $0.83^{+1.1}_{-0.6}$ keV.

3C 120 is a Sy1 galaxy. This source was observed by ASCA. The best fit to ASCA and BAT data is an absorbed power law model with absorption consistent with the galactic one and photon index $1.80^{+0.04}_{-0.04}$ and a black body component with a temperature of $0.27^{+0.026}_{-0.025}$.

J0959.3+0550 is a new source detected in Ajello et al. (2007). The BAT spectrum is consistent with a power law model with photon index of $1.9^{+1.3}_{-1.0}$.

3C 227 is a Sy1 galaxy and also a Radio galaxy. The spectrum is not significant above 70 keV. Below this energy it is consistent with a power law model of photon index $1.37^{+0.42}_{-0.55}$. This source was detected at a level of 0.016 ct s^{-1} in a 11 ks long ROSAT-PSPC observation (0.1–2.4 keV) (Crawford & Fabian, 1995). In order to match the ROSAT observed count rates, the extrapolation of the BAT power law to the 0.1–2.4 keV band requires an absorbing column density of at least 1×10^{22} atoms cm^{-2}.

J0811.5+0937 is a new BAT source detected in Ajello et al. (2007). The BAT spectrum is consistent with a power law with photon index of $2.2^{+2.1}_{-0.9}$. Rau et al. (2007) identified RX J081132.4+093403 as possible counterpart. Optical spectroscopy revealed that this source is a candidate X-ray Bright Optically Normal Galaxy (XBONG). If we extrapolate the BAT power law to the ROSAT-PSPC energy band (0.1–2.4 keV) we get that, in order to match the observed 0.035 ± 0.004 ct s^{-1}, the source is required to be absorbed by an intrinsic column density in the range $N_H = 10^{22} - 10^{23}$ H-atoms cm^{-2}.

V* BG CMi is a well known intermediate polar. The BAT spectrum is consistent with a power law with photon index of $1.34^{+3.4}_{-1.4}$.

J0923.3+1024 is a new X-ray source detected in Ajello et al. (2007). The BAT spectrum is not consistent with a power law model. Instead we got a good fit with a bremsstrahlung model with a plasma temperature of $10.6^{+17.2}_{-4.3}$keV.

J0847.4+1219 is a new X-ray source found in Ajello et al. (2007). The best fit to BAT data is a bremsstrahlung model with plasma temperature of $24.0^{+26.3}_{-11.3}$keV.

J0528.0+1435 is a new source found in Ajello et al. (2007). The BAT spectrum cannot be fitted by a simple power law model($\chi^2_{red} > 2.7$). If we use an absorbed power law model we get a photon index of $3.7^{+3.0}_{-1.5}$ and a column density of $2^{+1.9}_{-1.2} \times 10^{26}$ atoms cm^{-2} with a $\chi^2_{red} = 1.1$. The F-test yields a probability of 11% of the absorbed model to be spurious.

J0854.7+1502 is a new hard X-ray source detected in (Ajello et al., 2007) and identified in Rau et al. (2007) as a Sy2 galaxy. It has a very flat spectrum which can be modeled as a power law with photon index 1.34 ± 0.7. A lower limit on the absorbing column density of 5×10^{21} atoms cm^{-2} can be derived by the non-detection of this source in the ROSAT all-sky survey.

Mrk 0704, or SWIFT 0918.5+1618, is another source found thanks to our algorithm (Ajello et al., 2007). During an XRT followup, the galaxy Mrk 704 was found as the BAT counterpart. Mrk 704 was previously detected in soft X-rays by ROSAT (Schwope et al., 2000). In a recent optical followup, the galaxy was found to be a Sy1 (Masetti et al., 2006a). We have analyzed ASCA, XRT and BAT data for this source. The best fit to the three datasets is a a partial covering model where the covering fraction is 0.5 and the power-law photon index is $1.36^{+0.07}_{-0.1}$. The source is highly absorbed with a column

density of $1.4^{+0.6}_{-0.3} \times 10^{23}$ atoms cm^{-2}. We also detected an Iron line whose equivalent width is 160eV.
However the spectral slope is very hard if compared to the typical photon index 2 of other BAT AGN; moved by this consideration we also tried a reflection model (pexrav in Xspec) with photon index and energy cutoff fixed at the usual AGN value of 1.9 and 300 keV respectively. We got that the model fits the data well and the source is required to be completely reflected thus being a Compton-thick object. Longer and more sensitive soft X-ray observations will clarify the real nature of this intriguing object.

CSV 6150, also known as IRAS 05078+1626, is cataloged as Sy1 in Simbad and as Sy1.5 in NED. The BAT spectrum can be fitted with a power law with photon index of 2.15 ± 0.2.

J0517.1+1633 is a new hard X-ray source (Ajello et al., 2007). The BAT spectrum is best fit by a power law model with photon index of $3.17^{+0.7}_{-0.5}$.

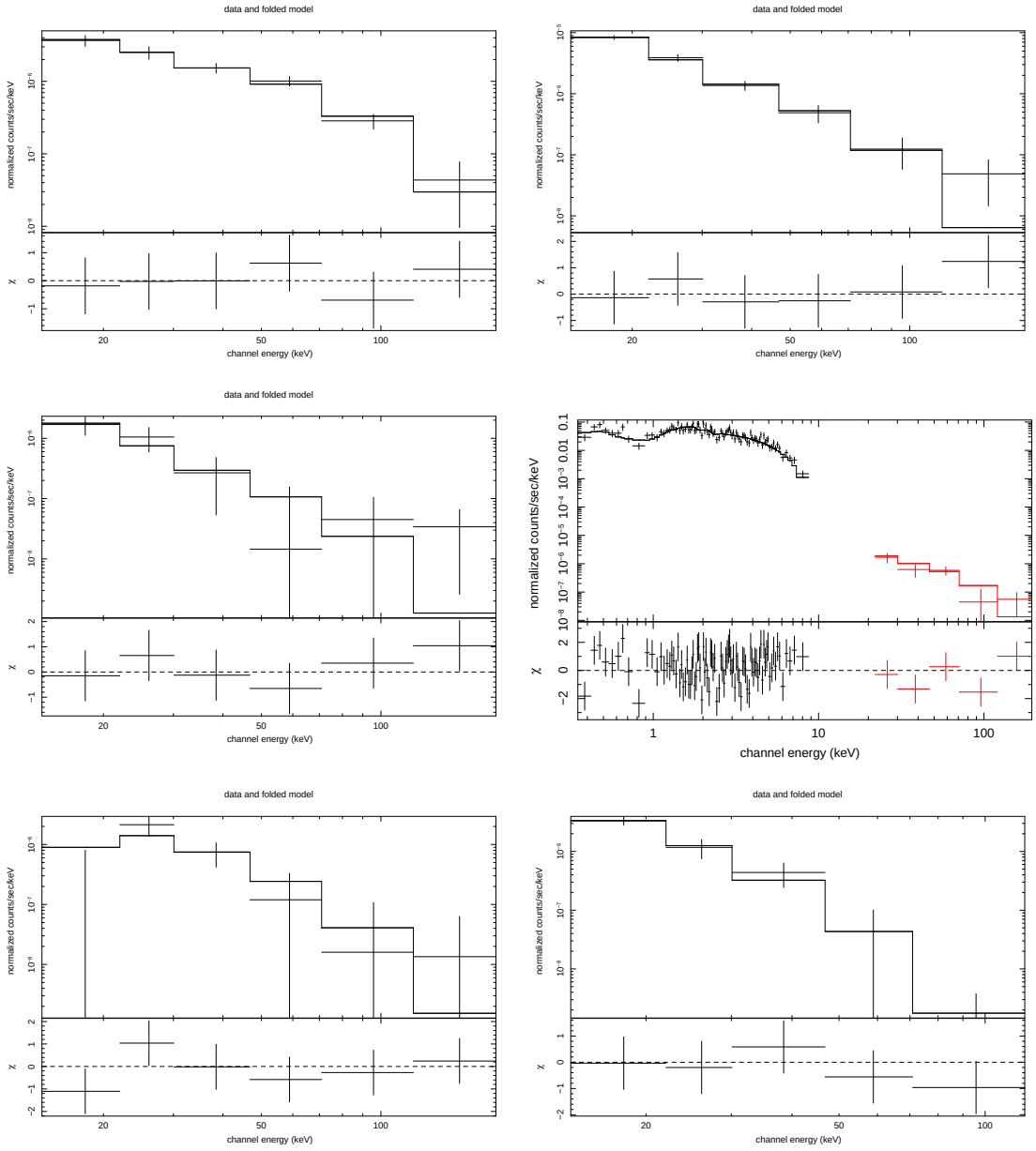

Figure 6.9: Folded spectra and best fit models as described in the text. From left to right and up to bottom the spectra are for: PSR B0540-69.3, LMC X-1, LMC X-3, LEDA 90443, J0957.0-5847 and V* TW Pic.

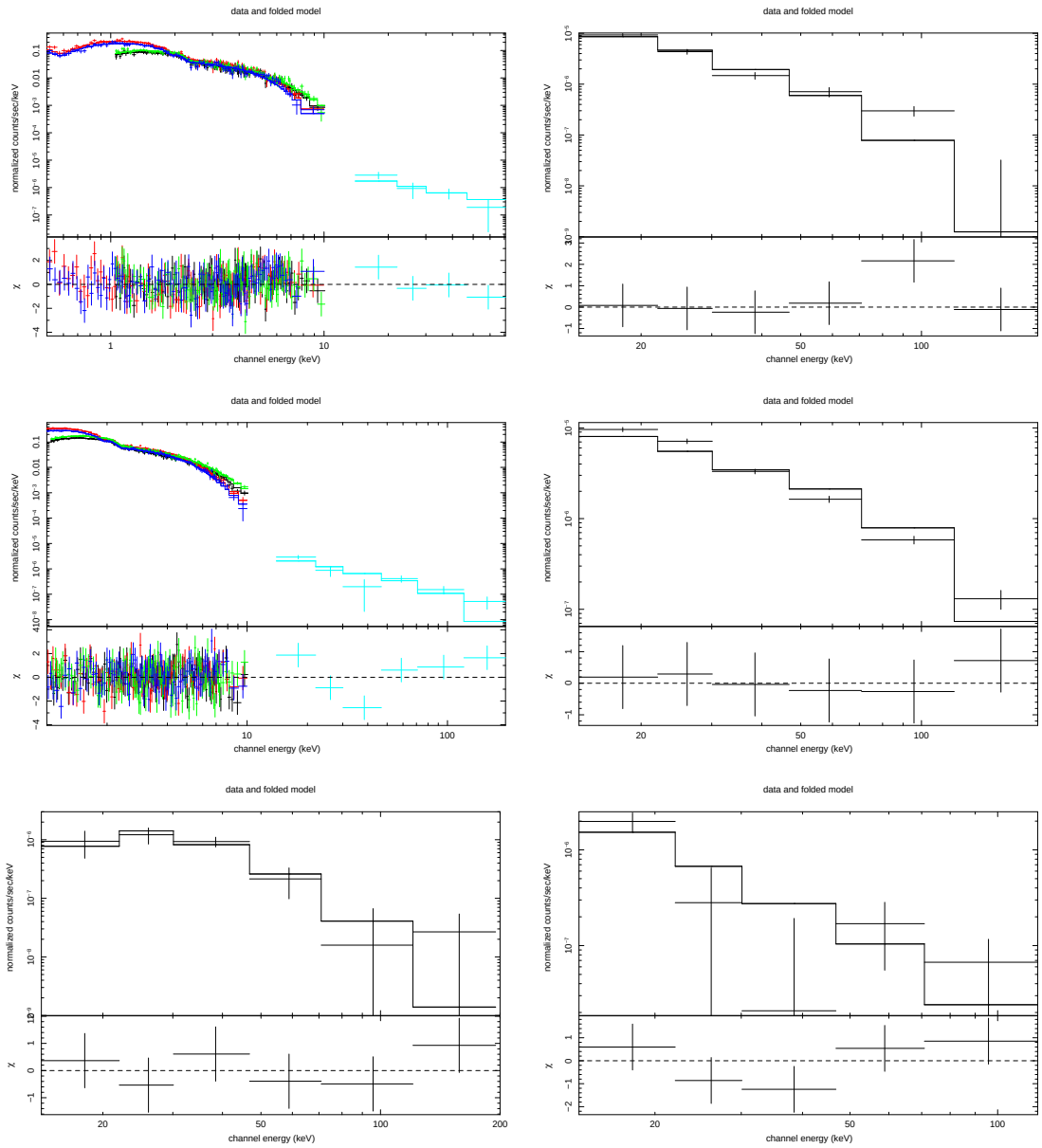

Figure 6.10: Folded spectra and best fit models as described in the text. From left to right and up to bottom the spectra are for: 1 AXG J042556-5711, 4U 0919-54, Pictor A, Vela PSR, J0405.8-4345 and J0447.8-4112.

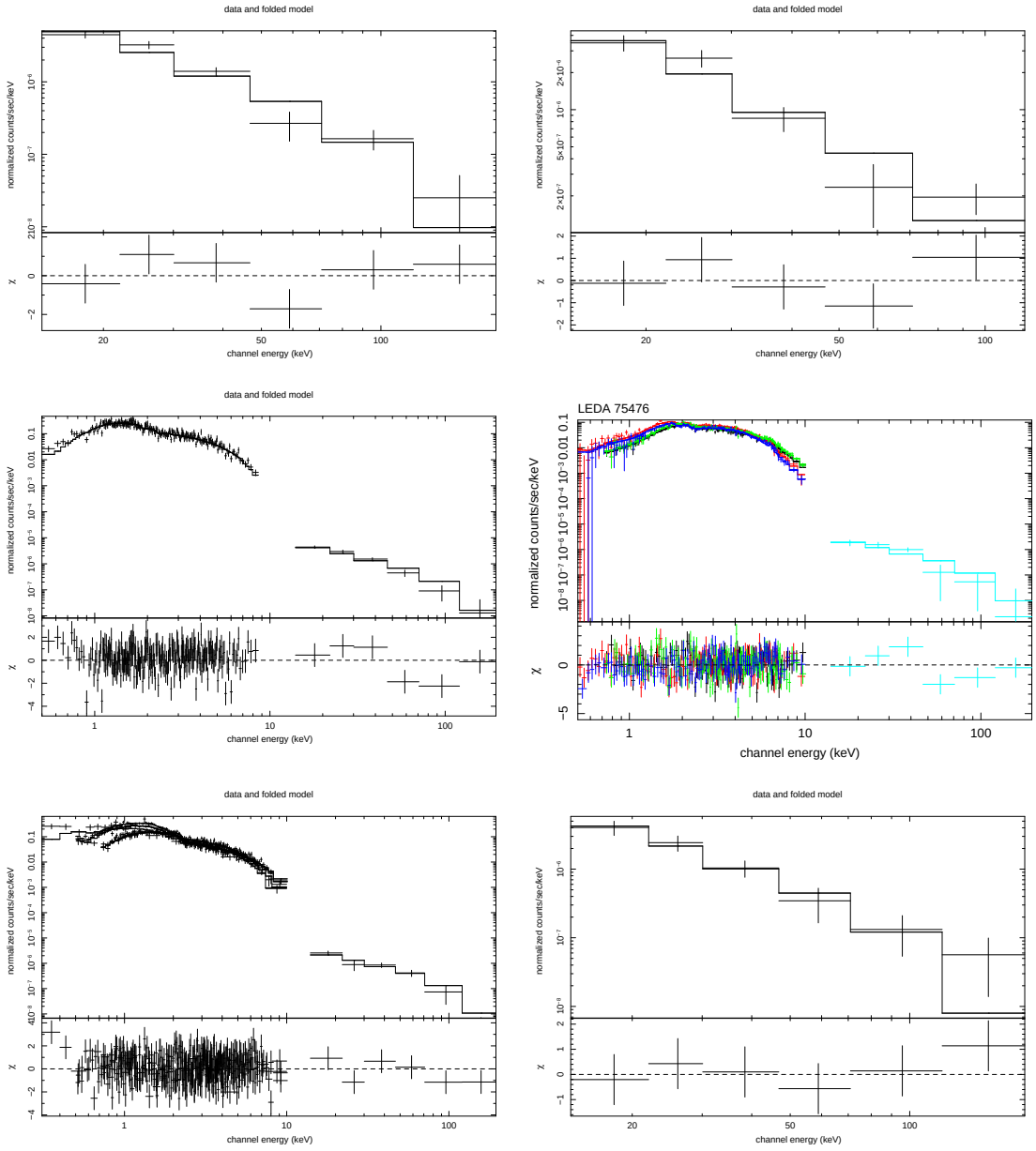

Figure 6.11: Folded spectra and best fit models as described in the text. From left to right and up to bottom the spectra are for: 4U 0513-40, J0837.1-3912, IGR 07597-3842, LEDA 75476,, ESO 362-G021 and FRL 1146.

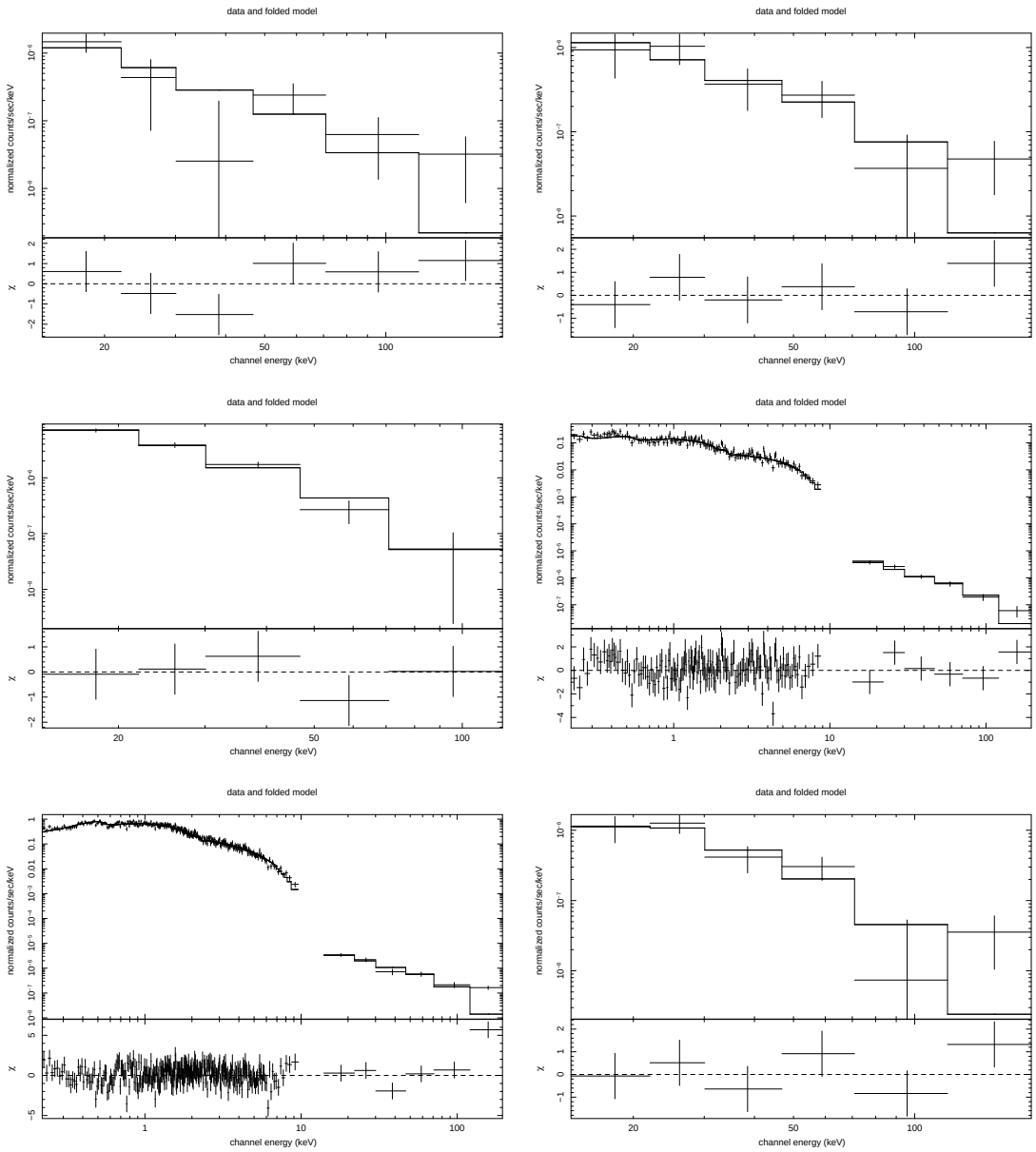

Figure 6.12: Folded spectra and best fit models as described in the text. From left to right and up to bottom the spectra are for: J0446.2-3537, J0844.9-3531, V* TV Col, ESO 362-G018, PKS 0548-322 and J0739.6-3144.

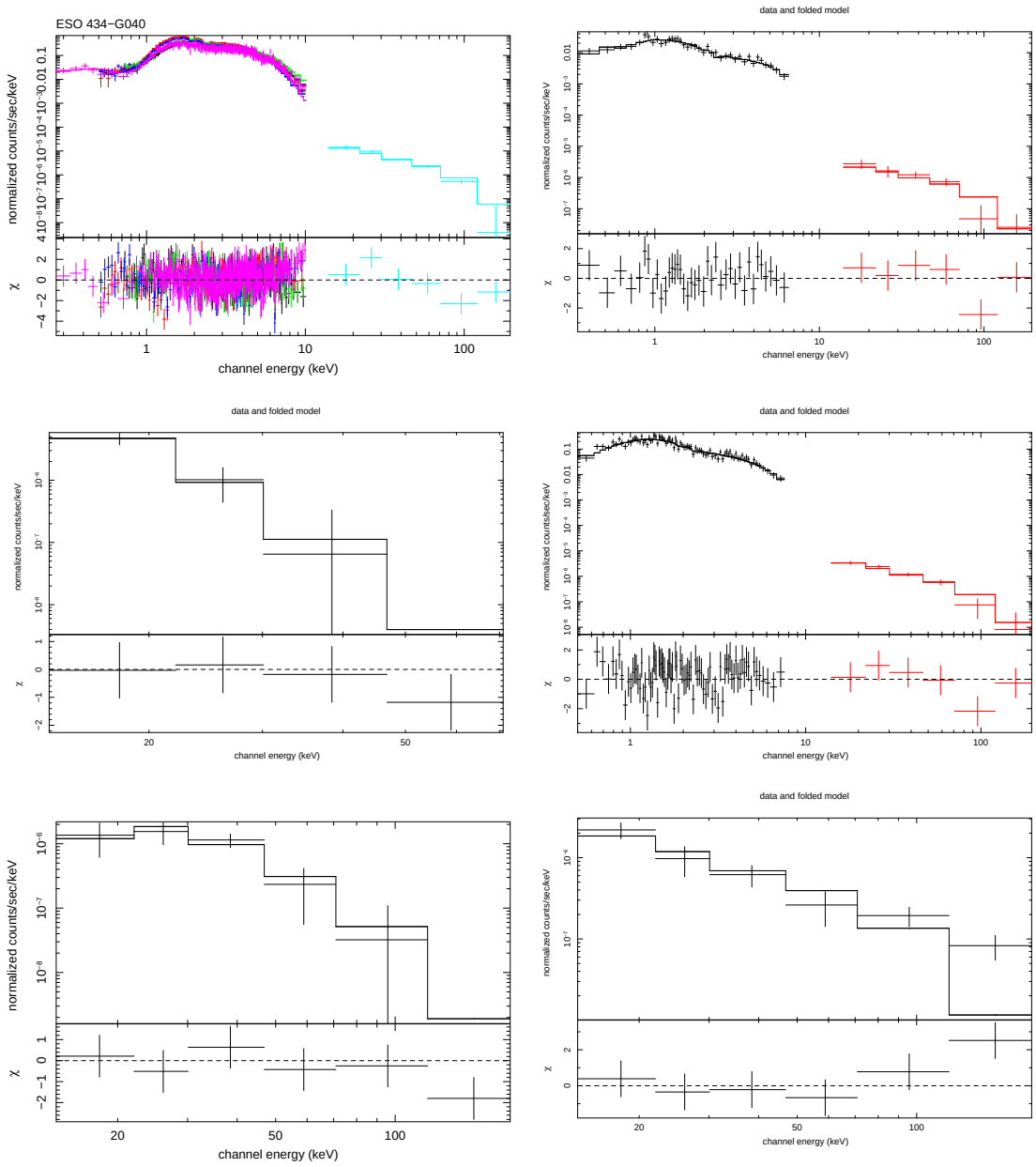

Figure 6.13: Folded spectra and best fit models as described in the text. From left to right and up to bottom the spectra are for: ESO 434-G018, PKS 0537-286, V* V441 Pup, ESO 490-G26, J0902.4-2418 and J0727.5-2406.

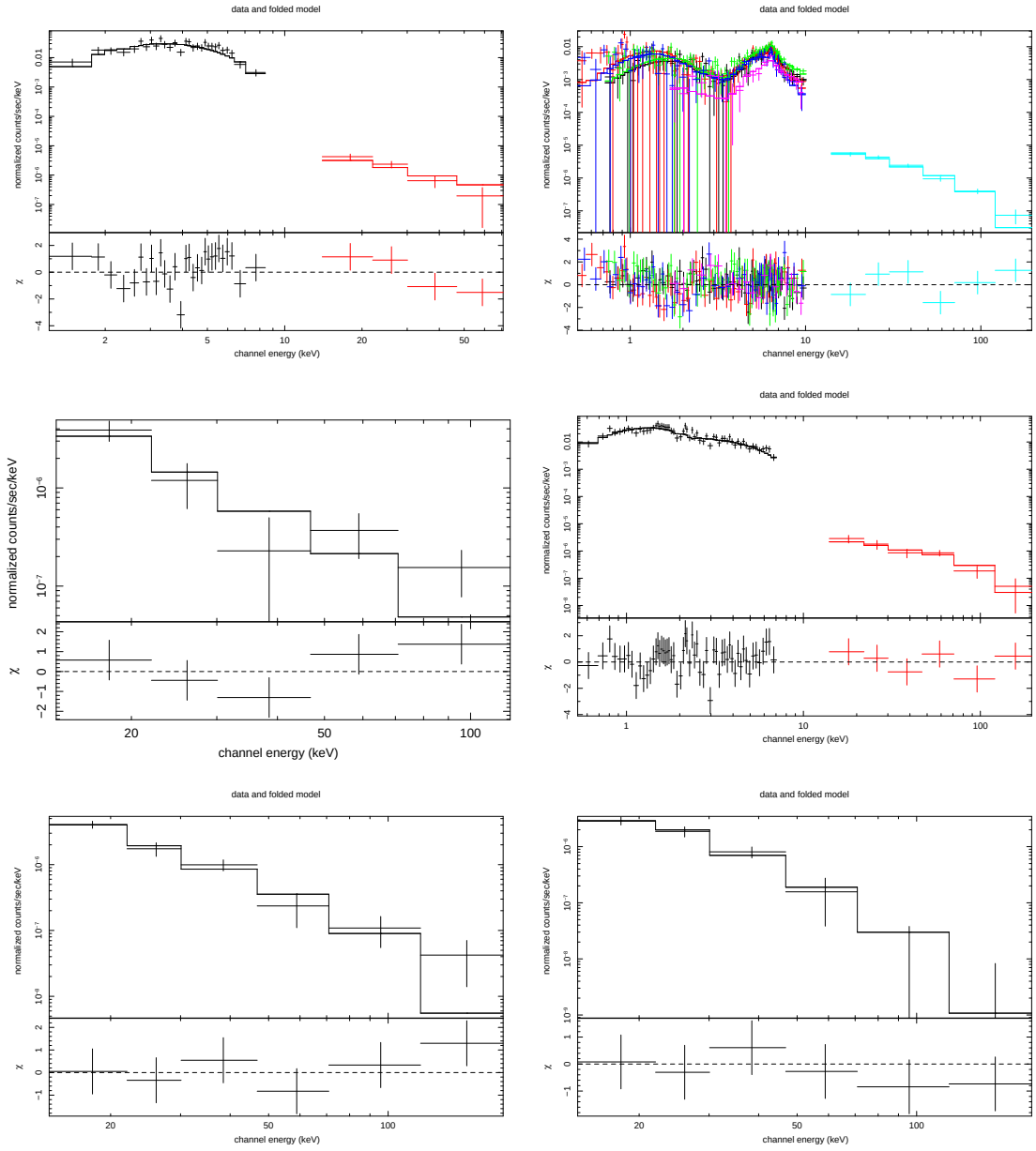

Figure 6.14: Folded spectra and best fit models as described in the text. From left to right and up to bottom the spectra are for: SWIFT J0505.7-2348, NGC 3081, J0418.6-1847, NGC 2992, SWIFT J0732.5-1331 and 3C 206.

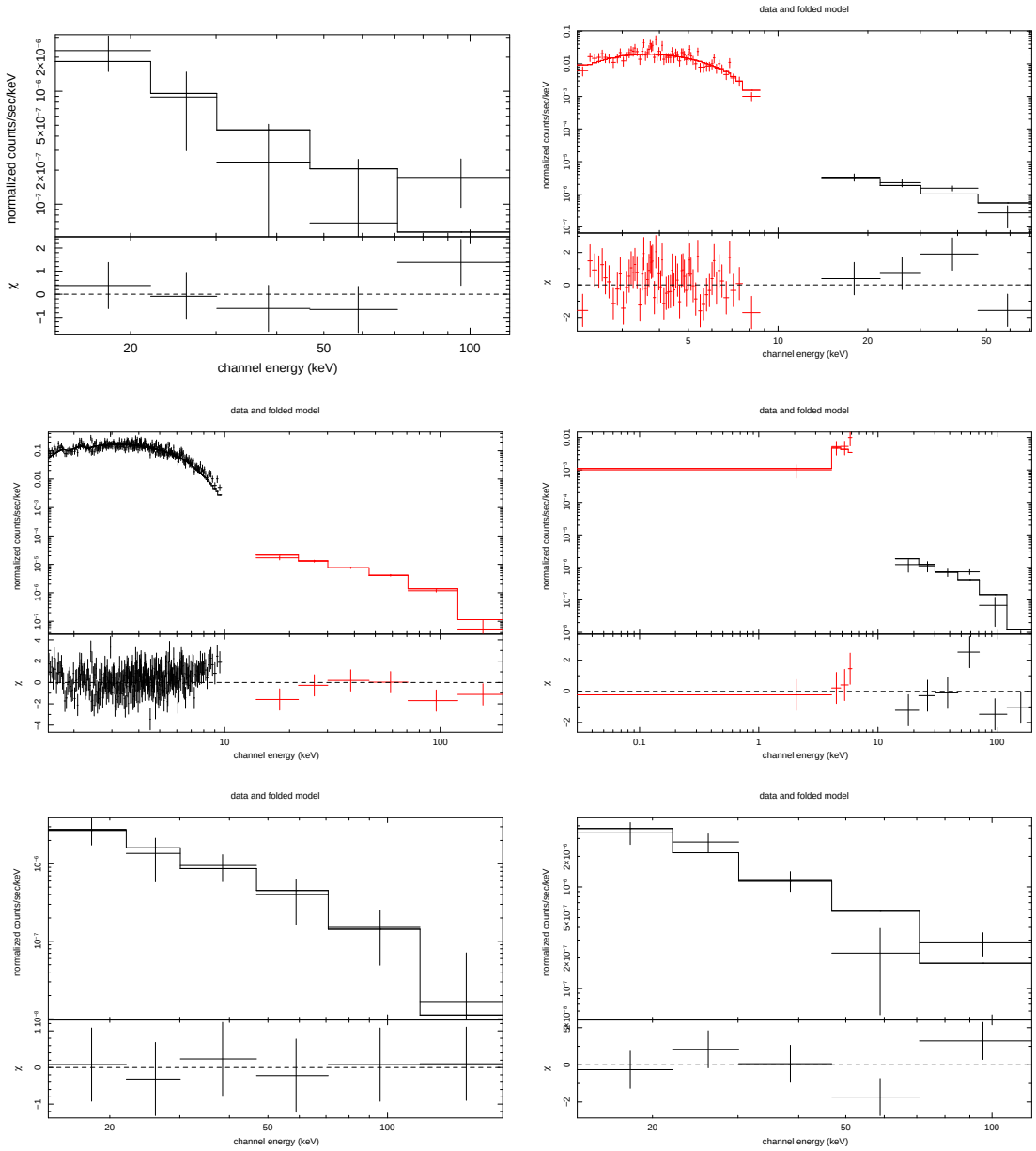

Figure 6.15: Folded spectra and best fit models as described in the text. From left to right and up to bottom the spectra are for: J0722.6-0931, MCG -01-24-012, NGC 2110, SWIFT J0823.4-0457, MCG -01-13-025 and QSO B0513-002.

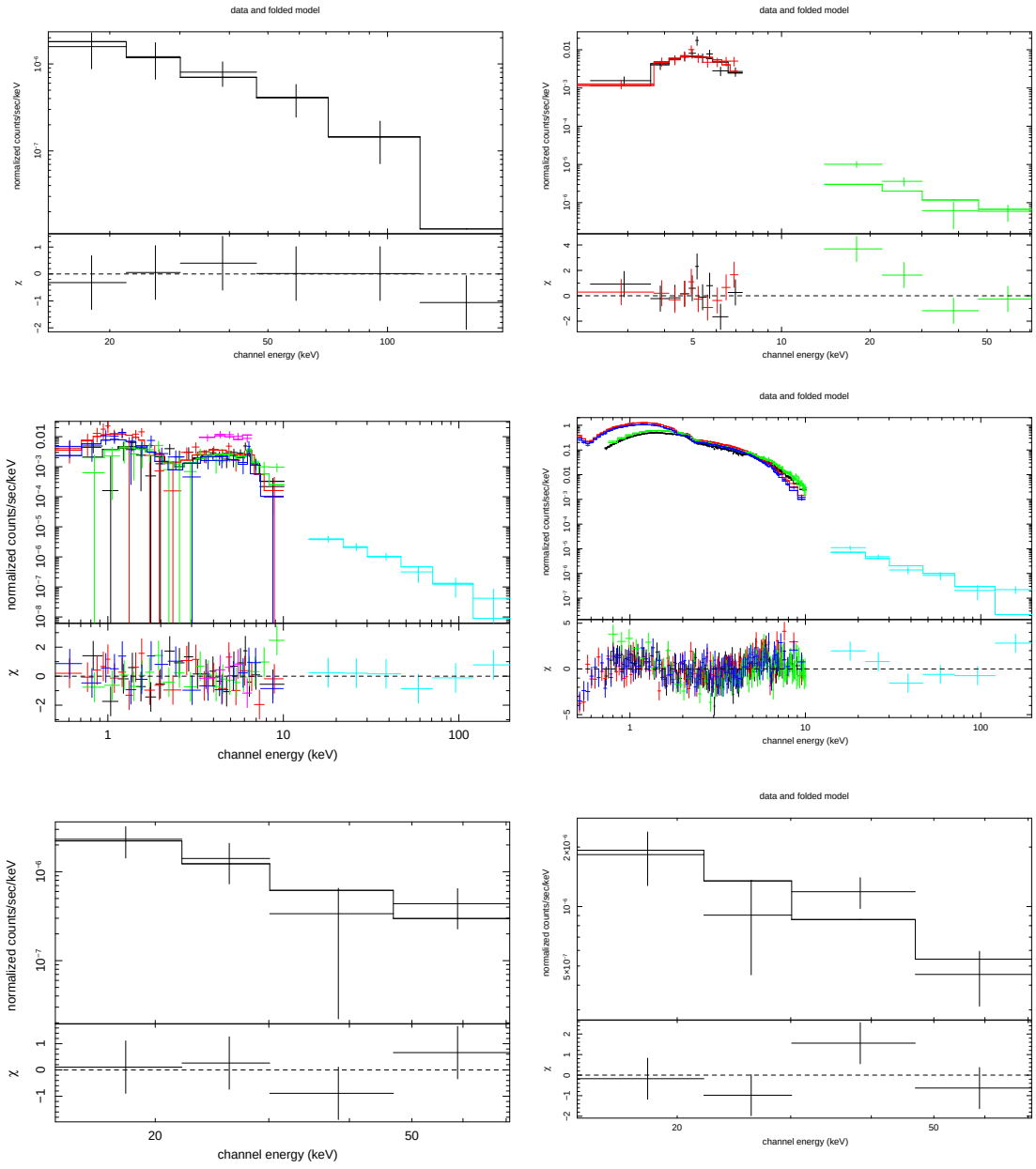

Figure 6.16: Folded spectra and best fit models as described in the text. From left to right and up to bottom the spectra are for: J0834.6+0217, 3C 105.0, UGC 4203, 3C 120, J0959.3+0550 and 3C 227.

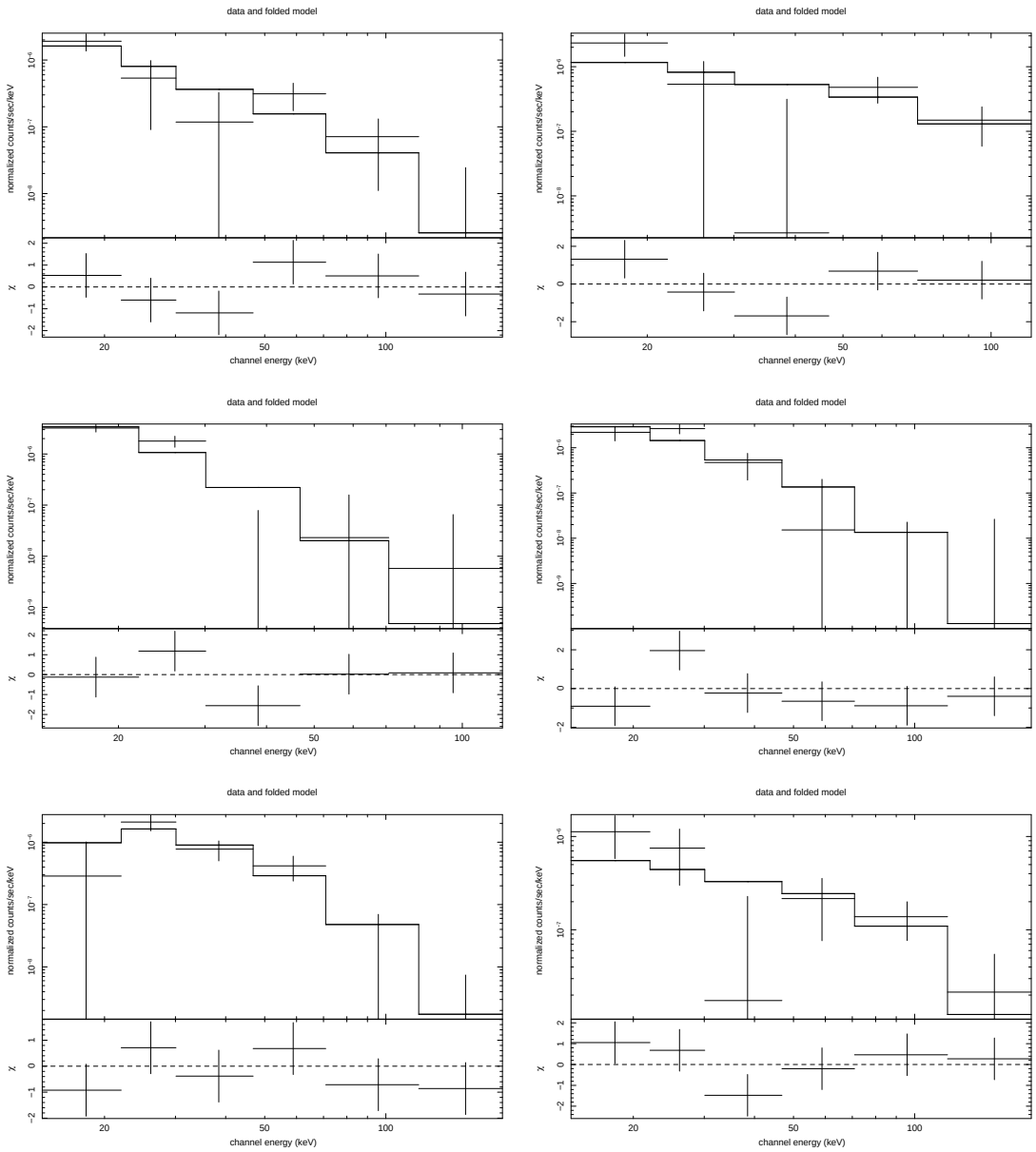

Figure 6.17: Folded spectra and best fit models as described in the text. From left to right and up to bottom the spectra are for: J0811.5+0937, V* BG CMi J0923.3+1024, J0847.4+1219, J0528.0+1435 and J0854.7+1502.

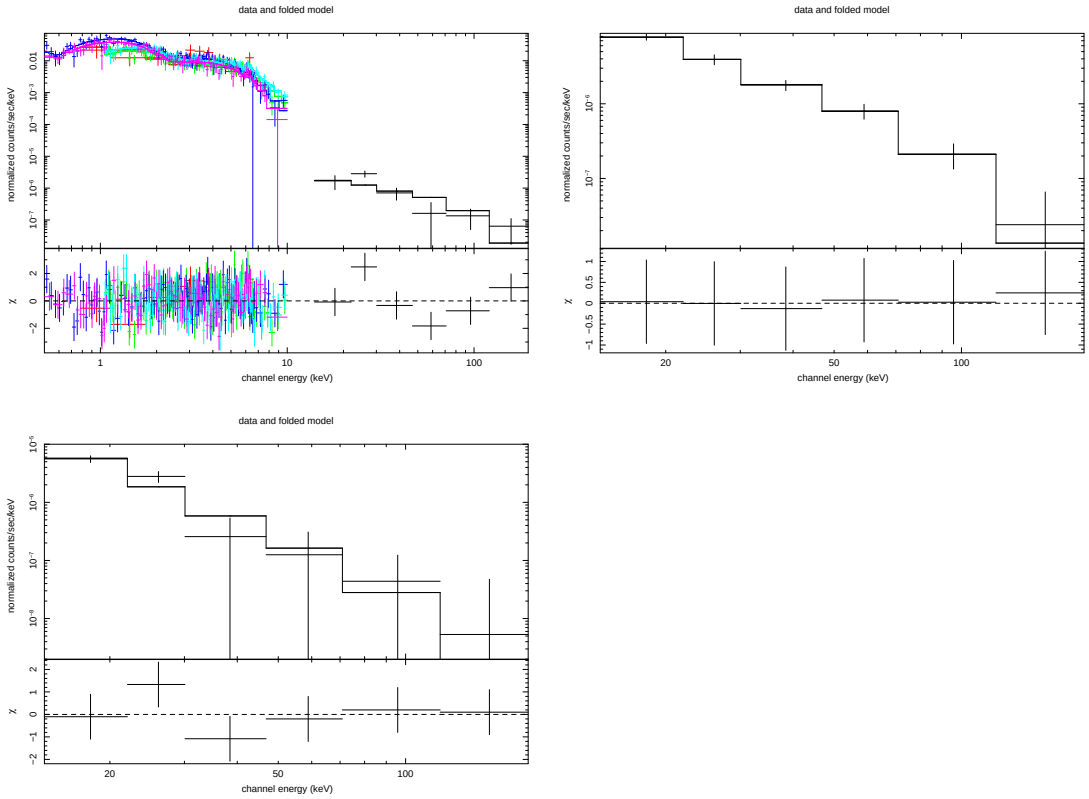

Figure 6.18: Folded spectra and best fit models as described in the text. From left to right and up to bottom the spectra are for: Mrk 704, CSV 6150 and J0517.1+1633.

Chapter 7

Swift/BAT measurements of the X-ray background and Earth's Atmospheric Spectra

M. Ajello, D. Willis, J. Greiner, G. Kanbach, and A. W. Strong

7.1 Introduction

There is a general consensus that the cosmic X-ray background (CXB), discovered more than 40 years ago (Giacconi et al., 1962), is produced by integrated emission of extra-galactic point sources. The deepest X-ray surveys to date (Hasinger, 2004; Giacconi et al., 2002; Alexander et al., 2003) have shown that up to virtually 100% of the < 2 keV CXB radiation is accounted for by Active Galactic Nuclei (AGN) hosting accreting super-massive black holes (SMBHs).

However, the fraction of CXB emission resolved into AGNs declines with energy (and with the efficiency of X-ray mirrors) being $< 50\%$ above 6 keV (Worsley et al., 2005) and the unresolved component is consistent as being the emission of a yet undetected population of highly absorbed AGN; such AGN should be characterized by having column densities $\sim 10^{24}$ H-atoms cm^{-2} and a space density peaking at redshift below 1 (Worsley et al., 2005). Such population of Compton-thick AGN is invoked by population synthesis models (e.g. Comastri et al., 1995; Treister & Urry, 2005; Gilli et al., 2006) to explain the peak of the CXB emission at 30 keV (Marshall et al., 1980).

Thus, an accurate measurement of the CXB spectrum in the 15–150 keV energy range is important to assess and constrain the number density of Compton-thick AGNs. Such measurements are complicated by the fact that instruments sensitive in this energy range

are dominated by internal detector background and are not designed to measure the CXB spectrum directly (excluding HEAO-1). The typical approach is to produce an $ON - OFF$ measurement, where the difference between the ON and the OFF pointings cancels the internal background component.

The HEAO-1 measurement of the CXB spectrum in the 13–180 keV range was obtained by blocking the aperture with a movable CsI crystal. Also the Earth disk can be used to modulate the CXB emission. This approach is behind the recent CXB flux measurements performed by INTEGRAL and BeppoSAX (Churazov et al., 2006a; Frontera et al., 2006). However, since the Earth is a powerful source of hard X-rays the $ON - OFF$ measurement is contaminated by the Earth's emission. Thus, without knowledge of the Earth's emission the two components cannot be disentangled.

Here we report about the *Swift*/BAT measurement of the CXB and Earth's spectra in the 15-150 keV range. We use the Earth occultation technique similarly to the INTEGRAL and BeppoSAX measurements. The main difference is that we develop an Earth's emission model, based on observations and confirmed by a Monte Carlo simulation, which allows us to disentangle the two spectra without prior knowledge of their spectral shapes.

The structure of the paper is as follows. In Section 7.2 we present the details of the observations. We also derive a rate-rigidity relation which is fundamental both for suppressing the background variability due to Cosmic Rays (CRs) and to characterize the Earth model. In Section 7.3 we present the details of the Earth's occultation episodes undergone by BAT and the Earth's model. In Section 7.5 we discuss the results in comparison with previous observations. The last section summarizes our findings.

7.2 Observations

The Burst Alert Telescope (BAT) (Barthelmy et al., 2005), on board the *Swift* mission (Gehrels et al., 2004), launched by NASA in 2004, represents a major improvement in sensitivity for X-ray imaging of the hard X-ray sky. BAT is a coded mask telescope with a wide field of view (FOV, $120^\circ \times 90^\circ$ partially coded) aperture sensitive in the hard X-ray domain (15-200 keV). BAT's main purpose is to locate Gamma-Ray Bursts (GRBs). While chasing new GRBs, BAT surveys the hard X-ray sky with an unprecedented sensitivity. Thanks to its wide FOV and its pointing strategy, BAT monitors continuously a large fraction of the sky (up to 80%) every day.

The *Swift* flight constraints impose that the pointing direction be at least 30° above the Earth's horizon. Nevertheless, due the extent of the BAT FOV, it may happen that the Earth disk occults a substantial portion (up to 30%) of it. Moreover, the BAT survey data

contain episodes of large occultations (up to ∼70%) by the Earth when the spacecraft was in safe mode.

We use 8 months of BAT data which constitutes a well characterized dataset of BAT survey data (see Ajello et al. 2007 for details) to study the different components of the BAT background. Our aim is to derive the BAT background spectrum in the infinite-rigidity approximation. We then use all occultation episodes, as described in Section 7.3, to derive a measurement of the CXB and the Earth's atmosphere spectra.

7.2.1 The BAT background

The BAT background is highly complex and structured; it exhibits variability dependence on either orbital position and pointing direction. BAT employes a graded-Z shield fringe shield to suppress the in-orbit background. The fringe shield, located around and below the BAT detector plane, reduces the isotropic cosmic diffuse flux and the anisotropic Earth albedo by ∼95% (Barthelmy et al., 2005). The two main background components are the CXB emission and the cosmic ray induced (prompt and delayed) backgrounds.

The CXB spectrum in the 3-400 keV range is based on HEAO-1 data. The following analytical approximation was suggested by Gruber et al. (1999):

$$S_{CXB}(E) = \begin{cases} 7.877E^{-0.29}e^{-E/41.13} & 3 < E < 60\,\mathrm{keV} \\ 0.0259\left(\frac{E}{60}\right)^{-5.5} + 0.504\left(\frac{E}{60}\right)^{-1.58} + 0.0288\left(\frac{E}{60}\right)^{-1.05} & E > 60\,\mathrm{keV} \end{cases} \tag{7.1}$$

Where $S_{CXB}(E)$ is expressed in units of keV cm^{-2} s^{-1} sr^{-1} keV^{-1}. Given the large FOV (∼1.4 sr), the CXB is the dominant background component in BAT up to ∼50–60 keV.

The prompt CR background is due to spallation effects of incident CRs on the materials of the spacecraft; since the Earth magnetic field modulate the flux of incident CRs at any point of the orbit, such background component is expected to vary with the cut-off rigidity R_c (i.e. the minimum energy an incident charged particle must have in order to reach a position in the Earth's magnetic field). The delayed component is caused by the excitation of the materials by the incoming CR flux. The delayed component varies slowly and usually builds up asymptotically with time. Due to the nature of the magnetic field surrounding the Earth the southern hemisphere has an indentation in the magnetosphere called the South Atlantic Anomaly (SAA). During each SAA passage, BAT experiences a sharp increase in count rate due to the increase of the incident CR flux and a delayed background due to de-excitation of the spacecraft materials.

In order to discriminate the various components of the BAT background, we have correlated the BAT whole array rate (in each energy channel and normalized by the number of working detectors) with several orbital parameters. The final goal is to derive a

"steady-state" BAT background which is unaffected by orbital variations.

7.2.1.1 Data cuts

Our aim is to determine a rate-rigidity relation in order to extrapolate the BAT array rates in the infinite rigidity case; this allows to suppress the background variability due to the prompt and delayed CR components.

We start excluding all observations where sources with signal-to-noise ratio (S/N) greater than 8 are detected. A 8σ source produces an increase in rate of less than 0.5% in a typical 300 s observation; thus all point-like sources below this limit give a negligible contribution to the background level.

The next step is to eliminate all observations whose exposure time is less than 300 s. The rates show a clear anti-correlation with exposure time for exposures below 300 s with an increase of a factor $\sim$3 in the rates for few seconds of exposures. Exposures below 300 s are usually the result of a truncated exposure. Exposures are generally truncated because: 1) BAT detects a GRB or 2) BAT enters in the SAA and data acquisition is suspended. For both reasons, data of truncated exposures are excluded by the present analysis because not representative of the average BAT background.

Everytime the spacecraft exits from the SAA, BAT experiences a decay in the rate due to de-excitation of spacecraft materials. As shown in Fig. 7.1 the rates come to their normal level after $\sim$5600 s after each SAA passage. We thus exclude all observations taken within $\sim$5600 s of an SAA passage.

The BAT rates show also a correlation with the angle between the Sun and the pointing direction. The correlation starts at angles $>120^{\circ}$ and decreases with energy disappearing at $70-80$ keV. All these observations are at elevation angles (ELV, e.g. angle between the BAT pointing direction and the Earth horizon) of $\sim 45^{\circ}-65^{\circ}$ and thus given the large FOV, it is well possible that the Sun illuminated Earth limb be in the BAT FOV. Therefore, all these observations are excluded from the present analysis.

The BAT effective area at $\sim$ 200 keV reduces to 1/5 of its peak value at 50 keV; moreover, at these energies the fringe shield becomes partially transparent. Thus, it is possible to use the last energy channels as "particle" detector to monitor the background level of the instrument (i.e. these channels do not yield much information on any celestial signal). We found that imposing that the rate of the last energy channel (194 keV–6.5 MeV) be in the range 10–20 ct s^{-1} eliminates roughly 1% of the observations which are outliers in all the correlations here verified.

After these cuts, we find that the rates in each energy channel decrease as a function of the cut-off rigidity R_C. We modeled this behavior with an exponential and a constant ($Rate = C + e^{\alpha R_C}$) and fitted this model to each energy channel. The constant term C of

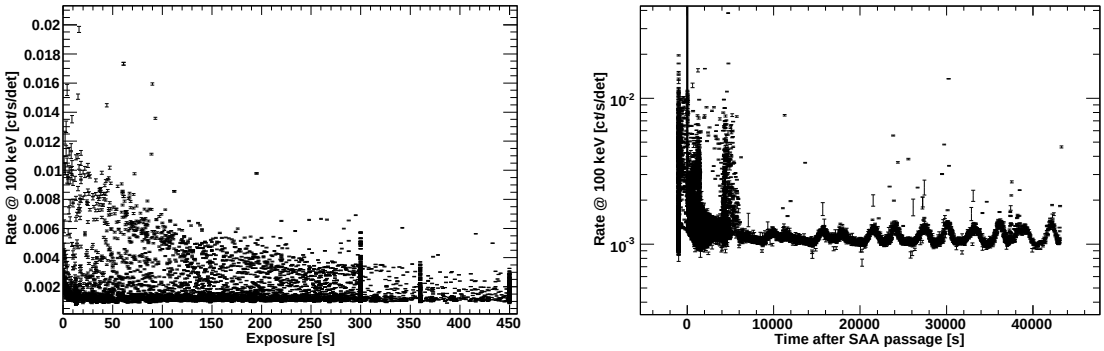

Figure 7.1: Left Panel: BAT rate at 100 keV versus exposure time. The "truncated" exposures below 300 s are noisy. Despite the impression most of the observation have exposure larger (or equal) than 300 s. **Right Panel:** BAT rate at 100 keV versus time after each SAA passage. Note the sharp increase in rate and decay behaviour when the spacecraft exits the SAA. The second sharp peak at ∼4000 s is due to a second passage inside the trail of the SAA. The rate modulation visible after ∼6000 s is due to Earth magnetosphere.

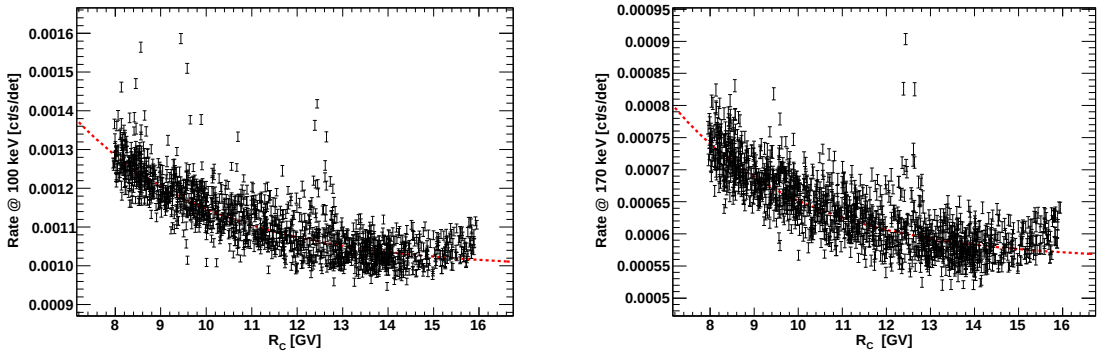

Figure 7.2: Left Panel: Correlation of BAT rate with the cut-off rigidity at 100 keV. The dashed line is an exponential plus a constant fit. **Right Panel:** Correlation of BAT rate with the cut-off rigidity at 170 keV. The dashed line is an exponential plus a constant fit.

every fit provides an estimate of the BAT rate in the infinite rigidity extrapolation. The distribution of the α values, shown in left panel of Fig. 7.3, has a mean of -0.34 and a RMS of 0.04 in perfect agreement with previous measurements (Imhof et al., 1976).

The BAT spectrum obtained extrapolating the rates of each energy channel is shown

in the right panel of Fig. 7.3. The BAT spectrum shows a clear line at 59 keV most probably due to the radioactive Americium source used on board for calibration purposes. The bumpiness between 60 and 100 keV is given by numerous fluorescence emission lines from the fringe shield (see Willis 2002 for details).

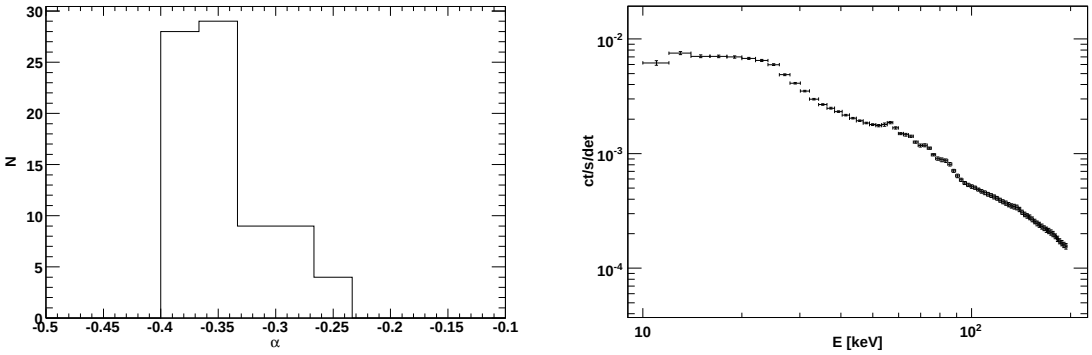

Figure 7.3: Left Panel: Distribution of the α values. The mean of -0.34 is in good agreement with measurements from Imhof et al. (1976). **Right Panel:** BAT background spectrum extrapolated in the infinite rigidity case.

7.3 Earth occultation

The *Swift* orbital constraints impose that the BAT pointing direction be always at least 30° away from the Earth horizon. This is requested because the Earth is bright in the Optical and X-rays and it can damage the UV/Optical telescope (UVOT) and the X-ray telescope (XRT). On May 31, June 12 and July 28, 2005, the Swift spacecraft entered into safe-mode because the of star tracker loss of lock. In safe-mode operations, the XRT and UVOT telescopes are closed, but BAT still takes data. The spacecraft remains in sun reference pointing until a recovering operation commanded from the ground brings *Swift* back to its normal status. In the timespan between the safe-mode and the recovering operation, the satellite uses the magnetometers and the sun sensor to derive the pointing direction. At least in the occasions mentioned above[1] the Earth passed in the BAT field of view (FOV). Fig. 7.4 shows the BAT pointing directions during the deep occultation episodes described here. As the Earth occults partially the FOV, BAT registers a sharp decrease in rate due to occultation of the CXB emission. This is especially valid below

[1] A few episodes of Earth occultation were found in BAT data, but some did not pass the criteria explained in Sec. 7.2.1.1

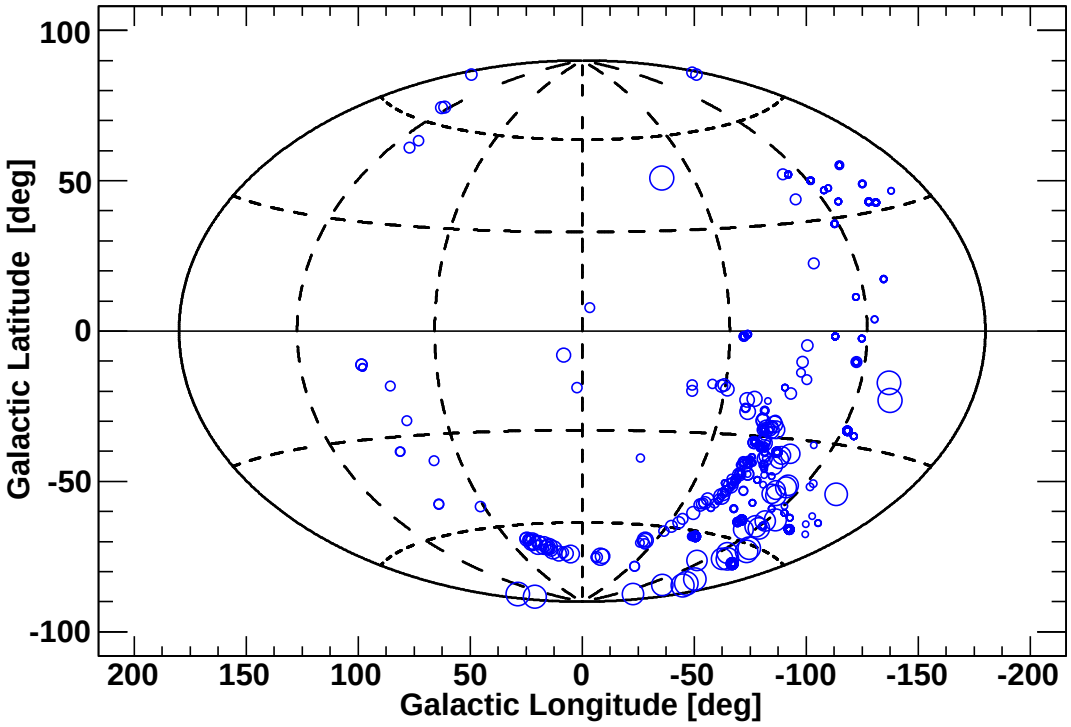

Figure 7.4: Pointing directions for the occulted observations. Marker sizes vary linearly with the occulted FOV fraction. Occultations vary from 0.1% to $\sim$ 60%. In order to avoid contamination of the CXB signal from the Galactic Ridge emission, we used only occultation episodes at $|b| > 20^{\circ}$.

40 keV where the CXB radiation dominates above the Earth atmospheric components. Left panel of Fig. 7.5 clearly shows the drop in rates caused by the occulting Earth; between 18–20 keV the rates drop of a factor 3.5 when $\sim$ 60% of the BAT FOV is occulted (as shown in the right panel of 7.5).

Thus, the Earth occultation can be used to measure the CXB emission by means of the depression caused in the BAT rates. Such approach was used several times in the past. Recently this technique was adopted to derive a measurement of the CXB normalization at hard X-rays with INTEGRAL and Beppo-SAX (Churazov et al., 2006a; Frontera et al., 2006).

Unfortunately, the Earth is not only a passive occulter, but also an active emitter. The Earth is a powerful source of X- and gamma-rays due to cosmic rays bombardment of its atmosphere (see Petry et al., 2005). This radiation is usually referred to as Albedo and it is discussed briefly in the next section.

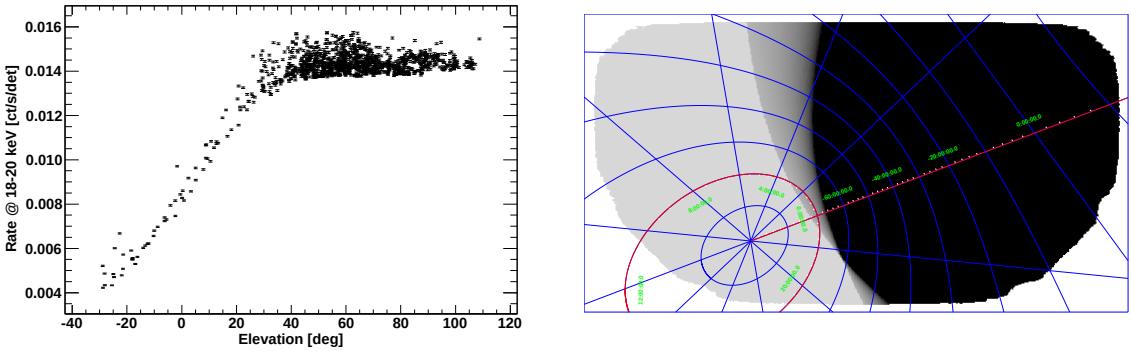

Figure 7.5: Left Panel: BAT rate, in the 18–20 keV range, as a function of the elevation angle above the Earth horizon. For ELV $<$30–60°, BAT starts to experience Earth occultations. The decrease in rate is expected to vary linearly with the occulted solid angle if Earth emission is negligible. Note that this graph is not a light curve as each data point is a separate (in time) 300 s observation. **Right Panel:** Example of deep Earth occultation of the BAT FOV. The black area is the region of the BAT FOV which is completely occulted by the Earth during the 300 s observation; the lighter gray is the un-occulted part of the FOV, while the region in between the black and the lighter gray is partially occulted due to the spacecraft moving in the 300 s.

7.3.1 Atmospheric Albedo Gamma-rays

The atmospheric Albedo flux is produced by cosmic ray interactions in the Earth's atmosphere. Pionisation of atmospheric nuclei by the incident cosmic ray flux leads to the production of muons, nuclear fragments, and other hadrons as shown in the schematic reported in left panel of Fig. 7.6. Gamma-rays above 50 MeV are produced directly by the decay of mesons while below at X-ray energies the main source can be attributed to bremsstrahlung radiation from secondary electrons from cosmic ray interactions.

Moreover, the Earth atmosphere reflects, via Compton interaction, part of the CXB and of the discrete X-ray source radiation.

Measurement of the X-ray Albedo radiation are reported in Schwartz & Peterson (1974) in the 1–100 keV energy range and by Imhof et al. (1976) above 40 keV. The Albedo spectrum measured by Schwartz & Peterson (1974) shows a cut-off below 30 keV, probably due to self-absorption of the radiation emitted from the inner layers of the atmosphere and a progressive flattening around 40 keV. Above 40 keV the Albedo emission decrease consistently with a power law with photon index of $\sim$1.4-1.7. The power-law behavior is also confirmed by Gehrels (1992). However the absolute normalization of the

observed Earth spectrum depends on the altitude and the inclination of the satellite's orbit.

A recent Monte Carlo simulation of the hard X-ray emission of the Earth's atmosphere (Sazonov et al., 2006) shows that the emerging X-ray photon spectrum is barely sensitive to the energy of the parent cosmic ray particle and can be described by the following formula:

$$f(E) = \frac{C}{(E/E_{\rm B})^{\Gamma_1} + (E/E_{\rm B})^{\Gamma_2}} \tag{7.2}$$

where C is a constant. The authors determine for Γ_1 and Γ_1 the values of -5.5 and 1.4 respectively and for E_b the value of 44 keV.

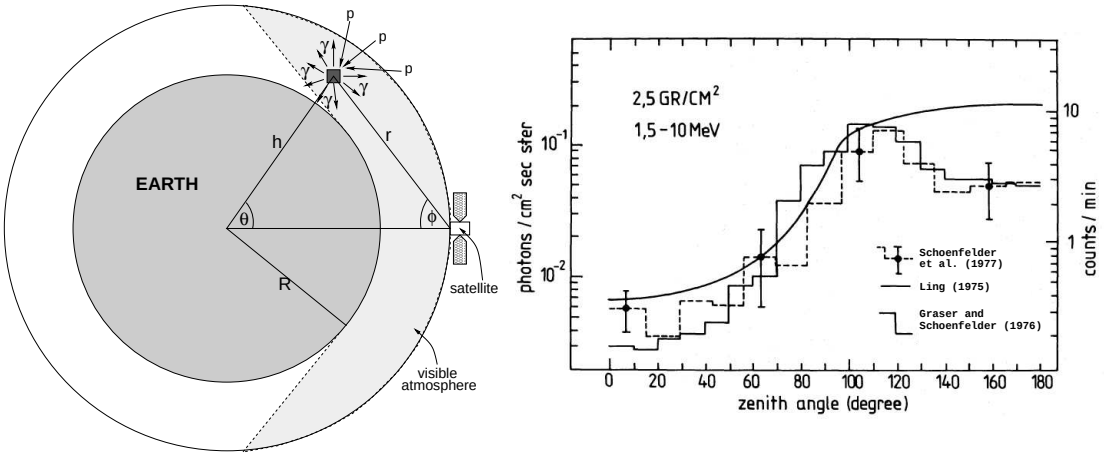

Figure 7.6: Left Panel: A schematic illustration of the generation of gamma-rays due to cosmic rays bombardment (adapted from Shaw et al. 2003). **Right Panel:** The zenith angle distribution of the 1.5–10 MeV atmospheric albedo gamma ray flux at an altitude of 42 km and at local rigidity of 4.7 GV, taken from Schönfelder et al. (1977).

It is worth noting that since the Earth's atmospheric component depends on the cosmic ray flux, its intensity is expected to be modulated by the Earth's magnetosphere in the same way as the parent cosmic ray flux. The effect of the Earth's magnetosphere (and thus of rigidity) on the Albedo emission are clearly shown in the analysis of Shaw et al. (2003).

7.3.2 Method of analysis

The rate $R(E)_i$ measured at the energy E by BAT in a 300 s observation, during which the Earth is in the FOV, can be described as:

$$R(E)_i = I(E)_i - \Omega_i \cdot R(E)_{CXB} + \Omega_i \cdot R(E)_{Earth} \tag{7.3}$$

where the subscript i refers to the $i-th$ observation, Ω_i is the solid angle occulted by the Earth and $R(E)_{CXB}$ and $R(E)_{Earth}$ are the CXB and the Earth emission respectively.

Equation 7.3 shows the "degeneracy" problem which limits the Earth occultation technique when used to determine the CXB emission. Indeed, the measured depression of the rates with respect to the normal level are a measurement of the difference of the CXB flux and the Earth's atmospheric emission. The studies of Churazov et al. 2006 and Frontera et al. 2006 "solve" this problem deriving the "difference" spectrum (i.e. the spectrum of the difference between the CXB and Earth emissions) by measuring the depression in each energy channel. The difference spectrum is then fitted with two components, the CXB and the Earth, whose spectral shapes are assumed to be known. Thus, the fit determines the normalizations of the two components.

Here, our aim is to solve the degeneracy problem by assessing the differences of the CXB and Earth signatures in each energy channel and thus deriving directly the two spectra.

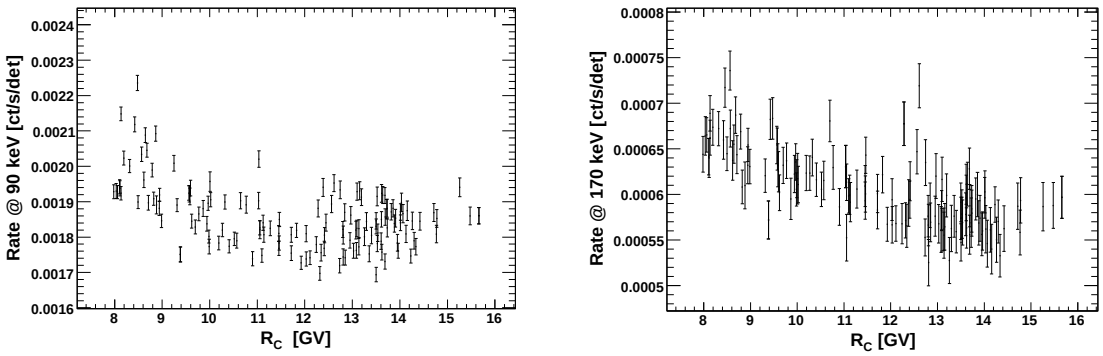

Figure 7.7: Rate-rigidity relation at 90 keV (left) and at 170 keV (right) for occulted observations (ELV$< 30°$). Rates were extrapolated in the infinite rigidity case using the relations determined from the unocculted data. The residual correlations with rigidity are due to the enhanced Albedo emission in regions of low rigidity. Note that different observations (data points) suffer from different levels of occultation. Errors are statistical plus systematic.

A signature of the Earth's atmospheric emission is its correlation with rigidity. This effect is present at all energies, but most noticeably at high energies where the Albedo component dominates over the CXB flux. Fig. 7.7 shows such cases; occulted observations whose rates were extrapolated in the infinite rigidity case show a residual correlation with rigidity. Since the unocculted data do not present such residual correlation, we attribute this to enhanced Albedo emission. The amplitude of this correlation is in perfect

agreement with what was derived also by Shaw et al. (2003).

Measurements of the Earth's Albedo emission in gamma-rays (e.g. Schönfelder et al. 1977) show that a large fraction of the Albedo emission comes from the limb (i.e. the atmosphere layers in the direction of the Earth's horizon as seen from the satellite, see also Fig. 7.6). A recent analysis of EGRET, 35 MeV–10 GeV, data (Petry et al., 2005) shows that the limb is much brighter than the internal part of the disk. Considering the 300–1000 MeV radial profile in Petry et al. (2005) (which yields the best compromise in terms of signal and point spread function size), we see that ∼70% of the total emission comes from zenith angles in the range 105°–120°. Thus, ∼70% of the total Earth's emission originates within the first ∼500 km of the Earth disk (as seen from a satellite in Low Earth Orbit, LEO).

This is also confirmed by detailed Monte Carlo simulations in the 15-200 keV energy band (Willis, 2002). Thus, we decide to split the contribution of the Earth emission into two components: the limb and the disk emission. The limb is limited within 5878 km$< R <$6378 km and the disk within $0 < R <$5878 km. We also note that our model is insensitive to small variations (∼50 km) of the limb and disk sizes.

The complete model which we use to explain the observed count rates, in each energy channel, as a function of local rigidity and different Earth components, can be described as follows:

$$\begin{aligned} R(E,R_C)_i &= I(E)_i - \bar{\Omega}_i \cdot R(E)_{CXB} + \\ &+ \left[\bar{\Omega}_i^{Limb} \cdot K + \bar{\Omega}_i^{Disk} \cdot (1-K)\right] R(E)_{Earth} \cdot f(R_C) \end{aligned} \tag{7.4}$$

where $\bar{\Omega}_i = \bar{\Omega}^{Limb} + \bar{\Omega}_i^{Disk}$ is the total "effective" solid angle (see below) occulted by the Earth, K and $(1-K)$ are the fractions of Earth emission radiated by the limb and the disk, $f(R_C)$ is the rate-rigidity function determined by unocculted data and $R(E)_{CXB}$ and $R(E)_{Earth}$ are the CXB and the Earth components.

The observations we are dealing with are generally non-contiguous and thus the changes in the instrument configuration (e.g. number of working detectors) must be taken into account. We do this computing exactly the "effective" solid angle occulted by the Earth for each observation. This is defined as:

$$\bar{\Omega}_i = \sum_{j=0}^{N_p} \omega_j \cdot (1 - \Delta T_j^{Frac}) \cdot V_j^i \tag{7.5}$$

where N_p is the total number of sky pixels, ΔT_j^{Frac} is the fractional exposure time[2] a sky pixel of solid angle ω_j is unocculted and V_j^i is the vignetting affecting that sky pixel during the i-th observation.

[2]The fractional exposure time is the fraction of the exposure time the sky pixel is unocculted. Thus, it varies from 0 to 1 for completely occulted and unocculted pixels respectively.

Hence, the final fitting model is a function of three variables $g = g(\bar{\Omega}^{Disk}, \bar{\Omega}^{Limb}, R_C)$ and the Least-Square fit to each energy channel yields separately the 3 components: the instrumental, the CXB and the Earth components. In our fitting procedure, besides the requirement that all three parameters are constrained to be non-negative, the parameters are left unbound. Fig. 7.8 shows a fit example. The typical reduced χ^2 of every fit is $\sim$1500/1700 and so it is generally very good.

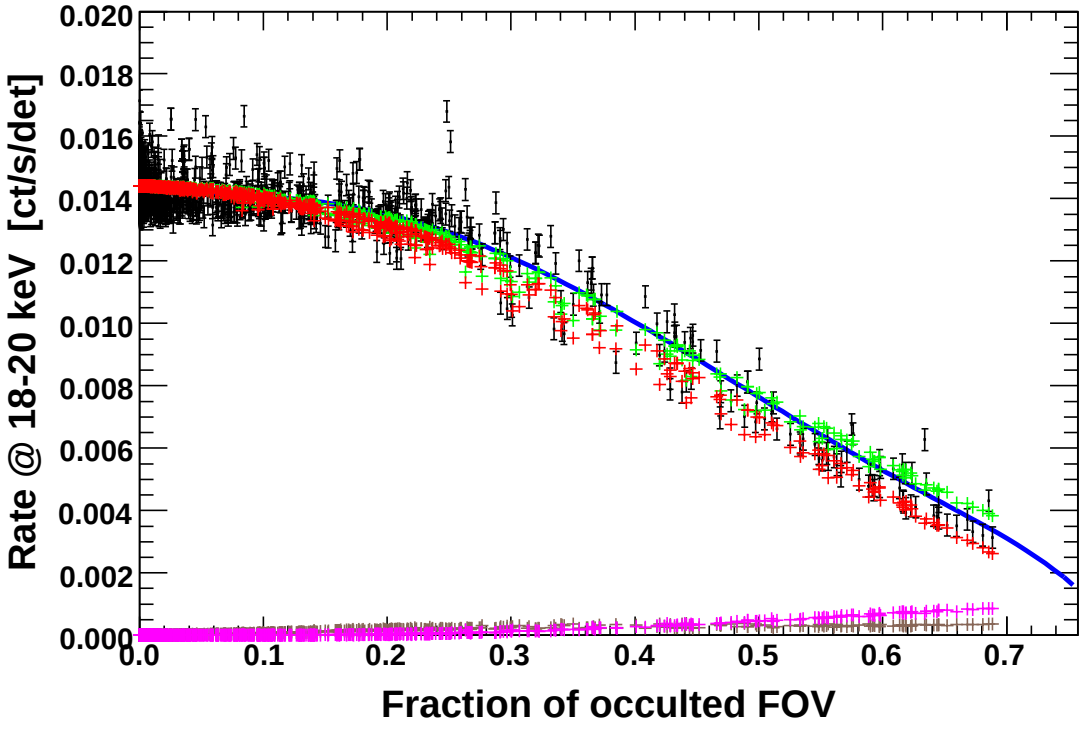

Figure 7.8: Fit example for the 18-20 keV energy channel. The green crosses are the best fit to the data. The red crosses shows the occultation of the CXB, while the brown and the purple crosses show the emission from the limb and the disk respectively. The solid line is an analytical function used to derive the initial values of the fitting routine.

The conversion from the detector count space to source photon space has necessarily to take into account the non-diagonal response of BAT. The BAT response is based on ground calibrations and observations of the Crab nebula. The adopted Crab spectrum, as derived by the use of the standard BAT response, is described as: $dN/dE = 10.3\,E^{-2.128}$ photons cm^{-2} s^{-1} keV^{-1}.

However, it is not strictly correct to use a response for a point-like source when dealing with a diffuse source like the CXB. The development of such response, which requires extensive Monte Carlo simulations of the instrument performances, is outside the scope of this work. Until a proper response will not be generated this measurement has to be considered preliminary. We also remark that such problem is encountered by all measurements of CXB emission using the occultation technique when the Earth is occulting a substantial part of the FOV.

7.4 Analysis of the Errors

7.4.1 Rate Variation

The rate-rigidity graphs (examples are shown in Fig. 7.2) show a scatter in the rate around the best fit which is generally larger than the rate statistical errors. These scatters are most probably due to other effects which are not considered in this analysis. The pointing directions, the solar cycle, the spacecraft orientation with respect to the Earth and the Sun can be the reasons for the observed scatter in the rates. Since the scatter is limited in amplitude (less than 10%) we modeled the distribution of the scatters as a Gaussian. The $1\,\sigma$ width of this distribution gives for each energy channel an estimate of the total (statistical plus systematic) error of the extrapolated rates. This error constitutes the baseline error of this analysis and it is propagated throughout all the further steps.

The left panel of Fig. 7.9 shows the ratio between the total $1\,\sigma$ error and the extrapolated rate as a function of energy. Notwithstanding the fact that the systematic rate variation dominates the statistical errors, the total error is still small when compared to the rates (extrapolated to infinite rigidity) and it reaches its minimum in the 30–40 keV range.

7.4.2 Errors connected to unprecise attitude determination

Analysis of sources detected during safe-mode pointings shows that the attitude differs from the nominal pointing direction by 2–3 degrees. The effective solid angle, computed in Eq. 7.5, is a slowly varying function for degree of occultation. As shown in the right panel of Fig. 7.9, the fractional effective solid angle can be approximated, in the 0.4–0.8 range, by a straight line with a slope of 0.010 deg^{-1}. This means that an error of (at most) 3 degrees in the attitude determination translates into an uncertainty of $\sim$3% in the determination of the portion of BAT FOV which is occulted. This additional systematic error is taken into consideration in the analysis. We also note that the total error is still

dominated by the systematic error due to the scatter of the rates.

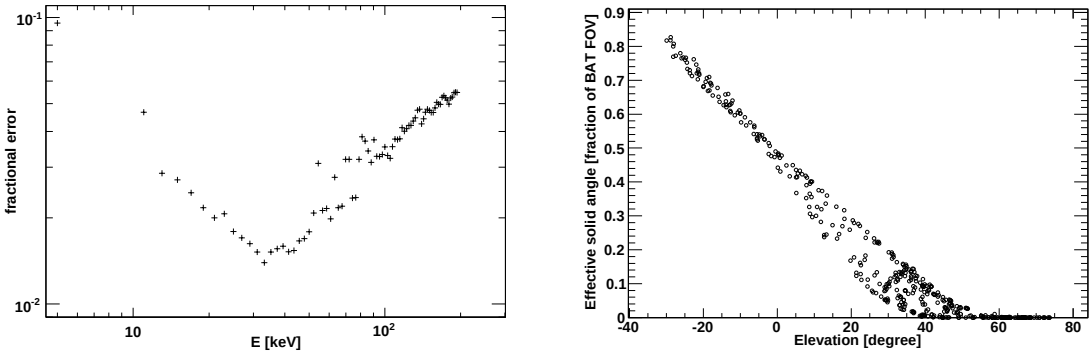

Figure 7.9: Left Panel: Fractional 1 sigma error as a function of energy. The fractional error is the 1 sigma error (computed in the way described in the text) divided by the rate in each energy channel. **Right Panel:** Variation of the fractional effective solid angle as a function of elevation.

7.5 Results of the analysis

In this section we present the main results of the analysis: the CXB and the Earth's atmosphere spectra. In order to avoid contamination by Galactic Ridge emission we used only occultation episodes at $|b| > 20^{\circ}$. To verify our results we also derive the "difference" spectrum in a similar way to Churazov et al. (2006a) and Frontera et al. (2006). All spectra include systematic errors due to residual rate variation as described in 7.4.1, systematic errors due to unprecise attitude determination and systematic errors due to the uncertainty in the instrument's response. All quoted errors are 90% confidence for one interesting parameter.

7.5.1 The X-ray Background Spectrum

The CXB spectrum is shown in Fig. 7.10. As a first test we fitted Eq. 7.1 for the CXB spectral shape. Only the normalization of the function was allowed to vary. We found that our CXB spectrum is in excellent agreement with the HEAO-1 measurement and that the normalization of the two spectra agrees within 0.7%. We find that the CXB intensity in the 20–50 keV band is 6.10 ± 0.07 erg cm^{-2} s^{-1} sr^{-1} The observed flux near the peak of the CXB spectrum at 29 keV is 42.4 keV^2 cm^{-2} s^{-1} keV^{-1} sr^{-1}. We find that the

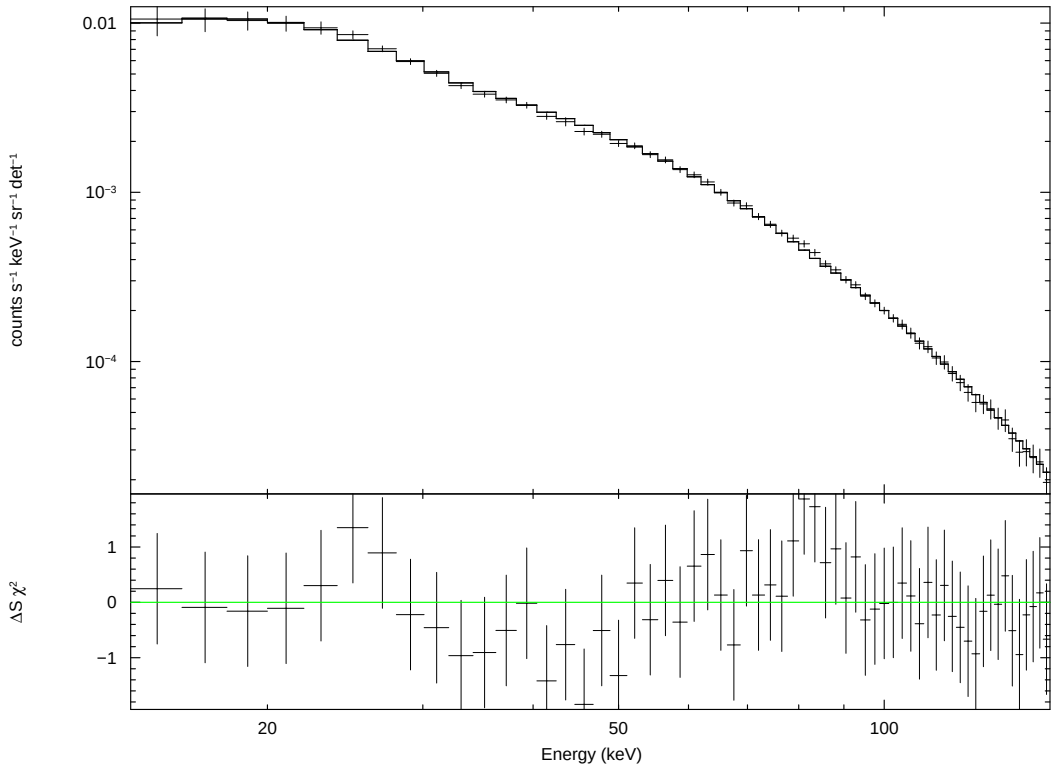

Figure 7.10: CXB spectrum fitted with the function suggested by Gruber et al. (1999). The normalization of the fit is in perfect agreement with the HEAO-1 measurement. The reduced χ^2 of the fit using Gruber et al. (1999) formula, with normalization as the only parameter, is 38.37/55.

shape of the CXB is well described by Eq. 7.1. Tab. 7.1 shows the comparison of our measurement with past measurements of the CXB intensities in similar energy bands. The discrepancy between the BAT and the INTEGRAL measurements ($\sim$10%) is compatible with the different Crab normalizations adopted by the two instruments.

Fig. 7.11 shows a compilation of the X- and gamma-ray diffuse backgrounds from keV to GeV energies. With respect to the work of Gruber et al. (1999), we use SMM (MeV) data (Watanabe et al., 1997) and a revision of COMPTEL and EGRET data (Weidenspointner et al., 2000; Strong et al., 2004). In particular, the new analysis of EGRET data shows that the range of validity of the Gruber et al. (1999) formula (Eq. 7.1) is now restricted to 3 keV$<$ E $<$ 1 MeV.

We find that a good description of the available data in the 2 keV – 2 MeV range is achieved using a jointly smoothed double power-law of the form:

$$E^2 \cdot \frac{dN}{dE} = E^2 \cdot \frac{C}{(E/E_{\rm B})^{\Gamma_1} + (E/E_{\rm B})^{\Gamma_2}} \quad [\mathrm{keV}^2 \mathrm{photons\ cm}^{-2}\mathrm{s}^{-1}\mathrm{sr}^{-1}\mathrm{keV}^{-1}] \qquad (7.6)$$

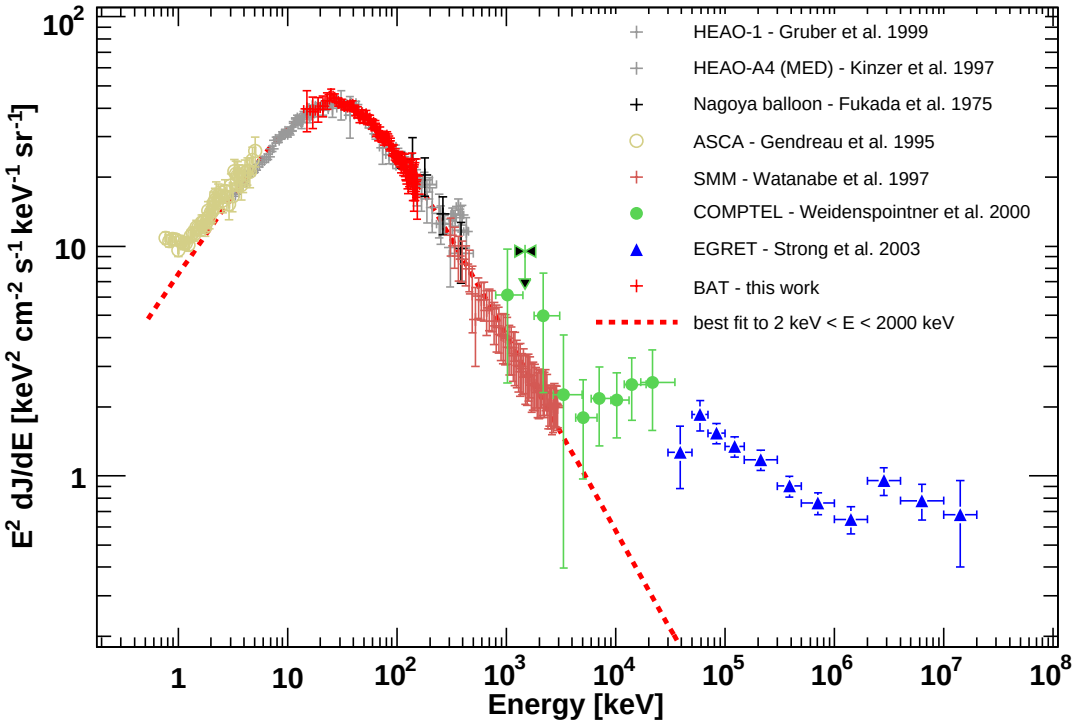

Figure 7.11: BAT CXB spectrum compared with previous results. The dashed line is the best fit to 2 keV< E < 2000 keV as reported in the text.

The best fit, shown in Fig. 7.11, yields the following parameters (and $1\,\sigma$ errors): $C = (9.33 \pm 0.72) \times 10^{-2}$, $\Gamma_1 = 1.29 \pm 0.018$, $\Gamma_2 = 2.85 \pm 0.015$ and $E_{\rm B} = 29.79 \pm 1.1$

7.5.2 Analysis of the Earth spectrum

The Earth spectrum derived by our analysis is shown in Fig. 7.12. We used Eq. 7.2 as a model to fit the data. The best fit parameters (χ^2 =45.60/57) are $\Gamma_1 = -4.0^{+1.06}_{-1.39}$, $E_{\rm B} = 33.4^{+1.75}_{-1.59}$ keV, $\Gamma_2 = 1.7^{+0.06}_{-0.06}$ and $C = 5.8^{+0.32}_{-0.30} \times 10^{-2}$ ph cm^{-2} s^{-1} keV^{-1} sr^{-1}.

The BAT Earth's spectrum is marginally consistent with the simulation performed by Sazonov et al. (2006). In particular our data are not consistent with an high-energy photon index (Γ_2) of 1.4.

The satellites *OSO-3* and *BeppoSAX* flew in Low Earth Orbits (LEOs) as *Swift*, but with different inclinations (33° and 4° respectively). The BAT Earth's spectrum is compatible (within the large error bars of those two missions) with the measurements obtained by these two satellites (Schwartz & Peterson, 1974; Frontera et al., 2006). It is worth not-

Table 7.1. Comparison with previous results

Instrument	Ref.	Energy band keV	F_{Crab}[a]	I_{CXB}[b]	I_{CXB} this work[b]	BAT Crab Flux[a]
HEAO-1/A2+A4	1	20–50	9.92[c]	6.06 $\pm$0.06	6.10$\pm$0.07	9.75
HEAO-1/A2	2	20–50	NA	5.60 $\pm$0.3	6.10$\pm$0.07	9.75
RXTE	3	15–20	3.72	2.36 $\pm$0.02	1.81$\pm$0.02	3.30
BeppoSAX	4	20–50	9.22	5.89 $\pm$0.19	6.10$\pm$0.07	9.75
INTEGRAL	5	20–100	17.6	$\sim$ 10.45 [d]	9.50$\pm$0.10	16.4

[a]Crab flux quoted by the authors expressed in 10^{-9} ph cm^{-2} s^{-1} keV^{-1}

[b]Intensity of the CXB quoted by the authors in 10^{-8} keV^2 cm^{-2} s^{-1} sr^{-1} keV^{-1}

[c]Gruber et al. (1999) do not report about the adopted Crab spectrum; however the HEAO-A4 spectrum of the Crab Nebula can be described as $dN/dE = 8.76\,E^{-2.0.75}$ photons cm^{-2} s^{-1} keV^{-1} (Jung, 1989).

[d]Authors do not give an exact measurement of the CXB flux, but report that their measurement is $\sim$10% higher than the Gruber et al. (1999) spectrum.

References. — (1) Gruber et al. (1999); (2) Marshall et al. (1980); (3) Revnivtsev et al. (2004); (4) Frontera et al. (2006); (5) Churazov et al. (2006a).

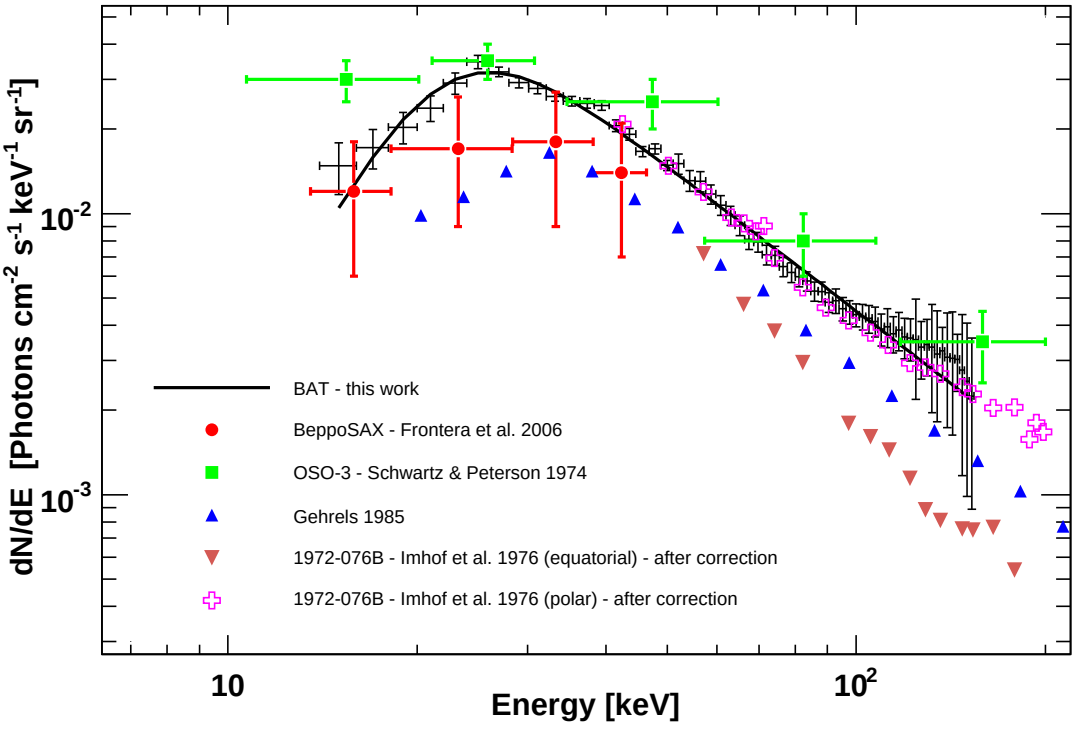

Figure 7.12: BAT Earth's spectrum and best fit (solid line) as compared to past measurements. References are shown in the legend. The datapoints (triangles) from Gehrels (1985) are a fit to the *downward* gamma-ray flux at 5 g cm^{-2} over Palestine, Texas. The measurements from Imhof et al. (1976) were corrected to take into account the correct CXB emission (details are in the text).

ing that we derived (as BeppoSAX and OSO-3) the Earth intensity using different orbital positions and thus averaging over magnetic latitude. Moreover, as generally the Earth comes at large angles in the FOV, we do not observe the upward albedo, but the albedo emerging at different zenith angles. This also seems confirmed by the similarity of our spectrum with the *downward* gamma-ray flux measured over Palestine, Texas (Gehrels, 1985).

In the case of the polar-orbiting satellite *1972-076B*, Imhof et al. (1976) found that above 40 keV the photon spectrum is consistent with a power-law with index ranging from 1.34 to 1.4 depending on the latitude scanned. Their measurement is based on the difference between pointings towards the atmosphere (*Down*) and pointing towards the sky (*Up*). In order to derive the Albedo spectrum the authors sum the CXB emission to the *Down-Up* spectrum (see Eq. 5 in Imhof et al. 1976 for details). For the CXB emission,

they use the measurement from Pal (1973) which describes the CXB photon spectrum as $dN/dE = 25E^{-2.1}$. This formula differs in the 40–200 keV range in both normalization and photon index from the HEAO-1 CXB spectrum. Thus, we corrected the Imhof et al. (1976) Albedo spectra taking into account the differences between the Gruber et al. (1999) and the Pal (1973) CXB spectra. After the correction, the two (equatorial and polar) Albedo spectra are consistent with a power-law whose photon index is $\sim$1.7 and are in excellent agreement with the BAT Albedo spectrum.

Since RXTE flies in a similar LEO orbit (height of 580 km and 23° inclination) as BAT we can use the BAT Earth's spectrum to predict the emission in the 15–20 keV band (which is neglected in the analysis of Revnivtsev et al. 2003). The expected flux from the Earth results in $2.46 \pm 0.5 \times 10^{-9}$ erg cm^{-2} s^{-1}sr^{-1}. Thus, the difference between the RXTE and the BAT CXB spectra, in the 15–20 keV, is compatible (after correcting for the different Crab normalizations) with Earth's emission.

7.5.3 Analysis of the difference spectrum

In order to verify our results, we derive the "difference" spectrum as derived by Churazov et al. (2006a) and Frontera et al. (2006). This spectrum is the difference between the CXB and the Earth emission. It is readily derived from Eq. 7.3 as:

$$R(E)_i = I(E)_i - \bar{\Omega}_i \cdot [R(E)_{CXB} - R(E)_{Earth}] \tag{7.7}$$

where $\bar{\Omega}_i$ is the solid angle occulted by the Earth during the i-th observation. The fit to each energy channel produces the difference spectrum shown in Fig. 7.13. As in Churazov et al. (2006a), we fitted the difference spectrum with two component models: 1) the CXB spectrum as determined by Gruber et al. (1999) and 2) the Earth emission approximated by Eq. 7.2 as suggested by Sazonov et al. (2006). Thus, the fit yields the normalization of the two components. Freezing the photon indexes of Eq. 7.2 to -5 and 1.4 respectively (as suggested by Sazonov et al. (2006)) gives an unacceptable result (reduced $\chi^2 > 10$). The fit does not improve even if we take into account the fraction of CXB emission reflected by the Earth's atmosphere as suggested by Churazov et al. (2006b).

We, thus, decided to leave as additional variables of the fit the Γ_2 index of Eq. 7.2. The best fit (χ^2=55.65/53) yields a steep photon index $\Gamma_2 = 1.95 \pm 0.15$. The fit residuals are shown in Fig. 7.13. The normalization of the CXB, as derived from the fit, is consistent with the CXB spectrum derived in Sec. 7.5.1.

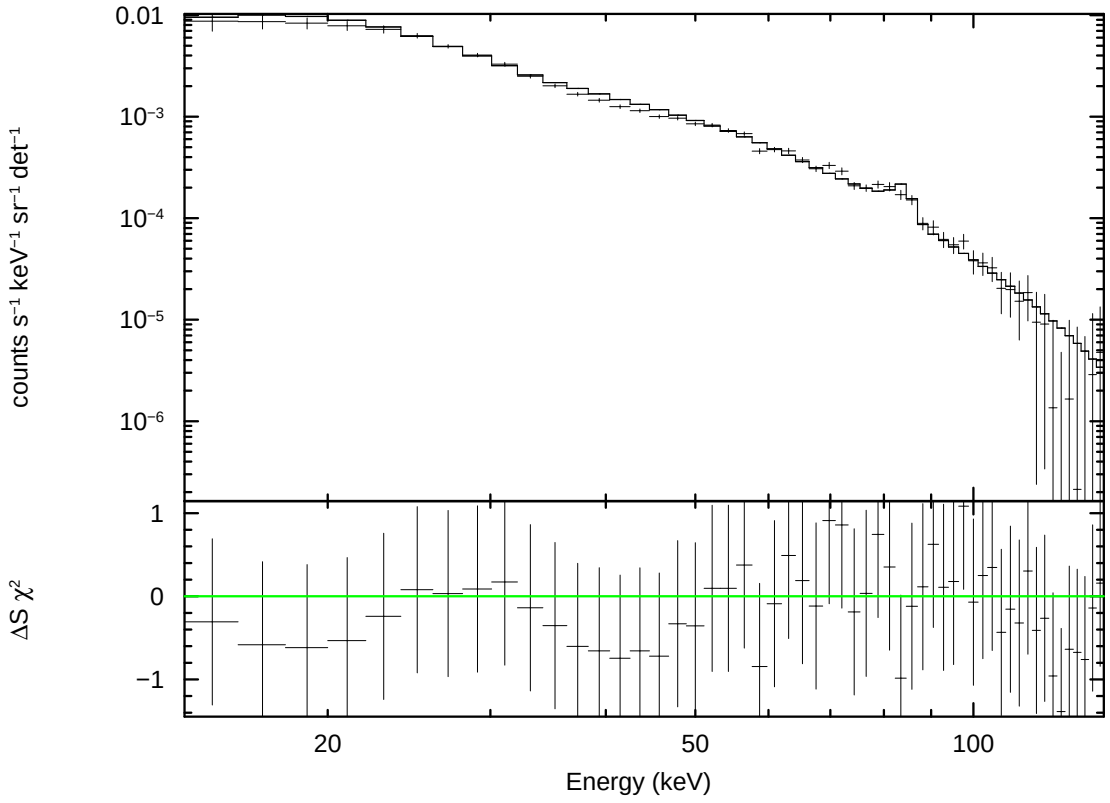

Figure 7.13: Difference spectrum $D = R_{CXB} - R_{Earth}$ with the best fit model. The CXB was modeled using the Gruber et al. (1999) formula were only the overall normalization is left free to vary. The Earth spectrum is approximated with Eq. 7.2 as suggested by Sazonov et al. (2006) except that the high-energy photon index (Γ_2) is left free to vary.

7.5.4 Checks on the solution

We repeated the analysis for different values of the K parameter of Eq. 7.4. Since the Earth occultation technique is highly sensitive on the Earth model used, we expect that variations of the K parameter will reflect on the goodness of the solution. There is a general consensus that the spectral shape of the CXB is well described by Eq. 7.1. Thus, we can assess the goodness of our solution in terms of deviation from the canonical CXB spectrum using the reduced χ^2 of each fit using Eq. 7.1 as model (with only the normalization as parameter). Results are shown for clarity in Fig. 7.14. It is apparent that the only K values which yields an acceptable solution are those in the range $\sim$0.7 with a surprisingly narrow allowed range. The 0.7 factor is in agreement with the Comptel and EGRET measurements (Schönfelder et al., 1977; Petry et al., 2005). As soon as K

departs from 0.7, the Earth model becomes inadequate to fit the occultation profiles and this translates in a CXB spectrum which deviates from the canonical one consistent with earlier measurements.

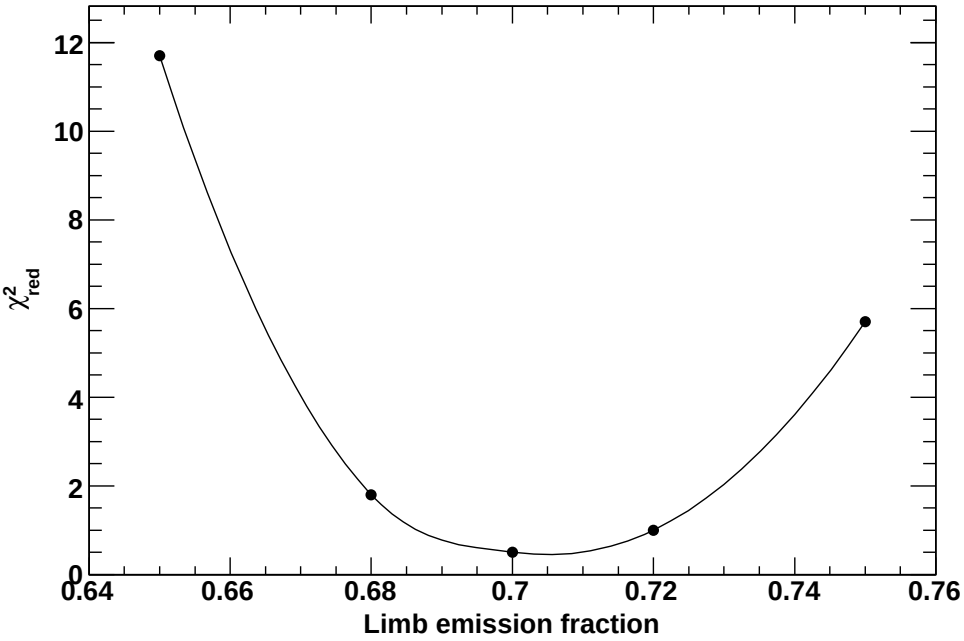

Figure 7.14: Reduced χ^2 of the fit to different CXB spectra obtained varying the fraction of limb emission. The solid line is a smooth line connecting datapoints.

7.6 Conclusions

BAT is the first instrument after HEAO-1 to measure the spectrum of the CXB in the 15–150 keV range. This measurement takes advantages of several episodes of CXB flux modulation due to Earth's passages in the BAT FOV. We develop a simple Earth's emission model based on COMPTEL and EGRET observations of the Earth's Albedo. The model, which is also based on a detailed Monte Carlo simulation, allows us to investigate the shape of the CXB and Earth's spectra. We find that the BAT and the HEAO-1 CXB spectra are in excellent agreement. Additionally, we verify the value of the CXB flux in the 15–100 keV range adopting an approach similar to the one recently used by INTEGRAL and BeppoSAX (Churazov et al., 2006a; Frontera et al., 2006). This procedure confirms our previous result.

Remarkably, this study also shows that all the available measurements in the > 10 keV range agree with the BAT CXB spectrum after correcting for different Crab normalizations and residual Earth's emission. The new analyses of COMPTEL and EGRET data (Weidenspointner et al., 2000; Strong et al., 2004) show that the formula suggested by Gruber et al. (1999) for the diffuse X- and gamma-ray backgrounds is only valid in the < 2 MeV energy range.

Our study also derives the Earth's Albedo spectrum averaged over magnetic latitude. The BAT spectrum is in agreement with all the previous observations performed by satellites flying at similar LEO orbits. This work shows that the Earth's spectrum declines at energies $>$40 keV as a power-law with photon index of $\sim$1.7 and not as 1.4 as previously thought. A re-analysis of the measurements performed by Imhof et al. (1976) is in perfect agreement with the BAT Earth's spectrum. The good agreement among all the available measurements allows to use the BAT Earth's spectrum to predict background contribution from the Earth for other instruments.

Bibliography

Ajello M., et al. , 2007, in preparation

Alexander, D. M., Bauer, F. E., Brandt, W. N., et al. 2003, AJ, 126

Antonucci, R. R. J., 1993, ARA&A, 31, 473

Barthelmy, S. D., et al. 2005, SSRv 120, 143

Comastri, A., et al. 1995, A&A, 296, 1

Churazov, E., et al., 2006a, astro-ph/0608250

Churazov, E., et al., 2006b, astro-ph/0608252

Frontera, F., et al., 2006, astro-ph/0611228

Fukada, Y., et al. 1975, Nature, 254, 398

Gehrels, N., 1985, NIMP, 239, 324

Gehrels, N., 1992, NIMP, 313, 513

Gehrels, N., et al. 2004, ApJ 611, 1005

endreau, K. C., et al. 1995, PASJ, 47, 5

Giacconi, R., Gursky, H., Paolini, F. R.,Rossi, B. B. 1962, Phys. Rev. Lett., 9, 439

Giacconi, R., et al. 2002, ApJS 139, 369

Gilli, R., Comastri A. & Hasinger, G., A&A in press, astro-ph/0610939

Gruber, D. E., et al. 1999, ApJ, 520, 124

Hasinger. G. 2004, Nuc. Phys. B Proc. Supp., 132, 86

Jung, G. V., 1989, ApJ, 338, 972

Kinzer, R. L., et al. 1997, ApJ, 475, 361

Imhof, W. L., Nakano, G. H., & Reagan, J. B. 1976, J. Geophys., 81, 2835

Marshall, F. E., et al. 1980, ApJ, 235, 4

Pal, Y. 1973, Int. Astron. Union Symp. 55, 279, 1973

Petry, D. 2005, in AIP conference proceedings, 745, 709

Sazonov, S., et al., 2006, astro-ph/0608253

Shaw, S. E., et al. 2003, A&A, 398, 391

Schönfelder, V., Graser, U, & Daugherty, J., 1977, ApJ, 217, 306

Schwartz D. A., & Peterson, L., 1974, ApJ, 190, 297

Strong, A. W., et al. 2004, ApJ, 613,956

Treister E. & Urry M., 2005, ApJ 630, 115

Revnivtsev, M., et al. 2003, A&A 411,, 334

Watanabe, K., et al. 1997, AIP Conference Proceedings, 410, 1223

Weidenspointner, G., et al. 2000, AIP Conference Proceedings, 510, 467

Willis, D. R., 2002, PhD thesis, Dept. of Physiscs and Astronomy, University of Southampton, UK.

Worsley, M.A., et al. 2005, MNRAS 357, 1281

Conclusions and Outlook

Conclusions

In this work I have developed a new method to detect and analyze the hard X-ray sources revealed by Swift-BAT and studied different aspects of the Cosmic X-ray background (CXB). In the current understanding the CXB radiation arises from the integrated emission of all the Active Galactic Nuclei (AGN) present in the Universe. Current evidence points toward the existence of a *yet undetected* population of highly obscured (Compton-thick, $N_H > 1.5 \times 10^{24}$ H-atoms cm^{-2}) AGN. These sources are normal AGN viewed at an angle such that our line of sight passes through a dense, Compton-thick, torus which absorbs most of the emitted radiation below 10 keV. The density of such AGN is inferred from population synthesis models which try to reproduce the intensity of the CXB (in particular around 30 keV).
In this thesis, I investigated the density of such a population of Compton-thick AGN by direct detection of such objects in the 15-200 keV band, realized 1) by imaging techniques and then 2) by spectral and statistical analysis of the detected source sample; and finally 3) performing a new accurate measurement of the CXB background spectrum.

Surveys at > 10 keV can provide an unbiased census of the AGN population since the emitted radiation is, above this energy, unaffected by obscuration. Unfortunately, the impossibility (at present) of focusing hard X-rays limits greatly the sensitivities of such surveys. The launch of the Burst Alert Telescope (BAT) hard X-ray detector, on board the *Swift* mission, has opened a new window on the hard X-ray sky. The expectations that it would provide the first sensitive all-sky survey in the 15-200 keV band are being fulfilled day-by-day. In order to take the maximum advantage from the BAT survey I developed an imaging reconstruction algorithm based on the Maximum Likelihood (ML) method which allows to reach the statistical limit of the survey. The ML approach preserves the full statistical information in the data and allows to reduce the systematic noise connected to image mosaicking techniques which other methods cannot avoid. The first part of the

thesis is centered around the implementation of the ML method. This method is used to reconstruct, in the 14–170 keV band, the image of a 90x90 deg^2 region of the sky which BAT surveyed to $\sim$ 1 Ms of exposure. The study was conducted in parallel to a campaign for optical spectroscopic identification of BAT-selected extragalactic objects.
The full analysis of the noise properties of the image shows that this survey is the most sensitive for a given exposure time and that systematic noise is negligible. 61 hard X-ray sources are detected above the 4.5 σ threshold and only 12 of them were previously known as hard X-ray emitters. Monte Carlo simulations show that at most 1 out of the 61 source candidates is a spurious detection. I showed that the correlation of our source sample with the ROSAT-PSPC (0.1–2.4 keV) All-Sky Survey Bright Source Catalog provides reliable counterparts for 30 objects. This also denotes the presence of photoelectric absorption in at least half of the sample. *Swift*-XRT observations (0.1–10 keV) allowed to firmly identify the counterpart for additionally 7 sources.

In the second part of the thesis a method to extract accurate X-ray spectra for all the detected sources is presented and an analysis of the statistical properties of the sample is performed. Whenever archival data from sensitive soft X-ray observations (ASCA, *Swift*-XRT and BeppoSAX) were available, I produced a joint fit to soft and hard (BAT) X-ray data. Analysis of the X-ray colors shows that the population of Compton-thick sources may represent a fraction as high as 20% of the total AGN population. In order to support this claim with observational data, I performed a stacked X-ray spectral analysis of the 3 classes of emission line AGN detected in our survey: Seyfert-1 (Sy1), Seyfert-2 (Sy2) and candidate Compton-thick objects. This analysis reveals that: Sy2 sources have harder spectra than Sy1 objects and show evidence of moderate absorption along the line of sight ($N_H \sim 10^{23}$ H-atoms cm^{-2}); on the other hand the stacked spectrum of candidate Compton-thick sources shows evidence, in the lowest energy channels (14–22 keV) , of photoelectric absorption by Compton-thick matter. In order to exclude that instrumental effects or systematic errors were biasing the analysis I extracted the spectra of two bright well known Compton-thick sources (the Circinus galaxy and NGC 4945). These two spectra are not only in agreement with previous observations, but clearly reveal the Compton-thick nature of the sources. The photoelectric cut-off present at low energy (E$<$30 keV), in the spectra of these known sources, is very similar to the one found in the stacked spectra of candidate Compton-thick sources. Thus, this analysis shows that BAT is currently the only operational instrument which can reveal new Compton-thick objects by detection of the photoelectric cut-off. The fraction of Compton-thick sources is, from this analysis, bound in the range 10–20%; the determination of the exact value must await

sensitive soft X-ray observations to confirm the nature of the sources. Proposed XMM-Newton observations of 7 candidate Compton-thick sources were accepted and will be performed in 2007.
The $<V/V_{MAX}>$ test additionally shows that the significance threshold used for detecting sources was correctly set. The sample of sources detected away from the galactic plane ($|b| > 15^{\circ}$), is used to construct the cumulative source count distribution (also known as logN-logS relation). This shows that the AGN density, above fluxes of 10^{-11} erg cm^{-2} s^{-1}, is 0.0287 deg^{-2} and that the AGN spatial distribution is in agreement with the Euclidean distribution. Moreover, at the current flux limit of $\sim 2 \times 10^{-11}$ erg cm^{-2} s^{-1}, BAT resolves only 1–2% of the CXB emission into AGN in the 14–170 keV band. In order to resolve a bigger portion of the CXB emission in point sources, one would need an instrument able to probe, in the hard X-ray band, fluxes of the order of $\sim 10^{-13}$ erg cm^{-2} s^{-1}. This kind of measurement has to wait for the next generation of hard X-ray missions like eROSITA or Simbol-X. In the meantime, important information can be derived from the statistical properties of hard X-ray selected AGN. A sub-sample of 21 extragalactic sources which is 90% complete (i.e.: 90% of the sources have also an optical classification) can be used to derive statistically solid quantities. The analysis shows that the BAT AGN sample is truly local (mean redshift is 0.031) and that 2/3 (12/18) of Seyfert galaxies are of type-II. Intrinsic absorption is present in $\sim$ 63% of the AGN; this is lower than the 75% predicted by the Unified AGN model, but in agreement with previous measurements. Highly luminous highly absorbed QSOs, which are thought to give an important contribution to the CXB emission, were never found in large numbers in the past. This survey suggests that the fraction of these objects could be in the 5-15% range of the total population. However, the uncertainty on this value is given by the lack of sensitive observations in the 2–10 keV range which does not allow to derive a solid estimate of the absorption for 3 QSO candidates.

The last part of the thesis is devoted to derive a new spectrum of the CXB emission in the 15–150 keV range from *Swift*/BAT data. This measurement is of interest because the intensity of the CXB peak at $\sim$30 keV is the only observational evidence used to constrain the density of Compton-thick objects. Moreover, the last measurement of the CXB spectrum in hard X-rays dates back to 1980[3] and many authors have recently questioned its correctness. Measurements in hard X-rays are generally difficult as presently flying instruments do not have a simple way to discriminate the CXB radiation from other components of the instrumental background. Thus, the typical approach is to produce

[3]Revised analyses of the same data were performed more recently.

an *ON-OFF* measurement where the difference between the *ON* and the *OFF* pointings cancels the instrumental background. For wide field of view telescopes, the observation of the Earth provides a suitable *OFF* pointing. Unfortunately, above 10 keV the Earth is a powerful emitter of X-rays due to Cosmic Ray bombardment of its atmosphere. This severely limits this technique since an assumption on both type of spectra (the CXB and the Earth's emission) has to be made. This is the technique adopted in the recent (2006) measurements of the CXB emission performed by the INTEGRAL and the BeppoSAX satellites. Both measurements test the normalization of the CXB spectrum, but not its spectral shape. In this thesis, BAT data are used to derive the CXB and Earth's spectra using the Earth occultation technique. The difference between this measurement and the previous ones is that a detailed Earth's emission model is used to disentangle the two (CXB and Earth's) spectra without prior knowledge of their spectral shapes. The Earth model is based on well known observational facts. In particular, it is well known that the Earth's limb is brighter (in X-/gamma-rays) than the central part of the Earth (disk). Moreover, the Earth's X-ray flux is expected to correlate with cut-off rigidity as the parent Cosmic Ray flux does. Both effects (bright limb and modulation of the Earth's flux with rigidity) are present in BAT data and thus they can be used to characterize the Earth model. This analysis is also based on a thorough knowledge of the BAT orbital background and of its variability along the orbit. The resulting CXB spectrum is in excellent agreement with the previous HEAO-1 measurement; moreover, all recent measurements are in agreement with the BAT one when taking into account instruments' inter-calibrations and neglected Earth's emission. Thanks to this approach, BAT is the only instrument after HEAO-1 able to produce a measurement of the CXB spectral shape. Indirect confirmation of the goodness of this study comes from the analysis of the Earth's X-ray spectrum. The BAT spectrum is the best measurement of the Earth emission in hard X-rays. The very few measurements available (some date back to 1970) are all in agreement with the BAT spectrum. My analysis shows that the Earth's X-ray spectrum declines above 40 keV as a power law with photon index of 1.7 instead of 1.4 as commonly believed. This finding is independently confirmed by a re-analysis of *1972-076B* satellite data which constitutes the only good-quality Earth's data (excluding BAT). The original author's measurement was biased by the use of a wrong CXB spectrum; when using the correct CXB spectrum the *1972-076B* measurement is in excellent agreement with the BAT spectrum confirming the 1.7 power law spectrum at high energy. All this confirms that this dual analysis (the CXB and Earth's emission spectra) is one of the most sensitive ever performed in this energy range.

Outlook

This study represents a step towards the understanding of the "missing" AGN population. Whether there are enough Compton-thick AGN to explain the unresolved fraction of the CXB depends primarily on the detection of new objects. The new Compton-thick candidates found in this study may account for the "missing fraction" of Compton-thick AGN (10% is the observed fraction while 20% is what is predicted by theory). However, an answer to such a delicate question needs always an independent confirmation. I thus proposed and obtained, as part of the INTEGRAL key programmes, a 6 Ms INTEGRAL observation (3-300 keV) of the North Ecliptic Pole (NEP). This observation should not only produce the deepest and most sensitive hard X-ray observation to date, but its primary goal is to constrain, in a very well studied extragalactic region, the fraction of Compton-thick sources.

A survey always unveils all kind of different objects. Among the most interesting ones found in this work, I can report about the high redshift Blazars. Blazars are part of the AGN family, but have a jet of matter moving at relativistic speed pointing towards us. The emission process which explains the observed Blazar properties is, probably, Inverse Compton scattering of low energy photons off relativistic electrons. This produces a spectrum which peaks at MeV-GeV energies. The objects which are detected by BAT lie at high redshift (≥ 1) and have their peak emission redshifted into the the BAT energy band (15–200 keV). Given the high redshift (and other properties like radio-emission, etc.) Blazars constitute, in the BAT survey, a completely different population with respect to the Seyfert-like AGN. A proposed 1 Ms INTEGRAL observation of the most luminous high redshift gamma-loud Blazar ever discovered has been approved and partially performed. This observation has not only the goal of understanding the acceleration mechanism of such powerful class of objects, but also to study the mean properties of Blazars detected in the BAT survey. Indeed, Blazars which are thought to produce most of the extragalactic background at MeV–GeV energies, constitute a fraction close to 10% of the total AGN population detected in the BAT survey. This fraction is, at present, equivalent to the fraction of Compton-thick sources and thus its contribution to the CXB emission should be evaluated in the future.

It is also worth to mention that the effort to identify the newly detected objects of this work will continue. This will provide new insights on the source populations detected by

BAT. In particular, I do expect, considering the source locations and X-ray colors, that a relevant fraction of the unidentified sources be of Galactic origin. As this work shows, a good fraction of them could be Cataclysmic Variables (CVs). This is today of extreme interest as some authors claim that the Galactic ridge X-ray emission is not truly diffuse, but produced by millions of low luminosity objects (in particular CVs).

Though it is always a blind guess to estimate the long-term performances of an instrument (background-dominated) like BAT, there are good expectations that after three years BAT will have acquired a deep quite uniform exposure of the whole sky. Considering the density of AGN, as determined by this work, and a mean exposure of 2 Ms, the BAT extragalactic catalog should count more than 500 sources. With such statistics BAT can pose tight constraints on the number of Compton-thick objects, the shape of the absorption distribution and the anticorrelation of luminosity and absorption.

Appendix A

Calibration of the MEGA ACS

In Section 2.3 we have studied how the instrumental background, the dead-time and the effective area affect the instrument's sensitivity. Since in the gamma-ray energy range the fluxes from astronomical sources are generally much smaller than the instrumental background, it is necessary to make every effort to suppress the orbital background to achieve the best sensitivity. Background suppression can be achieved using passive or active shielding. In passive shieldings, the suppression is obtained through absorption of radiation and charged particles in the materials of the shielding. The active systems use scintillator materials coupled to photo-multipliers to detect charged particles; once a background event is detected a veto signal is issued to block the data acquisition. Two similar instruments, BAT and IBIS (on board the *Swift* and INTEGRAL missions), employ a passive and active system respectively. Most classical gamma-ray telescopes like COMPTEL or EGRET (Schönfelder et al., 1993; Kanbach et al., 1988) on CGRO have been equipped with large anticoincidence systems made of plastic scintillators in the form of domes surrounding the detector units.

Here, we describe the calibration of the Anticoincidence system (ACS) planned to be used during a balloon flight for the MEGA prototype. Such study is also of interest because the Gamma-ray Large Area Space Telescope (GLAST, Thompson 2004), planned to be launched in October 2007, employes a similar ACS to suppress the orbital background.

A.1 MEGA

The *Medium Energy Gamma-ray Astronomy* (MEGA) instrument is a telescope sensitive in the 0.4–50 MeV energy band (Kanbach et al., 2004). MEGA is designed as a successor of COMPTEL and EGRET (low energies) in order to fill the severe sensitivity gap between the operating and scheduled hard X-ray and gamma-ray missions. Fig. A.1

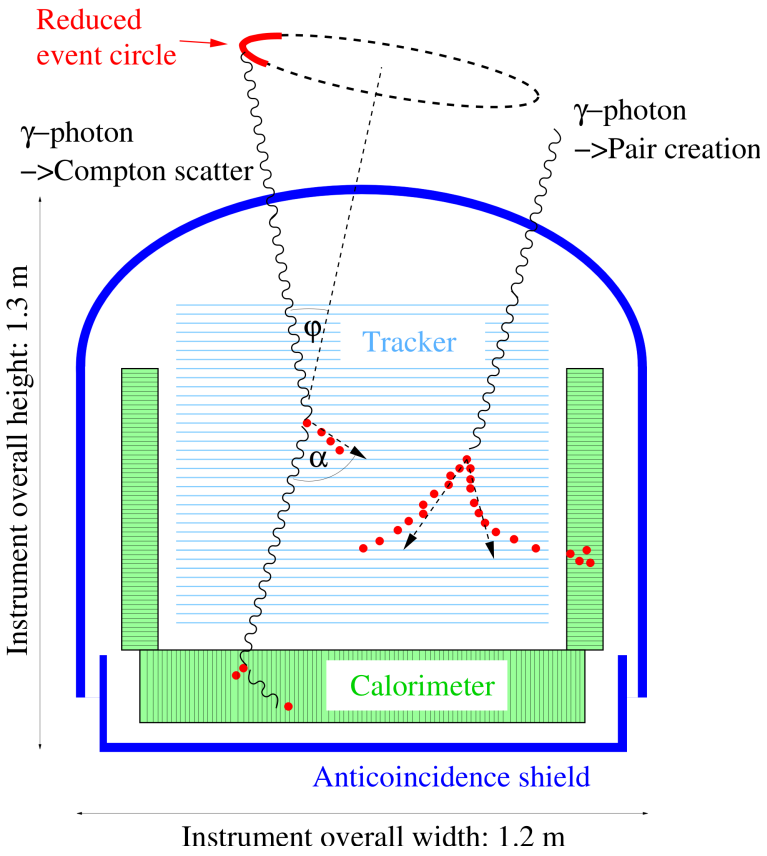

Figure A.1: Schematic drawing and working principle of MEGA.

shows the design and the working principle of the MEGA telescope. In the 0.4–50 MeV energy range, MEGA exploits the two dominating interaction mechanisms for gamma-rays: Compton scattering and Pair creation. To fulfill this purpose best, MEGA has two detectors: a tracker, consisting of double-sided silicon strip detectors, and a calorimeter, consisting of highly segmented CsI(Tl) bars. In case of Compton interaction the tracker measures the vertex position, energy and momentum vector of the electron while the scattered photon interactions are recorded in the calorimeter. From the positions and energies of the correctly sequenced interactions the incident photon direction is computed from the Compton equation. The primary photon's incident direction is either constrained to an "event circle" (untracked primary electron) or to an "event arc" as shown in A.1. Since the electron scattering direction occurs preferentially perpendicular to the direction of the electric vector of the incoming photon, MEGA can also be used as a polarimeter.

In the case of pair production, the incident photon converts into an electron-positron pair in the tracker. The momenta of the pair particles are tracked and determine the incident photon direction. The total energy is given by the total deposit in the tracker

and/or in the calorimeter.

As a proof of concept a prototype of the MEGA telescope has been built and fully calibrated (Zoglauer, 2005; Andritschke, 2006). The prototype tracker contains 11 layers with 3×3 arrays of 500 μm thick silicon wafers, each $6 \times 6\,\mathrm{cm}^2$ in size and fitted with 128 orthogonal p and n strips on opposite sides. A typical energy resolution of 15–20 keV full-width-half-maximum (FWHM), a position resolution of 290 μm and a resolution time of $\sim$1 μs was achieved. The prototype calorimeter consists of 20 modules, each with an array of 10×12 CsI(Tl) scintillator bars of cross-section 5×5 mm^2. The upper side modules are 2 cm deep, the lower side wall 4 cm, and the bottom calorimeter is 8 cm deep. Depending on type, the energy resolution of the calorimeter varies between 40 and 100 keV for 0.5–1.3 MeV photons.

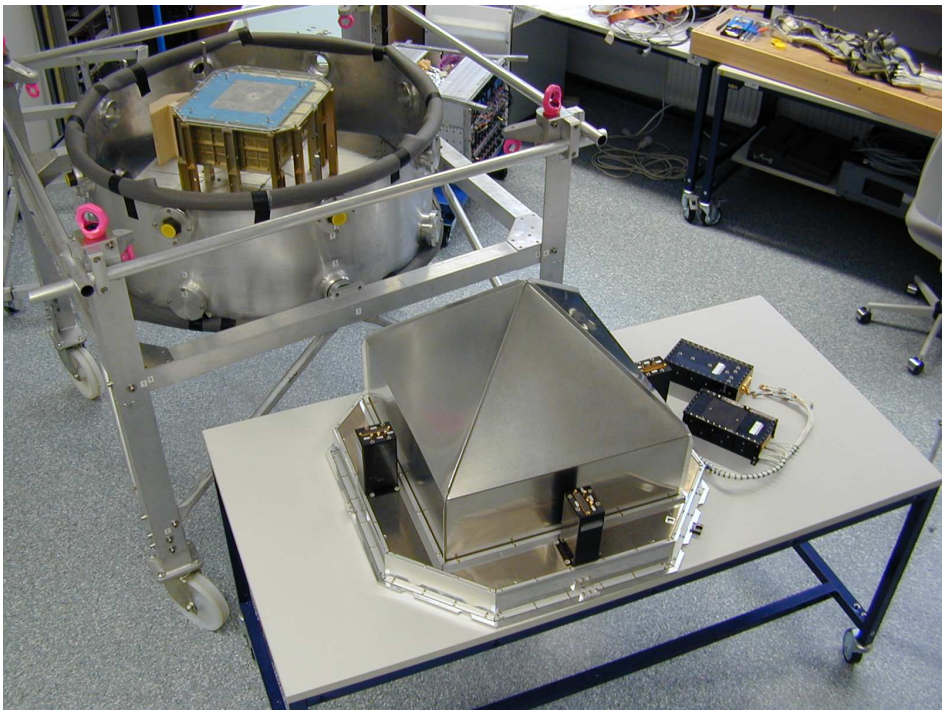

Figure A.2: Photograph of a model of the MEGA prototype inside the open pressure vessel. The upper part of the ACS is shown on the table. The black boxes attached to the ACS are the EGRET PMTs while those on the table are the Main Electronic Box (MEB) and the Low Power Control (LPC).

A photograph of the prototype detector integrated on a robust support structure, which allows to transport and handle the telescope in beam test calibrations and on a balloon payload, is shown in Fig. A.2.

A.2 Anticoincidence Shield

The MEGA prototype is equipped with an Anticoincidence Shield (ACS) to suppress the background generated by the impact of charged cosmic rays and other energetic particles. The ACS surrounds completely the tracker and the calorimeters. The upper part of the ACS comprises 4 panels while a single flat panel is placed below the tracker. The ACS has a base with an area of $625 \times 625\,\mathrm{mm}^2$ and height of 620 mm. It is made of 0.5 in plastic scintillator plates (Bicron BC 412) with a maximum emission wavelength of 434 nm and a refractive index of 1.58. Light collection is achieved through wavelength shifting fibers which are glued internally with a pitch of 1 cm. The fibers are the Bicron BCF-92 which shift the emission peak to 492 nm and yield a decay time of $\tau = 2.7$ ns. The fiber assembly is shown in the left panel Fig. A.4 where the bundling of the fibers onto the PMT attachments is visible. The right panel of the same figure shows a drawing of the MEGA prototype surrounded by the ACS. The photo-multipliers tubes (PMTs) are spare units from the EGRET satellite project (Kanbach et al., 1988). The electronic boxes are also flight spare modules from EGRET, one is the Main Electronic Box (MEB, responsible for the pulse forming) and the other is the Low Power Control (LPC). The signals from the PMTs are summed for the upper ACS unit (PMT 1–4) and for the lower plate (PMT 5–6) separately. These 2 vero signals are fed into the MEGA coincidence unit where the upper signal is treated as an absolute veto. The lower plate veto signal can be enabled or ignored by commanding the coincidence unit. This is done in order to avoid the self-veto of high-energy pair creation events. A schematic of the ACS electronic is shown in Fig. A.3. The use of the fibers favours the uniformity of the response over the whole ACS

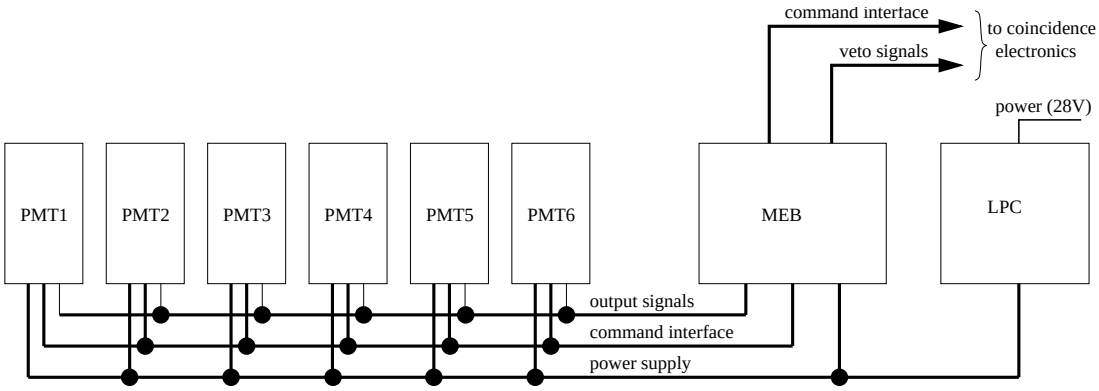

Figure A.3: Schematic of the ACS electronic (Andritschke, 2006).

surface. This solution was adopted after the experience with the EGRET ACS. Indeed the EGRET ACS (which did not use fibers and achieved light collection through internal

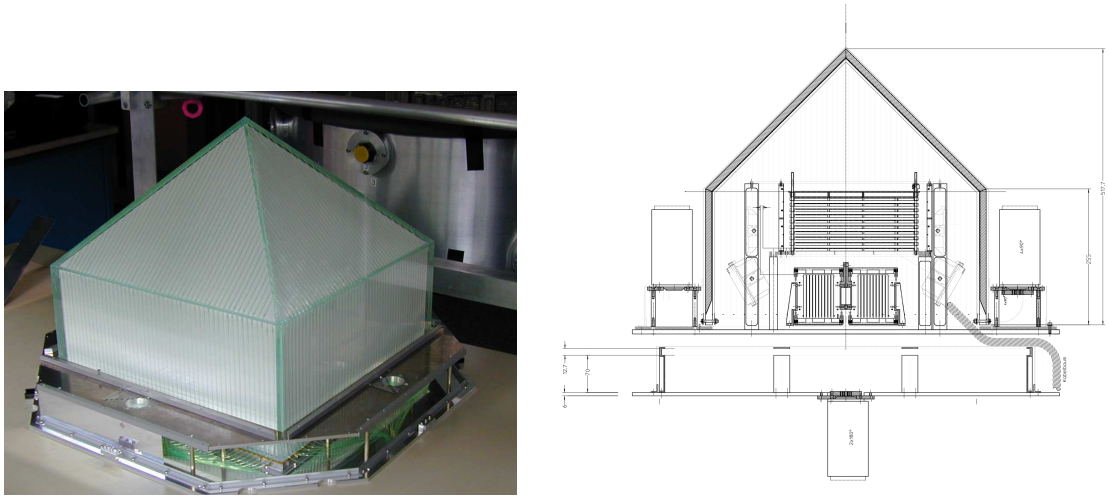

Figure A.4: *Left Panel:* View of the (uncovered) upper part of the ACS. *Right Panel:* Technical drawing of the MEGA prototype surrounded by the ACS.

light reflection) observed a sharp variation in energy threshold as a function of hit position. This is clearly shown in Fig. A.5 where the energy threshold varies of a factor ~ 20 with the distance from the PMT. This variation is mostly due to internal light absorption and reflection loss over a long path.

A.2.1 Uniformity measurements

We measured the uniformity of the response of each ACS face. The measurement was performed moving a ^{133}Ba radioactive source (37.7 MBq) over each ACS panel with a pitch of 2.5 cm. At each point, we measured the count rates registered by the PMT connected to the ACS face being tested. Each measurement was corrected for the environmental background. The radioactive source was collimated using a 5 cm thick lead collimator with an approximate solid angle of 0.003 sr. Figure A.6 shows the setup of the experiment.

In the energy range of interest (> 50 keV), ^{133}Ba emits gamma-rays after an electron capture with the following energies (and probabilities): 81 keV (34%), 276.4 keV (7%), 302 keV (18%), 356.01 keV (61.9%), 383.85 keV (9%). Before performing the measurement we verified that there was no leakage of gamma-rays through the lead collimator. We checked this by monitoring the registered count rate as a function of the collimator distance from the ACS. We determined that the radiation leaking through the collimator was negligible as the count rate remained stable from 2 cm to 50 cm.

Fig. A.7 and A.8 show the result of our measurements for the upper and lower part

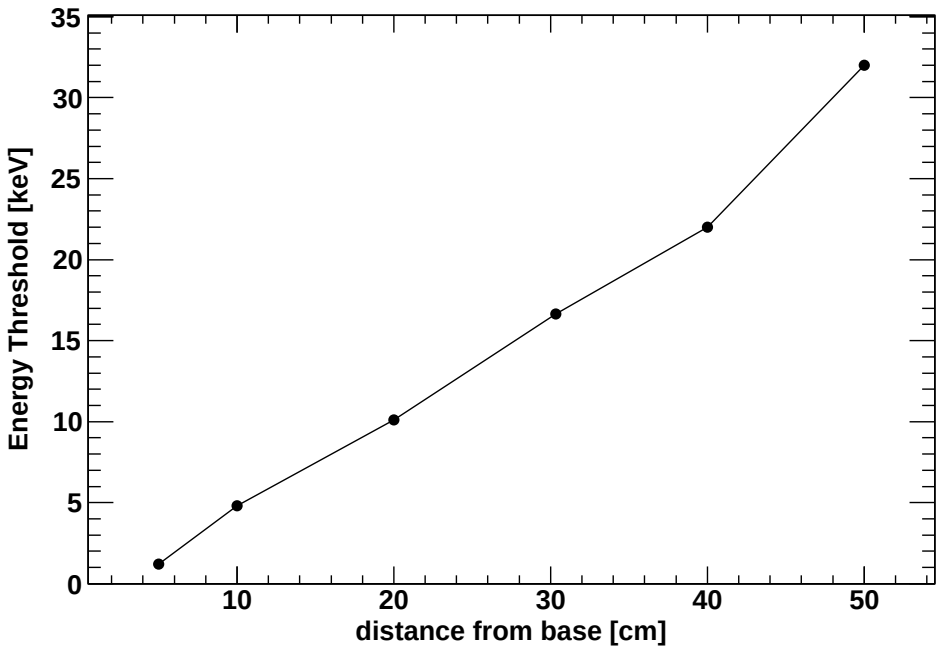

Figure A.5: EGRET-ACS energy threshold as a function of the distance from the base where the PMTs are located. Datapoints are from G. Kanbach (private communication).

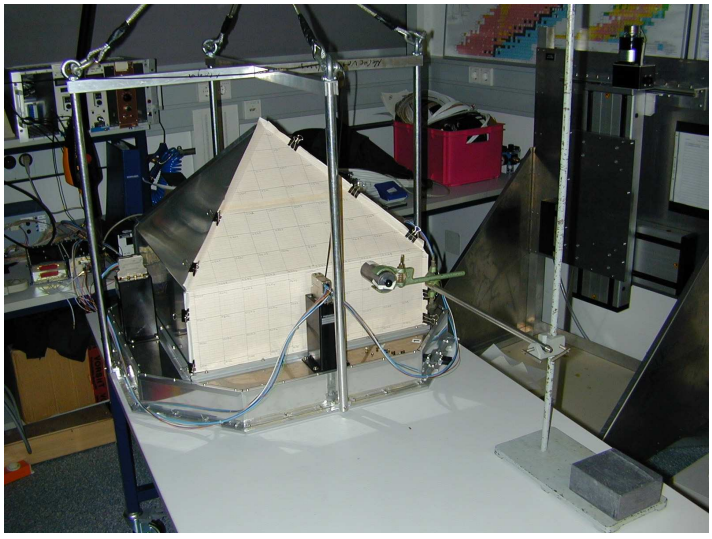

Figure A.6: Experimental setup for the uniformity measurement.

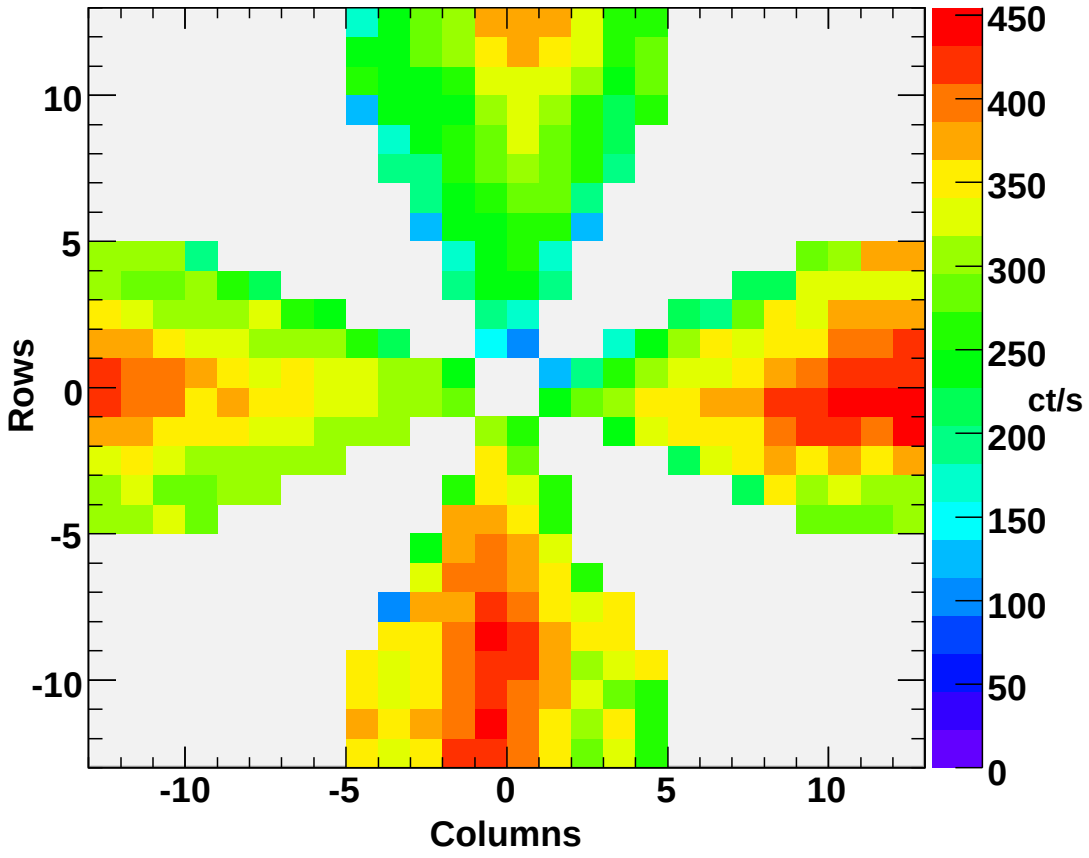

Figure A.7: Background-subtracted count rate as a function of beam position. Units are ct/s. The most sensitive regions of the ACS are generally those located closely to the PMTs (*zero* positions of the *Rows* and *Columns* axes).

of the ACS respectively. There is a noticeable increased sensitivity in the regions close to the PMT positions due to a better light collection. The differences of the registered rates between different faces is consistent with the diverse sensitivities of the 6 PMTs. We verified this measuring cosmic ray (CR) events with the 6 PMTs attached in turn to the same plastic scintillator.

In order to take into account the different PMTs sensitivities we divided the detected rates by the mean rate value of each ACS panel. The overall distribution is shown in Fig. A.9. The uniformity over the whole ACS surface is extremely good as 68% of all measurements are within 15% of the mean rate value of each face. However, we must note that the real ACS performances will be even better. Since the plastic scintillators are internally connected, some light can pass from one scintillator to the next one and

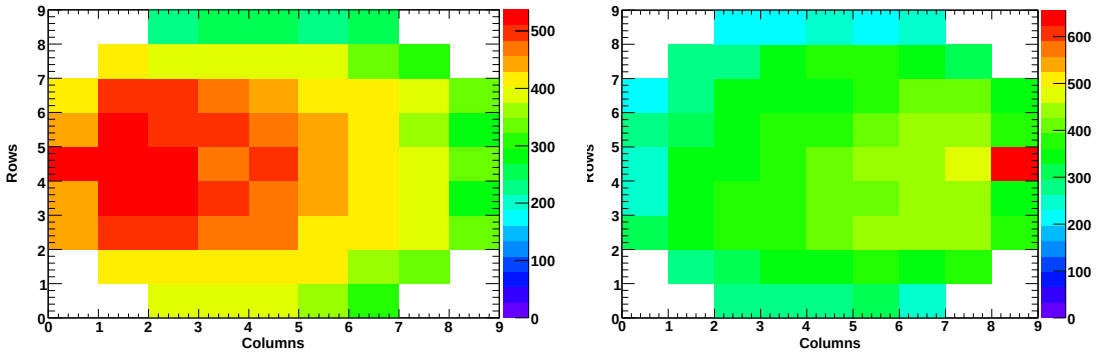

Figure A.8: Bottom panel of the ACS read out by the left-hand PMT (left) and the right-hand PMT (right). Units are ct s^{-1}.

generate a signal. Here this effect could not be noticed as we were reading only the PMT connected to the face on which we were performing the measurement.

A.2.2 Inefficiency measurements

The orbital background level an instrument will experience depends on the capability of the ACS to reject CR events. Thus, it is important to assess the ACS inefficiency (i.e. the number of undected events divided by the total number of events).

We set up a muon telescope using three scintillators/PMTs in the way shown in Fig. A.10 (pictures are shown in Fig. A.11). Between the lower PMTs we used a 5 cm thick lead plate to improve the overall efficiency for muons and stop any low-energy secondary or shower particles. The total number of detected events is given by the triple coincidence of the muon telescope. The number of ACS detected events is given by the coincidence of the ACS and muon telescope signals. We assessed the number of background events (most probably given by air showers) displacing the intermediate PMT so that muons (which travel straight) could not trigger the telescope. The efficiency measurement could only be performed for the upper part of the ACS as the lower part was already mounted inside the pressure vessel and there was no space left for mounting the muon telescope.

After correcting for background events, we derived the inefficiencies shown in Tab. A.1. Thus, the inefficiency vary in the range 0.1–0.7%. Again, we must note that the different values of inefficiency are due to the different PMTs used.

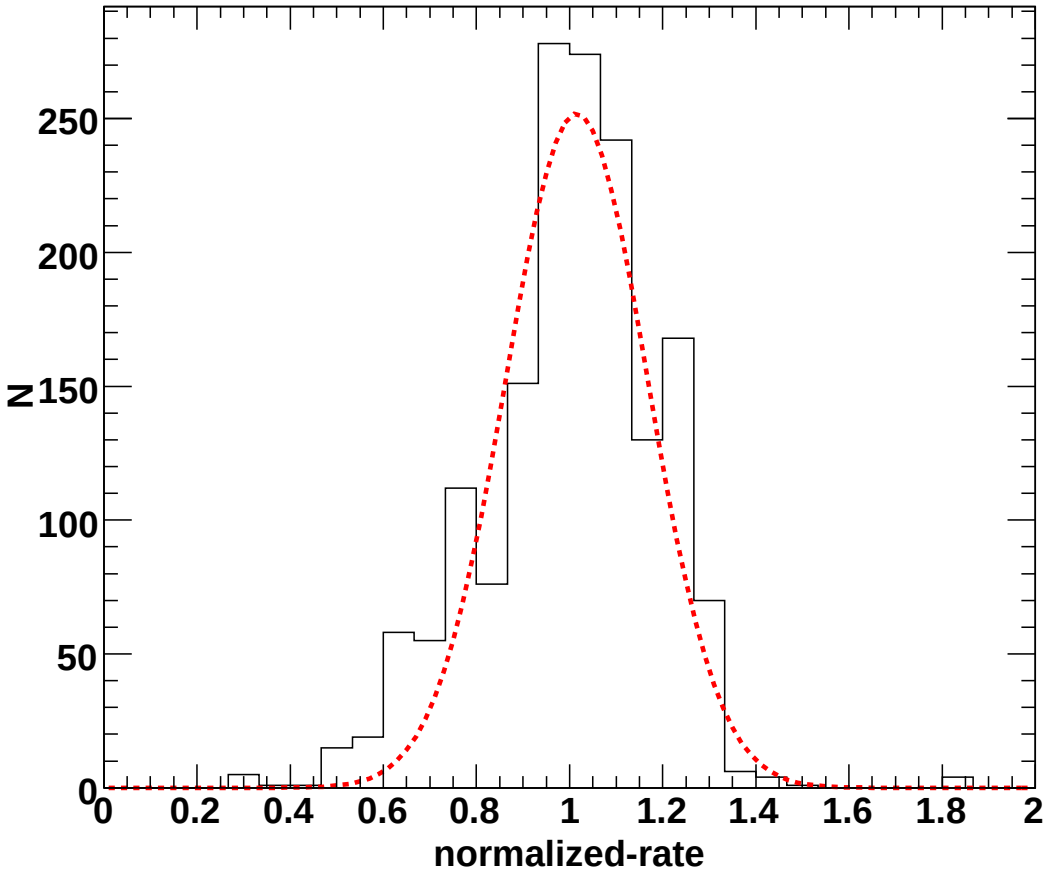

Figure A.9: Distribution of all uniformity measurements (Fig. A.7 and A.8) divided by the mean rate of each ACS panel to take into account the different sensitivities of the PMTs. The dashed line is a Gaussian fit to the distribution. The 1 σ width is 0.15.

Table A.1: ACS inefficiencies.

	Face A	**Face B**	**Face C**	**Face D**
Inefficiency	0.0068	0.00488	0.0036	0.0017

A.2.3 Energy Threshold measurements

In order to derive the energy threshold of the ACS, we performed a set of 3 measurements to calibrate the energy in the detector. The first measurement was done to evaluate the spectrum of the background while the other two were performed with ^{133}Ba and ^{57}Co

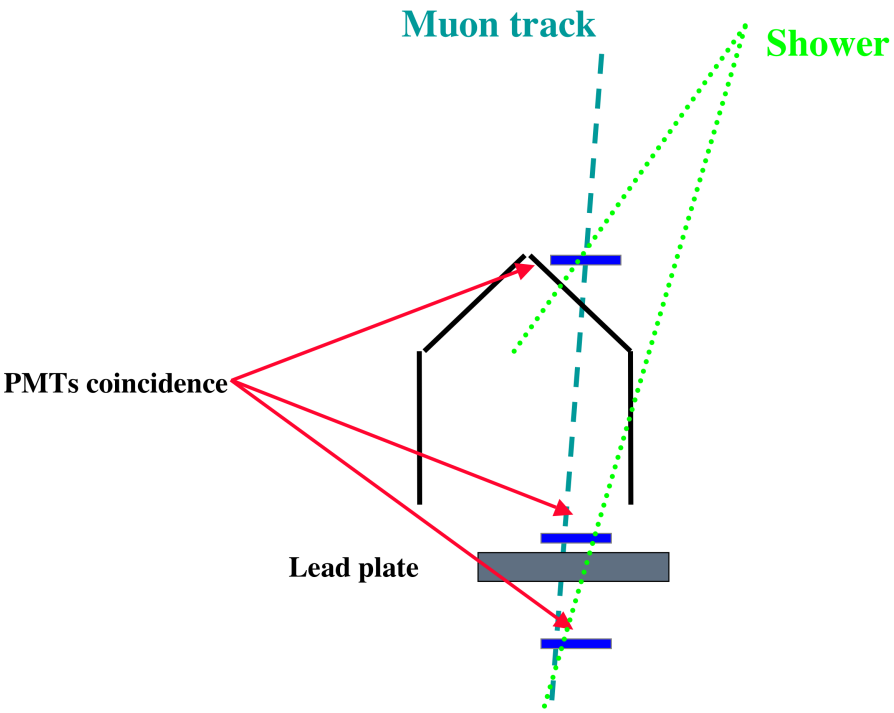

Figure A.10: Schematic of the muon telescope setup. A CR air-shower could be exchanged for a muon if secondary particles are detected in all three PMTs at the same time.

radioactive sources. The spectra taken with the radioactive sources are shown in Fig. A.12. The presence of a background line at high energy (consistent with ^{40}K) also allowed us to evaluate the non-linearities of the calibration. The relation used to calibrate the ACS is a quadratic fit to the energy-channel relation shown in Fig. A.13.

Once the ACS has been calibrated the energy threshold can be computed and this results to be around 70 keV. The energy resolution of the ACS is good, being 44.18 keV and 63.215 keV (FWHM) at 356 and 122 keV respectively.

A.3 Conclusions

The calibration highlighted the good performances of the ACS. The capability of the ACS to reject up to 0.993 of the particle background influences directly the final sensitivity of the instrument. Thanks to the use of wavelength shifting fibers, the efficiency is expected to vary only slightly over the whole ACS surface (with respect to its mean value).

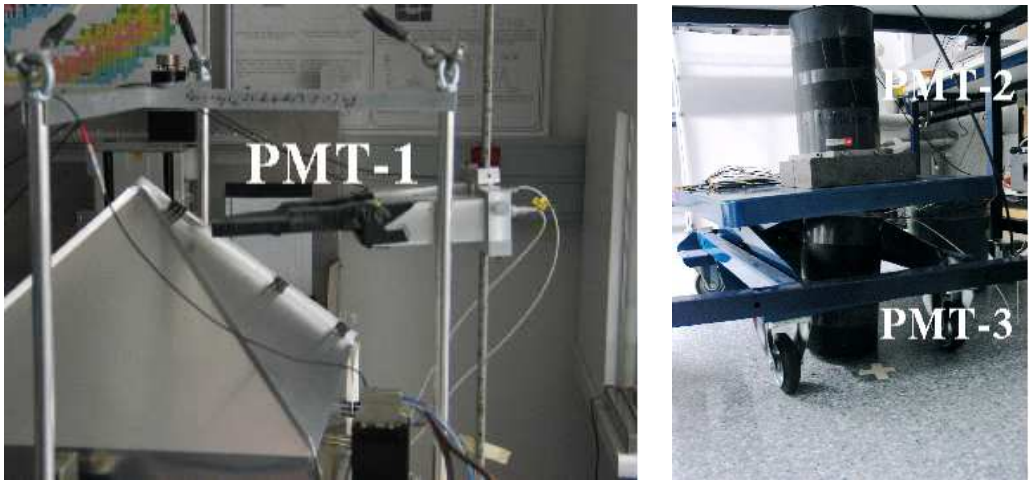

Figure A.11: Muon telescope set-up for the inefficiency measurement. The telescope consists of three PMTs. The upper one is shown on the left panel while the the lower PMTs are shown on the right. To reject events originated by low-energy secondary particles we inserted a 5 cm thick lead brick between the two lower PMTs.

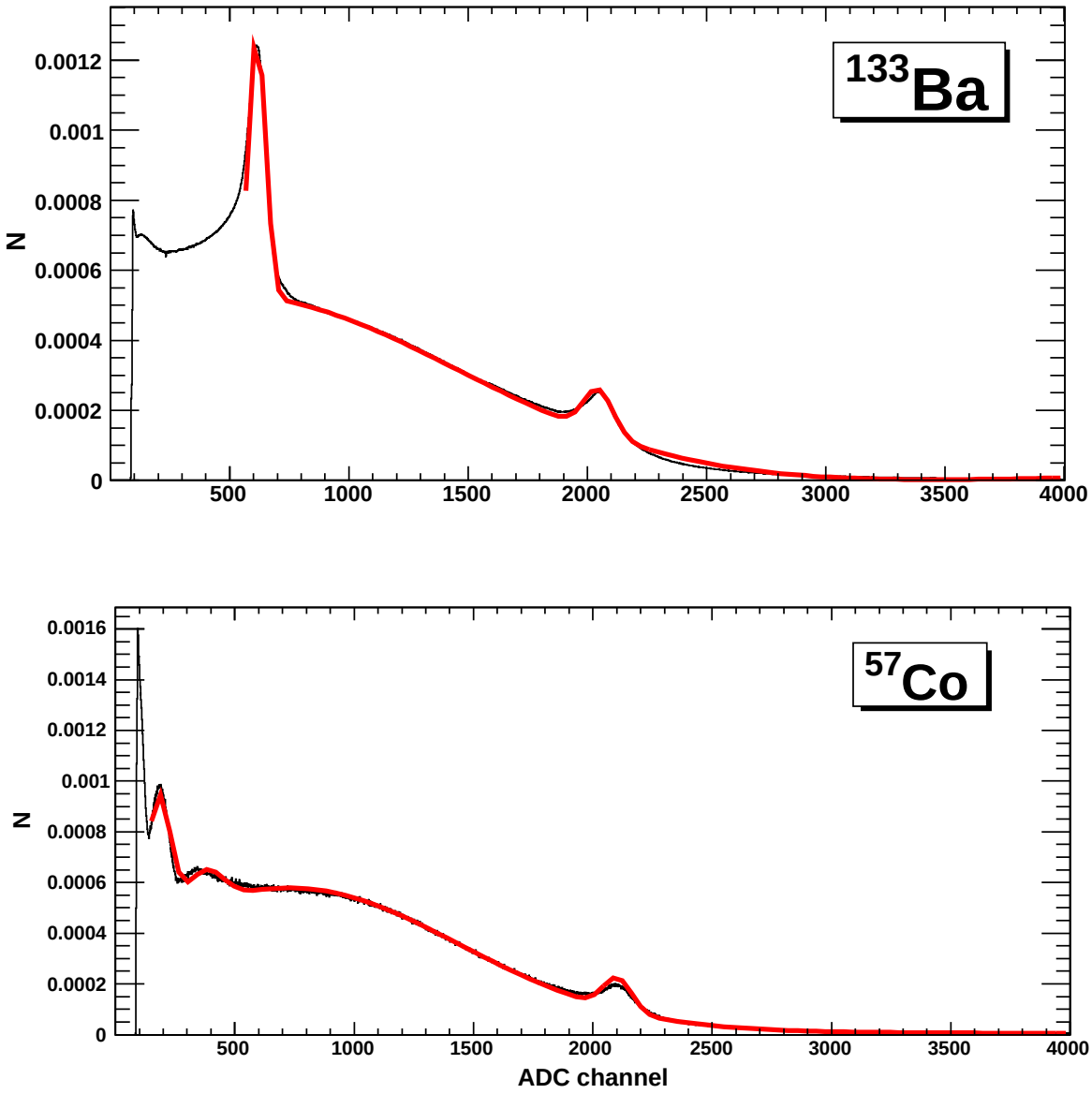

Figure A.12: ^{133}Ba (upper panel) and ^{57}Co (lower panel) spectra. The feature around 2200 ADC channels is consistent as being emission from environmental ^{40}K. The red solid line is a fit to the data.

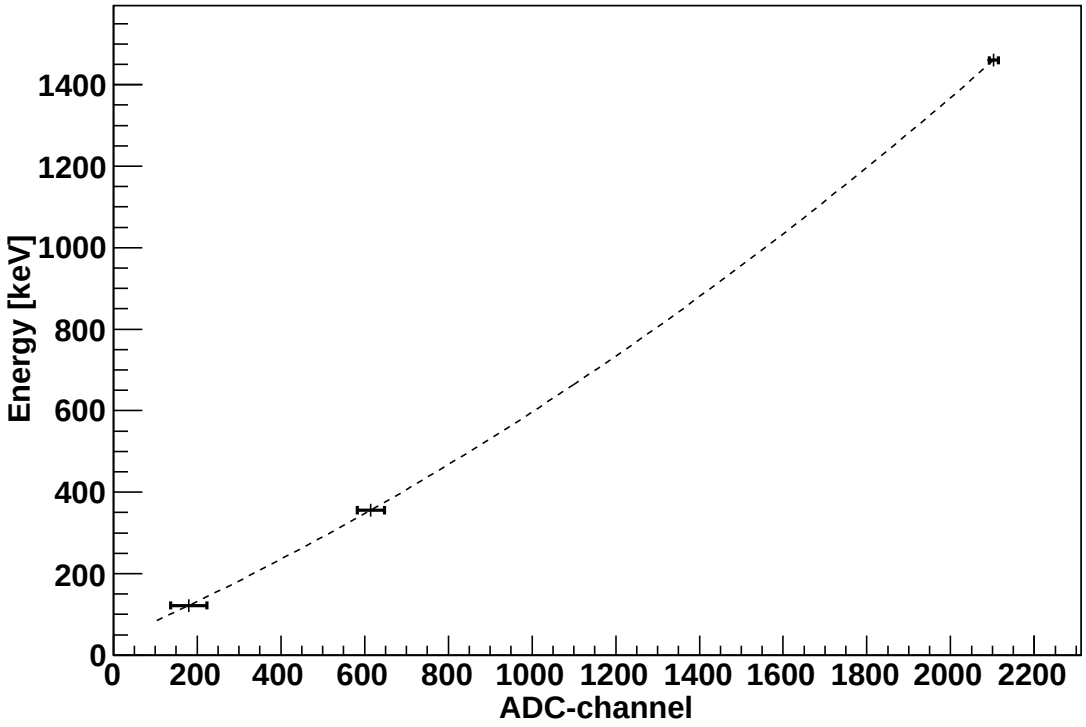

Figure A.13: ACS energy calibration. The datapoints are from the measurements using ^{57}Co, ^{133}Ba and ^{40}K (background line). The dashed line is quadratic fit to the data.

Bibliography

Ables, J. G., Proc. Astron. Soc. Australia **1** (1968), 172

Alexander, D. M., et al., AJ **122** (2001), 2156

Alexander, D. M., et al., AJ **126** (2003), 539

Andritschke, R., *Calibration of the MEGA prototype*, Dissertation thesis (2006), Technische Universität München, available at *http://www.mpe.mpg.de/gamma/instruments/mega/www/documents/thesis/-PhD_RobertAndritschke.pdf*.

Antonucci, R. R. J., & Miller, J., ApJ **297** (1985), 621

Antonucci, R. R. J., ARA&A **31** (1993), 473

Aschenbach, B., Rep. Proc. Phys. **48** (1985), 579

Baldwin, J. A, Phillips, M. M., & Terlevich, R., PASP **93** (1981),5

Barcons, X., Mateos, S., & Ceballos, M. T., & MNRAS **316** (2000), L13

Barger, A. J., et al., AJ **124** (2002), 1839

Barger, A. J., et al., AJ **129** (2005), 578

Barthelmy, S. D., et al., SPIE **4140** (2000), 50

Bassani, L., et al., ApJ **635** (2006), 65

Baumert, L. D., J. Appl. Math. **17** (1969), 826

Beckmann, V., et al., ApJ **638** (2006), 624

Bevensee, R. M., *Maximum Entropy Solutions to Scientific Problems*, Prentice Hall (1993), ISBN 0-13-563818-6

Boldt, E., *Phys. Rep.* **146** (1987), 215

Boyle, B. J., et al., MNRAS **260** (1993), 49

Brand, W.,N.,et al., AJ **122** (2001), 2810

Busboom, A., Exp. Astron. **8** (1998), 97

Burrows, D. N., et al., SPIE **4140** (2000), 64

Caroli, E., et al., SSRV **45** (1987), 349

Ceglio, N.M., et al., J. Appl. Phys. **48** (1977), 1566

Churazov, E., et al., (2006) astro-ph/0608259

Comastri, A., et al., A&A **296** (1995), 1

Comastri A., in Barger A. J., ed., Astrophys. Space Sci. Library Vol. (2004), 245

Daddi, E., et al., **600** (2004), 127

Dicke, R. H., ApJ **153** (1968), 101

Dwelly, T., & Page, M. J., MNRAS **372** (2006), 1755

Eckart, A., Genzel, R., & Schödel, R., PThPS **155** (2004), 159

Elvis, M., et al., ApJ **615** (2004), L25

Evans, I. N., et al., ApJ **369** (1991), 27

Fabian, A.C., et al., MNRAS **242** (1990), 14P

Fabian, A. C., MNRAS **308** (1999), 39

Fanaroff, B. L., & Riley, J. M., MNRAS **167** (1974), 31

Fath, E. A., LicOB **5** (1908), 71

Fenimore, E. E. & Cannon, T. M., Appl. Opt. **17** (1978), 337

Ford, H. C., et al., ApJL **435** (1994), 27

Forman, W., et al., ApJS **38** (1978), 357

Frontera, F., et al, A&AS **122** (1997), 357

Frontera, F., et al., submitted to Nature, (2006) astro-ph/0611228

Gandhi, P. & Fabian, A. C., MNRAS **339** (2003), 1095

Gehrels, N., NIM **313** (1992), 513

Gehrels, N., et al., ApJ **611** (2004), 1005

Giacconi, R., et al., PhRvL **9** (1962), 439

Giacconi, R., et al., ApJS **27** (1974), 37

Giacconi, R. et al., ApJ Letters **234** (1979), 1

Giacconi, R., et al., ApJ **139** (2002), 369

Giavalisco, M., et al., ApJ **600** (2004), 93

Gioia, I. M., et al., ApJS **72** (1990), 576

Gilli, R., Comastri A. & Hasinger, G., A&A in press, astro-ph/0610939

Golay, M. J. E., J. Opt. Soc. Am. **61** (1971), 272

Griffiths, R.E. et al., ApJ **269** (1983), 375.

Gruber, D. E., et al., ApJ **520** (1999), 124

Guainazzi M., Matt G., & Perola G. C., A&A, **444** (2005), 119

Jaffe, W., et al., *Nature* **364** (1993), 213

Jaffe, W., et al., IAU Proceeding **222** (2004), 37

Janesick, J. et al., *Optical and Optoelectronic Applied Scienec and Engineering Symposium; X-ray Instrumentation in Astronomy* (1988), SPIE, Bellingham, WA

Halloin, H. et al., Proceedings of the 5th INTEGRAL Workshop on the INTEGRAL Universe 16-20 (2004) edited by V. Schönfelder, G. Lichti & C. Winkler, 739

Hasinger, G., et al., *Astr.Ap.* **275** (1993), 1

Hasinger, G., et al., A&A **365** (2001), 45

Hasinger. G.,NuPhS **132** (2004), 86

Hasinger. G., Miyaji, T. & Schmidt, M., A&A **441** (2005), 417

Hickox R. C. & Markevitch M., ApJ **645** (2006), 95

Kanbach, G., et al., SSRv **49** (1988), 61

Kanbach, G., et al., NewAR **48** (2004), 275

Kappadatah, S. C., et al., in AIP Conf. Proc. **410**, Fourth Compton Symp., ed. C. Dermer, M. Strickman, & J. Kurfess (1997), 1218

Kauffmann, G., et al., MNRAS **353** (2004), 713

Keel, W. C, ApJ **269** (1983), 466

Kennea, J. A., et al. 2005, ATel, 677

Klein, K. L., & Trottet, G., SSRv **95** (2001), 215

Kinzer, R. L., et al., ApJ **475** (1997), 361

Kniffen, D. A., et al., A&A **120** (1996), 615

Kraemer, S. B., & Crenshaw D. M., ApJ, **544** (2000), 763

Kunieda, H., et al., *Nature* **345** (1990), 786

Inoue, H., et al., Experimental Astronomy **4** (1993), 1

Labanti, C., et al., A&A **411** (2003), 149

La Franca, F., et al., ApJ **635** (2005), 864

Lebrun, F., et al., A&A **411** (2003), 141

Lehmann, I., et al., A&A (2000), 354, 35

Levine, A. M., et al., ApJS **54** (1984), 581

Lucy, L. B., MNRAS **7** (1994), 31

Matt G., et al., A&A **377** (2001), 31

Matteson, j. L., AIAA 16th Aerospace Science Meeting (1978), 78-35

McHardy, I. M., et al., BAAS **12**, (1980), 835

Mainieri, V., et al., A&A **393** (2002), 425

Maraschi, L., Ghisellini, G., & Celotti, A., ApJ **397** (1992), 5

Markwardt, C. B., et al., ApJ Lett. **633** (2005), L77

Marshall, F.E. et al., ApJ **235** (1980), 4

Marshall, H., et al., SPIE **5165** (2004), 457

Mertz, L. & Young, N.O., *Proceedings of the conference on Optical Instruments and Techniques* (1962), edited by K. J. Habell , 305

Miller, J. S., et al., ApJ **378** (1991), 47

Morisawa, K., et al., *Astr.Ap.* **263** (1990), 299

Mushotzky, R.F., *Advances in Space Research* **3** (1984), 157

Mushotzky, R.F., et al., MNRAS **272** (1995), 9

Nandra, K., Ph.D. Thesis (1991), Leicester University

Owen, F. N., et al., ApJ **352** (1990), 440

Penrose, R., Proc. Cambridge Philos. Soc. **41** (1955), 406

Peterson, B., M., in *An introduction to active galactic nuclei* (1997), Cambridge University Press

Piccinotti, G., et al., ApJ **253** (1982), 485

Pounds, K. A., et al., *Nature* **344** (1990), 132

Ramsey, B. D., et al., SSRV **69** (1994), 193

Rees, R. J., Ann. Rev. Astr. Ap. **22** (1984), 471

Reichert, G. A., et al., ApJ **296** (1985), 69

Revnivtsev, M., et al., A&A **411** (2003), 329

Revnivtsev, M., et al., A&A **444** (2005), 381

Risaliti, G., et al., ApJ **522** (1999), 157

Roming, P., W., et al., SPIE **4140** (2000), 76

Rothschild, R. E., et al., *Space Sci. Instr.* **4** (1979), 269

Sazonov, S., et al., astro-ph/0608418

Sazonov, S., et al., astro-ph/0608253

Schwartz, D.A. & Tucker, W.H., Ap.J. **332** (1988), 157.

Schönfelder, V., ApJS **86** (1993), 675

Sembay, S., et al., SPIE **5488** (2004), 264

Setti, G. & Woltjer, L., A&A **224** (1989), L21

Seyfert, C. K., ApJ **97** (1943) , 28

Skinner, G., et al., SPIE **5168** (2003), 459

Strong A. W., A&A **411** (2003), 127

Tanaka, Y., et al., *Nature* **375** (1995), 659

Thompson, D. J., NewAr **48** (2004), 543

Tozzi P., et al., A&A **451** (2006), 457

Tran, H. D., ApJ **554L** (2001), 19

Treister E. & Urry M., ApJ **630** (2005), 115

Trümper, J., in *Advances in Space Research* **3** (1984), 483

Tueller, J., et al. 2005, ATel, 668

Tueller, J., et al. 2005, ATel, 669

Turner, T. J., & Pounds, K. A., MNRAS **240** (1989), 833

Ueda, Y., et al., ApJ **598** (2003), 88

Urry, C. M., & Padovani, P., PASP **107**, 803

van Allen, J. A., in *Radiation belts around the earth* (1958), San Francisco: Freeman

Veilleux, S., & Osterbrock, D. E., ApJS **63** (1987), 295

von Montigny, C., et al., ApJ **440** (1995), 525

Wang, J. X., et al., ApJ in press, astro/ph-0611251

Weisskopf, M. C., ApL&C (1987) **26**, 1

Weisskopf, M. C., et al., PASP **114** (2002), 1

Winkler, C., et al., A&A **411** (2003), L1

Woltjer, L., in *Active Galactic Nuclei* (1990), ed. T.J.-L. Courvoisier & M. Mayor, 1

Wood, K. S., et al., ApJS **56** (1984), 507

Worsley, M. A., et al., MNRAS **137** (2005), 1281

Wright, E. L., et al., ApJ **420** (1994), 450

Wunderer, C. B., *Imaging with the Test Setup for the Coded-Mask INTEGRAL Spectrometer SPI*, Dissertation thesis (2002), Technischen Universität München

Zamorani, A., in Proceedings of: *Extragalactic Background Radiation: a meeting in honor of Riccardo Giacconi* (1994), Cambridge Univ. Press, 37 1994

Zdziarski, A.A., et al., ApJ **405** (1993), 125

Zoglauer, A., *First Light for the Next Generation of Compton and Pair Telescopes*, Dissertation thesis (2005), Technische Universität München, available at *http://www.mpe.mpg.de/gamma/instruments/mega/www/documents/thesis/-PhD_AndreasZoglauer.pdf*.

Zombeck, M. V.: *Handbook of Sapce Astronomy and Astrophysics*, Cambridge University Press, Cambridge (1990)

Acknowledgments

Sovvertendo l'ordine nella mia terza, e si spera ultima, tesi incomincio dai ringraziamenti meno formali. La prima persona e' in questo caso Enrico, un amico straordinario. Grazie per avermi organizzato la festa piu' bella di sempre e per essermi sempre vicino. Il resto dei miei amici non e' da meno: Dani, Pietro, Rasmus, Fabio, Andrea, Giuseppe, Ceci; un grazie di cuore per il tempo passato insieme, per essere venuti a Monaco, per avermi strappato un sorriso e per non avermi mai e dico mai permesso di sentirmi solo. Guidonio e' sempre stato il primo a venirmi a trovare in tutti i posti dove mi sia spostato, grazie fratellino. Ciccio un grazie se lo merita per la sua simpatia e per tutti i caffe' che gli devo! E come non ringraziare la simpatia scodinzolante di Mister balu' ? Un grazie a tutta la combriccola degli Italiani (abitanti di Garching e non): Paola, Nico, Elena, Elisabetta, Filiberto, Mattia e Betta. Il ringraziamento finale e' sempre per i miei genitori che piu' di tutti mi hanno sempre appoggiato nelle mie scelte.

Now it is time for the more formal acknowledgments. I thank all the gamma group members for the nice time spent together. In particular I thank my three supervisors, Jochen Greiner, Gottfried Kanbach and Andy Strong: thanks for being always available for discussions of every kind and accepting all my questions. I am grateful to Jochen especially for forcing me to submit all kind of proposals, thus allowing to widen my scientific interests, and for supporting me in so many travels. I thank my office mate, Abdullah Yoldas, for all his help (and for his friendship) during the "coding-phase" of my thesis; without his computer skills I would have never managed to accomplish all the work presented here. I acknowledge all the help received by the two MEGA-men, Andreas Zoglauer and Robert Andritschke, during the first months of my PhD when I was dealing with the great MEGA prototype and its ACS.
I am grateful to Arne Rau for proof-reading whatever text I sent him and for the many suggestions I received. Many thanks also to Dave Willis for all his help and assistance for the X-ray background measurement with BAT. I also thank the International Max-Planck Research School on Astrophysics which gave the opportunity of being here.

Oversea thanks go to all BAT-team members; in particular I am grateful to Jack Tueller, Craig Markwardt and Neil Gehrels for interesting discussions, for accepting me in the team and for supporting many of the visits to Goddard.